TURUN YLIOPISTO
UNIVERSITY OF TURKU

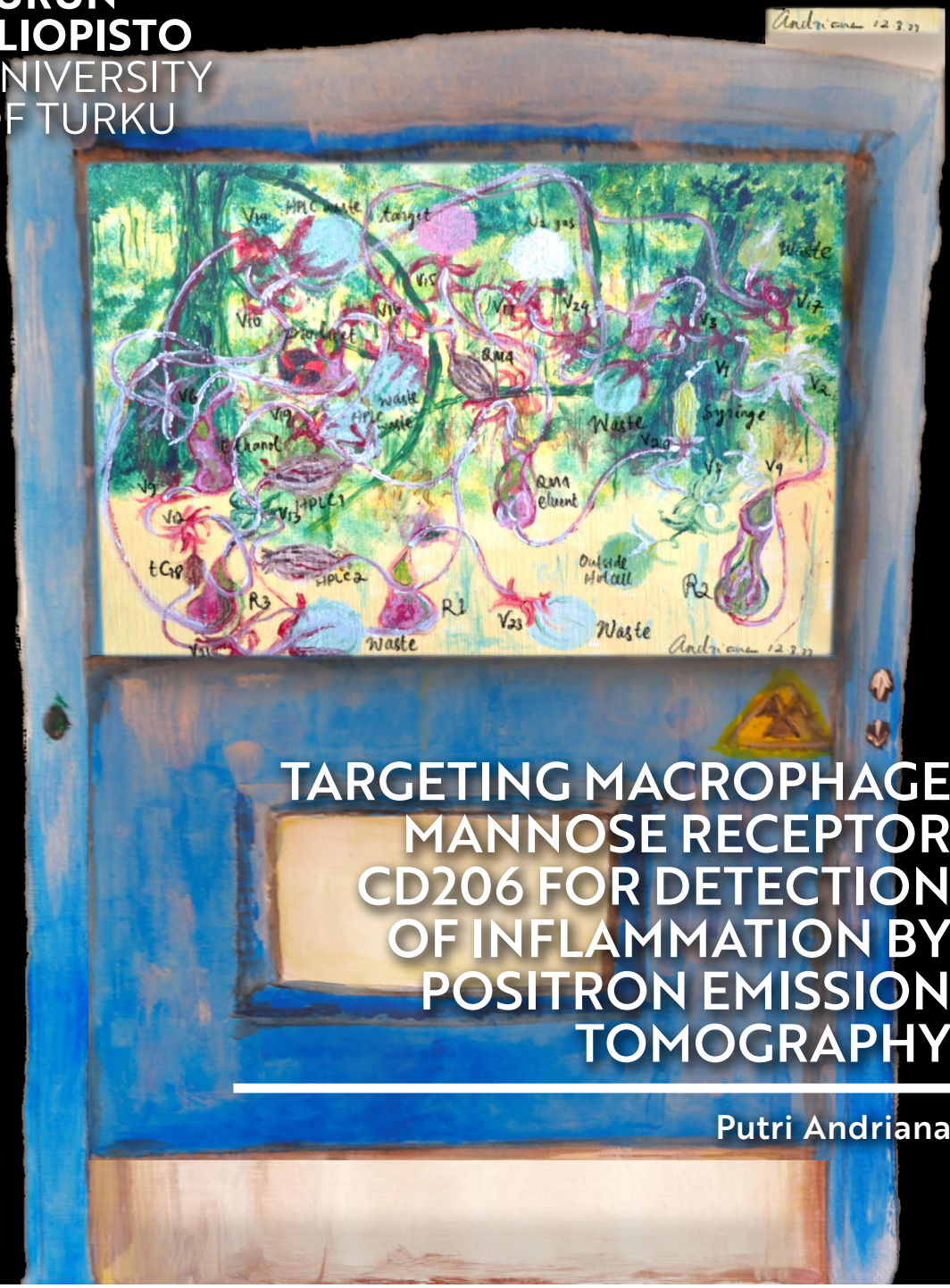

TARGETING MACROPHAGE MANNOSE RECEPTOR CD206 FOR DETECTION OF INFLAMMATION BY POSITRON EMISSION TOMOGRAPHY

Putri Andriana

TURUN YLIOPISTON JULKAISUJA – ANNALES UNIVERSITATIS TURKUENSIS
SARJA – SER. D OSA – TOM. 1895 | MEDICA – ODONTOLOGICA | TURKU 2025

TURUN
YLIOPISTO
UNIVERSITY
OF TURKU

TARGETING MACROPHAGE MANNOSE RECEPTOR CD206 FOR DETECTION OF INFLAMMATION BY POSITRON EMISSION TOMOGRAPHY

Putri Andriana

TURUN YLIOPISTON JULKAISUJA – ANNALES UNIVERSITATIS TURKUENSIS
SARJA – SER. D OSA – TOM. 1895 | MEDICA – ODONTOLOGICA | TURKU 2025

University of Turku

Faculty of Medicine
Department of Clinical Medicine
Clinical Physiology and Nuclear Medicine
Drug Research Doctoral Programme
Turku PET Centre

Supervised by

Professor Anne Roivainen, PhD
Turku PET Centre
and Turku Center for Disease Modelling
University of Turku
Turku, Finland

Professor Antti Saraste, MD, PhD
Heart Center and Turku PET Centre
University of Turku and
Turku University Hospital
Turku, Finland

Assistant Professor Xiang-Guo Li, PhD
Turku PET Centre
and Department of Chemistry
University of Turku
Turku, Finland

Reviewed by

Professor Olof Eriksson, PhD
Department of Medicinal Chemistry
Uppsala University
Uppsala, Sweden

Assistant Professor Outi Keinänen, PhD
Department of Chemistry
University of Alabama at Birmingham
Birmingham, United States

Opponent

Professor Adriana Tavares, PhD
Institute of Neuroscience and Cardiovascular Research (INCR)
Edinburgh Imaging
University of Edinburgh
Edinburgh, United Kingdom

Cover Image: Biosynthesis in a hot cell / Oil and acrylic paint by Putri Andriana

ISBN 978-952-02-0253-8 (PRINT)
ISBN 978-952-02-0254-5 (PDF)
ISSN 0355-9483 (Print)
ISSN 2343-3213 (Online)
Painosalama, Turku, Finland 2025

To past, present and future

UNIVERSITY OF TURKU
Faculty of Medicine
Department of Clinical Medicine
Clinical Physiology and Nuclear Medicine
Turku PET Centre
PUTRI ANDRIANA: [Targeting Macrophage Mannose Receptor CD206 for Detection of Inflammation by Positron Emission Tomography]
Doctoral Dissertation, 216 pp.
Drug Research Doctoral Programme
July 2025

ABSTRACT

Inflammation is a regulated adaptive response that protects the body's normal function and homeostasis. However, when dysregulated, it can contribute to the development of chronic disease. Chronic cardiovascular diseases, such as atherosclerosis, can lead to myocardial infarction, in which the cardiomyocyte death is recognized as an inflammatory stimulus. Macrophages, professional phagocytes involved in the regulation of inflammation, can be polarized into M1 and M2 phenotypes depending on the mediators present in their microenvironment. The increase of M2 macrophages is a hallmark of the anti-inflammatory phase, as they play a significant role in resolving the inflammatory process, including cardiac healing after MI.

The aim of this thesis was to develop and preclinically evaluate a novel positron emission tomography (PET) tracer for targeted M2 macrophage imaging. [^{18}F]AlF-NOTA-D10CM, a fluorinated, mannosylated dextran derivative, was designed to recognize the mannose receptor CD206, which is predominantly expressed on M2 macrophages. To evaluate the suitability of [^{18}F]AlF-NOTA-D10CM for PET imaging, studies were conducted on cells and experimental animals.

In vitro cell studies revealed that [^{18}F]AlF-NOTA-D10CM selectively binds to CD206-positive M2 macrophages, and the results were further confirmed *in vivo* using CD206 deficient versus wild-type mice. [^{18}F]AlF-NOTA-D10CM PET enabled the detection of skin inflammation and lymph node activation in mice as well as inflammation associated with experimental acute MI in rats. Immunostaining of tissue samples verified that tracer uptake positively correlated with the amount of the macrophage mannose receptor CD206.

In summary, these results demonstrate that [^{18}F]AlF-NOTA-D10CM is a valid tool for PET imaging of CD206-positive M2 macrophages, and for non-invasive assessment of inflammation.

KEYWORDS: PET, M2 macrophage, macrophage mannose receptor CD206, fluorine-18, inflammation, myocardial infarction.

TURUN YLIOPISTO
Lääketieteellinen tiedekunta
Kliininen Laitos
Kliininen fysiologia ja isotooppilääketiede
PET-keskus
PUTRI ANDRIANA: [Makrofagin mannoosireseptori CD206:ään kohdentuva positroniemissiotomografia tulehduksen havaitsemiseksi]
Väitöskirja, 216 s.
Lääketutkimuksen tohtoriohjelma (DRDP)
Heinäkuu 2025

TIIVISTELMÄ

Inflammaatio eli tulehdustila on kehon säädelty vaste ulkopuolisille ärsykkeille, jonka tarkoituksena on suojata kehon normaalia toimintaa ja ylläpitää homeostaasia. Säätelyn epäonnistuessa tulehdus voi kuitenkin edistää kroonisten tautien, kuten sydän- ja verisuonisairauksien, kehittymistä. Esimerkiksi ateroskleroosi voi johtaa sydäninfarktiin, jossa sydänlihassolujen kuolema aiheuttaa tulehdustilan. Makrofagit ovat syöjäsoluja, jotka osallistuvat tulehduksen säätelyyn. Ne voivat erilaistua mikroympäristön välittäjäaineiden vaikutuksesta M1- ja M2-fenotyypeiksi. M2-makrofagien lisääntyminen on merkki tulehdusta hillitsevästä vaiheesta, ja ne ovat tärkeitä tulehduksen lievittämisessä, kuten sydäninfarktin jälkeisessä paranemisessa.

Tämän väitöskirjan tavoitteena oli kehittää ja prekliinisesti arvioida uutta positroniemissiotomografia (PET)–merkkiainetta, jota voidaan käyttää kohdennettuun M2-makrofagikuvantamiseen. Kyseessä on [^{18}F]AlF-NOTA-D10CM, fluorinoitu, mannosyloitu dekstraanijohdannainen, joka on suunniteltu tunnistamaan mannoosi-reseptori CD206, jota esiintyy pääasiassa M2-makrofageissa. Tutkimukset tehtiin sekä soluilla että kokeellisilla eläinmalleilla, jotta voitiin arvioida merkkiaineen soveltuvuutta PET-kuvantamisessa.

In vitro solututkimukset osoittivat, että [^{18}F]AlF-NOTA-D10CM sitoutuu selektiivisesti CD206-positiivisiin M2-makrofageihin. Nämä tulokset vahvistettiin *in vivo* kokeilla, joissa käytettiin sekä CD206-puutteisia että villityypin hiiriä. PET-kuvantaminen mahdollisti ihotulehduksen ja imusolmukkeiden aktivoitumisen havaitsemisen hiirillä sekä kokeelliseen akuuttiin sydäninfarktin aiheuttaman tulehduksen tunnistamisen rotilla. Kudosnäytteiden vasta-ainevärjäys vahvisti, että merkkiaineen kertyminen kudokseen korreloi positiivisesti makrofagien mannoosi-reseptori CD206:n määrän kanssa.

Yhteenvetona voidaan todeta, että [^{18}F]AlF-NOTA-D10CM soveltuu hyvin CD206-positiivisten M2-makrofagien PET-kuvantamiseen ja tulehduksen arviointiin tutkittavassa, kajoamatta kehoon merkittävästi.

AVAINSANAT: PET, M2-makrofagit, makrofagin mannoosi-reseptori CD206, fluori-18, tulehdus, sydäninfarkti.

Table of Contents

Abbreviations

APCs	Antigen-presenting cells
AT1R	Angiotensin II subtype 1 receptor
CCR2	C-C chemokine receptor type 2
CD	Cluster of differentiation
$CD206^{-/-}$	CD206 deficient
CFA	Complete Freund's adjuvant
CHO	Chinese hamster ovary
CRD	Carbohydrate recognition domain
CT	Computed tomography
CTLD	C-type lectin domains
CysR	Cysteine-Rich
D10CM	Dextran10-cysteine-mannose
DAB	3,3′-Diaminobenzidine
DAMPs	Damage-associated molecular patterns
DAPI	4′,6-diamidino-2-phenylindole
DTPA	Diethylene triamine pentaacetic acid
EOS	End of synthesis
FAP	Fibroblast activation protein
FBA	*N*-(maleoylethyl-4)-[^{18}F]fluorobenzamide
FDG	[fluorine-18]fluoro-2-deoxy-D-glucose
FNEM	*N*-(2-(2,5-dioxo-2,5-dihydro-1H-pyrrol-1-yl)ethyl)-6-fluoronicotinamide
FNII	Fibronectin type II domain
GC	Gas chromatography
GLUT	Glucose transporter
GMP	Good manufacturing practice
H&E	Hematoxylin-eosin
H3L1	1,4,7-tris(2-hydroxybenzyl)-1,4,7-triazacyclononane
H3L3	2-(mercapto)ethylaminoacetyl-L-cysteine
H3RESCA	Tetrafluorophenyl ester derivative of restrained complexing agent
HEPES	*N*-(2-hydroxyethyl)piperazine-*N'*-(2-ethanesulfonic acid)

HPLC	High-performance liquid chromatography
IFN-γ	Interferon-gamma
Ig	Immunoglobulin
IHC	Immunohistochemistry
IL	Interleukin
ILC	Innate lymphoid cell
iNOS	Nitric oxide synthase
K_D	Dissociation constant
KO	Knockout
LAD	Left anterior descending
LAL	Limulus amebocyte lysate
LAMPs	Lifestyle-associated molecular patterns
LN	Lymph node
LPS	Lipopolysaccharide
LV	Left ventricle
M0	Non-activated macrophages
M1 / M2	Macrophage type 1 / macrophage type 2
MHC-II	Major histocompatibility complex class II
MI	Myocardial infarction
MMR	Macrophage mannose receptor
MRC-1	Mannose receptor C-type 1
MRI	Magnetic resonance imaging
MSA	Mannosylated serum albumin
NaOAc	Sodium acetate
NALP3	Nucleotide-binding-domain, leucine-rich–containing family, pyrin domain-containing-3
Nb	Nanobody
NHS	N-hydroxysuccinimide
NK	Natural killer
NLRs	Nod-like receptors
NMR	Nuclear magnetic resonance
NODA	1,4,7-triazacyclononane-1,4-diacetic acid
NODAGA	2-(4,7-bis (carboxymethyl)-1,4,7-triazonan-1-yl) pentanedioic acid
NOTA	1,4,7-triacyclononane-1,4,7-triacetic acid
OSEM-3D	Ordered subsets expectation maximization 3-dimensional
PAMPs	Pathogen-associated molecular patterns
PBMC	Peripheral blood mononuclear cell
PBS	Phosphate-buffered saline
PDGF	Platelet-derived growth factor
PET	Positron emission tomography

PLA(2)R	Phospholipase A(2) receptor
PMN	Polymorphonuclear neutrophil
PRR	Pattern recognition receptor
PSL	Photostimulated luminescence
PSMA	Prostate specific membrane antigen
QMA	Quaternary methyl ammonium
RAS	Renin-angiotensin system
RCP	Radiochemical purity
RGD	Arginyl-Glycyl-Aspartic acid
ROI	Region of interest
ROS	Reactive oxygen species
SD	Standard deviation
sdAb	Specialized domain antibody
SFB	*N*-(hydroxysuccimidyl)-[^{18}F]fluorobenzoate
SPECT	Single photon emission computed tomography
SSRT-2	Somatostatin receptor-2
SUV	Standardized uptake value
TAC	Time-activity curve
TAM	Tumor-associated macrophage
TBR	Target-to-background ratio
Tc	Cytotoxic T cells
TCRs	T-cell receptors
TFA	Trifluoroacetic acid
TGF-β	Transforming growth factor-beta
Th cells	T helper cells
TLC	Thin-layer chromatography
TLR	Toll like receptor
TNF	Tumor necrosis factor
Treg cell	Regulatory T cell
TRIB1	Tribbles pseudokinase 1
TSPO	18 kDa translocator protein
UPLC	Ultra-performance liquid chromatography
UV	Ultraviolet
VEGF	Vascular endothelial growth factor
WT	Wild-type

List of Original Publications

This dissertation is based on the following original publications, which are referred to in the text by their Roman numerals:

I Putri Andriana, Konstantina Makrypidi, Heidi Liljenbäck, Johan Rajander, Antti Saraste, Ioannis Pirmettis, Anne Roivainen, Xiang-Guo Li. Aluminum fluoride-18 labeled mannosylated dextran: radiosynthesis and initial preclinical positron emission tomography studies. *Molecular Imaging and Biology*, 2023; 25: 1094–1103. https://doi.org/10.1007/s11307-023-01816-7

II Putri Andriana, Ruth Fair-Mäkelä, Heidi Liljenbäck, Salli Kärnä, Imran Iqbal, Konstantina Makrypidi, Johan Rajander, Ioannis Pirmettis, Xiang-Guo Li, Sirpa Jalkanen, Antti Saraste, Marko Salmi, Anne Roivainen. Macrophage mannose receptor CD206 targeting of fluoride-18 labeled mannosylated dextran: A validation study in mice. *European Journal of Nuclear Medicine and Molecular Imaging*, 2024; 51: 2216–2228. https://doi.org/10.1007/s00259-024-06686-x

III Putri Andriana, Heidi Liljenbäck, Senthil Palani, Imran Iqbal, Vesa Oikonen, Jenni Virta, Konstantina Makrypidi, Johan Rajander, Erika Atencio Herre, Aino Suni, Sirpa Jalkanen, Juhani Knuuti, Luisa Martinez-Pomares, Ioannis Pirmettis, Xiang-Guo Li, Antti Saraste, Anne Roivainen. Macrophage mannose receptor CD206-targeted PET imaging in experimental acute myocardial infarction. *EJNMMI Research,* 2025; 15: 66. https://doi.org/10.1186/s13550-025-01254-2

1 Introduction

Inflammation is a manifestation of adaptive defence mechanism where the immune cells recognize and control the pathogen clearance or eliminate the inflammatory response triggers, to restore the homeostasis in injured tissues regardless of the causes. (Tracey *et al*., 2006; Cronkite *et al*., 2018). A controlled inflammatory response is beneficial for the physiological function and homeostasis recovery. However, when the inflammation process fails to eliminate its cause and the damage is not repaired, inflammation become persistent and dysregulated and this switches the beneficial adaptive response to maladaptive function and detrimental (Okin *et al*., 2013). Inflammation contributes to the development of many modern human diseases caused by the failure to adapt to changes in current lifestyle and environment, such as obesity, cancer, neurodegenerative diseases and atherosclerosis that can manifest as myocardial infarction (MI) (Furman *et al*., 2019). In this context, understanding and monitoring inflammation is critical for precise diagnosis and effective therapeutic strategies.

Positron emission tomography (PET) remains a cutting-edge molecular imaging technique that provides real-time information on tissue molecular function, making it invaluable for the detection of inflammation and the development of radiopharmaceuticals (Berger, 2003; Son *et al*., 2019). While glucose analogue 2-[fluorine-18]fluoro-2-deoxy-D-glucose ([^{18}F]FDG) remains the golden standard for PET detection routine worldwide, its unavoidable lack of specificity can result in false positives, thus limiting its diagnosis accuracy (Fletcher *et al*., 2008; Shreve *et al*., 1999). To overcome this limitations, the development of new PET tracers targeting specific inflammatory cell biomarkers such as macrophages, has been one of the focuses of recent PET tracer development. Macrophages are essentially involved in inflammatory cascade during pro-inflammatory state: macrophage type 1 (M1), and anti-inflammatory state: macrophage type 2 (M2). Among these two, M2 macrophages are of particular interest in this thesis subject, due to their association with tissue repair and resolution of inflammation. Mannose receptor cluster of differentiation 206 (CD206), which is predominantly expressed on M2 macrophages, presents an ideal target for PET imaging to specifically detect inflammation. With this background information, this dissertation explores the

potential of macrophage mannose receptor CD206-targeting for detection of inflammation by PET imaging. The study design is illustrated in **Figure 1** and outlines the process starting with the development of the PET tracer, followed by *in vivo* evaluation in an animal model. We developed the Fluorine-18 labeled mannosylated dextran derivative: dextran10-cysteine-mannose (D10CM) using aluminum fluoride-18 ([^{18}F]AlF) chelation technique, yielding [^{18}F]AlF-NOTA-D10CM with excellent *in vivo* and *in vitro* stability. Then, we investigated [^{18}F]AlF-NOTA-D10CM uptake in macrophage mannose receptor CD206 rich tissues in healthy Sprague Dawley rats (**Study I**). Further, in mouse skin inflammation model, we evaluated the [^{18}F]AlF-NOTA-D10CM uptake in the inflamed area during acute and chronic inflammatory phases (**Study II**). Finally, [^{18}F]AlF-NOTA-D10CM was evaluated for its ability to detect inflammation following acute myocardial infarction in a permanent coronary artery ligation model (**Study III**).

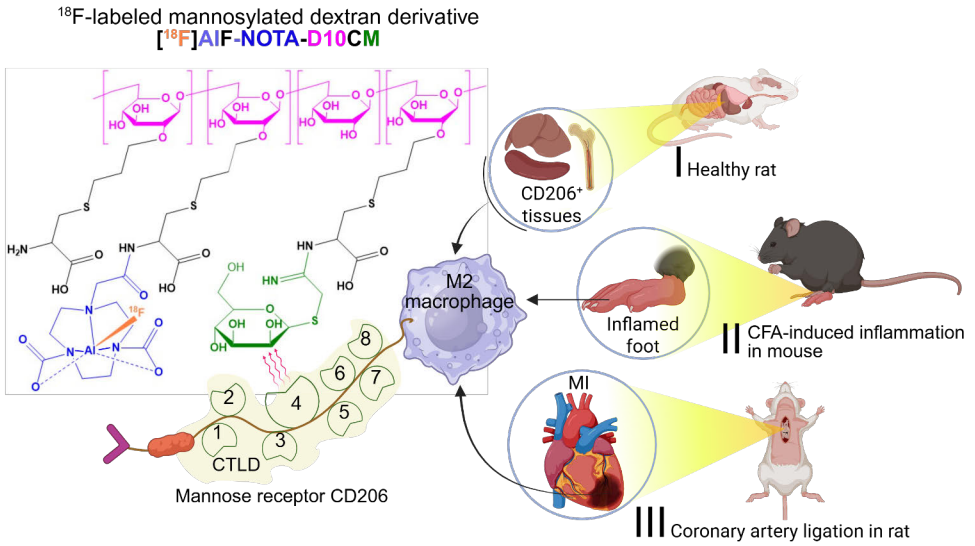

Figure 1. Study plan for dissertation project: Targeting macrophage mannose receptor CD206 for detection of inflammation by positron emission tomography using [^{18}F]AlF-NOTA-D10CM. Three sub-projects are included to evaluate [^{18}F]AlF-NOTA-D10CM PET in (I) healthy rats, (II) mice with skin inflammation and lymph node activation, and (III) rats with acute myocardial infarction.

2 Review of the Literature

2.1 Inflammation

A brief historical perspective

Signs of morbid phenomena were observed in the bones of dinosaurs, and similar signs were later found in early humanoids and Homo sapiens (Cavilling, 2021). The term "inflammation," derived from the Latin *inflammare* (to set on fire), was first used to describe these phenomena (Scott *et al*., 2004). In the 5th century BC, Hippocrates defined inflammation as part of the healing process following injury, using the term *edema* to describe it. Aulus Cornelius Celsus (30 BC – 45 AD) identified the four cardinal signs of inflammation: *rubor* (redness), *calor* (heat), *tumor* (swelling), and *dolor* (pain). Aelius Galenus (130 – 200 AD) later added a fifth sign, *functio laesa* (loss of function), completing the classic signs of inflammation (Punchard *et al*., 2004). In 1858, the father of modern pathology, Rudolf Virchow, incorporated the loss of function into his theory of inflammation, recognizing it as a universal sign that accompanies all inflammatory phases, while the Celsus's four cardinal signs are primarily applied to acute inflammation caused by wounds and infections. The work of Virchow shifted the understanding of inflammation from an imbalance of the four signs at the surface level to a cellular basis for the pathology of inflammation (Medzhitov, 2010). Later, in 1892, another major breakthrough by Eli Metchnikoff, was the discovery of phagocytosis by macrophages and microphages (neutrophils), which are involved in defense mechanisms following inflammatory cascade (Tauber, 2003). The first precise diagnosis of an inflammatory disorder was made by Sir Marc Armand Ruffer (1859 – 1917), who identified atherosclerosis in the mummified remains of an Egyptian pharaoh (Cavaillon, 2021). The evolution of inflammation is depicted in **Figure 2**.

What exactly is inflammation (and what is not?) Is inflammation always destructive?
(Oronsky *et al*., 2022).

Inflammation has traditionally been regarded as a detrimental pathological condition requiring intervention and suppression (Fioranelli *et al*., 2021). This

perception is further reinforced by the promotion of terminology such as anti-inflammatory agents or inflammation inhibitors (Oronsky *et al*., 2022). Although this viewpoint contains elements of truth, it fails to acknowledge the essential physiological roles of the inflammatory response. An effective acute inflammatory reaction leads to the clearance of infectious agents and subsequently facilitates the healing process (Medzhitov, 2008).

Accordingly, is inflammation always protective?

There is no definitive answer to this. The role of inflammation as a protective mechanism is complex and lacks a definitive dichotomy. Inflammation is characterized by its non-binary nature and is not governed by a singular regulatory pathway (Scott *et al*., 2004). The intricate interplay of molecular, immunological, and physiological processes that occur during the inflammatory response complicates the precise characterization of inflammation (Netea *et al*., 2018). In contemporary understanding, inflammation is recognized as a protective biological response elicited by harmful stimuli, including pathogenic infections, toxic substances, and endogenous signals arising from cellular damage due to tissue injury. This multifaceted response encompasses the eradication of the primary cause of tissue injury, the removal of necrotic cells, and subsequent tissue repair (Netea *et al*., 2018; Medzhitov, 2008). While inflammation is a fundamental aspect of the immune response to infection, it can become detrimental when excessive or uncontrolled, leading to chronic inflammatory conditions (Bennet *et al*., 2018). The successful resolution of inflammation hinges on the equilibrium between pro-inflammatory mediators that initiate pathogen clearance and anti-inflammatory factors that promote the cessation of the inflammatory process (Caches *et al*., 2018).

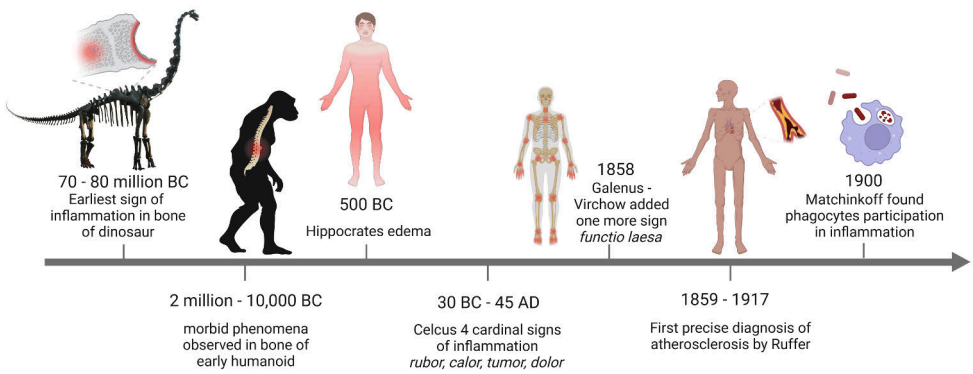

Figure 2. Time line of inflammation concept evolution from Mesozoic to modern human era, until the discovery of phagocytes involvement.

Modern human inflammatory diseases

Human evolution has been shaped significantly by environmental factors, leading to adaptations in the immune system aimed at achieving homeostasis in response to these changes. Over extended evolutionary timeframes, the inflammatory response has been fine-tuned, albeit at the expense of normal tissue function (*trade off*). This evolutionary optimization has resulted in an equilibrium that is specifically tailored to specific environmental conditions (Medzhitov *et al*., 2010; Okin *et al*., 2012). However, the current rapid environmental changes have outpaced the rate at which human physiology can adapt, creating a *mismatch* whereby the evolutionary characteristics of the immune system fail to align with modern environmental conditions. This discordance contributes to dysregulated inflammation and the emergence of inflammatory-related pathologies (Okin *et al*., 2012; Chen *et al*., 2017). For instance, the human mucosal epithelia, which have evolved to protect against particulate matter and infectious agents, may, when excessively protective, impair diffusion and overall function. This impairment can increase susceptibility to conditions such as asthma and allergies (Palm *et al*., 2012). Likewise, adaptations that favored energy storage during periods of scarcity, such as famines, now predispose individuals to obesity and sedentary lifestyles in modern contexts (Speakman, 2007). A variety of modern diseases, including cardiovascular conditions such as atherosclerosis, obesity, certain cancers, neurodegenerative disorders, and type 2 diabetes mellitus, are increasingly recognized as manifestations of the imbalance between the costs and benefits of the inflammatory response (Okin *et al*., 2012).

2.1.1 Acute and chronic inflammation

Inflammation may present as acute, characterized by the extravasation of leukocytes, predominantly neutrophils, which are programmed to reinforce resolving the inflammatory response. Acute inflammation resolution process can ideally last for days to weeks since the inflammatory stimuli eradication until it reaches back the baseline status. However, persistent inflammatory stimuli may lead to the development of chronic inflammation (Furman *et al*., 2019; Kaur *et al*., 2022; Oronsky *et al*., 2022). The inflammatory response generally follows a generic pathway that encompasses four primary components: (1) inducers, (2) sensors, (3) mediators, and (4) effectors (target tissues). (Furman *et al*., 2019; Kaur *et al*., 2022; Oronsky *et al*., 2022). Inducers initiate inflammatory cascade which include infectious (such as lipopolysaccharide from bacteria) and non-infectious stimuli (such as foreign bodies, allergens, and damaged / necrotic cells signals). These inducers activate sensors, which are specialized molecules (e.g. toll like receptor 4 (TLR4), IgE, Nucleotide-binding-domain, leucine-rich–containing family, pyrin

domain–containing-3 (NALP3), Hageman factor) that can stimulate the inflammatory mediators (e.g. tumor necrosis factor- α (TNF-α), interleukin-6 (IL-6), PGE_2, interleukin-1 β (IL-1β). The mediators are responsible for eliciting the cardinal signs of inflammation and activating the effectors, which include various tissues and cells implicated in the inflammatory response (e.g., endothelial cells, hepatocytes, leukocytes, hypothalamus, and smooth muscle cells) (Varela *et al*., 2018; Medzhitov, 2010).

2.1.1.1 Acute inflammation

Acute inflammation requires the presence of external stimuli (Abudukelimu *et al*., 2018). These stimuli may be classified into infectious agents, such as bacteria, viruses, fungi, and parasites, or non-infectious factors, including physical trauma, foreign objects, chemical substances, toxins, cancer cells, biological damage, and psychological stressors. Both infectious and non-infectious triggers can elicit similar inflammatory responses (Marshall *et al*., 2018; Chen *et al*., 2017).

Upon exposure to these stimuli, pattern recognition receptors (PRRs) located on immune and non-immune cells recognize pathogen-associated molecular patterns (PAMPs) or danger signals released by damaged or necrotic cells, known as damage-associated molecular patterns (DAMPs). These PRRs sensors then activate the innate immune cells and pro-inflammatory cascade (Li *et al*., 2021).

Following PRR activation, inflammatory stimuli, including microbial products and cytokines, engage with specific receptors such as Toll-like receptors (TLRs), interleukin-1 (IL-1) receptors, IL-6 receptors, and tumor necrosis factor (TNF) receptors (Li *et al*., 2021). This receptor-ligand interaction promotes the production of various inflammatory mediators, including cytokines and chemokines, such as TNF-α, IL-1, and IL-6, as well as prostaglandins (Abdulkhaleq *et al*., 2018; Turner *et al*., 2014). These inflammatory mediators exert effects on multiple organs and tissues, including the heart, pancreas, liver, kidneys, lungs, brain, gastrointestinal tract, and reproductive system, where they can contribute to both acute and chronic inflammation-related tissue damage (Chen *et al*., 2017).

When the mediators act on local blood vessels in the organs, they induce vasodilation, thereby enhancing the extravasation and influx of neutrophils and plasma components, including antibodies, to the site of inflammation. This process initiates phagocytic activity aimed at eliminating pathogens, clearing infected and necrotic cells, and facilitating tissue repair. The resulting physiological changes manifest as the cardinal signs of inflammation, including edema, exudate formation, and pain (Soares *et al*., 2023; Kany *et al*., 2019; Westman *et al*., 2020). Additionally, the released inflammatory mediators also activate antigen-presenting cells (APCs), such as dendritic cells, macrophages, and B cells, which subsequently interact with T cells,

resulting in the activation of the adaptive immune response, thereby augmenting the overall defense mechanisms (Cronkite *et al*., 2018; Gaudino *et al*., 2019).

In cases where neutrophil response is inadequate, macrophages are recruited from the circulation to aid in the clearance of dead cells and debris and to initiate tissue repair at the affected site (Mosser *et al*., 2021). The acute inflammatory response typically resolves upon the clearance of the inciting stimuli and the repair of damaged tissues (Germolec *et al*., 2018). The resolution of acute inflammation is principally mediated by tissue-resident and recruited macrophages (Serhan *et al*., 2005).

2.1.1.2 Chronic inflammation

Chronic inflammation is the manifestation of unresolved acute inflammation. When the initial inflammatory stimuli persist and fail to be cleared, neutrophils are gradually replaced by increased macrophage infiltration, and more inflammatory mediators are continuously produced. This dysregulation may lead to various chronic diseases, including cancers, type 2 diabetes, rheumatoid arthritis, cardiovascular diseases, and atherosclerosis (Chen *et al*., 2018).

The transition from the acute to the chronic phase of inflammation is characterized by a significant alteration in leukocyte composition. Initially, short-lived neutrophils are replaced by macrophages, lymphocytes, and plasma cells at the site of tissue injury. This shift enhances the production of inflammatory cytokines, growth factors, and enzymes, thereby exacerbating tissue damage and initiating secondary repair mechanisms, including tissue remodeling and the formation of fibrotic scar tissue. Such phenomena are evident in conditions such as post-myocardial infarction cardiac remodeling, granuloma formation resulting from the aggregation of macrophage clusters, and the development of tertiary lymphoid structures (Pahwa *et al*., 2023; Lambert *et al*., 2008; Yousuf *et al*., 2019; Milenkovic *et al*., 2019; Cutolo *et al*., 2019; Needham *et al*., 2019).

Chronic inflammation differs from acute inflammation in several key aspects. It is characterized by a prolonged duration, lasting from months to years, and is marked by persistence and an inability to resolve. The progression of chronic inflammation is gradual and is associated with collateral tissue damage (Pahwa *et al*., 2023; Furman *et al*., 2019). The etiology of the chronic inflammatory phase is not solely attributed to the unsuccessful resolution of acute inflammation. Various triggers, including DAMPs—such as those arising from the exposome, metabolic dysfunction, and tissue injury—and lifestyle-associated molecular patterns (LAMPs), which encompass inflammatory factors derived from specific social, environmental, and lifestyle influences (e.g., excessive cholesterol intake, monosodium urate, oxidized low-density lipoprotein, alcohol consumption, and smoking), can contribute to the development of chronic inflammation (Furman *et al*.,

2019; Oronsky *et al*., 2022). In contrast to the pronounced magnitude typically observed in acute inflammation, the initiation of chronic inflammation is generally characterized by low-grade intensity, often lacking overt signs and symptoms (Fioranelli *et al*., 2021; Furman *et al*., 2019). This phenomenon, referred to as low-grade chronic inflammation, engages immune components that are distinct from those activated during the acute immune response (Chen *et al*., 2019; Furman *et al*., 2019; Kaur *et al*., 2022).

2.1.2 Overview of immune cells in inflammation

Immune cells in general are migratory cells that are able to change their shape and physical characteristics in response to different stimuli as key component of human natural defense against outside invaders (Margraf *et al*., 2022). Within the immune system, distinct lineages of immune cells consist of various subsets, each with specific roles in modulating both immune activation and immune suppression (Fang *et al*., 2018). The diverse subsets of immune cells and their corresponding functions during inflammation can be delineated based on their specific actions and contributions to immune homeostasis. The immune system is commonly divided into two main branches: innate immunity and adaptive immunity, which both are engaged in acute and chronic inflammation (Turvey *et al*., 2010; Bonilla *et al*., 2010; Vaknin *et al*., 2011). Human immune system division and the immune cells are briefly described in **Figure 3**.

Innate immunity constitutes the initial line of defense in the human body, delivering prompt and non-specific protection against a diverse array of pathogens. This system encompasses:

(1) Anatomical barriers, including the integumentary system (skin) and mucous membranes, serve as the initial line of defense in the human body (Chaplin, 2003; Medina, 2016). Additionally, physiological secretions such as tears, sweat, and urine contribute to this defense mechanism by facilitating the expulsion of potential pathogens (Kalló *et al*., 2022).

(2) Physiological barriers encompass various chemical defense mechanisms, including the production of lysozyme and interferon, which establish inhospitable conditions for pathogens. Additionally, the regulation of temperature and pH serves to suppress microbial growth. These factors contribute to the overall efficacy of the immune response (Medina, 2006; Ragland *et al*., 2017; Schieber *et al*., 2016; Costa *et al*., 2022).

(3) Endocytic and phagocytic defenses are mediated by specialized immune cells, including blood monocytes, neutrophils, and tissue macrophages (Medina, 2006; Tan *et al*., 2015; Gordon, 2016). In instances where pathogens evade these anatomical barriers, the innate immune system is activated, engaging

immune cells such as neutrophils, macrophages, and dendritic cells. These cells utilize PRRs to identify conserved structures on pathogens (Thomson *et al*., 2011). Specifically, PRRs detect PAMPs, including lipopolysaccharides (LPS) and RNA, thereby initiating an immune response aimed at eliminating the invading pathogens (Vercammen *et al*., 2008).

(4) Inflammatory response. The inflammatory response is initiated by infection and tissue damage, which serve as triggers for the inflammatory process. These stimuli lead to increased vascular permeability, resulting in the extravasation of fluid that contains serum proteins, including antibodies and bactericidal agents. This vascular response facilitates the rapid recruitment of additional phagocytic cells to the affected area (Medina, 2006; Borton, 2008; Soares *et al*., 2023; Asija *et al*., 2014; Kumar *et al*., 2012).

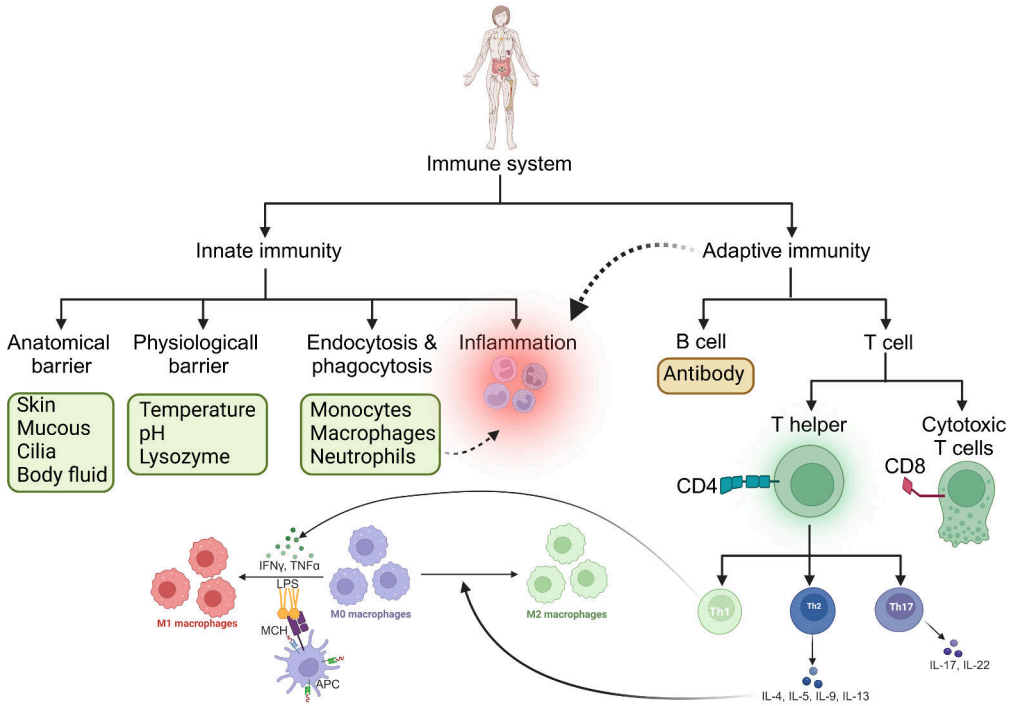

Figure 3. Human immune system is an intricate network of cells and molecules working together to maintain homeostasis and protect the body. Inflammatory response is one of the barrier that bridge innate and adaptive immunity due to the involvement of leukocytes e.g. neutrophils, lymphocytes (T cells, B cells) and mast cells in both phases.

Innate immunity employs numerous cells, including phagocytes (macrophages and neutrophils), dendritic cells, mast cells (which produce cytokines early after infection or injury), basophils, eosinophils, natural killer (NK) cells, innate lymphoid

cells (ILCs, which produce pro-inflammatory cytokines including interleukin-4 (IL-4), interferon- γ (IFN-γ), and interleukin-17 (IL-17) that are needed to direct an appropriate immune response to specific pathogens), and lymphocytes (natural killer T cells) (Takeuchi *et al*., 2010; Kumagai *et al*., 2010; Beutler, 2009; Bedoui *et al*., 2016). Each type of these cells serves a different function and targets different pathogens, which are discussed further in this chapter.

Adaptive immunity is a highly specialized and antigen-specific component of the immune system. It requires a longer activation period compared to innate immunity but offers long-term protection against pathogens (Bonilla *et al*., 2010; Chi *et al*., 2024; Lanier *et al*., 2009). Adaptive immunity is characterized by the ability to recognize specific pathogens through the use of T cells that are activated via APCs and B cells, which further producing antibodies transported by plasma to the site of inflammation (Wang *et al*., 2024). A notable characteristic of adaptive immunity is its ability to retain a memory of previous infections. This immunological memory enables a more rapid and effective response upon subsequent exposure to the same pathogen (Lanier *et al*., 2009).

Innate and adaptive immunity are intertwined to each other during inflammation by immune cells.

Antigen presenting cells

When pathogens bypass the innate immune defenses, adaptive immunity is called upon to target and neutralize specific threats (Farber *et al*., 2016). This process begins with APCs, such as dendritic cells, macrophages and lymphatic B cells, which capture and present pathogen fragments to lymphatic T cells (Netea *et al*., 2019).

Lymphatic cells (T cell and B cell)

Each T cell is equipped with a unique receptor, T-cell receptors (TCRs) that is activated upon recognizing fragments of antigens presented to them by the major histocompatibility complex (MHC) of APCs (Shah *et al*., 2021). These T cells then proliferate and patrol (trafficking) throughout the body via the bloodstream and lymphatic systems, searching for APCs presenting the corresponding antigens. Eventually, they accumulate in lymph nodes after finding the matched APCs (Hunter *et al*., 2016; Bajénoff *et al*., 2003).

T cells then differentiate into different subsets, including T helper (Th) cells and T cytotoxic (Tc) cells. Th cells are CD4+ and function to help coordinate the immune response by releasing cytokines that activate other immune cells (Luckheeram *et al*., 2012). Meanwhile, cytotoxic Tc cells are CD8+ and target and kill infected cells,

tumor cells, or virus-infected cells by inducing apoptosis (Jaime-Sanchez *et al*., 2020).

Several APCs further induce Th cells into subtypes: Th1, Th2, and Th17, each with distinct roles in the immune response (Martynova *et al*., 2022). Th1 cells produce IFN-γ, which promotes the activation of macrophages and promotes macrophage polarization to M1 type macrophages upon exposure to PAMPs, such as LPS during microbial infection (Arora *et al*., 2017). Th1 cells also support B cell differentiation to produce antibodies that aid in pathogen clearance (Mitsdoerffer *et al*., 2010). Th2 cells help to resolve inflammation by releasing cytokines such as IL-4, IL-5, and IL-13, which are necessary mediators to polarize macrophages to the M2 phenotype, which contributes to the resolution of inflammation and becomes the main topic in this dissertation (Liu *et al*., 2014; Gitto *et al*., 2020).

Another T helper cell subset, designated as Th17 cells, is implicated in the pathogenesis of chronic inflammation and autoimmune disorders (Zambrano-Zaragoza *et al*., 2014). Th17 cells are engaged in the persistent inflammatory responses associated with conditions such as rheumatoid arthritis and multiple sclerosis (Waite *et al*., 2012). The equilibrium among Th1, Th2, and Th17 responses is essential for maintaining effective immune function while preventing the excessive inflammatory processes.

B cells, another key player in adaptive immunity, produce antibodies that bind to specific antigens, neutralizing pathogens or marking them for destruction by phagocytes. Antibodies are transported through the bloodstream to sites of infection, where they can bind to and neutralize harmful microbes (Tsai *et al*., 2019). The process of antigen-specific immunity ensures that each pathogen is recognized and eliminated efficiently.

2.2 Macrophages

Macrophages are integral components of the innate immune system, playing pivotal roles in inflammatory responses and exhibiting significant plasticity in their functional adaptations to microenvironmental stimuli (Chen *et al*., 2023; Mosser *et al*., 2008). These cells are involved in a wide array of physiological processes, including the regulation of homeostasis, modulation of immune responses, and facilitation of tissue repair. Under homeostatic conditions, macrophages are designated as homeostatic macrophages (*in vivo*) and baseline macrophages (*in vitro*). During embryonic development, the human organism acquires tissue-resident macrophages from the yolk sac and fetal liver, which are influenced by their specific tissue environments and contribute to local homeostasis. Furthermore, monocyte-derived macrophages migrate from the bloodstream into sites of tissue damage, where they perform essential functions in host defense and facilitate pathological

signaling (Lee *et al*., 2022; Ruytinx *et al*., 2018). Activation of macrophages (**Figure 4**) occurs upon the recognition of stress signals via PRRs, as well as through the engagement of cytokine, chemokine, or growth factor receptors (Schultze *et al*., 2016). Once activated, macrophages maintain their inherent plasticity, allowing them to transition between various functional phenotypes. This adaptability enables them to execute critical roles in immunomodulation, phagocytosis, and antigen presentation (Chen *et al*., 2023). In response to diverse stimuli, macrophages can polarize into distinct functional states, reflecting their ability to adapt and respond to the needs of their microenvironment (Mantovani *et al*., 2004).

The macrophages classification continues to be a topic of considerable discussion within the scientific community. Nevertheless, the traditional designations of M1 and M2 macrophages, along with their respective subtypes, remain widely used for elucidating the role of macrophages in inflammatory processes (Chen *et al*., 2021; Wang *et al*., 2020). This binary classification offers a structured approach to comprehending the anti-inflammatory properties associated with CD206.

M1 and M2 macrophages are often described as pro-inflammatory and anti-inflammatory macrophages, respectively, each demonstrating distinct functional roles (Xia *et al*., 2023). As part of the first line of defense, macrophages engage in phagocytosis to eliminate noxious stimuli. Furthermore, they process and present antigens to guide a specific immune response (Sheu *et al*., 2022). Macrophage polarization is influenced by various inducers of inflammatory pathways (Figure 4) (Zhu, 2015; Nakayama *et al*., 2017; Endo *et al*., 2011; Walker *et al*., 2018; McAleer *et al*., 2008). PRRs, including TLRs and NOD-like receptors (NLRs), expressed on immune cells such as macrophages and dendritic cells, recognize PAMPs like lipopolysaccharides, glycoproteins, or nucleic acids, as well as DAMPs resulting from tissue injury or necrosis, which are often observed following events such as myocardial infarction (Zhao *et al*., 2021; Mogensen, 2009; Tang *et al*., 2012). In response, these immune cells release inflammatory mediators, including cytokines (e.g., IFN-γ, IL-6, IL-1β, TNF-α, chemokines, proteolytic enzymes, and lipid mediators (Medzhitov, 2008).

M1 macrophages are typically activated following the recognition of LPS and IFN-γ, resulting in the secretion of various pro-inflammatory mediators, including IL-6, IL-1β, TNF-α, inducible nitric oxide synthase (iNOS), and various chemokines. These macrophages also exhibit the expression of surface markers such as CD40, CD80, CD86, and major histocompatibility complex class II (MHC-II). M1 macrophages play a pivotal role in the immune defense against pathogens and are instrumental in promoting the T helper 1 (Th1) response during the initial stages of inflammation. Furthermore, they are involved in the generation of reactive oxygen species (ROS), which, while contributing to pathogen elimination, may also lead to

tissue damage and hinder tissue regeneration and wound healing processes (Yadav *et al*., 2022; Zhao *et al*., 2010).

The exact timing of when immune cells begin to produce anti-inflammatory cytokines, such as IL-4, IL-13, IL-10, and transforming growth factor-beta (TGF-β), which initiate the tissue repair or regeneration phase, remains unclear (Nikovics *et al*., 2023). However, it is established that exposure to secreted IL-4 (from granulocytes, T cells, mast cells, macrophages, and many others) and IL-13 (from CD4 T cells, basophils, eosinophils, mast cells, and NK T cells) induces the polarization of M0 macrophages into M2-type macrophages (Paul, 2015; Junttila, 2018; Iwaszko *et al*., 2021; Song *et al*., 2021). M2 macrophages play a crucial role in mitigating inflammation, promoting tissue repair, and aiding in wound healing by secreting additional anti-inflammatory molecules, such as IL-10 and TGF-beta. Notably, these cytokines are not exclusively produced by macrophages; various immune cells can also release both cytokines and their associated receptors to

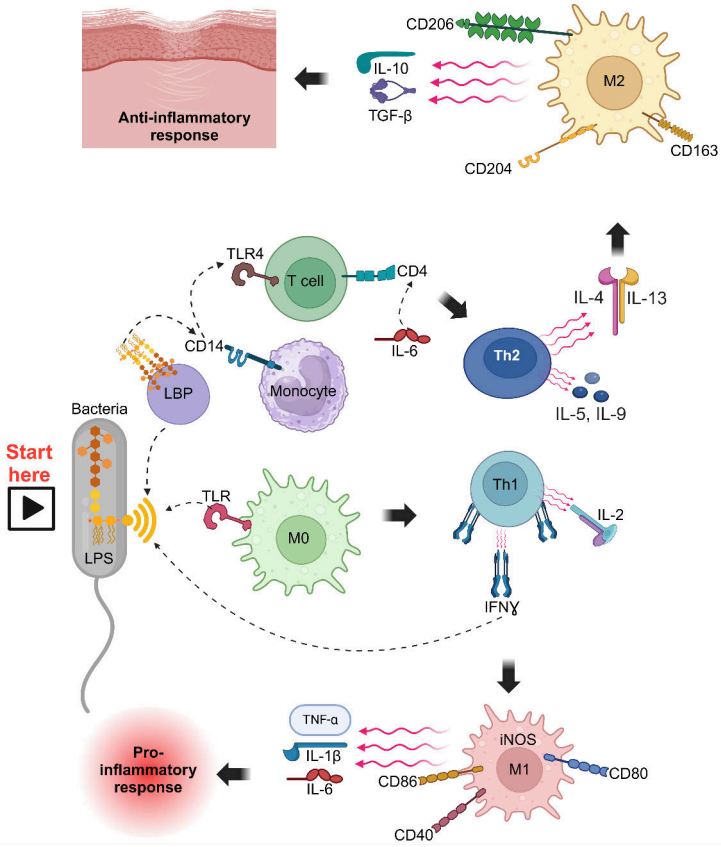

Figure 4. Macrophage polarization from non-activated macrophages (M0) to M1 and M2 type macrophages. The figure illustrates one example of macrophage polarization signaling cascade amongst the other complex polarization pathway.

amplify their functions. For instance, Th2 cells produce IL-4 and IL-13, which facilitate the polarization of macrophages to the M2 phenotype. In turn, M2 macrophages secrete additional anti-inflammatory cytokines, such as IL-10 and TGF-β, contributing to the resolution of inflammation (Wynn *et al*., 2013).

M2 macrophages can be categorized into distinct subtypes, namely M2a, M2b, M2c, and M2d, which are differentiated based on their expression of cell surface proteins, cytokine production, and various other biological functions. Regardless of these subtype-specific characteristics, all M2 macrophages consistently express the mannose receptor CD206 on their cell surfaces. This makes CD206 one of the most specific markers for M2 macrophages, which are activated during the inflammation resolution process (Nikovics *et al*., 2023; Stein *et al*., 1992; Gordon, 2003; Atri *et al*., 2018).

2.3 Macrophage mannose receptor

Mannose is classified as a type of glycan. Glycans, which are also known as carbohydrates, saccharides, or sugars, represent one of the essential macromolecular building blocks of life, found naturally alongside nucleic acids (DNA and RNA), proteins, and lipids (Schnaar, 2016). The human glycome, which is the complete set of glycans, is primarily composed of nine fundamental building blocks: mannose (mannan), glucose, galactose, N-acetylglucosamine, N-acetylgalactosamine, L-fucose, sialic acid, xylose, and glucuronic acid (Schnaar, 2016). These glycan building blocks can covalently bond to proteins or lipids through a process known as glycosylation, resulting in glycoproteins or glycolipids, which play vital roles in cell-cell and pathogen-cell recognition, as well as in the regulation of cellular functions (Reily *et al*., 2019; Loke *et al*., 2016).

Glycoproteins can be classified into two major groups consisting of lectins and glycosaminoglycan-binding proteins (Varki, 2009). Furthermore, lectins are structurally subgrouped into several types, including C-type lectins (Ca^{2+} dependency), P-type lectins (phosphate dependency), I-type lectins (immunoglobulin-like carbohydrate recognition domains), S-type lectins (thiol dependency), and pentameric lectins (pentraxins) (Raposo *et al*., 2021). The mannose receptor family is classified as C-type lectins, with four family members: mannose receptor CD206, also known as the macrophage mannose receptor (MMR) or mannose receptor C-type 1 (MRC-1), due to its predominant expression on the surface of activated macrophages (specifically M2 type), Endo 180 (CD280, MRC-2), DEC-205 (CD205), and phospholipase A(2) receptor (PLA(2)R). All four of these members share a similar domain arrangement, including an N-terminal cysteine-rich (CysR) domain, a single fibronectin type II domain (FNII), and eight to ten C-type lectin-like domains (CTLD) (Boskovic *et al*., 2006).

2.3.1 Mannose receptor CD206 and other types

The mannose receptor CD206 belongs to the mannose receptor family, which also includes three other glycoprotein receptors: the recycling endocytic receptor Endo180 (CD280), the thymic epithelial cell receptor DEC-205 (CD205), and the phospholipase A2 receptor (PLA2R). These four receptors share a common structural framework characterized by a single polypeptide backbone that contains an N-terminal CysR domain, an FNII domain, and eight to ten CTLDs. As depicted in **Figure 5**, the mannose receptor family is categorized as a subgroup within the C-type lectin superfamily. These receptors engage with carbohydrate-containing

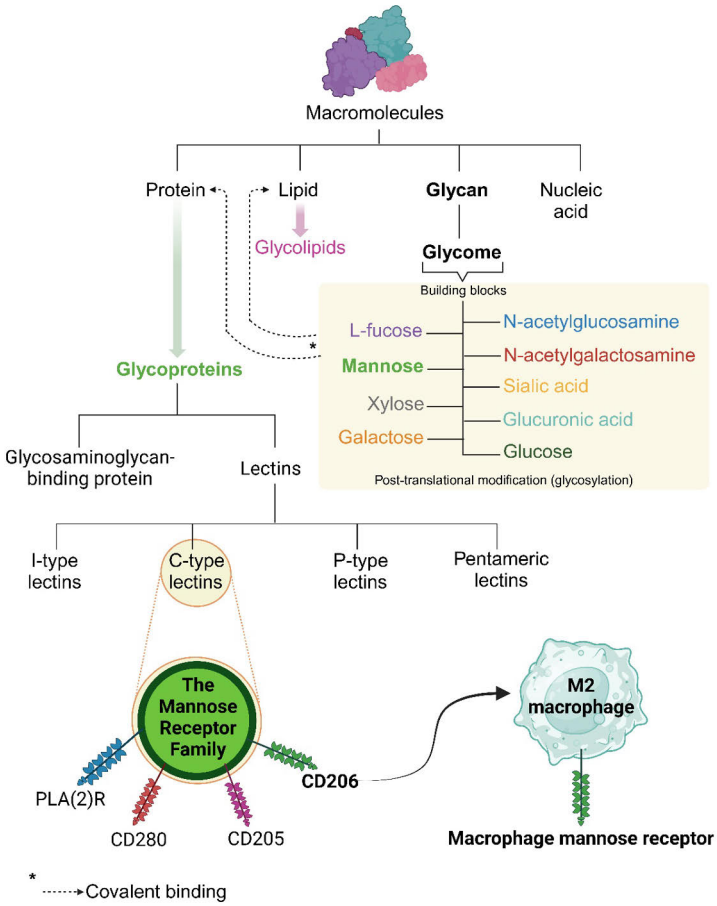

Figure 5. Protein, lipid, glycan and nucleic acid are four major kind of macromolecule, which further modified such as for synthesis of glycoprotein and glycolipid via covalent bonding with building blocks from carbohydrate set (glycome). C-type lectins is one subclass of lectins, which originating from glycoproteins and the Mannose Receptor family belongs to C-type lectins family.

ligands in a calcium-dependent manner and are classified as Type I transmembrane receptors (Boskovic *et al*., 2006; East *et al*., 2002; Brown *et al*., 2018). While they possess similar domains, each receptor employs a specific domain for interaction with its particular ligands, leading to differences in their ability to mediate endocytic and phagocytic pathways (East *et al*., 2002). Given their diverse multidomain structure and multifunctional roles, each member of the mannose receptor family exhibits a unique repertoire of ligands and is integral to the regulation of physiological homeostasis and the innate and adaptive immune responses through sugar ligand recognition (Brown *et al*., 2018; Boskovic *et al*., 2006).

While the family members share common domains, CD206 is the only one with a functional CysR domain that binds sulfated carbohydrates or N-acetylgalactosamine (GalNAc) sulfated. These ligands are found in lymphoid tissues, kidneys, the anterior pituitary (lutropin), and major cat allergens, while the other three family members lack sugar-binding ability in their CysR domains. The conserved FNII domain is functional only in CD206 and Endo180, where it binds collagen, including types I, II, III, IV, and V in CD206 and types I, IV, and V in Endo180. The CTLD domain functions exclusively in CD206 (CTLD4) and Endo180 (CTLD2), both of which are capable of calcium-dependent carbohydrate binding, such as mannose, fucose, or GalNAc. Functional CTLDs are beneficial to the immune system by recognizing and binding endogenous and exogenous molecules, including allergens and pathogens (viruses, fungi, bacteria, and helminths), as discussed in the inflammation chapter (Llorca, 2008; Martinez-Pomares, 2012). Despite both CD206 and Endo180 having functional CTLDs for ligands such as mannose, one study revealed that CTLD2 in Endo180 contacted the CysR domain due to the globular structure of the Endo180 receptor tip, and this unique conformation is suspected to shift the ligand binding to Endo180 (**Figure 6–7**) (Llorca, 2008).

In general, the functional domains of the whole mannose receptor family are to recycle between the plasma membrane and the endosomal environment so that extracellular ligands can be internalized and delivered to the cell interior (Llorca, 2008). Prof. Martinez-Pomares from the University of Nottingham has consisstently conducted remarkable investigations into the mannose receptor CD206 and has been an instrumental source of knowledge on mannose receptor CD206.

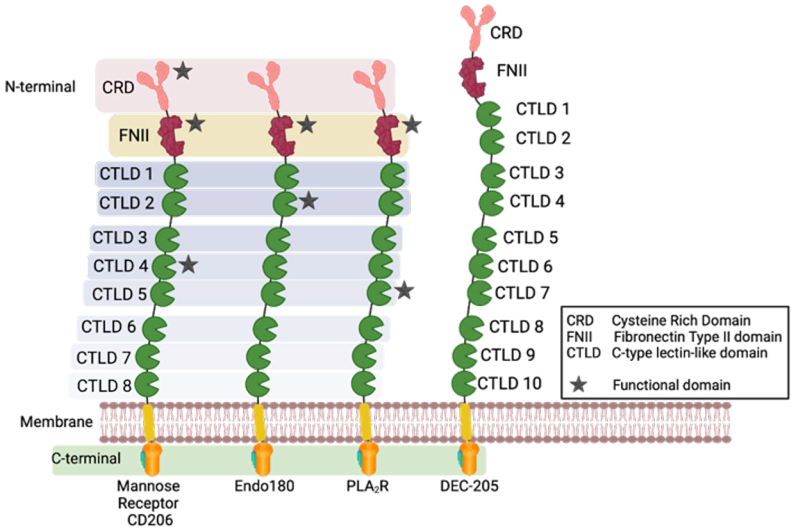

Figure 6. Organization of domains assembling the mannose receptor family members in linear arrangement. The functional domains for ligand interaction are marked with black star. (Modified from Llorca, 2008).

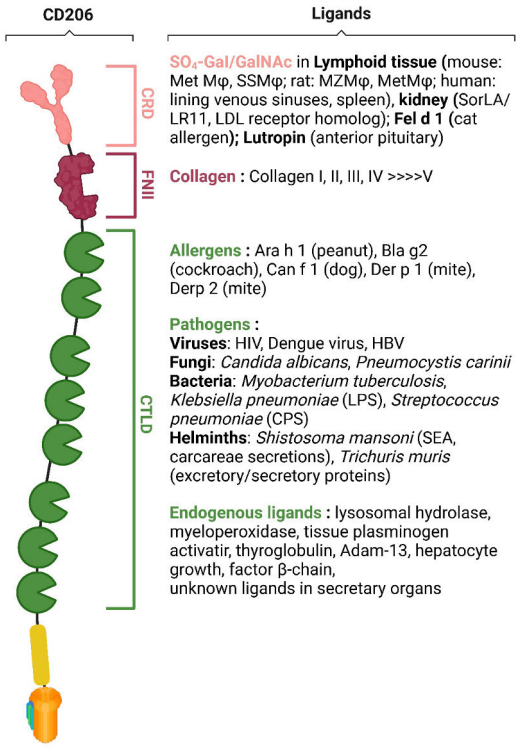

Figure 7. Diagram of ligands for each of functional domain in mannose receptor CD206. (Modified from Martinez-Pomares, 2012).

2.3.2 Mannose receptor role in inflammation

Table 1 Member of the Mannose Receptor family with their different functions and the location where they are expressed.

Family member	Location	Function
CD206 [1-4]	Macrophages, dendritic cells, selective lymphatic, liver endothelial cells	Scavenger of harmful glycoproteins; phagocytosis mediator
Endo180 [5-12]	Mesenchymal cells including fibroblasts and osteogenic cells	Extracellular matrix remodeling through interaction with collagen; pathway of collagen turnover during malignancy, collagen biding receptor
PLA2R [13, 14]	Podocytes	Internalize soluble lipolytic enzymes (PLA_2)
DEC-205 [15, 16]	Thymic cortical epithelium and dendritic cells, T and B lymphocytes, epithelial cells	Antigen internalization to be presented to T lymphocytes

References [1]Taylor *et al*., 2005; [2]Taylor *et al*., 2005; [3]Taylor *et al*., 1992; [4]Azad *et al*., 2014; [5]Behrendt *et al*., 2000; [6]Thomas *et al*., 2005; [7]Wienke *et al*., 2003; [8]Kjoller *et al*., 2004; [9]Curino *et al*., 2005; [10]Wagenaar-Millet *et al*., 2007; [11]Melander *et al*., 2015; [12]Evans *et al*., 2023; [13]Lambeau *et al*., 1990; [14]Hoxha *et al*., 2012; [15]Jiang *et al*., 1995; [16]Butlet *et al*., 2007.

The role of the mannose receptor CD206 in maintaining physiological homeostasis and recognizing pathogens during the initiation of inflammation is well established. The expression of the mannose receptor can be interpreted as a signal that the anti-inflammatory clearance response has effectively begun. Although the mannose receptor does not directly cause a fixed effect on inflammation, its cooperation with other signaling receptors promotes the reduction of pro-inflammatory cytokines, modulates the secretion of anti-inflammatory cytokines, and ultimately contributes to the resolution of inflammation (Gazi, 2009). Anatomically, 10-30% of the mannose receptor is found on the cell surface, whereas the remaining 70% is located intracellularly (Gazi, 2009). As mentioned earlier, the mannose receptor consists of three distinct binding domains: CTLD, FNII, and CysR. Each of these domains has a unique functions and specific ligands that initiate various biological cascades, including those associated with inflammation. In our study, we utilized the mannose moiety as the ligand for our tracer, with the CTLD as responsible domain for the binding of the tracer to CD206 (Andriana *et al*., 2023; Andriana *et al*., 2024). The FNII domain of the mannose receptor is suggested to play a role in the migration of myeloid cells and in the degradation of collagen (Martinez-Pomares *et al*., 2006; Napper *et al*., 2006).

Mannose receptor CD206's involvement in antigen processing and presentation stimulates CD8+ T cells via the class I MHC pathway, which is crucial for immune

responses against viruses and cancers (Burgdorf *et al*., 2008; Apostolopoulus *et al*., 1995; Apostolopoulus *et al*., 2000). As an antigen-presenting cell, the mannose receptor directs ligands to the endosomal compartment, where antigen presentation occurs via class I and class II MHC, especially in the presence of infection.

The mannose receptor's role in pathogen phagocytosis is well documented, including pathogens such as *Mycobacterium kansasii*, *Mycobacterium tuberculosis*, *Francisella tularensis*, and *Candida albicans*, by delaying phagosome maturation following phagocytosis (LeCabec *et al*., 2005; Kang *et al*., 2005; Schulert *et al*., 2006; Marodi *et al*., 1991; Astarie-Dequeker *et al*., 1999). Furthermore, the mannose receptor is considered a professional phagocytic receptor (Taylor *et al*., 2005).

Mannose receptors are categorized as non-canonical PRRs because they can bind both endogenous molecules and pathogens, mediating physiological clearance and bridging homeostasis with immunity. Therefore, the mannose receptor's role in facilitating PRR-induced responses in inflammation is complex and involves intracellular signaling activation. In collaboration with other receptors, the mannose receptor triggers further signaling cascades. Upon pathogen binding, the mannose receptor may form a functional complex with TLR2 on the cell surface, facilitating signal transduction (Tachado *et al*., 2007).

2.4 Myocardial infarction

Myocardial infarction, the most severe manifestation of coronary artery disease, is described as the cell death of cardiomyocytes caused by prolonged ischemia, which means an imbalance between oxygen demand and supply after the absence of blood flow to the heart (Reed *et al*., 2017; Thygesen *et al*., 2018; Frank *et al*., 2012). The European Society of Cardiology (ESC) and the American College of Cardiology (ACC) redefine the universal definition of MI using a biochemical and clinical approach as myocardial injury detected by biomarker abnormality (elevated cardiac troponin) in the setting of acute myocardial ischemia, which includes type 1 MI (due to atherothrombotic events) and type 2–5 MI (due to other potential causes of myocardial ischemia and myocyte necrosis) (Thygesen *et al*., 2018; Byrne *et al*., 2023). MI remains one of the leading causes of mortality and morbidity. Following MI, several complications can arise when it is left untreated or the treatment is inadequate (Stephens *et al*., 2019). Despite developments in the treatment of acute MI, chronic left ventricular dysfunction and heart failure remain common after MI.

2.4.1 Inflammation in myocardial infarction

Inflammatory response following MI is a naturally innate and adaptive immune function aiming for cardiac recovery. Despite the ultimate goal of inflammatory

response being to recover the physiological function of the damaged tissue, it also critically contributes to the determination of the infarct size and adverse post-MI left ventricle (LV) remodeling (Matter *et al*., 2024).

Cardiomyocytes death following ischemia then lead to the activation of a cascade of inflammatory pathway including the infiltration of inflammatory cells and mediators, which in a number of ways are potentially harmful, but also scavenge the debris and promote the healing process (Matter *et al*., 2024; Swirski *et al*., 2013; Libby *et al*., 2016). Hence, a controlled inflammatory response plays a pivotal role in cardiac recovery.

Cardiac ischemia caused the myocytes death and tissue damages (Thygesen *et al*., 2012; Anderson *et al*., 2017). The necrotic cells then released DAMPs signal and ROS that contribute to clearance of dead cells, but can also damage healthy cells (Prabhu *et al*., 2017; Frangogiannis *et al*., 2022; Lefer *et al*., 2000; Dhalla *et al*., 2000). DAMPs were then recognized by the PRR on resident immune cells, get activated and release the pro-inflammatory cytokines such as IL-1, IL-6 which promote the recruitment of neutrophil (PMNs) from blood circulation (Pittman *et al*., 2013; Florentin *et al*., 2021).

Neutrophil is one of the earliest innate immune cells that become the first line defense to clean the debris or damaged cells. Neutrophil also releases toxic content such as ROS, reactive nitrogen species, proteinase 3, cathepsin G and elastase which also cannot discriminate between the damaged cells and host targets; this can cause collateral damages to the host tissues and cause the pro-inflammatory response to keep getting worse (Nathan, 2006; Serhan *et al*., 2005). This inflammatory cascade can occure during the first 4 hours to 24 hours post-acute MI. When neutrophil phagocytose is insufficient to eliminate the damage source, then new characteristic of defense is needed (Medzhitov, 2008). The neutrophil and the damaged cell release chemotactic factors that stimulate the recruitment of myeloid macrophages to the damaged tissue and replace the infiltration of neutrophil, which can start from day 1 post MI (Frodermann *et al*., 2017; Shen *et al*., 2025; Medzhitov, 2008).

Togather with the macrophages, the T cells are activated in the cardiac draining lymph node, which then differentiate to T-helper cells and regulatory T (Treg) cells (Matter *et al*., 2024; Hoffman *et al*., 2016; Corthay, 2009). The differentiated Th1 cells release the cytokines such as IFNγ that promote inactivated macrophages to M1 type macrophages (classically activated macrophages, pro-inflammatory macrophages), which also phagocytose the debris (Ruan *et al*., 2023; Jayasingan *et al*., 2020; Sica *et al*., 2012). However, M1 macrophages also release cytokines that stimulate more neutrophil recruitment from blood circulation. These waves together are known as pro-inflammatory phase and can occur from day 1 to day 3, with a peak on day 3 – 4 and start to decrease on day 5 post MI (Ong *et al*., 2018; Nahrendorf *et al*., 2007; Nahrendorf *et al*., 2010).

On the other hand, Th-cell also polarize into Th2 cells which promote the inactivated macrophages to M2-type macrophages (alternatively macrophages, anti-inflammatory macrophages) via their released cytokines such as IL-4 and IL-10 (Guan *et al*., 2023; Gonzales *et al*., 2022; Sica *et al*., 2012). These concepts are used in *in vitro* setting to artificially polarize human blood monocytes, either to M1 macrophages with LPS and IFNγ, or to M2 macrophages with IL-4 and IL-10. In addition, Treg cells from activated T cell also release the anti-inflammatory cytokines and together with Th2 cells promote the macrophage polarization to M2 type and stimulate the healing or inflammation resolution process (Saraiva *et al*., 2010; Wynn *et al*., 2016). M2 macrophages were known to peak day 7 following MI (Ong *et al*., 2018; Nahrendorf *et al*., 2007; Nahrendorf *et al*., 2010).

When the anti-inflammatory macrophages attempt to engulf and clean the debris and damaged cells, the macrophages will form granulomas, which are the clusters of macrophages, in attempt to protect the host (Li *et al*., 2023; Guan *et al*., 2023; Medzhitov, 2008). M2 macrophages secretes the pro-fibrotic activities factors such as TGF-β1, IL-4, (Platelet-derived growth factor) PDGF and IL-13 and determine the repair of infarcted heart by regulating fibroblast activation, stimulate fibroblast proliferation and myofibroblast activation (Shen et al., 2025; Shiraisi *et al*., 2016; Wang *et al*., 2019; Jiang *et al*., 2024). Fibrotic tissue formation compensates for the loss of cardiomyocytes due to necrosis (Shen *et al*., 2025; Shiraisi *et al*., 2016). These cascade are illustrated in **Figure 8**.

Within 1 week following MI, macrophage function related to recovery and inflammation are increasing and these cardiac macrophages interact with other professional immune cells and various other cell types such as cardiomyocytes themselves, PMNs, monocytes, B cells, apoptotic cells, Treg cells, lymphatic endothelial cells, endothelial cells, fibroblast and myofibroblasts. One of those interactions is efferocytosis (clearance of the apoptotic cells by the macrophages) which contribute to myofibroblast activation and scar formation (Thorp, 2023).

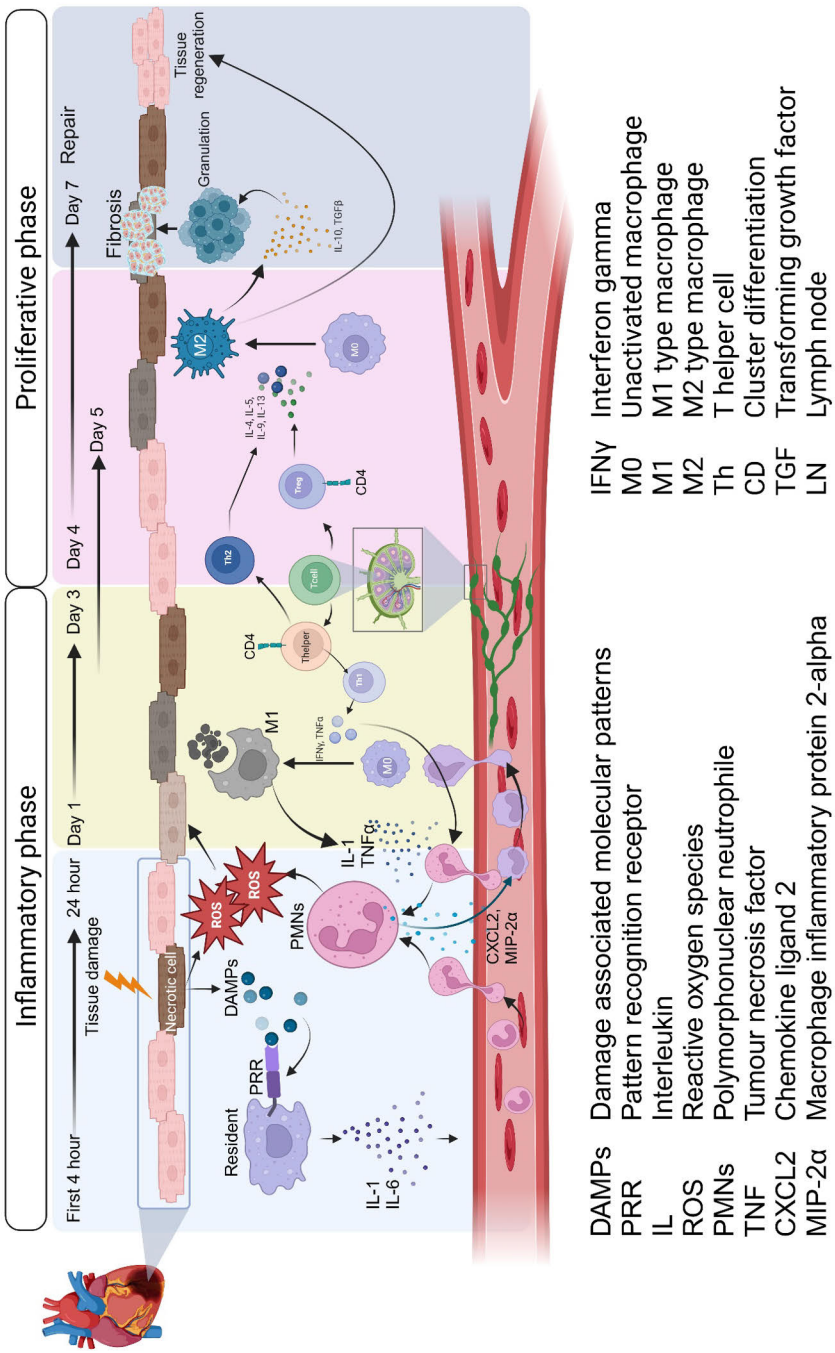

Figure 8. Inflammatory response following acute myocardial infarction. Not all cytokines, chemokines and immune cells involved in the actual inflammatory cascade are mentioned in the figure.

2.4.2 Macrophage mannose receptor CD206 in MI

The role of the mannose receptor CD206 in inflammation was discussed in the previous chapter, along with three other types of mannose receptors. Due to its predominant expression on macrophages, CD206 is often referred to as the MMR (Azad *et al*., 2014). As inflammation plays a crucial role in restoring physiological homeostasis after MI, several studies have explored targeting CD206 for MI imaging and therapy.

The role of CD206 in MI has been primarily explored in the context of the inflammatory response that follows the event. In addition to its role as a pattern recognition receptor expressed on anti-inflammatory macrophages (M2 macrophages), CD206 is a signature receptor of the resolution of the inflammation phase (García *et al*., 2021).

Following MI, tissue regeneration and enhanced cardiomyocyte proliferation are the ultimate goals. Considering that all cell surfaces and extracellular matrices are glycosylated, carbohydrates, especially mannose (CD206 ligand), play a major role in tissue regeneration after MI, as mannose has been found to be the most abundant glycan in the left and right ventricles. This indicates the key contribution of mannose and CD206 in glycosylation to achieve effective tissue regeneration post-MI (Varki, 2017; Contessotto *et al*., 2020). The involvement of CD206 in cardiac recovery was also demonstrated by Siraishi and coworkers, who ablated tribbles pseudokinase 1 (TRIB1) in mice, which depleted M2 macrophages after MI and caused impaired fibroblast activation in the infarct, leading to an increased rate of myocardial rupture (Shiraishi *et al*., 2016).

In addition to sentinel lymph node detection, CD206 targeting has been investigated with a focus on cancer detection due to its overexpression in tumor-associated macrophages (TAMs), also known as M2-like macrophages. Expanding the focus to cardiovascular diseases has also been investigated, especially in atherosclerosis, with promising results in detecting vulnerable plaques. However, CD206 targeting in MI is very limited. One preclinical study on experimental acute MI was conducted in rodents with permanent ligation of the left anterior descending (LAD) coronary artery. The anti-MMR nanobody-based fragment was labeled with Gallium-68 [^{68}Ga]Ga-NOTA-anti-MMR nanobody) and showed higher tracer uptake in the MI area of LAD-ligated rats (infarct-to-remote ratio of 1.3 ± 0.2 in rats 7 days after LAD ligation) and mice, compared to the sham-operated control group (Varasteh *et al*., 2022). Research focusing on CD206-targeting PET tracers for imaging MI remains very limited, in addition to its application in the detection of other inflammatory-related diseases by PET, as summarized earlier in table II.

2.5 Nuclear molecular imaging

Molecular imaging is generally described as the *in vivo* characterization and quantification of biological, physiological, and pathological processes at the cellular and molecular levels in the body (Weissleder *et al*., 2001; MacRitchie *et al*., 2020). In clinical imaging practice, anatomically based imaging techniques, including computed tomography (CT), magnetic resonance imaging (MRI), and ultrasound, remain the first line for the detection of inflammation (Subramaniam *et al*., 2007; Gotthardt *et al*., 2010). Anatomical information is crucial for disease diagnosis but is not sufficient to provide the functional information needed to determine the precise diagnosis, especially in the early phases when many diseases have barely established structural changes (Kumar *et al*., 2008). Therefore, nuclear molecular imaging is useful for complementing the role of structural imaging modalities, creating hybrid imaging modalities such as PET/CT, Single photon emission computed tomography/computed tomography (SPECT/CT), and PET/MRI for the diagnosis of inflammatory-related diseases in most clinical settings (MacRitchie *et al*., 2020).

Nuclear imaging is one medical specialty of nuclear medicine applied for disease diagnosis that utilizes radioactive materials, which involve the non-invasive administration of a small quantity of radiotracers or radiopharmaceuticals by injection, inhalation, or ingestion (Sureshkumar *et al*., 2020). In cardiology, nuclear imaging is considered to play a significant role in the diagnosis and management plan for patients with coronary artery disease, in addition to inflammatory-related diseases such as rheumatoid arthritis, inflammatory bowel diseases, osteomyelitis, sarcoidosis, and others (Pedretti *et al*. 2024; Jamar *et al*., 2023; Noriega–Álvarez *et al*., 2023; Valero - Martínez *et al*., 2024). Nuclear imaging can be divided into positron emission tomography (PET) and single-photon emission computed tomography (SPECT).

2.5.1 PET

PET imaging has its roots in 1932, when the positron was first discovered. This breakthrough was followed by the invention of the cyclotron and the development of artificial radioisotopes such as carbon-11, nitrogen-13, oxygen-15, and fluorine-18—key components used in PET imaging today. Between 1950 and 1970, cyclotrons were first installed at medical centers, enabling the local production of positron-emitting radioisotopes. In the mid-1970s, the development and implementation of dedicated PET imaging systems began, marking the start of clinical PET imaging as we know it today (Rich, 1997).

PET imaging is a visualization technique that assesses physiological functions at the molecular level by analyzing blood flow, metabolic activities, their metabolites, and neurotransmitters. This approach enables quantitative analysis, facilitating the

monitoring of relative changes over time, which provides insights into the progression of disease by utilizing positron-emitting radionuclides (Berger, 2002). There are several radionuclides used for PET imaging that are produced by cyclotrons, including: fluorine-18 ($t_{1/2}$ 109.8 min), carbon-11 ($t_{1/2}$ 20.4 min), nitrogen-13 ($t_{1/2}$ 10 min), oxygen-15 ($t_{1/2}$ 2 min), Iodine-124 ($t_{1/2}$ 4.2 d), Cupper-64 ($t_{1/2}$ 12.7 h), yttrium-86 ($t_{1/2}$ 14.7 h), and zirconium-89 ($t_{1/2}$ 78.4 h), and by generators, including gallium-68 ($t_{1/2}$ 67.7 min), scandium-44 ($t_{1/2}$ 4 h), and rubidium-82 ($t_{1/2}$ 1.3 min) (Rong *et al*., 2023; Ametamey *et al*., 2008; Wei *et al*., 2020; Taïeb *et al*., 2019; Müller *et al*., 2018; Reiner *et al*., 2014; Knight *et al*., 2014). An exception is that gallium-68 and scandium-44 can also be produced by cyclotrons, and Cupper-64 can be produced by reactors (Pandey *et al*., 2014; Nelson *et al*., 2020; Severin *et al*., 2012; Mikolajczak *et al*., 2021; Cakravarty *et al*., 2020).

The basic principle of PET imaging is based on the detection of photons by the PET scanner detector (**Figure 9**). Neutron-deficient unstable positron-emitting radionuclides are attached to the ligand that will direct the tracer to a specific target. A spontaneous decay occurs to reach a stable form of the radionuclide by converting the extra proton (p) to a neutron (n) and simultaneously emitting a positron (e^+) and a neutrino (v). Positron emission is one form of beta decay, which emits a positively charged beta particle (β^+), in addition to the other two modes: negative beta decay (β^-) and electron capture (Welsh, 2007; Welsh, 2006). The emitted positron travels and scatters until it encounters an electron (e^-) and collides. This collision causes positron-electron annihilation, which converts mass to energy in the form of two photons. Each photon generates 511 keV of energy according to Einstein's relativity formula $E = mc^2$. The two photons are emitted in opposite directions at approximately 180 degrees with a small deviation (± 0.3 degrees) due to random variations in residual momentum at the time of annihilation. These two photons are simultaneously detected by the PET scanner through a process called coincidence detection, which allows the system to accurately localize the point of annihilation along a straight line, thereby enabling high-resolution, three-dimensional imaging of tracer distribution within the body (Cherry *et al*., 2012). The photons are absorbed by the crystal scintillator, producing light that is converted into an electrical signal, which is processed as quantitative data (Berger, 2002; Vaquero *et al*., 2015; Cole *et al*., 2015; Spinks, 1999). The basic principle of PET imaging is depicted in **Figure 9** below. The fluorine-18 decays to the stable nuclide oxygen-18:

$$^{18}_{9}\mathrm{F} \rightarrow {}^{18}_{8}\mathrm{O} + e^{+} + v_{\varepsilon}$$

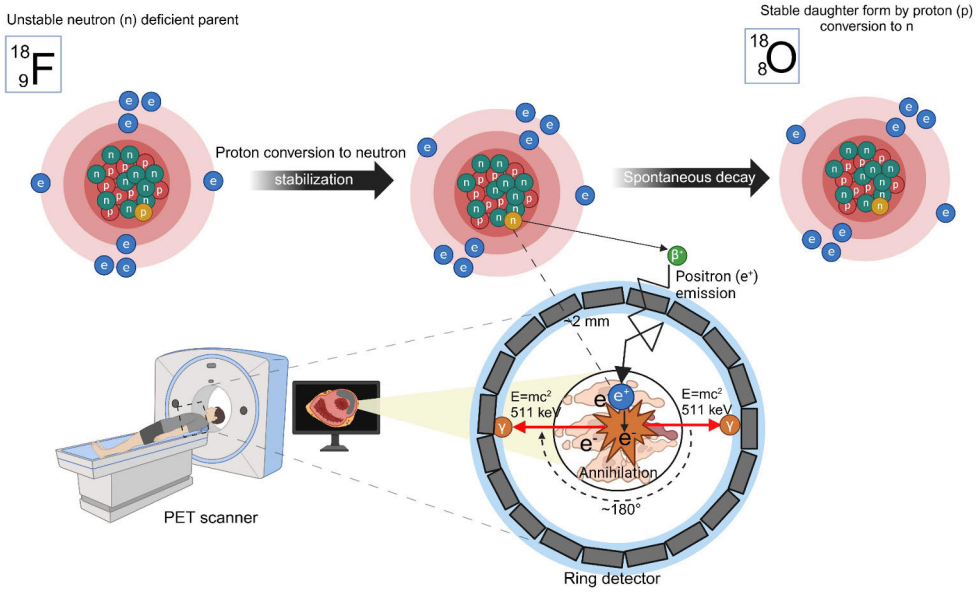

Figure 9. Schematic representation of annihilation coincidence that is detected by PET detector. Fluorine-18 and cardiac imaging is used for representative illustration. (Modified from Vaquero *et al*., 2017)

Currently, the most widely used positron emitters in clinical practice is fluorine-18, particularly for small molecule (such as D10CM) and peptide tracers, even though other radionuclide such as ^{68}Ga are also commonly used both in clinical and preclinical settings. Additionally, isotopes such as ^{89}Zr are increasingly used in immune-PET and antibody-based applications (Rong *et al*., 2023; Sonderlund *et al*., 2015). The longer physical half-life of fluorine-18 ($t_{1/2}$ 109.77 min) compared to ^{68}Ga ($t_{1/2}$ 67.83 min) accommodates tracer production requiring longer protocols as well as imaging. The lower positron energy of fluorine-18 (E_{max} 0.63 MeV) compared to ^{68}Ga (E_{max} 1.90 MeV) provides higher image spatial resolution, which is desirable for the visualization of small targets. On the other hand, ^{68}Ga offers generally straightforward radiolabeling protocols. ^{68}Ga can be conveniently obtained from a ^{68}Ge/^{68}Ga generator that can be situated in laboratories along with imaging facilities, while fluorine-18 production requires a cyclotron-equipped facility. However, nowadays, fluorine-18 transportation to a non-cyclotron-equipped facility can be easily realized. One other major advantage of ^{18}F-labeled tracers is the possibility to produce them with high molar activity, which is important for imaging low tissue density (Ajenjo *et al*., 2021; Eskola *et al*., 2012). Up until now, [^{18}F]fluoride is the

most widely used radionuclide due to the relatively pure positron emission process and low beta-energy of fluorine-18. The emitted positron from fluorine-18 travels a shorter distance (typically 1–2 mm) until it interacts with the tissue electron, compared to other radionuclides with higher beta-energy.

2.5.2 SPECT

Single photon emission computed tomography (SPECT) is another type of nuclear imaging that provide physiological function similar to PET. However, the basic principle of SPECT imaging is step-wise simpler. Unlike PET imaging that requires the use of positron emitters, SPECT directly measures the photon (gamma radiation) emitted during the decay of unstable radionuclide to the stable form and generates lower energy. There is only one photon produced from the decay that is then absorbed by the collimator and detected by the SPECT detector to eventually produce three-dimensional images. Another imaging method that detects energy for image generation is gamma scintigraphy, also referred to as planar imaging, which generates two-dimensional images. The basic principle of conventional planar imaging and SPECT imaging is similar, but SPECT acquires multiple 2D images while rotating around the object of imaging. This factor makes SPECT superior, offering greater precision in quantifying the accumulation of tracers in targeted tissues (Conway, 2012). Additionally, SPECT imaging is more cost-effective compared to PET. It does not require a local cyclotron for radionuclide production, and SPECT scanners are more widely available and less expensive than current PET/CT scanners that combine both positron emission tomography and computed tomography technologies (Davis *et al*., 2020). The radiopharmaceuticals used in SPECT are also cheaper and easier to distribute (Crișan *et al*., 2022). Furthermore, SPECT radionuclides typically have relatively long physical half-lives, which allow for extended preparation times—a feature that is particularly advantageous in hospital settings (Yandrapalli et al., 2022; Brooks, 2005; Xu et al., 2012). Although long-lived PET radionuclides such as ^{89}Zr, ^{124}I, and ^{64}Cu are available, they are valuable for specialized applications like immuno-PET and targeted theranostics. Additionally, they produce higher radiation burden and require more complex production and handling protocols. In contrast, ^{99m}Tc offers a more favorable balance of safety, availability, and logistical ease, making it more suitable for routine diagnostic imaging.

SPECT imaging detects gamma energy ranging from 30 to 300 keV from radionuclides. The metastable form of technetium-99 (^{99m}Tc) is currently the most used gamma-emitting radionuclide for SPECT imaging, with a physical half-life ($t_{1/2}$) of 6.03 hours and a gamma energy of 140 keV (Papagiannopoulou, 2017). Other commonly used radionuclides for SPECT imaging include ^{123}I ($t_{1/2}$ 13.22 hours, 159

keV), ^{111}In ($t_{1/2}$ 2.80 days, 171.25 keV), ^{67}Ga ($t_{1/2}$ 78.20 hours, 93 keV), ^{155}Tb ($t_{1/2}$ 5.32 days, 105 keV), and to a lesser extent, some use ^{201}Tl ($t_{1/2}$ 73 hours, 167.4 keV) (Müller *et al*., 2014; Hutton, 2014; Khalil *et al*., 2011; Koniar *et al*., 2024; Blanchardon *et al*., 2005; Gomes *et al*., 2011). The higher the gamma energy, the more scintillation photons reach the photomultiplier tube, contributing to fewer variations in the recorded position of the source (Finn *et al*., 2023). It is evident that each of the radionuclides mentioned here emits gamma rays within different spectra. This allows for the simultaneous SPECT imaging of multiple probes labeled with different radionuclides and the visualization of multiple cellular or molecular events (Gomes *et al*., 2011).

^{99m}Tc is produced using generator from the mother radionuclide molybdenum-99 (^{99}Mo, $t_{1/2}$ 66 h) decay (Green, 2012). Relatively easy preparation of ^{99m}Tc labeled tracer which are usually carried out through freeze-dried instant kit formulation, longer physical half-life than most PET radionuclide, and sufficient Eγ radiation are beneficial for hospital preparation before administration to patient and able to collect high quality images (Duatti, 2021). Basic principle of SPECT imaging is depicted below in **Figure 10**.

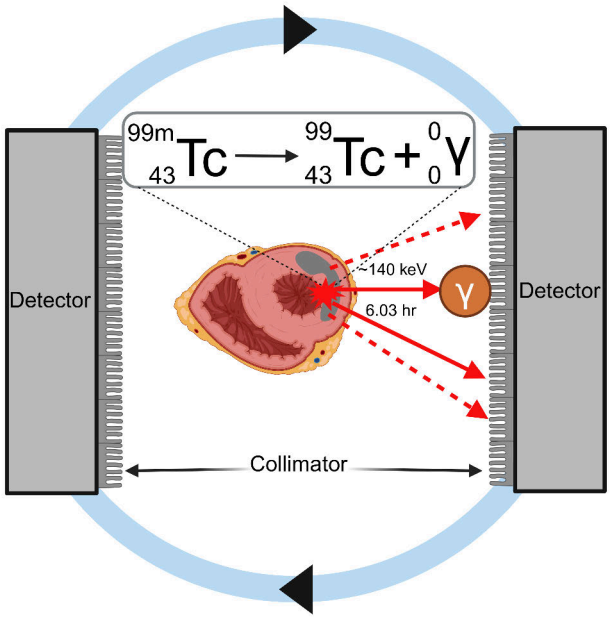

Figure 10. Schematic representation of photon emitted during ^{99m}Tc decay to the stable ^{99}Tc. Dash line show the emitted photon absorbed by the collimator and the full line represent the photon that pass through collimator and reach the SPECT crystal detector that later are converted as digital signal as quantitative data. ^{99m}Tc and cardiac imaging is used for representative illustration.

2.5.3 PET and SPECT: comparative imaging modalities

Multiple factors are considered between PET and SPECT imaging to be employed in radiopharmaceutical development. In clinical evaluation, PET generally has better spatial resolution (4-6 mm) compared to SPECT, which has a clinical standard maximum spatial resolution of 6-8 mm and can achieve resolutions below 1 mm, respectively (Dall'ara *et al*., 2016). For preclinical evaluation, the spatial resolution of PET and SPECT should ideally accommodate the smaller organ size of the animal subjects. PET can provide a spatial resolution of 1.5–1.6 mm with advanced light detector technology, and even below 1 mm. With some research systems, PET can achieve sub-millimeter spatial resolution for structures as small as 0.7–0.8 mm. Even though this resolution is still relatively low considering the small size of animals such as mice, improvements in PET modality have been consistently observed over the last few years (Dall'Ara *et al*., 2016; España *et al*., 2014; Weissler *et al*., 2015). SPECT, on the other hand, can provide resolutions below 1 mm using different types of collimators, such as pinhole or multi-pinhole collimators, instead of using standard collimators that have a resolution of 6-8 mm (Van Audenhaege *et al*., 2015; Acton *et al*., 2003).

One other important aspect is sensitivity. SPECT is known to have lower sensitivity (approximately 10 times lower) compared to PET in clinical and preclinical settings. This is due to the basic mechanism of SPECT, which operates with collimators. Considerable amounts of emitted gamma rays are lost in absorptive collimation (Sandhu *et al*., 2010; Rowland *et al*., 2008). While PET is equipped with a crystal scintillator that absorbs both photons resulting from annihilation coincidence, consequently, PET has higher sensitivity, providing functional and molecular information by detecting tracers within nanomolar and picomolar concentrations (Khalil *et al*., 2011; Gotthardt *et al*., 2010).

While both PET and SPECT are valuable molecular imaging modalities, PET offers several key advantages that justify its use even when a corresponding SPECT tracer exists. Most importantly, PET enables absolute quantification of tracer uptake, whereas SPECT is generally limited to semi-quantitative or relative measurements. This difference arises because PET systems are calibrated to detect coincidence events from positron annihilation, which allows for more accurate measurement of tracer concentration in tissues (e.g., in Bq/mL or SUV). In contrast, SPECT detects single photons, which are emitted isotropically, and the process is more prone to attenuation and scatter, making accurate quantification more difficult without complex corrections. Although quantitative SPECT methods are evolving, PET remains the gold standard for applications requiring precise, reproducible measurements—such as monitoring inflammation, evaluating target expression, or assessing treatment response.

Furthermore, PET typically involves shorter-lived isotopes like ^{18}F, which contribute to lower radiation doses and faster image acquisition. These characteristics make PET particularly advantageous in preclinical and clinical settings where image

quality, quantification, and safety are critical. For these reasons, PET imaging provides meaningful technical improvements over SPECT that justify the repurposing of the D10M tracer for PET applications. In addition to improved resolution and sensitivity, PET offers absolute quantification of tracer uptake, enabling precise assessment of target engagement and dose–response relationships. This makes PET a particularly valuable tool in therapy development, where accurate measurements are essential for identifying effective doses, monitoring treatment response, and supporting translational research. When considering whether a tracer will progress to clinical trials or be used in therapeutic contexts, PET remains the gold standard due to its quantitative accuracy, reproducibility, and regulatory acceptance bodies such as the U.S. Food and Drug Administration and the European Medicines Agency for use in early-phase clinical studies and biomarker validation. Despite both imaging modalities have been rapidly employed in the early stages of drug development, and advances to improve their limitations have gradually increased, one systematic review revealed that PET was used 4.7 times more frequently than SPECT in clinical drug development (Son *et al*., 2019).

2.6 PET imaging of macrophages

Macrophages play a central role in inflammation, tissue remodeling, and immune regulation, making them a compelling target for molecular imaging in a variety of diseases, including cancer, neuroinflammation, and cardiovascular pathology. Several PET tracers have been developed to visualize macrophages *in vivo*, targeting molecular markers that reflect their activation state, recruitment, and phenotypic polarization.

Imaging macrophages offers valuable insights into the immune response following inflammatory processes. Several surface receptors and molecular features of macrophages have been investigated for their feasibility as imaging targets in inflammation and inflammation-related diseases. PET imaging of activated macrophages, regardless of their phenotypic subtype, has been developed for the diagnosis and monitoring of various conditions.

One of the most extensively studied targets is the 18 kDa translocator protein (TSPO), a mitochondrial protein upregulated in activated macrophages and microglia. TSPO-targeted PET tracers such as [^{11}C]PK11195, second-generation ligands like [^{18}F]DPA-714 and [^{18}F]FEMPA have been widely applied in neuroinflammation and cardiovascular imaging, including conditions such as myocarditis and atherosclerosis (Malpetti *et al*., 2021; Kaneko *et al*., 2022; Gaemperli *et al*., 2012; Hellberg *et al*., 2018; Kim *et al*., 2018). Another target, CCR2, a chemokine receptor expressed on macrophages, has been imaged using tracers like [^{68}Ga]ECL1i to assess cardiac injury (Cifarelli *et al*., 2021). CD68, a pan-macrophage lysosomal marker, has also been explored in PET imaging—for

example, using [^{18}F]FEPPA to visualize neuroinflammation in non-human primates (Zammit *et al*., 2020). However, TSPO, CCR2, and CD68 lack of ability to distinguish between macrophage phenotypes and their expression by non-macrophage cell types, limit their specificity for macrophage subset imaging.

Targeting specific polarized macrophage subsets enables differentiation between ongoing pro-inflammatory activity and the resolution phase of inflammation by imaging M1 and M2 macrophages, respectively. This strategy is important for inflammation imaging because it moves beyond simply detecting the presence of immune activity, enabling the characterization of the specific phase and quality of the inflammatory response. By distinguishing between pro-inflammatory and anti-inflammatory or reparative macrophage populations, it becomes possible to assess whether inflammation is escalating, persisting, or resolving. This phenotypic specificity enhances diagnostic accuracy, supports prognostic evaluation, and can guide personalized therapeutic interventions—especially in chronic or complex inflammatory conditions where standard imaging lacks sufficient resolution of immune dynamics. Several receptors of M1 and M2 macrophages have been evaluated as biomarkers for detection of various inflammatory diseases.

The PET tracer [^{18}F]NOS, which targets inducible nitric oxide synthase (iNOS), an enzyme specifically upregulated in classically activated (M1) macrophages, has been evaluated for imaging pulmonary and cardiovascular inflammation (Herrero *et al*., 2012; Wetherill *et al*., 2023). Another M1-associated target, CD80/CD86, consists of co-stimulatory receptors that are highly expressed on M1 macrophages and have been investigated in preclinical models using [^{64}Cu]NODAGA-abatacept PET imaging to monitor lipopolysaccharide (LPS)-induced local inflammation in mice (Taddio *et al*., 2021). Although these markers offer greater specificity toward the M1 phenotype compared to more general macrophage markers, each presents limitations. iNOS expression is tightly regulated, as excessive nitric oxide production can cause tissue damage. Moreover, iNOS expression is limited to the acute phase of inflammation, making PET imaging highly time-sensitive. If imaging is performed too early or too late, iNOS levels may be undetectable, even if inflammation is still ongoing or entering the resolution phase. On the other hand, CD80/CD86 are also expressed on dendritic cells and activated B cells, reducing macrophage specificity.

PET imaging targeting alternatively activated macrophages (M2) has shown steady progress, with increasing interest in surface receptors as biomarkers of inflammation. Among the most studied are the folate receptor-β (FR-β) and the mannose receptor CD206. Both have demonstrated promising results in preclinical models of inflammatory and tumor-related diseases.

While many successful studies have reported that FR-β is highly expressed on M2 macrophages, its expression appears to be context-dependent. For instance, in a

rheumatoid arthritis model, FR-β-targeted PET imaging revealed expression in M1 macrophages. In contrast, studies using glioblastoma and melanoma models identified FR-β expression in M2 macrophages. Similarly, in an atherosclerosis model, FR-β expression was not exclusive to either M1 or M2 macrophage subsets. These findings suggest that FR-β expression may vary in response to different microenvironmental stimuli, limiting its utility as a universal M2 marker (Furusho *et al*., 2012). Nonetheless, PET imaging targeting FR-β has advanced to clinical studies, including a 2020 trial using [^{18}F]fluoro-PEG-folate (Verweij *et al*., 2020). Ongoing efforts aim to optimize FR-β-targeting tracers through chemical structure modifications to improve specificity and performance.

Another potential M2 marker is the CD163 receptor, which has been identified as a promising biomarker for PET imaging of M2 macrophages and M2-like tumor-associated macrophages (TAMs). A novel tracer, [^{18}F]AlF-NODA-MP-C6-CTHRSSVVC, has been developed for the purpose of tumor imaging (Fernandes *et al*., 2024). Although CD163 is mostly evaluated for tumor imaging, its expression has also been detected in both inflammatory and malignant disease contexts. A study using [^{64}Cu]/[^{68}Ga]-NODAGA-ICT-01 in ApoE$^{-/-}$ atherosclerotic mice and a reperfused myocardial infarction model demonstrated CD163's imaging potential in cardiovascular inflammation (Zhang *et al*., 2024). In another study, the CD163-targeted PET tracer [^{68}Ga]Ga-NOTA-anti-CD163 nanobody enabled dynamic tracking of TAMs during immunotherapy and linked their spatial distribution to therapeutic response (Lauwers *et al*., 2024). Despite these promising results, CD163-targeted imaging faces challenges. Ligand availability is currently limited to antibodies or antibody fragments, which are large, costly, and have slow pharmacokinetics that hinder efficient imaging. Moreover, CD163 is less abundantly expressed on general M2 macrophages compared to the M2c subtype, limiting its versatility across disease types.

CD206, also known as the macrophage mannose receptor, is currently the most widely used M2 macrophage marker in radiotracer development. Compared to CD163, CD206 is more extensively studied, and its expression is not limited to a specific M2 macrophage subtype. This broad expression pattern makes CD206 an attractive biomarker for imaging a wide range of inflammation-related diseases, including fibrosis, atherosclerosis, and myocardial infarction.

As a signature marker of alternatively activated (M2-like) macrophages, CD206 imaging may provide insights into the immune response during the resolution phase of inflammation. Importantly, CD206 has well-characterized natural ligands, such as mannosylated structures—most notably utilized in the clinically approved [^{99m}Tc]-tilmanocept (a mannosylated dextran) (Vera *et al*., 2001; Leong, 2022; Pirmettis *et al*., 2012; Tahara *et al*., 2014). This biological compatibility facilitates the development of radiotracers using small molecules, peptides, and nanoparticle platforms. Additionally, rapid advancements in CD206-targeted imaging have

improved the accessibility of chemical precursors, making CD206 a practical and scalable target for PET tracer development.

2.7 PET imaging of mannose receptor CD206

Over the past two decades, several radiotracers targeting the mannose receptor CD206 have been developed for preclinical and clinical imaging using both SPECT and PET modalities. **Table 2** summarizes representative examples of these tracers, illustrating the progression from early SPECT agents to more recent PET tracers designed for applications such as tumor-associated macrophage (TAM) imaging and cardiovascular inflammation.

A key milestone was the development of ^{99m}Tc-mannosyl-dextran for sentinel lymph node detection, targeting CD206 expressed in lymphatic tissues (Vera *et al*., 2021). Following its promising preclinical results, a Phase I clinical trial was conducted in 2003 in breast cancer patients, and the tracer was ultimately FDA-approved in 2013 for clinical use in lymphatic mapping and sentinel node biopsy (Wallace *et al*., 2003; Wallace *et al*., 2013). Building on this work, Pirmettis *et al*. developed a more stable chelator for labeling mannosylated dextran derivatives (DCM), optimizing ^{99m}Tc labeling and biodistribution (Pirmettis *et al*., 2012; Papassava *et al*., 2021). Their group has since produced a series of ^{99m}Tc-DCM tracers of varying molecular sizes (**Table 2**).

With growing interest in macrophage imaging and the known expression of CD206 on TAMs and anti-inflammatory macrophages, attention has shifted toward PET imaging to harness its advantages over SPECT — including better spatial resolution and quantification, as discussed in more detail in the previous section. In 2014, Tahara and his group introduced the first PET tracer targeting CD206 — [^{18}F]FDM — marking a shift from lymph node mapping to macrophage imaging in tumor contexts (Tahara *et al*., 2014). Since then, a variety of CD206-targeted PET tracers have been developed using different chemical platforms suited to various preclinical and translational settings.

The present study builds on this foundation by repurposing a clinically validated, FDA-approved SPECT tracer platform — mannosylated dextran — for PET imaging. Specifically, we collaborated with Pirmettis' group to develop ^{18}F-labeled DCM and for preliminary preclinical evaluation, a low-molecular-weight mannosylated dextran derivative was selected to optimize *in vivo* pharmacokinetics by balancing receptor binding, tissue penetration, and clearance. A NOTA chelator was conjugated via a cysteine linker in D10CM structure to enable radiolabeling through the Al[^{18}F]F method.

Repurposing this platform for PET offers the benefits of improved resolution, quantitative imaging, and translational potential, while retaining the biological

specificity and clinical familiarity of the parent SPECT tracer. [^{18}F]AlF-NOTA-D10CM thus represents a rational development of CD206-targeted imaging tools toward clinical PET applications in inflammation.

Table 2. Mannose receptor CD206-targeted imaging of inflammation-associated conditions.

Radiotracer	Mannosylated platform	Application	Imaging modality
^{64}Cu-labeled MAN-LIPs [1]	Vesicle	Tumor-associated macrophages detection	PET
[^{18}F]FB-anti-MMR Specialized domain antibody (sdAb) [2]	Antibody / Antibody fragment	Tumor-associated macrophages detection	PET
[^{68}Ga]Ga-NOTA-anti-MMR-sdAb [3,4]	Antibody / Antibody fragment	Human radiation dose and protumorigenic macrophages detection in solid tumors (Clinical study)	PET
[^{68}Ga]Ga-NOTA-anti-MMR nanobody (Nb) [5,6]	Antibody / Antibody fragment	Atheroslerosis, myocardial infarction	PET
[^{68}Ga]Ga-RP832c [7]	Peptide	Cancer detection	PET
[^{68}Ga]Ga-NOTA-MSA [8-10]	Human mannosylated serum albumin (MSA)	Myocarditis, atherosclerosis, inflammation in pulmonary artery hypertension	PET
[^{18}F]FDM [11]	Mannose derivative	Tumor associated macrophages detection, atherosclerosis	PET
[^{68}Ga]Ga-tilmanocept [12]	Mannosylated dextran derivative	Sentinel lymph node and tumor associated macrophages detection in early stage oral cavity carcinoma (human study)	PET
[^{18}F]AlF-NOTA-D10CM [13]	Mannosylated dextran derivative	Inflammation	PET
[^{99m}Tc]Tc-DCM; [^{99m}Tc]Tc$(CO)_3$-DCM20; [^{99m}Tc]Tc-D10CM; [^{99m}Tc]Tc-D20CM; [^{99m}Tc]Tc-D40CM; ^{99m}Tc-D75CM; [^{99m}Tc]Tc-D150CM; [^{99m}Tc]Tc -D500CM [14-17]	Mannosylated dextran derivative	Sentinel lymph node detection	PET
[^{99m}Tc]Tc-DTPA-mannosyl-dextran (Lymphoseek)[18]	Mannosylated dextran derivative	Sentinel lymph node mapping of breast cancer, (U.S. FDA approved)	PET

References: [1]Locke *et al*., 2012; [2]Blykers *et al*., 2015; [3]Xavier *et al*., 2019; [4]Gondry *et al*., 2023; [5]Varasteh *et al*., 2019; [6]Varasteh *et al*., 2022; [7]Parker *et al*., 2023; [8]Park *et al*., 2020; [9]Kim *et al*., 2016; [10]Lee *et al*., 2017; [11]Tahara *et al*., 2014; [12]Mahieu *et al*., 2021; [13]Andriana *et al*., 2023; [14]Pirmettis *et al*., 2012; [15]Yamaguchi *et al*., 2015; [16]Morais *et al*., 2011; [17]Papasavva *et al*., 2021; [18]Wallace *et al*., 2014.

2.8 PET imaging of myocardial infarction

Molecular imaging research and clinical applications have been expanding significantly over the past two decades and contribute greatly to all avenues of medical imaging, such as early detection, diagnosis, therapy monitoring, and treatment follow-up (Pysz *et al*., 2010; Kang *et al*., 2023). Molecular imaging provides advanced information on the pathological mechanisms of myocardial infarction by unraveling critical molecular and cellular events during myocardial infarction, complementing conventional anatomical imaging modalities (Osborn *et al*., 2013).

SPECT and PET are the most widely used non-invasive imaging techniques to evaluate tissue molecular function following MI, along with CT and MRI, which provide anatomical information. Although SPECT remains common practice for clinical use due to the lower cost of the tracer and scanner, as well as its ability to utilize variety of protocols and radiotracers for myocardial perfusion imaging, PET is still considered superior due to its higher spatial resolution, lower radiation dose, accurate attenuation correction, faster imaging times, and dynamic imaging for myocardial blood flow quantification. In general, the PET technique will include visualizing and quantifying metabolic activity in myocardial inflammation, angiogenesis, and fibrosis. The wound healing at the molecular level that occurs during the first 1 to 2 weeks following MI will determine the prognosis of the patients.

[^{18}F]FDG, a glucose analog-based radiopharmaceutical, has been the most clinically used PET tracer for imaging MI by marking the glucose metabolism activity in viable myocytes (Sogbein *et al*., 2014; Buck *et al*., 2004; Brown *et al*., 1993; Reske *et al*., 1997; Rempel *et al*., 1996). [^{18}F]FDG imaging can differentiate between viable and non-viable myocardium after MI (Lukovic *et al*., 2024; Evertz *et al*., 2023; Miller *et al*., 2023; Nyolczas *et al*., 2007). An infarct area is indicated by reduced [^{18}F]FDG uptake (Graf *et al*., 2004; Kazakauskaite *et al*., 2023; Masuda *et al*., 2018). In addition to detecting myocyte viability, [^{18}F]FDG has been clinically deployed to identify sites of inflammation and infection due to increased glucose metabolism, which is associated with high glucose transporters (GLUTs) in inflammatory cells and uptake by infectious organisms. [^{18}F]FDG is also used for monitoring the response to therapeutic interventions (Wahl *et al*., 2021). One important factor to be aware of is that the high physiological accumulation of [^{18}F]FDG in the myocardium makes assessing myocardial inflammation challenging. Normal myocytes use various energy sources, including glucose, free fatty acids, pyruvate, ketone bodies, lactate, and amino acids, which can interfere with accurate assessment of [^{18}F]FDG uptake. Therefore, fasting prior to imaging with [^{18}F]FDG has become a standard protocol in both clinical and preclinical applications (Norikane *et al*., 2024).

Nonetheless, the lack of specificity of [^{18}F]FDG, caused by its accumulation in any site with increased glucose metabolism, is vulnerable to positive false diagnoses

(Pijl *et al*., 2021; Kosinska *et al*., 2023; Strauss, 1996; Long *et al*., 2011; Gormsen *et al*., 2016). This is inconvenient for detecting small targets such as infarct areas, where specificity and accuracy are critical. Hence, studies targeting more specific markers of inflammation, such as inflammatory metabolism markers (e.g., neutrophils, macrophages, cytokines, and chemokines), have increased. In addition, tracers targeting angiogenesis and fibrosis following MI have been evaluated extensively (**Table 3**) (Varasteh *et al*., 2022).

Table 3. PET radiotracer for imaging of MI via mechanism of inflammation, angiogenesis and fibrosis following MI. (Modified from Varasteh *et al*., 2002).

PET tracer	Marker	Post MI inflammation targeting mechanism	Phase of usage
[^{18}F]FDG [1,2]	GLUTs	Targeting enhanced glucose transporters (GLUTs) and then phosphorylated by glycolytic enzymes hexokinases to FDG-6 which then stored within activated inflammatory cells	Clinical / preclinical
[^{68}Ga]Ga-DOTA-TOC [3-5]	SSRT-2	Targeting the overexpression of G-protein-coupled receptor somatostatin receptor subtype-2 (SSTR-2) by activated macrophages during inflammation[3,4]	Clinical / preclinical
[^{68}Ga]Ga-DOTA-TATE [3-7]			
[^{68}Ga]Ga-pentixafor [5-10]	Chemokine receptors CXCR4	Targeting transmembrane G-protein-coupled chemokine receptor CXCR4 which is essential in stem and progenitor cells recruitment to the infarct zone for inflammation resolution	Clinical / preclinical
[^{68}Ga]Ga-DOTA-ECL1i [11-13]	Chemokine receptors CCR2	Targeting chemokine receptor CCR2^{+} expressed on monocytes infiltrating to the heart which differentiate to CCR2^{+} macrophages contributing to heart failure pathogenesis	Preclinical
[^{18}F]GE180 [14,15]	TSPO	Targeting mitochondrial translocator protein (TSPO) expressed on activated macrophages and microglia involved in inflammatory cascade	Preclinical
[^{11}C]methionine [16,17]	Amino acid and protein tunrover	Targeting specific post-ischemic injury inflammatory component (amino acid) metabolism, transmethylation and protein synthesis which reflect the activity of inflammatory cells	Clinical / preclinical
[^{68}Ga]Ga-NOTA-anti-MMR Nb [18]	Mannose receptor CD206	Targeting CD206 positive macrophages which are heavily involved in inflammation resolution process and cardiac recovery following MI	Preclinical
[^{68}Ga]Ga-NOTA-MSA [19,20]			
PET tracer	**Marker**	**Post MI angiogenesis targeting mechanism**	**Phase of usage**
[^{64}Cu]NOTA-TRC105 [21-23]	CD105	Targeting disulphide-linked homodimeric transmembrane protein CD105 expressed selectively on endothelial cells of newly formed vessels	Preclinical

[^{64}Cu]-DOTA-VEGF$_{121}$ [24-26]	vascular endothelial growth factor (VEGF)	Post MI angiogenesis : Targeting VEGF which stimulate the angiogenesis and contribute to LV remodelling following MI	Preclinical
[^{68}Ga]Ga-NOTA-RGD [27]	$\alpha_v\beta_3/\alpha_v\beta_5$ integrins	Arginyl-Glycyl-Aspartic acid (RGD) peptide has strong affinity to heterodimeric glycoprotein receptor $\alpha_v\beta_3/\alpha_v\beta_5$that is higly upregulated on endothelial cells during angiogenesis in infarcted and border zone during early healing process following myocardial injury. peptide has stron	Preclinical
[^{68}Ga]Ga-DOTA-RGD [28]			
[^{68}Ga]Ga-NODAGA-RGD [29,30]			
[^{68}Ga]Ga-RGD [31]			
[^{68}Ga]Ga-TRAP-(RGD)$_3$ [32]			
[^{18}F]AlF-NOTA-PRGD2 [33]			
[^{18}F]Alfatide II [34]			
[^{18}F]galacto-RGD [35,36]			Preclinical / clinical
[^{68}Ga]Ga-PRGD2 [37]			Clinical
[^{18}F]Fluciclatide [38]			
PET tracer	**Marker**	**Post MI fibrosis targeting mechanism**	**Phase of usage**
[^{68}Ga]Ga-MHLL1 [39]	FAP	Targeting membrane-bound serine protease fibroblast activation protein (FAP) which are highly expressed by activated myofibroblast during healing phase for fibrotic tissue formation following MI	Preclinical
[^{68}Ga]Ga-FAPI-04 [40-42]			Clinical / preclinical
[^{68}Ga]Ga-FAPI-46 [43,44]			Clinical
[^{18}F]AlF-NOTA-FAPI [45]			
[^{18}F]galacto-RGD [46,47]	Fibroblast activity $\alpha_v\beta_3$ integrin	Targeting $\alpha_v\beta_3$ integrin to identify the myofibroblast proliferation	Clinical / preclinical
[^{11}C]KR31173 [48-51]	Angiotensin receptor	Targeting myocardial renin-angiotensin system (RAS) via angiotensin II subtype 1 receptor (AT1R) which its expression in myofibroblast are associated with interstitial fibrosis and ventricular dysfunction	Preclinical

References: [1]Rischpler *et al*., 2016; [2]Lukovic *et al*., 2024; [3]Perez *et al*., 2003; [4]Dalm *et al*., 2003; [5]Lapa *et al*., 2015; [6]Tarkin *et al*., 2017; [7]Thackeray *et al*., 2015; [8]Lapa *et al*., 2015; [9]Askari *et al*., 2003; [10]Gupta *et al*., 1999; [11]Strunk *et al*., 2024; [12]Lavine *et al*., 2014; [13]Heo *et al*., 2020; [14]Thackeray *et al*., 2018; [15]Jacobs *et al*., 2012; [16]Thackeray *et al*., 2016; [17]Morooka *et al*., 2009; [18]Varasteh *et al*., 2022; [19]Lucinian *et al*., 2024; [20]Lee *et al*., 2017; [21]Orbay *et al*., 2013; [22]Hong *et al*., 2013; [23]Zhang *et al*., 2013; [24]Rodriguez-Porcel *et al*., 2008; [25]McCOLL *et al*., 2004; [26]Goodsell *et al*., 2002; [27]Eo *et al*., 2013; [28]Kiugel *et al*., 2014; [29]Lang *et al*., 2020; [30]Grönman *et al*., 2017; [31]Bentsen *et al*., 2023; [32]Laitinen *et al*., 2013; [33]Gao *et al*., 2012; [34]Mandic *et al*., 2016; [35]Sherif *et al*., 2012; [36]Makowski *et al*., 2021; [37]Sun *et al*., 2014; [38]Jenkins *et al*., 2017; [39]Langer *et al*., 2021; [40]Notohamiprodjo *et al*., 2022; [41]Qiao *et al*., 2022; [42]Varasteh *et al*., 2019; [43]Kessler *et al*., 2021; [44]Diekmann *et al*., 2021; [45]Xie *et al*., 2022; [46]Jenkins *et al*., 2017; [47]Higuchi *et al*., 2008; [48]Weber, 1997; [49]Fukushima *et al*., 2012; [50]Higuchi *et al*., 2010; [51]Verjans *et al*., 2010.

2.9 Preparation of fluorine-18 radiolabeled tracer

2.9.1 Production of fluorine-18

Cyclotrons produce [^{18}F]fluoride ([^{18}F]F$^-$) or [^{18}F]fluorine ([^{18}F]F_2) through various nuclear reactions for different purposes of radiolabeling. [^{18}F]fluoride is most frequently used for nucleophilic radiolabeling and is, in most cases, produced via the nuclear reaction ^{18}O(p,n)^{18}F, using oxygen-18 enriched water ([^{18}O]H_2O) as the target material as depicted in **Figure 11** (Solin *et al*., 1988; Cole *et al*., 2015).

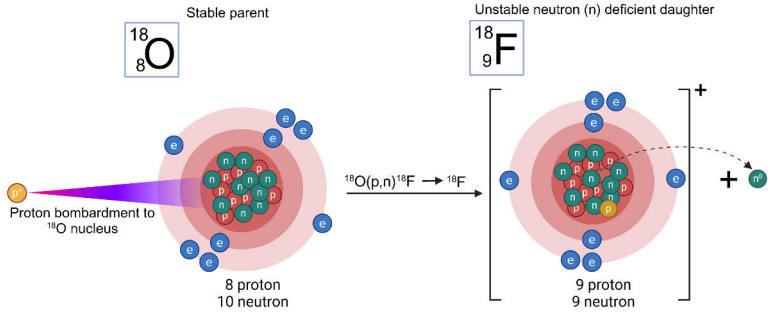

Figure 11. ^{18}O(p,n)^{18}F nuclear reaction scheme to produce nucleophilic fluorine-18. Proton beam is bombarded from cyclotron to oxygen-18 nucleus. ^{18}F then decays back to the stable ^{18}O and this phenomena is used as basic principle of PET imaging.

Another chemical form is [^{18}F]F_2, which is used for electrophilic ^{18}F-fluorination. Nuclear reactions that can produce [^{18}F]F$^-$ and [^{18}F]F_2 are listed in **Table 4** (Bergman *et al*., 1995; Bergman *et al*., 1997; Forsback *et al*., 2015).

Table 4. Nuclear reactions for production of nucleophilic and electrophilic fluorine. (Modified from Bergman, 2001).

Nuclear reaction	Target material	Product
^{18}O(p,n)^{18}F	[^{18}O]H_2O	Nucleophilic fluorine
^{20}Ne(^{3}He,αn)^{18}Ne, ^{18}Ne-^{18}F	Ne	Nucleophilic fluorine
^{16}O(^{3}He,p)^{18}F	H_2O	Nucleophilic fluorine
^{16}O(α,pn)^{18}F	H_2O	Nucleophilic fluorine
^{18}O(p,n)^{18}F	[^{18}O]O_2/noble gas + carrier (fluorine)	Electrophilic fluorine
^{20}Ne(d,α)^{18}F	Ne + carrier (fluorine)	Electrophilic fluorine
^{20}Ne(p,2pn)^{18}F	Ne + carrier (fluorine)	Electrophilic fluorine

[^{18}F]F^- is used for the nucleophilic fluorination of the ligand, while [^{18}F]F_2 is intended for electrophilic fluorination and will be discussed later. One important factor to consider is the molar activity of the produced fluorine-18. Even though [^{18}F]F_2 ([^{18}F]F^+) is the most reactive form of fluorine-18, which makes it easier for radiolabeling reactions with the ligand, the molar activity of [^{18}F]F_2 is much lower (maximum ~100 GBq/μmol) compared to [^{18}F]F^-, which can reach 10 TBq/μmol (Bergman *et al*., 1997; Solin *et al*., 1988). This can be attributed to the fluorine-19 carrier needed in the process of producing [^{18}F]F_2 (Coenan, 2007). The molar activity of the fluorine-18 used for radiolabeling affects the molar activity of the product and can influence the radiochemical yield of the radiolabeled tracer. Thus, when working with a ligand-receptor binding system with lower concentrations, the lower [^{18}F]F_2 molar activity due to the [^{19}F]F_2 added as a carrier may cause receptor saturation and reduce the PET signal from the binding (Chai *et al*., 2008).

2.9.2 ^{18}F-fluorination

Radiolabeling of PET tracers with fluorine-18 can be performed through nucleophilic fluorination, electrophilic fluorination, and chelation-based fluorination, as briefly mentioned before (Jacobson *et al*., 2015).

2.9.2.1 Nucleophilic fluorination

As previously indicated, nucleophilic fluorination is conducted by [^{18}F]fluoride, which is less reactive compare to electrophilic fluorine. This is caused by [^{18}F]F^- hydrogen bonding formed with water, which is used to trap fluoride for next step labeling (Kim *et al*., 2008). Thus, to facilitate the nucleophilic substitution with the ligand, [^{18}F]F^- nucleophilicity should be increased by dehydration, also known as azeotropic drying using organic solvent such as acetonitrile (Jacobson *et al*., 2015; Perrio *et al*., 2016). The drying process is considerably time consuming which can become one of the challenge in nucleophilic fluorination (Lahdenpohja *et al*., 2019).

There are multiple nucleophilic substitution mechanisms used for radiolabeling the ligand, including aliphatic nucleophilic substitution, as seen in the production of [^{18}F]FDG, and nucleophilic aromatic fluorination, such as that used in 6-[^{18}F]fluorodopamine (Bratterby *et al*., 2021; Timmers *et al*., 2009). Nucleophilic aromatic fluorination requires an electron-deficient aromatic ring to achieve [^{18}F]F^- substitution, which in some cases can be challenging to achieve. Several methods have been explored to achieve successful nucleophilic aromatic substitution, including incorporating heteroarenes that contain electron-deficient nitrogen, using the Balz-Schiemann reaction, the Wallach reaction, and employing diarylidenonium salts to introduce [^{18}F]F^- into arenes (Jacobson *et al*., 2015).

2.9.2.2 Electrophilic fluorination

Electrophilic fluorination utilizes the electrophilic fluorine $[^{18}F]F_2$, where the radiolabeling reactions are allowed to occur at mild temperatures and are less time-consuming compared to the nucleophilic method. Electrophilic fluorination requires electron-rich reactants to attach the F^+, such as electron-rich aromatic rings and alkenes (Lee *et al*., 2011; Wang *et al*., 2021).

Electrophilic F_2 is the most reactive form of fluorine, making radiolabeling reactions relatively straightforward to accomplish (Casella *et al*., 1980). However, the highly reactive nature of $[^{18}F]F_2$ can pose challenges when working with inactive precursors. $[^{18}F]F_2$ can be converted into other reactive electrophilic fluorine species, which act as impurities that can also label the precursor, resulting in unwanted by-products that are difficult to separate from the desired $[^{18}F]F_2$-labeled precursor. This potential issue should be considered when using electrophilic fluorination. Additionally, the low molar activity, as briefly mentioned before, is a consequence of the need to add a relatively large amount of carrier fluorine ^{19}F.

2.9.3 $[^{18}F]$AlF-chelation based fluorination

$[^{18}F]$fluoride is used in $[^{18}F]$AlF-chelation chemistry for the indirect ^{18}F-fluorination of target molecules. This is a revolutionary discovery by McBride and colleagues to harness the favourable imaging properties of fluorine-18 with the simplicity of metal-chelate chemistry. Traditional methods for ^{18}F-labeling (e.g. nucleophilic and electrophilic substitution) often involve complex, multi-steps syntheses that can be time-consuming and may not be suitable for sensitive biomolecules which prefer mild condition for labelling with fluorine-18.

$[^{18}F]$AlF-labeling method eliminates the azeotropic drying steps and provides a direct use of aqueous $[^{18}F]$fluoride for labeling (McBride *et al*., 2009). The basic principle involves introducing $[^{18}F]F^-$ to the ligand by incorporating the aluminum metal to form $[^{18}F]$AlF, which is known as a pseudo-radiometal complex (Archibald *et al*., 2021). This labeling method was used in the production of PET tracers in studies I, II, and III included in this dissertation.

$[^{18}F]$AlF radioalebing method is based on the general labeling scheme as shown by **Figure 12**:

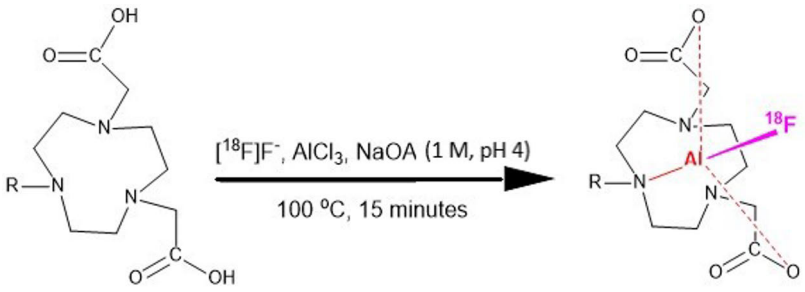

Figure 12. General radiolabeling scheme with [^{18}F]AlF method. 1,4,7-Triazacyclononane-1,4,7-triacetic acid (NOTA) chelator is used for representative illustration. (Modified from Allott *et al*., 2017)

The [^{18}F]fluoride in water medium needs to be extracted using a quaternary methyl ammonium (QMA) cartridge or other types of ion exchange cartridges. Several QMA cartridges have been explored in various studies, such as Sep-Pak Light QMA, using saline as the eluent for [^{18}F]F$^-$ (Jiang *et al*., 2021; Giglio *et al*., 2018), Sep-Pak Accell Plus QMA (Lütje *et al*., 2019; Karsemans *et al*., 2018), and Sep-Pak Accell Plus QMA Light (Tshibangu *et al*., 2020). The choice of eluent is important to recover the maximum amount of [^{18}F]F$^-$ trapped in the QMA cartridge. Several other eluents that can be used include sodium acetate (NaOAc, 0.05 M, pH 4.5), $NaHCO_3$ (0.5 M), and $NaNO_3$ (Kersemans *et al*., 2018). This extraction aims to concentrate [^{18}F]F$^-$ into a small volume and remove impurities coming from the water used in fluorine-18 production (Archibald *et al*., 2021). In addition, the reaction volume usually affects the radiolabeling efficiency (Het *et al*., 2014).

Bifunctional chelator selection is an important factor for the adequate sequestration of metallic or metal-mediated radionuclides and provides the requisite chemistry for tight attachment to the targeting vector of interest, such as peptides, proteins, carbohydrates, or nanoparticles. Bifunctional chelator selection can affect the stability of the final product and the efficiency of the radiolabeling reaction (Brechbiel, 2009). Aside from NOTA, several chelators have been tested for AlF chemistry, including diethylenetriaminepentaacetic acid (DTPA), 2-(4,7-bis (carboxymethyl)-1,4,7-triazonan-1-yl) pentanedioic acid (NODAGA), 1,4,7-triazacyclononane-1,4-diacetic acid (NODA), 2-AMPTA, NHB-2-AMPDA, 2-AMPDA-HB, 1,4,7-tris(2-hydroxybenzyl)-1,4,7-triazacyclononane (H3L1), 2-(mercapto)ethylaminoacetyl-L-cysteine (H3L3), and tetrafluorophenyl ester derivative of restrained complexing agent ((±)-H3RESCA) (McBride *et al*., 2009; Da Pieve *et al*., 2020; Da Pieve *et al*., 2016; Ruselli *et al*., 2020; Cleeren *et al*., 2017; Cleeren *et al*., 2016). [^{18}F]AlF-NOTA complexes have demonstrated both *in vitro* and *in vivo* stability, and several NOTA-based tracers have progressed to clinical evaluation, including [^{18}F]AlF-NOTA-Octreotide for imaging neuroendocrine

tumors, [^{18}F]AlF-NOTA-FAPI-04 for targeting cancer-associated fibroblasts, and [^{18}F]AlF-NOTA-PRGD2 for visualizing tumor angiogenesis. These precedents form the rationale for selecting NOTA as the chelator for [^{18}F]AlF-labeling of D10CM molecules (Laupe *et al*., 2024; Dong *et al*., 2024; Yang *et al*., 2012).

Temperature and pH used in the radiolabeling reaction are other key factors that determine the reaction efficiency. Higher temperatures (100 – 120 °C) are needed to chelate ([^{18}F]AlF^{2+}) with the NOTA chelator, and the formation of [^{18}F]AlF from [^{18}F]F^- and $AlCl_3$ in ammonium acetate buffer is highly pH dependent. The optimum pH is in the range of 4 – 5 to minimize the formation of [^{18}F]HF and $Al(OH)_3$ precipitation, with acidic pH < 4 and basic pH > 5, respectively (Martin, 1988; McBride *et al*., 2013). In short, the [^{18}F]AlF labeling method is one innovation that contributes to the advancement of fluorination with [^{18}F]fluoride.

2.9.4 Biomolecule fluorination

Apart from the ^{18}F-fluorination method, the characteristics of the ligand that will be labeled are another important factor to consider. Many biomolecules are incorporated as target compounds in molecular imaging, such as carbohydrates like sugars, proteins, and nucleic acids such as deoxyribonucleic acid (DNA) and ribonucleic acid (RNA), peptides, oligonucleotides, and other vectors. These molecules are typically sensitive to temperature and pH, and harsh radiolabeling conditions may affect their stability, leading to issues such as hydrolysis and denaturation (Felgueiras, 2023). These biomolecules can be labeled using direct or indirect labeling methods (Kniess *et al*., 2015). The direct labeling method may be simpler, as the fluoride is directly reacted with the biomolecules or the modified biomolecules, such as through ligation with a bifunctional chelator. The next necessary step is the purification of the results from the radiolabeling reaction. In contrat, indirect labeling refers to the use of a prosthetic compound to facilitate the fluoride attachment to the sensitive biomolecules.

Most peptides, proteins, and oligonucleotides are typically heat-sensitive and may undergo decomposition. Several types of ^{18}F- labeled prosthetic groups have been explored, such as *N*-succinimidyl 4-[^{18}F]fluorobenzoate ([^{18}F]SFB), 2,3,5,6-tetrafluorophenyl 6-[^{18}F]fluoronicotinate ([^{18}F]FPy-TFP), 1-alkylamino-7-[^{18}F]fluoro-8-azaisatoic anhydrides ([^{18}F]AFAs) and others (Gröner *et al*., 2023). The prosthetic group radiolabeling with fluorine-18 is first prepared and requires subsequent purification to remove unreacted precursors, byproducts, and reagents used in the labeling process. After purification, the fluorine-18 labeled prosthetic group complex is conjugated with biomolecules via alkylation, amination, and other methods (Jacobson *et al*., 2010). The recent innovation that won the Nobel Prize is the discovery of click chemistry, which provides a more efficient and effective way

to introduce prosthetic groups to biomolecules (Zaia, 2023). Click chemistry has revolutionized the labeling of bioactive compounds by enabling rapid and selective formation of carbon–heteroatom bonds (e.g. C–N or C–O) which are more commonly found in natural biomolecules and generally better tolerated in biological system than carbon–carbon bonds. This bioorthogonality makes click reactions suitable for radiolabelling peptides, proteins and other sensitive biological structures (Moses *et al*., 2007; Bauer *et al*., 2023).

2.9.5 Quality control of ^{18}F-radiolabeled tracer

Quality control is a critical process that must be performed before radiotracers are delivered for imaging, applicable to both clinical and preclinical settings. While the standards for preclinical applications may be less stringent compared to those for radiopharmaceuticals used in clinical practice, it remains essential to ensure the integrity of the products.

In both clinical and preclinical studies, a variety of tests are conducted to ensure the quality of radiopharmaceuticals. Some tests are performed for each batch, while others are made for selected batches. These tests encompass the identification of the product against a reference compound, pH measurement, evaluation of appearance, radiochemical and chemical purity, molar activity, solubility assessment, and stability evaluation.

For ^{18}F-labeled radiopharmaceuticals intended for clinical use, quality control is conducted under Good Manufacturing Practice (GMP) standards and includes additional critical parameters such as radionuclide identification and purity, enantiomeric purity (when applicable), sterility, bacterial endotoxin levels, and residual solvent and metal content. These requirements are outlined in detail in monographs from regulatory bodies such as the European Pharmacopoeia, the United States Pharmacopeia, and the British Pharmacopeia, as well as in the Chemistry, Manufacturing, and Controls (CMC) section of the U.S. Food and Drug Administration.

Taking [^{18}F]FDG as the reference standard, radionuclide verification involves confirming a physical half-life of 110 ± 5 minutes using a calibrated dose calibrator, and characteristic gamma energies of 511 keV or 102.22 keV using a gamma spectrometer. Chemical purity assessments include colorimetric tests for residual kryptofix—ensuring no darker spot appears in the sample than in the reference—and HPLC analyses to detect tetra-alkyl ammonium salts, where side product peaks should remain below that of the reference.

Residual organic solvents must also be carefully monitored, especially those used during radiosynthesis and purification processes. These solvents are necessary for dissolving precursors and intermediates, as well as for facilitating efficient

radiolabelling, such as acetonitrile and ethanol used in Al[^{18}F]F radiolabeling method. According to [^{18}F]FDG standards, residual acetonitrile should not exceed 4.1 mg per maximum dose volume for a single day's injection (Yu *et al*., 2006).

Sterility testing is mandatory to confirm the absence of microbial contamination in the final product. This includes a direct inoculation test and bacterial endotoxin testing using the Limulus Amebocyte Lysate (LAL) assay, with an acceptance limit of 175 IU per maximum dose volume. The integrity of the sterilizing filter must also be verified, typically via a bubble point test, such as the ≥3.5 bar threshold specified for the Cathivex-GV 0.22 μm filter, as applied in the quality control of [^{18}F]PSMA-1007 (Yu *et al*., 2006; Lau *et al*., 2020; Cardinale *et al*., 2017).

Ultimately, successful preclinical and clinical PET studies depend on the comprehensive application of quality control. Whether developing new radiotracers or conducting routine imaging, stringent quality control processes—including radiosynthesis monitoring, chemical analysis, and biological evaluation—are indispensable for ensuring safe and effective molecular imaging.

2.9.6 Identity

The identity of fluorine-18 labeled tracers includes both the reference compound identity and the radiolabeled compound. Typically, the identity and purity of the cold reference compound are determined using mass spectrometry, nuclear magnetic resonance (NMR) and high-performance liquid chromatography (HPLC) systems. The radiolabeled compound is usually identified with a reference standard using an HPLC system equipped with a radioactivity detector. In typical cases, the acceptance criteria state that the retention time of the radiolabeled compound is within ± 0.5 minutes of the retention time of the reference standard. This allows the coinciding retention times of the cold standard and the radiolabeled product to confirm the presence of the compound of interest and that the correct compound is radiolabeled (Mercado *et al*., 2023).

2.9.6.1 Physical parameters (pH, osmolality, visual appearances)

The final pH of the ^{18}F-labeled compound should be safe for the biological and physiological systems of the study subjects. The pH can be determined using potentiometric methods or strip indicators and needs to be in the range of 4.5–7.5, or 4.5–8.5 in [^{18}F]FDG quality control according to the British Pharmacopeia (Yu, 2006).

Osmolality is important to consider for intrathecal administration of radiopharmaceuticals due to the dilution and buffering capacity of the blood (Loveless, 2009). However, in general, the final radiopharmaceutical products

should be isotonic, which means they have the same osmotic pressure as human serum. The osmolality of the radiopharmaceuticals can be measured using an osmometer, and 250 to 350 mOsm/kg^{-1} are considered isotonic (Ekinci *et al*., 2022).

Visual appearances are evaluated through manual observation, and the final product is expected to be clear and colorless (Cardinale *et al*., 2017). Nonetheless, the [^{18}F]FDG guideline permits a slight yellow coloration (Yu, 2006).

2.9.6.2 Chemical and radiochemical purity

The chemical purity of the final product can be assessed using HPLC equipped with suitable detectors such as ultra-violet (UV) detector, refractive index detector, mass detector and electrochemical detectors, to identify impurities that could impact the quality of radiolabeled products or potentially lead to adverse reactions when administered to subjects (Mercado *et al*., 2023). Furthermore, other methods such as thin-layer chromatography (TLC) and gas chromatography (GC) have also been documented as viable options for evaluating chemical purity (Cardinale *et al*., 2017).

The conditions of the radiolabeling reaction can influence the final product, including the potential for radiolysis, which may lead to the formation of impurities. The presence of these impurities might affect the image, compromise its targeting capability, and ultimately affect the quality of the diagnostic results (Mercado *et al*., 2023). Impurities may also be introduced through the storage methods or during long-distance transportation, which can impact the stability of the precursor, as well as from inaccuracies during the synthesis of the precursor. Assessing radiochemical purity (RCP) is an essential quality control measure, defined as the ratio of the desired radiolabeled species to the total radioactivity in the sample (Maioli *et al*., 2017). The RCP of fluorine-18 labeled tracers can be evaluated using HPLC and TLC.

2.9.6.3 Molar activity

Molar activity (A_m) is described as the amount of radioactivity per mole of the compound and is expressed in GBq/µmol or Bq/mol. A_m can be identified when the molecular weight of the compound is known (Luurtsema *et al*., 2021). The determination of A_m is particularly important for bioactive or toxic molecules that may generate undesirable pharmacological or adverse reactions, making it crucial to administer non-pharmacological or non-toxicological doses. One example is [^{18}F]DOPA, which can cause serious adverse effects in subjects after the administration of low A_m [^{18}F]DOPA (6 GBq/µmol), and thus, it is necessary to produce it with as high an A_m as possible (Anderson *et al*., 2021). A_m is also crucial when aiming for low-density receptors, where an excessive amount of the compound may affect receptor availability at the binding site. [^{18}F]DCFPyL is one example for

prostate-specific membrane antigen (PSMA) imaging that can achieve an A_m of 1.40 ± 0.15 TBq/μmol (Dorman *et al*., 2018). High A_m is required in neuroreceptor and central nervous system receptor imaging to increase radioactivity uptake in the target area and obtain a high target-to-background ratio (Toomey *et al*., 2012; Liu *et al*., 2021). Theoretically, the occupancy of receptors by the non-radioactive compound should be < 5%. In PET kinetic modeling, high A_m is necessary to achieve a good signal-to-noise ratio, as it may affect the quantification process and the qualitative interpretation of the derived images. One study showed that using high A_m [^{18}F]F-DPA (990 ± 150 GBq/μmol) increased the tracer uptake by 1.5-fold in the brain of a mouse model with Alzheimer's disease compared to using low A_m [^{18}F]F-DPA (9.0 ± 2.9 GBq/μmol) (Keller *et al*., 2019).

The significance of A_m diminishes when the target concentration is sufficiently high within the body or when the biological target does not easily reach saturation. An example is the use of radiolabeled water for PET imaging of myocardial blood flow (Maaniitty *et al*., 2020), radiolabeled glucose for brain imaging (Graham *et al*., 1998), and radiolabeled acetate for assessing myocardial oxygen metabolism (Grassi *et al*., 2012).

A_m can be determined using HPLC or ultra-performance liquid chromatography (UPLC) with a suitable detectors. The fluorine-18 A_m also affects the A_m of the radiolabeled compound due to the decay process (Luurtsema *et al*., 2021). Theoretically, the highest fluorine-18 A_m is 63.3 TBq/μmol (Savisto *et al*., 2018). However, there is no consensus on the definition of high A_m of fluorine-18. One study considered that A_m > 185 GBq/μmol is high (Sergeev *et al*., 2018). As the standard, the typical A_m of [^{18}F]FDG is 63.3 GBq/μmol, with a starting activity of ≥ 140 GBq of fluorine-18 (Tippayamontri *et al*., 2022).

2.9.6.4 Lipophilicity

The lipophilicity of the fluorine-18 labeled tracer determines its penetration through the cell membrane and minimizes the radiotracer's non-specific binding in the background tissue (Liu *et al*., 2024). Lipophilicity or hydrophilicity of a PET tracer can be determined by a distribution coefficient (log*D*) study (Lee *et al*., 2017; 2006). A log*D* study is an important parameter that describes the ability of the PET tracer to transit through the blood-brain barrier to the binding site in the targeted tissues (Chang *et al*., 2006). Log*D* can be calculated from the ratio of radioactivity in the organic phase to that in the aqueous phase (Lee *et al*., 2017). Depending on the type of tissue target, either high to moderate lipophilicity or high hydrophilicity may be preferred as desirable tracer characteristics. Brain imaging generally requires a higher lipophilicity; for example, the log*D* value of [^{18}F]cEFQ was 3.25 for imaging of metabotropic glutamate receptor targeting in the brain, and the log*D* value of

[^{18}F]Fluspidine for imaging of tau receptor in the brain is between 2-3 (Lee *et al*., 2017; Ludwig *et al*., 2024). On the other hand, other fluorine-18 labeled tracers require a lower log*D* value, such as [^{18}F]vancomycin for imaging bacterial infection, which has a log*D* of -0.96 ± 0.03, indicating that the tracer's systemic distribution favors a hydrophilic nature (Spoelstra *et al*., 2024).

Lipophilicity plays a significant role in a tracer's interaction with plasma proteins, which can impact its biodistribution and availability for tissue distribution (Lever *et al*., 2016). Hydrophilic tracers exhibit higher availability when they have a lower tendency to bind to plasma proteins; in contrast, highly lipophilic tracers are more likely to associate with these proteins (Wanat, 2020; Lau *et al*., 2020; Liu *et al*., 2016).

2.9.6.5 Stability

The stability of the fluorine-18 labeled tracer is crucial and should be assessed from both *in vitro* and *in vivo* perspectives. These factors are significant due to issues such as defluorination and radiolysis. It is essential to utilize stable radiopharmaceuticals, as instability can compromise targeting efficacy and imaging quality. Additionally, considerations regarding stability are vital when developing PET kinetic models (Aarnio *et al*., 2022). Defluorination of the tracer can lead to fluorine-18 accumulation in bone tissue, which may disrupt both quantitative and qualitative image analysis (Lau *et al*., 2020). The stability of the PET tracer in its final production formulation, including its shelf-life, can be conveniently evaluated by injecting tracer samples into an HPLC system fitted with both a radioactivity detector and a suitable detector at the end of synthesis (EOS) and subsequently at intervals of 1 hour, 2 hours, 3 hours, 4 hours, and so on. The HPLC results will allow for the assessment of radiochemical purity and any variations in purity over time (Wang *et al*., 2020). Furthermore, *in vitro* stability in blood plasma or serum can also be analyzed using the same HPLC technique (Brömmel *et al*., 2021). Typically, *in vitro* stability is evaluated prior to the tracer's application *in vivo*.

In vivo stability is a critical parameter due to the role of enzymes in biological processes within plasma or target tissues, which can lead to the breakdown of the parent structure of the radiolabeled tracer (Lau *et al*., 2022). This degradation may result in defluorination or the conversion of the tracer into another radiolabeled species, potentially causing unintended uptake in target tissues as well as in non-target tissues. Research can be conducted using HPLC or TLC on blood or plasma samples collected from experimental animals following tracer administration (Aarnio *et al*., 2024). Furthermore, for peptide-based PET tracers, stability against enzymatic degradation can be evaluated by the co-administration of peptide inhibitors (Lau *et al*., 2022; Nock *et al*., 2014).

3 Aims

The purpose of this work was to develop a new PET tracer for the macrophage mannose receptor CD206-targeted imaging of inflammation, particularly the detection of M2 macrophages. Accordingly, we utilized a mannosylated dextran derivative for aluminum fluoride-18 labeling via the NOTA chelator and evaluated it in experimental animals.

Specifically, the aims of this study were to:

(1) Radiolabel a mannosylated dextran derivative to form [^{18}F]AlF-NOTA-D10CM and evaluate its suitability for *in vivo* PET imaging in healthy rats.

(2) Validate the ability of [^{18}F]AlF-NOTA-D10CM to specifically detect the macrophage mannose receptor CD206 in inflammation foci and active lymph nodes in a mouse model of skin inflammation, and by comparing CD206-deficient and wild-type (WT) mice.

(3) Investigate the ability of [^{18}F]AlF-NOTA-D10CM to detect CD206 expression in experimental acute myocardial infarction in rats.

4 Materials and Methods

Table 5. Summary of preclinical evaluation trajectory in each studies.

Study/ Imaging modality	Radiotracer/ Administration route	Experimental subjects	Complementary analysis
Study 1/ PET/CT	[^{18}F]AlF-NOTA-D10CM i.v.	SD rats (healthy)	• Distribution coefficient (Log*D*) determination • Molar activity determination • [^{18}F]FDG • *ex vivo* gamma counting • *in vivo* blocking study • *in vivo* stability study in SD rats (healthy) • CD206 IHC staining of liver, spleen and bone marrow
Study 2/ PET/CT	[^{18}F]AlF-NOTA-D10CM i.v. i.d.	• CD206 KO mice • CD206 WT mice • C57BL/6N mice with foot pad skin inflammation induced by CFA (Day 5) • C57BL/6N mice with foot pad skin inflammation induced by CFA (Day 14) • C57BL/6N mice (healthy)	• [^{18}F]FDG • *ex vivo* gamma counting • *ex vivo* ARG of popliteal LNs and inflamed foot pad skin • H&E and CD206 IHC staining of inflamed popliteal LNs and inflamed foot pad skins • IF staining (CD206, CD31, CD11b and DAPI) of inflamed and healthy popliteal LNs, and inflamed and healthy foot pad skin • Quantification of CD206 area-% • *in vitro* binding specificity study in inflamed popliteal LNs • *in vivo* stability study in C57BL/6N mice (healthy)
Study 3/ PET/CT	[^{18}F]AlF-NOTA-D10CM i.v.	• SD rats with MI induced by permanent LAD ligation (Day 3) • SD rats with MI induced by permanent LAD ligation (Day 7) • Sham operated SD rats (Day 3) • Sham operated rats (Day 7)	• Binding study in polarised human blood monocyte to MI and & M2 macrophages using flow cytometry • Affinity binding study in CD206 CHO transfected cells • [^{18}F]FDG • *ex vivo* gamma counting • *ex vivo* ARG of LV (all groups) • H&E staining and CD206 IHC staining of LV (all groups) • IF double staining (CD206 + CD68) of infarcted LV • Quantification of CD206 area-% (all groups) • *in vitro* binding specificity study in infarcted LV • Kinetic modeling of PET data

Abbreviations: SD: Sprague Dawley; i.v.: intravenous; i.d.: intradermal; IHC: immunohistochemistry; DAPI: 4′,6-diamidino-2-phenylindole; KO: knockout; WT: wild type; CFA: Complete Freund's Adjuvant; LNs: lymph nodes; ARG: autoradiography; H&E: hematoxylin and eosin; IF: immunofluorescence; CD (206, 31, 11b, 68); CHO: Chinese hamster ovary.

4.1 Radiotracer production and characterization

4.1.1 Production of [^{18}F]fluoride

[^{18}F]fluoride was produced in the Turku PET Centre, Accelerator Laboratory, Åbo Akademi University via $^{18}O(p,n)^{18}F$ nuclear reaction where oxygen-18 enriched water was irradiated with proton beam from cyclotron and the yielded fluoride [^{18}F]F^- was then harvested from accelerator target chamber as [^{18}F]F^- in water.

4.1.2 [^{18}F]AlF labeling strategy

Pseudo-radiometal labeling technique aims to convert the [^{18}F]F^- to a [^{18}F]AlF complex ready for a chelation reaction with the ligand (**Figure 13**). The principle is taking advantage of tight bond formation between F^- and Al^{3+}. Thus, the vector introduction to fluorine-18 is accessible via aluminum metal.

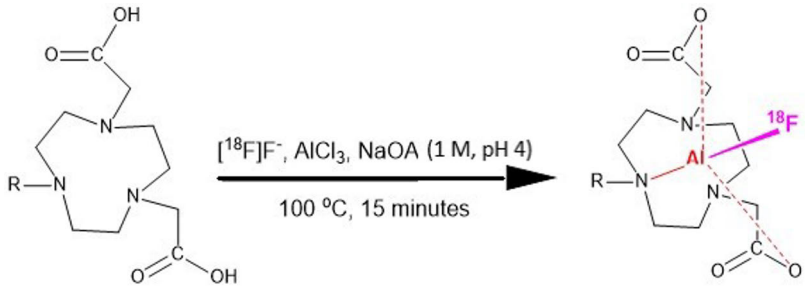

Figure 13. Chelation of Al[^{18}F]F with 2,2',2"-(1,4,7-triazacyclononane-1,4,7-triyl)triacetic acid (NOTA) chelate. (Modified from Allott *et al*., 2017).

4.1.3 [^{18}F]AlF-NOTA-D10CM production

4.1.3.1 Synthesis of D10CM

The mannosylated and cysteinylated dextran derivative (D10CM, 21.9 kDa), was synthesized using a method similar to those previously described by our collaborator, Prof. Ioannis Pirmettis group (Pirmettis *et al*. 2012; Papasavva *et al*., 2021; Tsoukalas *et al*., 2014).

The compound 2,2′-(7-(2-((2,5-dioxopyrrolidin-1-yl)oxy)-2-oxoethyl)-1,4,7-triazonane-1,4-diyl)diacetic acid (NOTA-NHS, the N-hydroxysuccinimide-activated ester of NOTA) was obtained from CheMatech (Dijon, France). All other chemicals were sourced from commercial suppliers.

4.1.3.2 NOTA-D10CM

A solution of NOTA-NHS ester (117 mg) in 2 mL of dimethyl sulfoxide was added to a solution of D10CM (100 mg) in 4 mL of borate buffer (0.1 M, pH 9.0). The reaction mixture was stirred at room temperature for 18 hours, then transferred to an ultrafiltration cell (model 8050, Millipore Corp, Bedford, MA) equipped with an ultrafiltration membrane (YM03). The volume was adjusted to 50 mL with deionized water, and the solution was concentrated to 5 mL by applying nitrogen gas under pressure directly to the ultrafiltration cell. This process was repeated four times, and the final residue was lyophilized, yielding the product as a white solid (100 mg).

4.1.3.3 Radiofluorination of NOTA-D10CM

Radiolabeling of NOTA-D10CM with [^{18}F]fluoride was carried out using a custom-made remote-controlled device (DM Automation, Nykvarn, Sweden), as described earlier (**Figure 14 and Appendix 1**) (Andriana *et al*., 2023). [^{18}F]Fluoride was produced in a cyclotron as described earlier in 4 mL H_2O. [^{18}F]F^- was then extracted into an anion-exchange cartridge (PS-$HCO3^-$). Physiological saline (0.9 mg/mL, 220 µL) was used to elute the [^{18}F]fluoride into a reaction vial containing NOTA-D10CM (1.5 mg) in 50 µL TraceSELECT water (Honeywell, Morristown, NJ), ascorbic acid (150 mM, 40 µL), $AlCl_3$ (2 mM) in CH_3CO_2Na buffer (pH 4.0, 1 M, 25 µL), and CH_3CN (50 mM, 60 µL). The mixture was heated at 100°C for 13 minutes, then cooled to 40°C before adding a mixture of water (810 µL) with 0.1% trifluoroacetic acid (TFA) and ascorbic acid (150 mM, 90 µL). The product was purified using HPLC with a semipreparative C18 Jupiter Proteo column (250 × 10 mm, 4 µm, 90 Å; Phenomenex, Torrance, CA). The mobile phases used were water with 0.1% TFA (solvent A) and acetonitrile with 0.1% TFA (solvent B). The flow rate started at 1 mL/min and increased to 4 mL/min from 0 to 1 minute, with 95% solvent A and 5% solvent B. Over the next 1–20 minutes, the solvent B content increased to 30%. The [^{18}F]AlF-NOTA-D10CM fraction was collected into a vial with water (30 mL) and ascorbic acid (150 mM, 400 µL). The product was extracted using a preconditioned tC18 cartridge (Waters, Milford, CT), rinsed with water, and then eluted with 1 mL of 30% ethanol (300 µL ethanol, 100 µL ascorbic acid in water, and 600 µL water). The final product was collected in a bottle containing 15 mM ascorbic acid in saline (1.5 mL), and 0.1 M phosphate-buffered saline (PBS) was used to adjust the pH for animal studies.

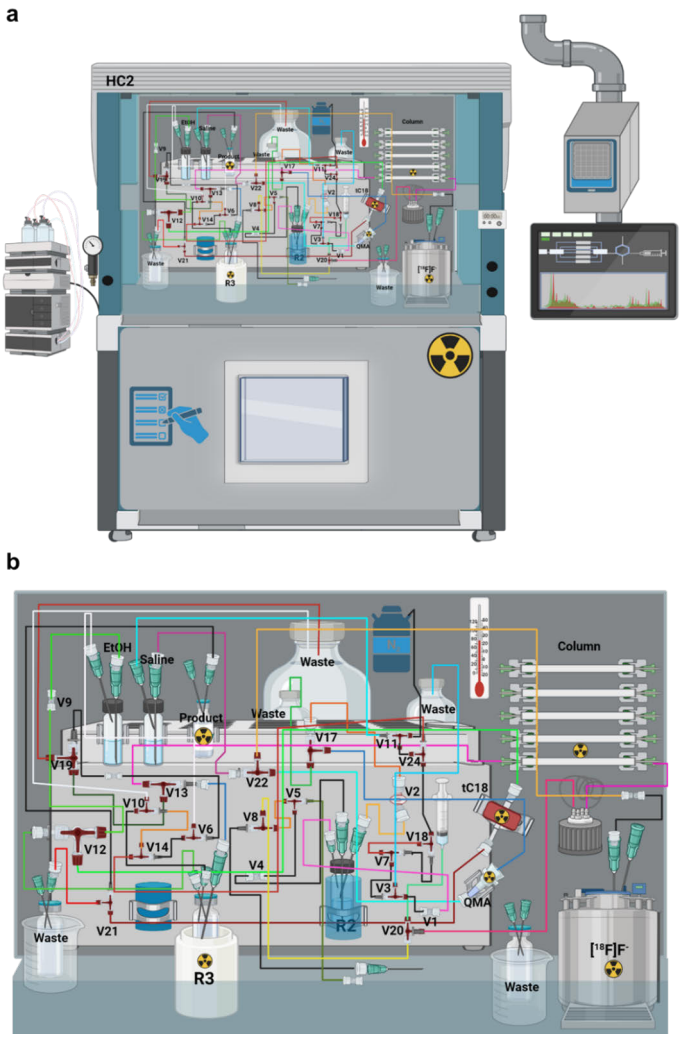

Figure 14. (**a**) Hotcell illustration used for tracer production of [^{18}F]AlF-NOTA-D10CM and others in Aurum radiochemistry laboratory, Turku PET Centre, with DM Automation synthesis device inside and (**b**) the magnified arrangement of the DM Automation system device. The real life picture of DM automation system devise is presented in **Appendix 1**.

4.1.4 Quality control of [^{18}F]AlF-NOTA-D10CM

[^{18}F]AlF-NOTA-D10CM was injected to animal after it passed the quality control. The radiochemical purity of the final product sample (0.3–0.8 MBq) was analyzed using an HPLC system (Hitachi; Merck, Darmstadt, Germany) with a Jupiter Proteo column (reversed-phase C18, 150 × 4.6 mm, 300 Å; Phenomenex) and a radioactivity detector (Radiomatic 150TR flow-through, Packard, Meriden, CT). Solvent A was water with 0.1% TFA, and solvent B was acetonitrile with 0.1% TFA. During the elution, the

solvent B content was gradually increased from 8% to 40% over 0–9 minutes, and then held at 40% for 9–10 minutes, with a flow rate of 1 mL/min. The stability of [^{18}F]AlF-NOTA-D10CM in the final product formulation buffer was checked by HPLC, with samples taken at 1, 2, 3, and 4 hours after the EOS.

4.1.5 Characterization of [^{18}F]AlF-NOTA-D10CM

4.1.5.1 Lipophilicity

Lipophilicity of [^{18}F]AlF-NOTA-D10CM was determined by Log*D* measurement. PBS (600 µL) and 1-octanol (600 µL) were added to a 1.5 mL Eppendorf tube, followed by 5 kBq of [^{18}F]AlF-NOTA-D10CM. The mixture was vortexed for 5 minutes, then centrifuged at 14,100 ×g for 3 minutes at room temperature to separate the water and organic phases. From each phase, 400 µL was collected for gamma counting using a Wizard 3″ gamma counter (PerkinElmer/Wallac, Turku, Finland). The experiment was performed in triplicate, and the LogD value was calculated using the corresponding formula:

$$logD = Log_{10}\left(\frac{counts\ in\ 1\text{-}octanol}{counts\ in\ PBS}\right)$$

4.1.5.2 Molar activity

The molar activity (A_m), indicates the amount of radioactivity per mole of the ligand. In this study, A_m was measured using HPLC with UV detection at 220 nm. Calibration curves were created by HPLC analysis of five NOTA-D10CM samples at concentrations of 1, 2, 4, 6, and 8 µM, and each concentration tested in triplicate. The same HPLC method used earlier for quality control was applied. To determine the product concentration, 50 µL of the decayed final product was analyzed, and the concentration (c, nmol/mL) was calculated using the calibration curve. The molar activity at EOS was then calculated using the following formula:

$$A_m = \frac{Total\ radioactivity\ at\ EOS\ (MBq)}{c\left(\frac{nmol}{mL}\right) \times volume\ (mL)\ of\ final\ product\ at\ EOS}$$

4.1.5.3 *In vivo* stability

The *in vivo* stability of [^{18}F]AlF-NOTA-D10CM was evaluated in healthy male Sprague-Dawley rats (n = 6, 457.5 ± 15.5 g, 15 weeks old) and female C57BL/6N mice (n = 6, 19.8 ± 0.7 g, 8–9 weeks old) following intravenous injection. Rats

received a dose of 49.1 ± 2.1 MBq, while mice were injected with 9.8 ± 0.4 MBq. Blood samples were collected into lithium heparin tubes at various time points including 5, 15, 30, 45 and 50 minutes post-injection using tail-cut in rats and cardiac or saphenous vein puncture method in mice. Plasma and cells were separated by centrifugation (14,000×g for 5 minutes at room temperature), and plasma proteins were precipitated with 10% sulfosalicylic acid. The filtered supernatant was diluted with 0.1% TFA in water and analyzed by radio-HPLC using a C18 Jupiter Proteo semipreparative column (Phenomenex, 250 × 10 mm, 5 µm, 90 Å) (**Figure 15**). The gradient used was 0.1% TFA in water (solvent A) and 0.1% TFA in acetonitrile (solvent B), starting with 5% B from 0 to 3 minutes, then increasing linearly to 60% B over 15 minutes, at a flow rate of 5 mL/min.

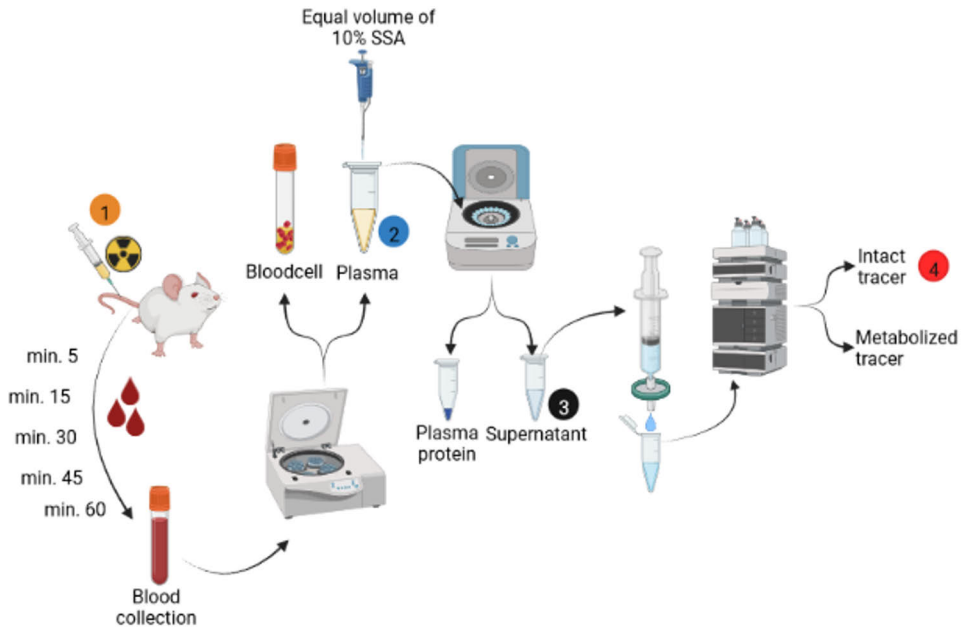

Figure 15. Stability study workflow of [^{18}F]AlF-NOTA-D10CM in rats or in mice.

4.2 Experimental animals

All animal experiments were approved by the national Project Authorization Board in Finland (license numbers ESAVI/43134/2019, ESAVI/8648/2020, and ESAVI/14685/2020) and conducted in compliance with EU Directive 2010/63/EU on the protection of animals used for scientific purposes. Animals were housed under controlled environmental conditions, including a 12:12-hour light-dark cycle, at the Central Animal Laboratory of the University of Turku and provided with free access to water and food *ad libitum*.

4.2.1 Healthy Sprague Dawley rats (Study I)

For initial *in vivo* PET imaging in Study I, healthy male Sprague-Dawley rats were used in the study, including six animals weighing 268.3 ± 31.8 g (7–8 weeks old) and four smaller rats weighing 94.9 ± 3.7 g (4 weeks old) to get whole body field of view for the *in vivo* blocking study. All rats were sourced from the Central Animal Laboratory at the University of Turku, Turku, Finland.

4.2.2 Wild-type and CD206 deficient mice (Study II)

CD206 knockout (CD206$^{-/-}$KO) and WT mice C57BL/6N mice were used in Study II to validate the specificity of [^{18}F]AlF-NOTA-D10CM uptake. The CD206$^{-/-}$ deficient (CD206$^{-/-}$ KO) MB6.129P2-*Mrc1*$^{tm1Mnz/J}$ mice alongside age- and sex-matched WT littermate controls, were sourced from Janvier Labs. The comparison included CD206$^{-/-}$ KO mice (n = 8; 4 females and 4 males, 25.2 ± 6.0 g, aged 10–15 weeks) and WT mice (n = 7; 4 females and 3 males, 26.7 ± 3.5 g, aged 10–23 weeks). Both groups underwent *in vivo* PET imaging, followed by *ex vivo* analysis on the same day.

4.2.3 Mice with skin inflammation (Study II)

To validate the [^{18}F]AlF-NOTA-D10CM uptake in inflamed tissue and active lymph nodes, mice with foot pad skin inflammation were developed for Study II.

Inflammation was induced in C57BL/6N mice by subcutaneous injection of 20 µL of a mixture containing CFA, F5881, Sigma Aldrich) and 2 µg of ovalbumin (vac-pova, InvivoGen) into the dorsal side of the left hind paws using 0.3 mL Microfine Demi syringes (BD) with a 30-G needle. The mice were studied either 5 or 14 days after CFA induction (day 0). CFA induction experiments were performed exclusively on WT mice, with non-inflamed, healthy C57BL/6N mice serving as controls. The CFA-induced mice were divided into two groups: Day 5 post-induction (n = 6 females, 20.2 ± 1.7 g, 9–10 weeks old) and Day 14 post-induction (n = 10 females, 20.1 ± 1.2 g, 11–12 weeks old). Healthy controls included 4 females (20.6 ± 0.5 g, 9 weeks old).

4.2.4 Rats with acute myocardial infarction and Sham control rats (Study III)

The last study on this thesis was aiming to investigate the application of [^{18}F]AlF-NOTA-D10CM *in vivo* PET for detection of myocardial infarction in a rat model. A total of 23 rats were assigned to four groups: 3 days post-myocardial infarction (n = 7), 3 days post-sham operation (n = 4), 7 days post-MI (n = 8), and 7 days post-sham operation (n = 4).

Myocardial infarction was induced in male Sprague-Dawley rats through permanent ligation of the LAD coronary artery. Approximately 30 minutes before anaesthesia, the rats received a subcutaneous (s.c.) dose of 0.5 mg/kg buprenorphine (Temgesic, Schering-Plough). Anaesthesia was induced via intraperitoneal (i.p.) injection of 80 mg/kg ketamine (Ketaminol®vet, Intervet) and 0.5 mg/kg medetomidine (Cepetor vet, Vetmedic). The thoracic area was shaved, cleaned, and treated with s.c. lidocaine (<7 mg/kg, Orion Pharma). Body temperature was maintained with a heating pad and monitored using a digital thermometer. Rats were intubated and connected to a rodent ventilator (TOPO dual mode ventilator, Kent Scientific). All surgical instruments and the surgical field were sterilized.

The LAD coronary artery was permanently ligated, and successful infarction was confirmed by myocardial paleness. Sham-operated rats underwent identical procedures without LAD ligation. The incisions were closed, and the rats were revived using 1 mg/kg i.p. atipamezole (Antisedan, Orion Pharma). Saline was administered s.c. before and after surgery. Post-surgical care included close monitoring and 0.5 mg/kg buprenorphine administration every 8 hours for three days. Mortality rates after LAD ligation were approximately 27% by MI Day 7 and 55% by MI Day 3, primarily due to severe infarction occurring on Day 0 or Day 1 post-surgery.

4.3 *In vivo* PET studies

4.3.1 Initial PET studies in healthy rats (Study I)

PET/CT imaging was conducted using an Inveon Multimodality scanner (Siemens Medical Solutions, Knoxville, TN). Rats were anesthetized with isoflurane (4–5% for induction and 1.5–2% for maintenance), and a tail vein cannula was placed. A CT scan was performed first for attenuation correction and anatomical reference, followed by a 60-minute PET acquisition starting at the time of intravenous injection of [^{18}F]AlF-NOTA-D10CM (51.6 ± 1.8 MBq, 431.1 ± 233.4 µL).

PET data were acquired in list mode and reconstructed using an ordered subsets expectation maximization 3-dimensional (OSEM-3D) algorithm into time frames of 30 × 3 s, 9 × 10 s, 4 × 30 s, 5 × 60 s, and 10 × 300 s.

Following PET/CT imaging, the animals were euthanized 70 minutes after [^{18}F]AlF-NOTA-D10CM injection, and tissues were collected, weighed, and analyzed with a gamma counter (Triathler 3″, Hidex, Turku, Finland). The radioactivity in tissues was expressed as a percentage of the injected radioactivity dose per gram of tissue (%ID/g), corrected for residual radioactivity in the cannula and tail.

PET/CT image analysis was conducted using Carimas 2.10 software (Turku PET Centre, Turku, Finland). Regions of interest (ROIs) were manually defined in organs

of interest using CT for anatomical reference. Time-activity curves (TACs) were generated from the 60-minute PET data and expressed as standardized uptake values (SUVs) over time post-injection.

4.3.2 PET studies in CD206 deficient and mice with skin inflammation (Study II)

A total of 35 mice were assigned to five groups: (1) $CD206^{-/-}$ KO, (2) WT, (3) day 5 post-CFA induction, (4) day 14 post-CFA induction, and (5) healthy controls. Imaging was conducted using PET and CT systems (Molecubes) under isoflurane anaesthesia (4–5% induction, 1.5–2% maintenance) with tail vein cannulation performed prior to scanning. CT scans were used for attenuation correction and anatomical reference. On consecutive days, PET imaging involved either a 20-minute static acquisition performed 90 minutes after intravenous injection of [^{18}F]FDG (4.95 ± 0.51 MBq), or a 120-minute dynamic acquisition initiated immediately after intravenous injection of [^{18}F]AlF-NOTA-D10CM (5.66 ± 2.18 MBq, 12.45 ± 4.80 µg, 0.57 ± 0.22 nmol), or intradermal injections of [^{18}F]AlF-NOTA-D10CM into the left hind paw (4.55 ± 1.69 MBq, 10.00 ± 3.73 µg, 0.45 ± 0.16 nmol) were performed for localized imaging. PET data were reconstructed using OSEM-3D algorithm into time frames of 10×60 s, 4×300 s, and 9×600 s and analyzed with Carimas 2.10 software. ROIs were manually defined on key organs using CT for anatomical guidance, and TACs (radioactivity concentration as a function of time after injection) were generated. The inflamed skin region was validated by increased [^{18}F]FDG uptake. Quantitative analysis was conducted using at least three consecutive planes acquired between 50–60 minutes post-injection of [^{18}F]AlF-NOTA-D10CM. On the final study day, mice received a 7.55 ± 2.84 MBq intravenous dose of [^{18}F]AlF-NOTA-D10CM for *ex vivo* analysis conducted 60 minutes post-injection.

4.3.3 PET studies in rats with acute myocardial infarction (Study III)

Rats were anaesthetized with isoflurane and imaged using an Inveon Multimodality PET/CT scanner (Siemens Medical Solution). For [^{18}F]FDG, a 10-minute static PET acquisition was performed 20 minutes post-injection. In the case of [^{18}F]AlF-NOTA-D10CM, a 60-minute dynamic PET acquisition was initiated at the time of injection and reconstructed into time frames of 30×3 s, 9×10 s, 4×30 s, 5×60 s, and 10×300 s. Image analysis was conducted using Carimas 2.10 software, where ROIs in main organs were defined using CT as an anatomical reference. ROIs of MI and remote area were delineated based on [^{18}F]FDG PET uptake where MI area were

determined by identifying regions with reduced [^{18}F]FDG uptake on short-axis images, while ROIs for the remote area were defined by selecting regions with high [^{18}F]FDG uptake in the septum. ROIs for the MI area were delineated in frames where [^{18}F]AlF-NOTA-D10CM uptake was visibly present and avoiding the apical region to prevent spill-over from the liver. H&E staining further confirmed the locations of both the MI and remote areas. Quantitative analysis included at least three consecutive planes evaluated at 50–60 minutes post-injection of [^{18}F]AlF-NOTA-D10CM. TACs were extracted from the dynamic PET data and presented as the mean SUV over time post-injection.

Sequential [^{18}F]FDG PET scans were further utilized to evaluate infarct size using Carimas 2.10's heart plugins. After segmentation of the loaded images, the LV contour was manually defined for short-axis, horizontal, and vertical long-axis views. These contours were automatically transformed into a 17-segment polar map. A threshold of 70% of the highest SUV value was applied to identify infarct regions, where areas with SUV below the threshold were marked as infarcted. The infarct size percentage was calculated by manually defining ROIs.

4.4 *Ex vivo* analysis

After the euthanasia, the organ of interest were dissected and measured for the accumulated radioactivity after [^{18}F]AlF-NOTA-D10CM injections. Animals were euthanized via cardiac puncture and cervical dislocation under isoflurane anaesthesia 60–70 minutes after the final intravenous injection of [^{18}F]AlF-NOTA-D10CM. Tissues of interest were excised, weighed, and analyzed for radioactivity using a gamma counter (Triathler 3″, Hidex, Turku, Finland). The measured radioactivity was decay-corrected to the time of injection, adjusted for residual activity in the cannula and tail, and expressed as %ID/g. Animals showing significant residual radioactivity at the tail were excluded from analysis, as this may indicate failed intravenous administration and could result in an unintended delivery route.

4.5 Autoradiography analysis

Main tissue of interests including inflamed foot pad skin and inflamed popliteal LN from CFA induced mice and LV samples from LAD ligated and sham operated rats were collected and prepared for autoradiography analysis.

The tissue samples of the LV of the heart were embedded and frozen in Tissue-Tek O.C.T. Compound (Sakura) and sectioned into serial 20 µm and 8 µm sections. The LV sections were made at approximately 1 mm intervals from the apex to the base and placed onto microscopic slides. The inflamed foot pad skin and inflamed popliteal LN were embedded in Tissue-Tek O.C.T. Compound (Sakura) and frozen,

then sectioned into three serial 20 µm slices and five 6 µm slices, which were mounted onto microscope slides. The slides were briefly air-dried and opposed to phosphor imaging plates (BAS-TR2025, Fuji), exposed overnight, and scanned using a Fuji Analyzer BAS-5000. Following autoradiography, frozen sections were stained with H&E for histological reference or stored in -70 degree freezer and used for CD206 immunohistochemical staining.

ROIs were analyzed on superimposed autoradiography and digitalized H&E images using the Carimas data processing tool. Results were expressed as photostimulated luminescence per square millimeter (PSL/mm²), decay-corrected for injection and autoradiography exposure times, and normalized to the injected radioactivity dose. For Study I, the target-to-background ratio (TBR) was calculated by comparing inflamed and non-inflamed regions identified through CD206 expression levels ($CD206_{high}$ area/$CD206_{low}$ area). These regions were classified based on histological analysis and immunohistochemical and immunofluorescence staining of sequential tissue sections. The region classification were completed automatically using a specific cut-off value in GIMP software.

4.6 Histological, immunohistochemical, and immunofluorescence staining

In Study II and III, histological staining were used as reference to point the inflamed area of foot pad skin, popliteal LN and LV. Histological staining were performed by H&E stains. Sections were fixed in 10% formalin, stained with hematoxylin (Fluka) and eosin (Reagena) using a Leica Autostainer, mounted with Pertex, and digitized using a Pannoramic P1000 slide scanner (3DHistech Ltd.). The H&E stained slides were used to make contour of inflamed foci that were superimposed to IHC stained slides.

CD206 immunohistochemistry staining were performed in Study I, II and III to depict the mannose receptor positive area on the tissue section. In Study I, sample of mannose receptor associated tissue including liver, spleen and bone marrow were CD206 stained to validate the high [^{18}F]AlF-NOTA-D10CM uptake on those tissues. In Study II and III, CD206 staining were performed in samples of inflamed foot pad skin and inflamed popliteal LN (6 µm) and LV (8 µm) from all animal groups. Anti-CD206 were used for immunohistochemical staining. First, the sections were fixed in 4% paraformaldehyde, followed by antigen retrieval, washing, and blocking of endogenous peroxidase activity. Next, the sections were incubated for 60 minutes at room temperature with a polyclonal rabbit anti-mannose receptor (CD206/MRC1) antibody (diluted 1:10,000; ab64693, Abcam), rinsed, and treated with a horseradish peroxidase-conjugated goat anti-mouse secondary antibody (BrightVision DPVR110HRP, WellMed) for 30 minutes at room temperature. The staining reaction

was developed using 3,3-diaminobenzidine (BrightDAB, BS04-110, WellMed), counterstained with Mayer's hematoxylin, mounted in Pertex, and left to dry overnight. The stained sections were scanned using a digital slide scanner (Pannoramic P1000 or Pannoramic 250 Flash, 3DHISTECH Ltd.) and analyzed with Pannoramic Viewer 1.15 software (3DHISTECH Ltd.).

Immunofluorescence staining were conducted in Study II for CD206, CD31 (for blood and lymphatic endothelial cells identification) and CD11b (for myeloid cells identification). In Study II, sample of healthy foot pad skin and popliteal LN and inflamed foot pad skin and inflamed popliteal LN were stained for both 5 Days and 14 Days after the CFA induction. Immunofluorescence staining were performed on sections that were fixed in ice-cold acetone for 3 minutes, followed by a 60-minute incubation in a humidified, light-protected chamber with Alexa Fluor® 488 monoclonal rat anti-mouse CD206 antibody (BioLegend® 14170, clone C068C2, 10 µg/mL), Alexa Fluor® 594 monoclonal rat anti-mouse CD31 antibody (BioLegend® 102520, clone MEC13.3, 10 µg/mL), and Alexa Fluor® 647 monoclonal rat anti-mouse CD11b antibody (BioLegend® 101220, clone M1/70, 10 µg/mL). The sections were then rinsed twice with PBS, counterstained with DAPI (Invitrogen D1306), and washed again with PBS. Finally, coverslips were mounted using ProLong Gold Antifade mounting medium (Invitrogen P36930). Tissue sections were scanned using a digital slide scanner (Pannoramic P1000 or Pannoramic 250 Flash, 3DHISTECH Ltd.) and analyzed with Pannoramic Viewer 1.15 software (3DHISTECH Ltd.).

Double immunofluorescence were performed in Study III for CD206 + CD68 (for macrophages identification) in LV sections. To do that, frozen LV sections were treated with pre-warmed citrate buffer (pH 6.0, BioSite), brought to a boil, and then cooled for 20 minutes. The sections were washed with PBS containing 0.05% Tween 20 (pH 7.4) and blocked with normal antibody diluent (BD09-125, WellMed). Next, the slides were incubated for 60 minutes at room temperature with primary antibodies: mouse anti-rat CD68 (1:1000, MCA341GA, Bio-Rad) and polyclonal rabbit MRC-1 (1:10000, ab64693, Abcam), prepared in normal antibody diluent. This was followed by sequential incubations with Alexa Fluor® 594-conjugated donkey anti-rabbit (A-21207, Invitrogen) and Alexa Fluor® 488-conjugated goat anti-mouse (A-11017, Invitrogen) secondary antibodies, each for 30 minutes at room temperature. The sections were mounted with Prolong Gold Antifade reagent containing DAPI (P36935, Invitrogen) and visualized using a Pannoramic Midi fluorescence slide scanner (3DHistech Ltd.). Images were analyzed with CaseViewer software (version 2.4, 3DHistech Ltd.).

4.7 Quantification of CD206 positive cells by immunohistochemical staining

CD206-positive area percentage (area-%) in inflamed foci were calculated from CD206 immunohistochemistry staining of the sections. At least 3 sections per slide were used for calculation. In Study II, CD206 area-% were calculated in foot pad skin inflammation area and inflamed popliteal LN both in Day 5 and Day 14 post CFA induction. Stained tissue sections were digitalized using a Pannoramic slide scanner (P1000 or 250 Flash, 3DHISTECH Ltd.) and analyzed with Pannoramic Viewer 1.15 software (3DHISTECH Ltd.). For quantifying the CD206 area-%, regions were categorized as $CD206_{high}$ or $CD206_{low}$ using fuzzy selection in GIMP (version 2.10.24) based on an RGB color threshold of 19, with H&E staining as a reference. The percentage of $CD206_{high}$ and $CD206_{low}$ areas was calculated through color deconvolution analysis of hematoxylin and 3,3′-Diaminobenzidine (DAB) stains using Fiji software (ImageJ 1.52n, Wayne Rasband, https://imagej.net/software/fiji/) (**Figure 16**).

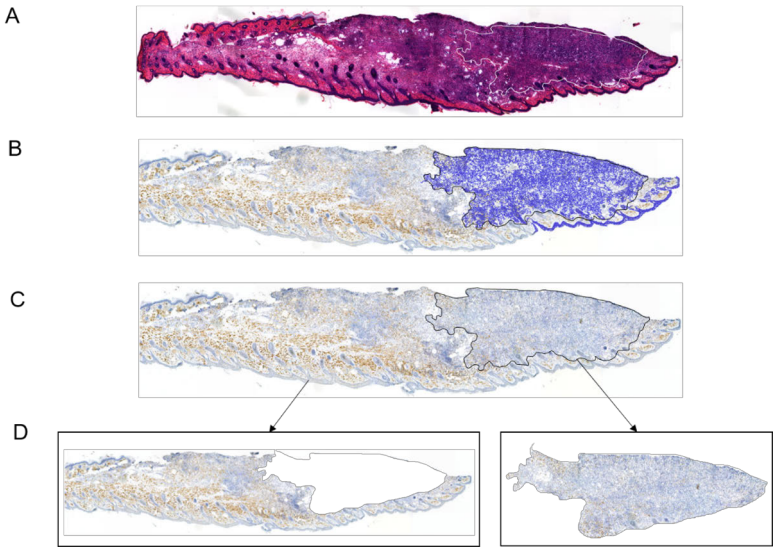

Figure 16. Histology and immunohistochemical analysis of footpad skin: (A) H&E staining shows inflammation in the skin caused by subcutaneous injection of complete Freund's adjuvant on the dorsal side of the left hind paw. (B) Less inflamed regions, identified as $CD206_{low}$ areas based on H&E staining, were visually distinguished and classified using fuzzy tools in GIMP. This classification employed an RGB color threshold of 19 and color inversion to define the CD206low area with a clear boundary. The outlined contours were transferred to the original CD206-stained section for accurate delineation. (C) The $CD206_{low}$ area (right panel) was separated from the $CD206_{high}$ area (left panel) along these contours, and DAB staining was subsequently analyzed for color deconvolution using the Fiji image processing software in ImageJ. (Adopted with permission from Andriana *et al*, 2023).

In Study III using experimental acute myocardial infarction model, H&E stained MI confirmed LV sections were used to calculate the CD206 area-%. LV sections were divided into MI and remote areas using the manual selection tool in GIMP (version 2.10.24), with clear boundaries defined based on H&E histological references. The CD206 area-% in both the MI and remote regions was quantified separately through color deconvolution analysis of hematoxylin and DAB staining using ImageJ 1.52n software (Wayne Rasband) (**Figure 17**).

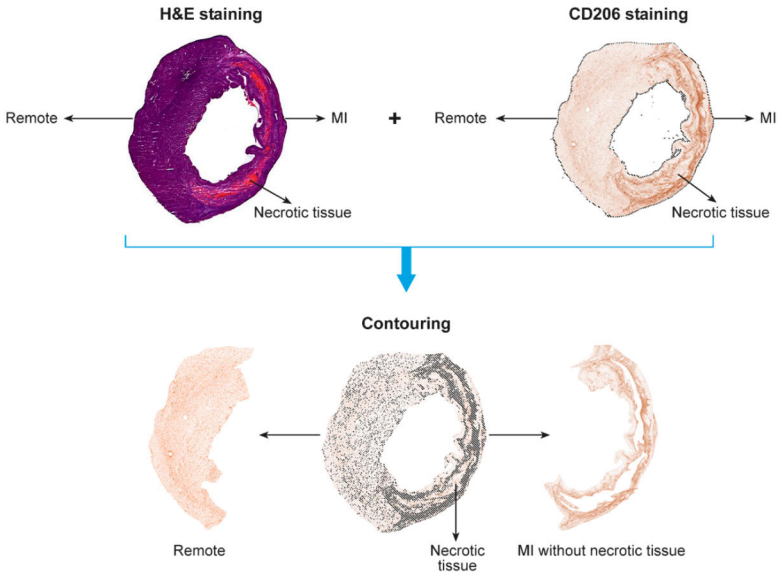

Figure 17. H&E staining served as an anatomical reference to identify infarcted and necrotic tissue. Adjacent LV sections stained for CD206 were contoured to distinguish the remote area, MI area, and necrotic tissue within. Contouring was performed using the automatic fuzzy selection tool in GIMP (version 2.10.24), with CD206-positive staining (dark brown) in the MI area as the basis for area selection. Threshold adjustments were made to ensure clear boundaries between the MI area, remote area, and necrotic tissue, as shown in the contoured section above. The remote and MI areas, excluding necrotic tissue, were then analyzed using ImageJ 1.52n (Wayne Rasband) (from Original submitted manuscript III).

4.8 *In vivo* blocking study and *in vitro* competitive binding study

In vivo blocking study were performed in initial PET study in healthy rats for studying [^{18}F]AlF-NOTA-D10CM *in vivo* specificity uptake by associated mannose receptor tissues. The blocking experiment were performed with a 100-fold molar excess of mannan from Saccharomyces cerevisiae (Sigma-Aldrich M7504) in 400 µL saline intravenous administration 15 minutes before the [^{18}F]AlF-NOTA-D10CM injection. After [^{18}F]AlF-NOTA-D10CM administration, rats were

undergone the PET/CT scan with the same protocol as previously described for Study I.

In vitro competitive displacement study were added in Study II and Study III in cryosections of inflamed popliteal lymph nodes and footpad skin (6 µm) from mice with CFA-induced inflammation in study (Study II), as well as cryosections of the LV (20 µm) from rats on MI Day 7 (Study III). First, frozen sections were defrosted at 4 °C for 40 minutes and pre-incubated at room temperature for 15 minutes in *N*-(2-hydroxyethyl)piperazine-*N'*-(2-ethanesulfonic acid (HEPES, Sigma-Aldrich) buffer (pH 7.4) containing 10 mM Ca^{2+}. For total binding assays, sections were incubated with [^{18}F]AlF-NOTA-D10CM at concentrations of 23 kBq/mL (2.3 nM) for mice tissue or 35 kBq/mL (3.5 nM) for rat tissue. For competitive binding assays, adjacent sections were co-incubated with [^{18}F]AlF-NOTA-D10CM and a molar excess of unlabeled NOTA-D10CM for 70 minutes (400-fold for mice sample and 200-fold for rat sample). After incubation, all slides were rinsed twice with cold buffer, dipped in cold water, air-dried, and exposed overnight to phosphor imaging plates for scanning and analysis. All experiments were performed in triplicate using tissue samples from three animals (n = 3) per group.

4.9 Binding specificity of NOTA-D10CM and [^{18}F]AlF-NOTA-D10CM to M1/M2-polarized human macrophages and CHO cells

4.9.1 Alexa-488-NOTA-D10CM preparation

Binding specificity of NOTA-D10CM to M1/M2 polarized macrophages was determined using flow cytometry (Fortessa, BD Biosciences) in Study III. First, NOTA-D10CM was labeled with the near-infrared dye AlexaFluor-488 tetrafluorophenyl ester using the AlexaFluor-488 Microscale Protein Labeling Kit (A3006; Invitrogen), following the protocol from the manufacturer. Solution stock of Alexa-488-NOTA-D10CM (1 mg/mL) was prepared by 100 µL of 1 mM NOTA-D10CM stock solution mixing with 10 µL of 1 M sodium bicarbonate in a reaction tube and homogenized manually with a micropipette. A stock solution of reactive dye was prepared by adding 10 µL of deionized water to the AlexaFluor-488 tetrafluorophenyl ester vial, yielding a concentration of 11.3 nmol/µL. Next, 8 µL of the reactive dye solution was added to the NOTA-D10CM mixture, and the reaction was incubated for 15 minutes at room temperature. Excess unreacted dye was removed using the purification resin and spin filters included in the labeling kit (**Appendix 3**). The degree of labeling (DOI) of AlexaFluor-488-labeled NOTA-D10CM was determined by measurement of absorbance at 280 nm and at 494 nm

using NanoDrop ND-1000 spectrophotometer and showed the DOI of 2 molecule of fluorophores per one molecule of NOTA-D10CM.

4.9.2 Peripheral blood mononuclear cells preparation

Peripheral blood mononuclear cells (PBMCs) were isolated from human buffy coats using Ficoll centrifugation. Monocytes were then enriched from PBMCs through positive selection with a magnetic-activated cell sorting kit (Monocyte Isolation Kit with CD14 MicroBeads; Miltenyi Biotec). These monocytes were cultured and polarized into M1 or M2 macrophages as described previously (Silvola *et al*., 2018). To evaluate CD206 expression, cells were first pre-blocked with human immunoglobulin (Ig 100 µg/mL; KIOVIG, Baxter) and subsequently incubated with an AlexaFluor-647-conjugated anti-human CD206 antibody (mouse IgG1; BioLegend) or an isotype control (mouse IgG1; BD Biosciences). After incubation, cells were fixed with paraformaldehyde and analyzed using flow cytometry (Fortessa, BD Biosciences) and Flowing software (Turku Center of Biotechnology).

4.9.3 Binding of Alexa-488-NOTA-D10CM to M1/M2 macrophages

To assess the binding of Alexa-488-NOTA-D10CM, macrophages were collected and incubated for 30 minutes or 4 hours at 37°C in a CO_2 incubator with fresh medium (Iscove's Modified Dulbecco's Medium containing 2% AB serum and 2 mmol L-glutamine; Gibco, Thermo Fisher Scientific) supplemented with Alexa-488-NOTA-D10CM (10 µg/mL). After incubation, the cells were washed twice with 1 mL of PBS to remove any unbound Alexa-488-NOTA-D10CM. The cells were then fixed with paraformaldehyde and analyzed using flow cytometry and Flowing software.

4.9.4 CHO cell culture

CHO cells stably expressing mouse CD206 (CHO-CD206$^+$) and CD206-negative CHO cells (CHO-CD206$^-$) were generously provided by Prof. Luisa Martinez-Pomares (University of Nottingham, United Kingdom). The cells were cultured at 37°C in a CO_2 incubator in RPMI 1640 medium (Gibco/Thermo Fisher Scientific) supplemented with 10% fetal bovine serum (Biowest), 2 mmol L-glutamine (Gibco/Thermo Fisher Scientific), 100 U/mL penicillin, and 100 µg/mL streptomycin (Sigma-Aldrich/Merck). CD206 expression were confirmed by flow cytometry. First, the cells were harvested and incubated with an AlexaFluor-488-conjugated anti-mouse CD206 antibody (rat IgG2; Bio-Rad) or an isotype control

(rat IgG2; BD Biosciences). Afterward, the cells were fixed with paraformaldehyde and analyzed by flow cytometry using Flowing software.

4.9.5 Binding of [^{18}F]AlF-NOTA-D10CM to CHO cells

Binding affinity of [^{18}F]AlF-NOTA-D10CM to CHO-CD206^{+} and CHO-CD206^{-} were investigated by the following protocol. Cells were cultured and allowed to adhere to opposite sides of a 92 mm Petri dish, following the LigandTracer (Ridgeview Instruments AB) guidelines. A region of the Petri dish without attached cells served as a background control to account for non-specific binding of [^{18}F]AlF-NOTA-D10CM. The dissociation constant (K_D) of [^{18}F]AlF-NOTA-D10CM was determined using a LigandTracer Yellow instrument. The assay involved sequentially measuring radioactivity in the target cells (CHO-CD206^{+}), the negative control cells (CHO-CD206^{-}), and the cell-free background areas of the dish.

4.10 Statistical analysis

All statistical analysis were conducted using GraphPad Prism (version 10.1.2 (324), 2023). Results are presented as mean ± standard deviation (SD). Normality of the data was assessed using the D'Agostino-Pearson or Shapiro-Wilk test. Group differences were analyzed using unpaired Student's t-tests, one-way ANOVA, or the Wilcoxon test for non-normally distributed data. P-values < 0.05 were considered statistically significant and are denoted as $*P < 0.05$, $**P < 0.01$, and $***P < 0.001$. Associations between variables were examined using Pearson's correlation coefficient.

5 Results

5.1 Radiosynthesis of [^{18}F]AlF-NOTA-D10CM and initial PET imaging of healthy rats

This Study I aimed to establish a radiolabeling method for NOTA-D10CM with [^{18}F]F$^-$ to produce [^{18}F]AlF-NOTA-D10CM and conduct an initial PET imaging in healthy rats using [^{18}F]AlF-NOTA-D10CM. The study revealed the favorable characteristic of a PET tracer with a straightforward and reproducible radiolabeling protocol.

5.1.1 Radiosynthesis of [^{18}F]AlF-NOTA-D10CM

First, NOTA-D10CM were synthesized as 21.3 kDa size of molecule with 17 mannosylated S-derivatized cysteine and 7 free cysteine content in each molecule of D10CM and at least there were one NOTA chelator per one D10CM molecule (**Figure 18)**.

The radiolabeling last for 91.8 ± 15.7 minutes (n = 10) from the end of bombardment with initial 6.1 ± 0.6 GBq [^{18}F]F$^-$. The average decay corrected radiochemical yield of was 24.8 % ± 13.1. [^{18}F]AlF-NOTA-D10CM was finally eluted to product vial containing PBS with ascorbic acid and <10% ethanol content with final average radioactivity concentration of 312.2 ± 140.7 MBq/mL at EOS.

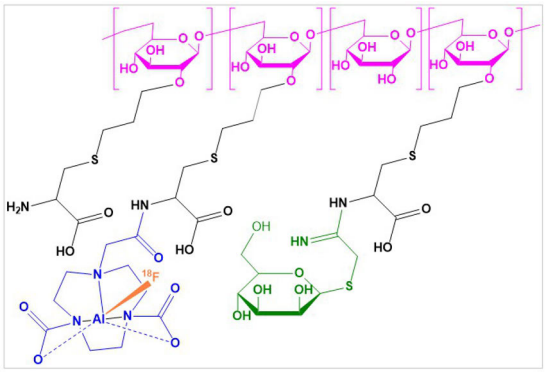

Figure 18. Chemical structure of [^{18}F]AlF-NOTA-D10CM. The structure contains D10CM (dextran10 in pink, cysteine in black and mannose moiety in green colored structure). After radiolabeling, NOTA chelator bind to [^{18}F]AlF-complex via aluminum (blue block) attached to cysteine.

[^{18}F]AlF-NOTA-D10CM underwent quality control by HPLC as previously describe and showed consistent radiochemical purity of >99% at EOS and over 4 hours at room temperature. In addition to excellent shelf-life, [^{18}F]AlF-NOTA-D10CM showed a favorable hydrophilicity with LogD of -3.10 and molar activity of 9.9 GBq/μmol.

5.1.2 *In vivo* PET imaging

The PET/CT imaging results revealed that the highest uptake of [^{18}F]AlF-NOTA-D10CM were found in mannose receptor associated tissues including liver, spleen and bone marrow with SUV of 10.38 ± 0.13, 3.71 ± 0.04 and 2.95 ± 0.02), respectively. These high SUVs due to abundance of CD206-positive cells were confirmed by colocalisation of CD206 positive immunohistochemical staining. The lower uptake were detected in other organs which also known to have some CD206 expression including salivary glands (1.40 ± 0.02), kidneys (1.37 ± 0.03), and pancreas (1.32 ± 0.05). Within 20 minutes after injection, tracer were cleared from blood circulation and the rest were accumulated in the liver, spleen, bone marrow (**Figure 19a, b**) and other tissues with CD206 expression.

In vivo blocking study with 100-fold of mannan injection 15 minutes prior to [^{18}F]AlF-NOTA-D10CM injection demonstrate the specific uptake of the tracer in mannose receptor associated tissues with a reduced uptake by 88.6% in liver, 35.1% in spleen and 59.9% in bone marrow (**Figure 19a–c**) . These results were supported by the *ex vivo* gamma counting of the correspondent tissues (**Figure 19c, d**).

5.1.3 *In vivo* stability

In vivo stability study revealed an excellent [^{18}F]AlF-NOTA-D10CM stability with intact tracer of 100% ± 0, 96.2% ± 1.8, 91.6% ± 3.0, 90.1% ± 5.3 and 84.1% ± 3.7 of total plasma radioactivity at 5, 15, 30, 45 and 60 minutes post-injection, respectively.

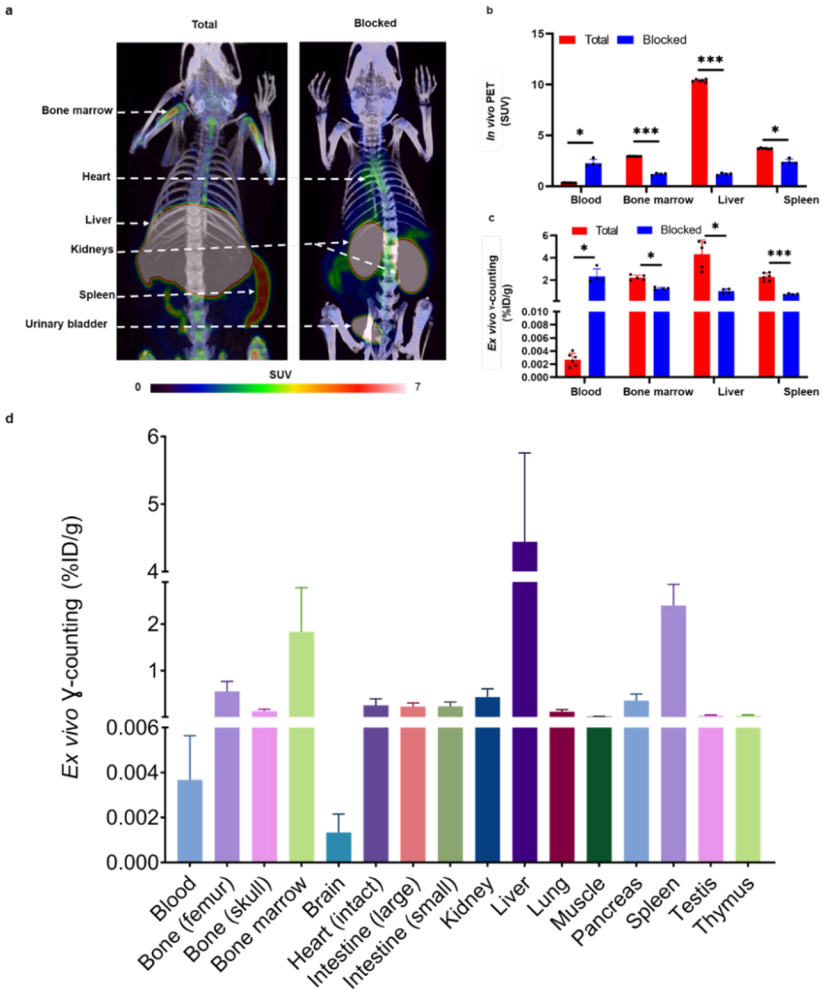

Figure 19. Representative coronal maximum intensity projection of [^{18}F]AlF-NOTA-D10CM PET/CT images in healthy rats between total binding and blocked binding by mannan at 60 minutes after injection (**a**). Quantification of the [^{18}F]AlF-NOTA-D10CM uptake in blood, bone marrow, liver and spleen at 35-60 minutes post injection in total versus block binding (**b**), as confirmed by *ex vivo* gamma counting measured at 60 minutes post-injection (**c**), and *ex vivo* gamma counting of the whole tissue of interest from total binding rats (**d**). *P < 0.05, **P < 0.001, ***P < 0.0001. (Modified from Original publication I)

5.2 Validation study in mice

In Study II, we aimed to investigate the [^{18}F]AlF-NOTA-D10CM ability to target macrophage mannose receptor CD206 in inflammation. We first evaluated the tracer's specificity in CD206$^{-/-}$ KO mice compared to WT mice. Then, we studied the [^{18}F]AlF-NOTA-D10CM uptake in mice with foot pad skin inflammation. The mice that underwent PET/CT were screened based on the clear visual of swollen foot

compared to the contralateral foot and the [^{18}F]FDG PET imaging 1 the day prior to PET imaging with [^{18}F]AlF-NOTA-D10CM. The foot size were also monitored since day 1 after CFA induction.

5.2.1 PET/CT study in CD206 deficient versus wild-type mice

PET/CT imaging results of [^{18}F]AlF-NOTA-D10CM indicated that WT mice showed highest SUV in mannose receptor associated tissues compared to CD206$^{-/-}$ KO mice including liver (8.21 ± 2.51 vs. 1.06 ± 0.16, $P < 0.001$), salivary glands (1.86 ± 0.34 vs. 0.61 ± 0.14, $P < 0.05$) and bone marrow (1.63 ± 0.37 vs. 0.22 ± 0.05, $P < 0.0001$). These results were in line with the results of Study I in healthy rats. Conversely, the SUV in CD206$^{-/-}$ KO mice were higher than WT mice in spleen (3.56 ± 0.85 vs. 4.92 ± 0.81, $P < 0.05$) and kidney (1.94 ± 0.93 vs. 6.03 ± 1.79, $P < 0.001$).

Table 6. *In vivo* distribution of [^{18}F]AlF-NOTA-D10CM at 50–60 minutes post-Injection in CD206$^{-/-}$ KO and WT mice. *P* value is from Student's t test.

Tissue	WT (*n* = 7) SUV mean ± SD	KO (*n* = 8) SUV mean ± SD	*P* value
Brown adipose tissue	0.11 ± 0.04	0.15 ± 0.05	0.09
Blood	0.56 ± 0.22**	1.22 ± 0.29	< 0.001
Bone marrow	1.63 ± 0.37***	0.22 ± 0.05	< 0.0001
Brain	0.22 ± 0.20	0.08 ± 0.03	0.12
Heart	0.50 ± 0.09*	0.76 ± 0.16	< 0.05
Intestine (small)	0.65 ± 0.30*	0.33 ± 0.07	0.03
Kidneys	1.94 ± 0.93**	6.03 ± 1.79	< 0.001
Liver	8.21 ± 2.51**	1.06 ± 0.16	< 0.001
LN (axillary, left)	0.14 ± 0.05*	0.40 ± 0.19	< 0.05
LN (inguinal, left)	0.18 ± 0.08*	0.37 ± 0.20	< 0.05
LN (mesenteric, left)	0.27 ± 0.13*	0.43 ± 0.15	0.05
LN (popliteal, left)	0.12 ± 0.05*	0.38 ± 0.21	< 0.05
Lungs	0.36 ± 0.10	0.46 ± 0.12	0.08
Muscle	0.10 ± 0.04	0.12 ± 0.04	0.46
Ovaries	0.38 ± 0.11	0.32 ± 0.20	0.58
Pancreas	0.96 ± 0.14**	0.40 ± 0.07	< 0.001
Salivary glands	1.86 ± 0.34	0.61 ± 0.14	0.02
Skin (foot pad, left)	0.21 ± 0.08	0.27 ± 0.15	0.38
Skull	0.21 ± 0.12*	0.08 ± 0.03	< 0.05
Spleen	3.56 ± 0.85	4.92 ± 0.81	0.02
Stomach	0.46 ± 0.23	0.28 ± 0.09	0.09

*$P < 0.05$, **$P < 0.001$, ***$P < 0.0001$.

5.2.2 PET/CT study in C57BL/6N mice with foot pad skin inflammation

[^{18}F]AlF-NOTA-D10CM PET imaging in CFA induced mice were conducted in two types of administration: intravenous and intradermal routes.

Using intravenous injection, significantly higher SUVs were observed in the left inflamed foot pad skin (0.41 ± 0.10 vs. 0.04 ± 0.01, $P < 0.0001$) high up to the left ankle joint (0.48 ± 0.13 vs. 0.18 ± 0.05, $P < 0.0001$), popliteal (0.24 ± 0.05 vs. 0.14 ± 0.06, $P < 0.0001$) and inguinal LN (0.37 ± 0.15 vs. 0.10 ± 0.04, $P < 0.05$) of CFA induced mice both in CFA Day 5 and CFA Day 14 group, compared to the healthy control, with no significant difference between CFA Day 5 and CFA Day 14 group (**Figure 20**).

The *in vivo* PET imaging results were supported by *ex vivo* gamma counting at 60 minutes after [^{18}F]AlF-NOTA-D10CM intravenous injection. Healthy mice showed a significantly lower uptake in foot pad skin compared to the both group of CFA induced mice (0.74 ± 0.21 vs. 1.44 ± 0.44, $P < 0.05$). The difference in popliteal LN were not determined due to insufficient size of the popliteal LN in healthy mice. However, the gamma counts of popliteal LN from CFA induced mice can be 4–7 times higher than healthy one and reliable enough for gamma counting measurement (1.34 ± 0.76). The size difference as well as autoradiography uptake of healhy LN and CFA induced LN is portrayed in **Figure 21.**

In addition, autoradiography confirmed the significantly higher accumulation of the [^{18}F]AlF-NOTA-D10CM in inflamed area of foot pad skin and popliteal LN, or in this study we refer to $CD206_{high}$ area and the control tissue background as $CD206_{low}$ area. The determination of $CD206_{high}$ area/ $CD206_{low}$ area were defined based on the histological contour derived from H&E staining of its adjacent section. Autoradiography revealed that [^{18}F]AlF-NOTA-D10CM uptake ratio of $CD206_{high}$ area (in inflamed foci of foot pad skin and popliteal LN) and $CD206_{low}$ area (in healthy tissue background) in CFA Day 5 group were 10.24 ± 0.79 (skin) and 32.32 ± 20.68 (LN) and in CFA Day 14 group were 10.36 ± 4.66 (skin) and 22.29 ± 6.27 (LN).

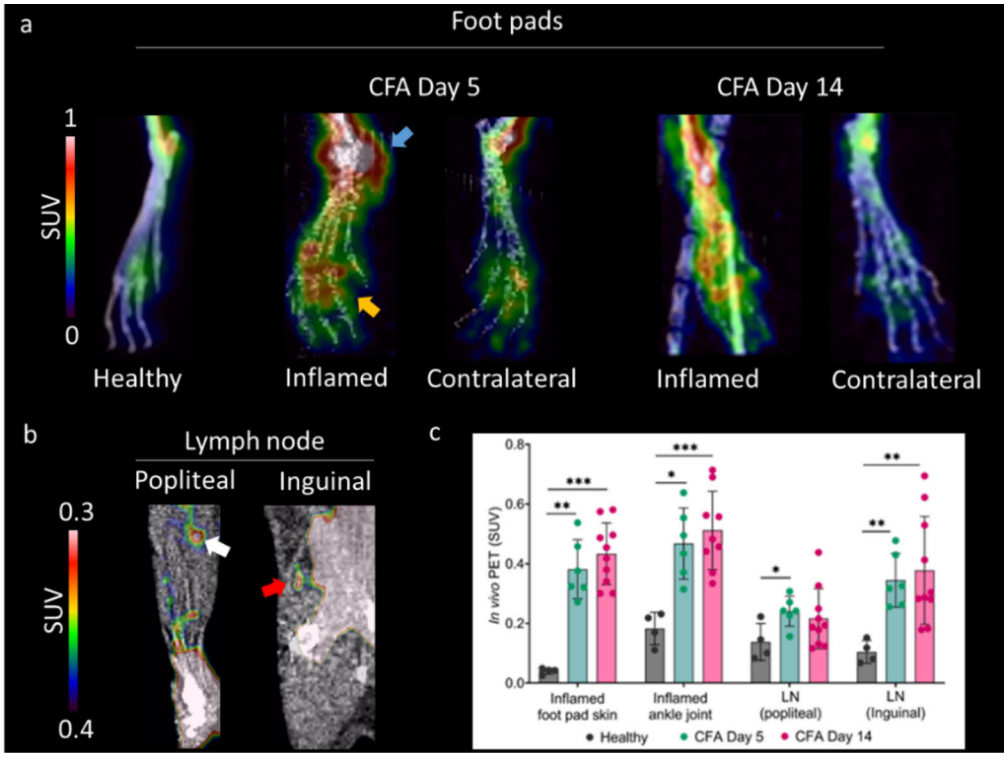

Figure 20. (**a**) Representative maximum intensity projection PET/CT images of intravenously (i.v) administered [^{18}F]AlF-NOTA-D10CM of the foot pad of healthy mouse and CFA induced mice on day 5 and 14, and (**b**) the inflamed popliteal LN (white arrow) and inguinal LN (red arrow) in mice, 5 days after CFA induction. (**c**) SUV quantification of PET imaging 50-90 minutes after i.v. injection. Bars represent mean and error bars are standard deviation. **P*<0.05, ***P*<0.01, ****P*<0.001. (Modified from Original publication II)

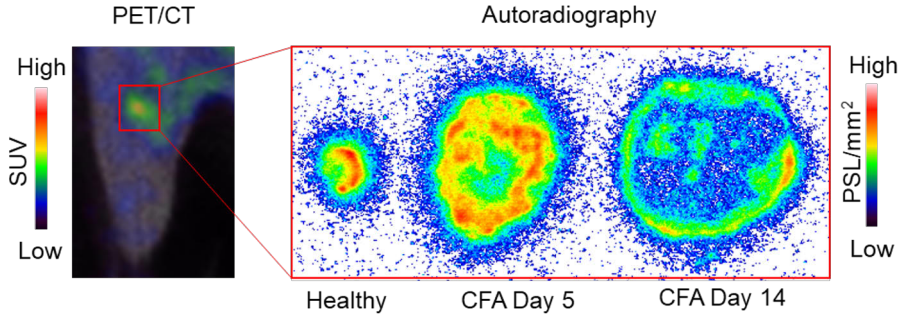

Figure 21. Autoradiography of popliteal LN from healthy, CFA Day 5 and CFA Day 14 illustrate the significantly bigger size of the LN in inflamed condition.

Intradermal injection of [^{18}F]AlF-NOTA-D10CM demonstrated the shift in lymphatic drainage during the inflammation development from healthy to inflammation stage (day 5 and day 14 after CFA induction) as shown in **Figure 22 and 23.**

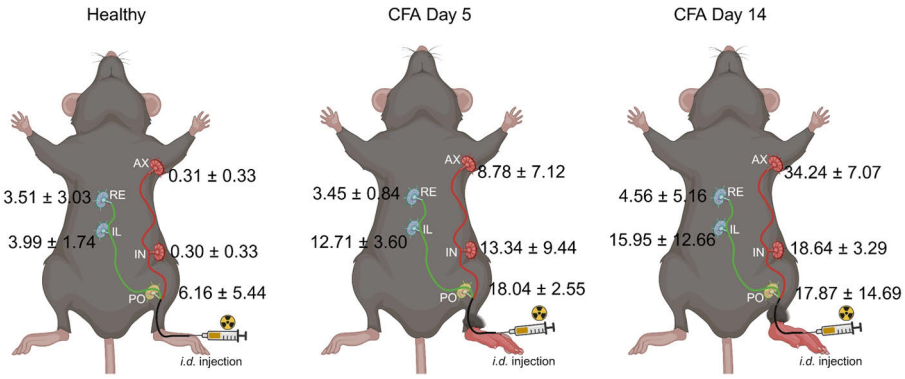

AX: axillary; IL: iliac; IN: inguinal; PO: popliteal; RE: renal.

Figure 22. Intradermal injection of [^{18}F]AlF-NOTA-D10CM illustration reveal the lymphatic drainage route from site of injection in healthy mouse compared to CFA Day 5 and CFA Day 14 groups. The figures demonstrate the activation of alternative drainage (red dotted line) in inflamed mice and significant increased of SUV in popliteal (PO), inguinal (IN) to axillary (AX) LN from healthy condition (blue dotted line), to day 5 and to the highest SUV in day 14 after CFA induction. The values are expressed as SUV mean ± SD. IL: Iliac LN; RE: renal LN.

Lymph nodes (SUV)	Study group		
	Healthy	CFA Day 5	CFA Day 14
Popliteal	6.16 ± 5.44	18.04 ± 2.55	17.87 ± 14.69
Iliac	3.99 ± 1.74	12.71 ± 3.60	15.95 ± 12.66
Renal	3.51 ± 3.03	3.45 ± 0.84	4.56 ± 5.16
Inguinal	0.30 ± 0.33	13.34 ± 9.44	18.64 ± 3.29
Axillary	0.31 ± 0.33	8.78 ± 7.12	34.24 ± 7.07

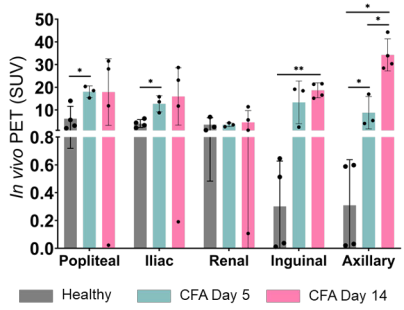

Figure 23. Quantification of Al[^{18}F]F-NOTA-D10CM uptake at 2 hours post intradermal injection. Results in the table are presented as mean ± SD and bars represent SUV mean with error bar as standard deviation. *P < 0.05, **P < 0.01 (Modified from Original publication II)

5.2.3 Histology

H&E staining defined the histological feature of inflamed area ($CD206_{high}$ area) and healthy area ($CD206_{low}$ area). Quantification of CD206 using CD206 immunohistochemical staining verify the significantly higher CD206 area-% in inflamed area of foot pad skin and lymph node compared to the healthy tissue and colocalized with focal autoradiography uptake of [^{18}F]AlF-NOTA-D10CM in the adjacent sections (**Figure 24**). The correlation matrix also found that the [^{18}F]AlF-NOTA-D10CM autoradiography uptake were positively correlated with CD206 area-% both in foot pad skin and popliteal samples from CFA Day 5 and CFA Day 14 groups (r = 0.80, P < 0.001).

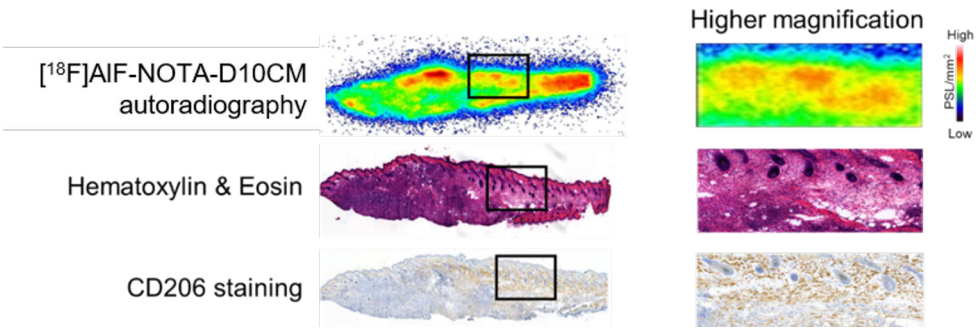

Figure 24. Representative autoradiography of [^{18}F]AlF-NOTA-D10CM, H&E histological staining and CD206 immunostaining of the foot pad skin 14 days after CFA induction. Visible hotspot on autoradiography co-localized with the inflamed area denoted by H&E staining and mannose receptor CD206 overexpression showed by CD206 IHC staining (positive stained seen as brown color).

5.3 PET imaging in experimental acute myocardial infarction

This study aimed to assess the feasibility of using [^{18}F]AlF-NOTA-D10CM to detect acute MI in experimental rat model, where MI was induced by permanent coronary artery ligation. Additionally, a sham control group was developed using the same surgical procedure, but without coronary artery ligation. Prior to this, we evaluated the Alexa-488-NOTA-D10CM specific uptake by M2 macrophages using human blood monocytes that were *in vitro* polarized into M1 and M2 macrophages. We also conducted another binding assay using LigandTracer to examine the tracer's binding affinity in CHO cells transfected with CD206. These two binding assays confirmed that Alexa-488-NOTA-D10CM bound to M2 macrophages more than to M1 macrophages (2914.76 ± 503.10 *vs.* 168.36 ± 137.30, respectively; $P = 0.001$) and that [^{18}F]AlF-NOTA-D10CM binding affinity to CHO-CD206^{+} cells was 1.83 ± 0.68 nM. In addition, *in vitro* competition study were performed to evaluate the [^{18}F]AlF-NOTA-D10CM specific uptake in MI area confirmed that the addition of excess unlabeled NOTA-D10COM reduced the tracer uptake in MI area by approximately 85%.

5.3.1 PET study

The rats that had been through LAD ligation surgery were divided into MI Day 3 and MI Day 7 group. In this study, the survival rate from LAD surgery were 45 % for MI Day 3 group and 73 % for MI Day 7 group. The rats were then imaged with [^{18}F]AlF-NOTA-D10CM based on their group time point.

[^{18}F]FDG were used to visualize the myocardial infarction. The average MI size were found to be 31.87% ± 18.20 of the LV for both MI Day 3 and MI Day 7 group. Only rats with a confirmed MI were used in data analysis.

In vivo PET imaging of [^{18}F]AlF-NOTA-D10CM is represented in **Figure 25** and demonstrated a significantly higher SUV in MI area compared to remote area (SUV 0.64 ± 0.19 vs. 0.40 ± 0.11; $P = 0.018$) and myocardium of the sham operated rats (SUV 0.43 ± 0.07; P = 0.002) in MI Day 3 group, and so did the MI Day 7 group with higher SUV in MI area compared to the remote area (SUV 0.61 ± 0.16 vs. 0.45 ± 0.12; $P = 0.047$) and sham operated rat's myocardium (SUV 0.42 ± 0.06; P = 0.017). There were no observed significant difference on [18F]AlF-NOTA-D10CM uptake in MI area of MI Day 3 and MI Day 7 group.

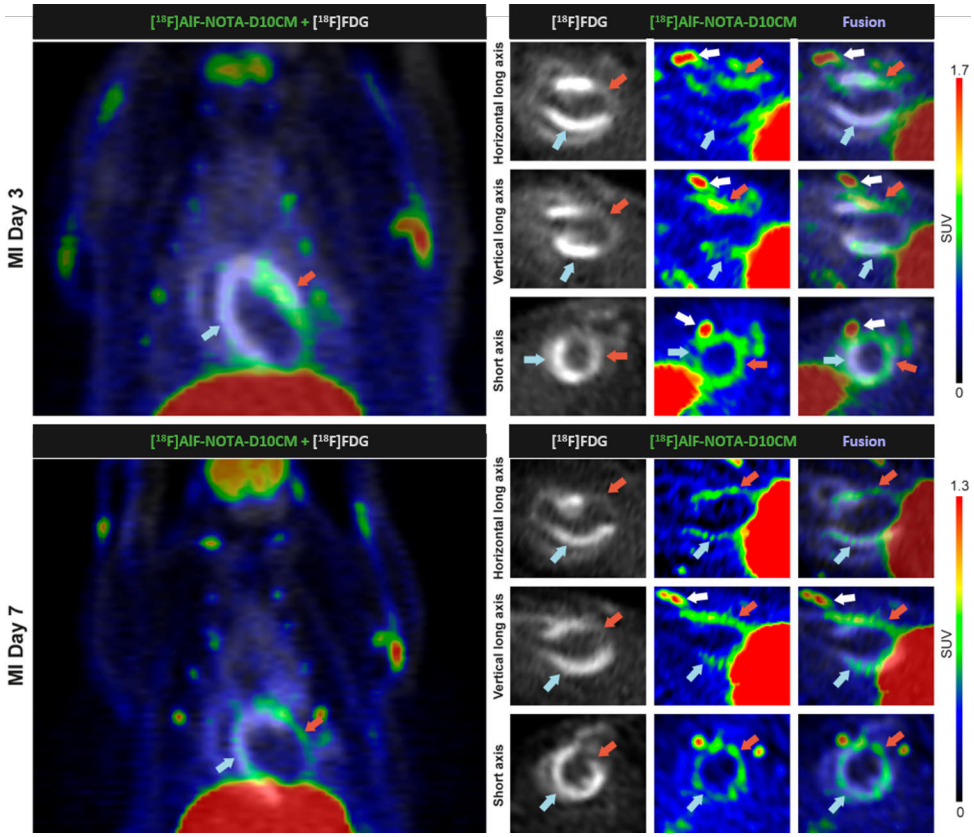

Figure 25. Representative PET images of rats on Day 3 (upper panel) and Day 7 (lower panel) post-myocardial infarction, using [^{18}F]AlF-NOTA-D10CM. [^{18}F]FDG PET imaging were performed the day before to highlights viable myocardium (indicated by blue arrows), while [^{18}F]AlF-NOTA-D10CM shows uptake in the infarcted and border zone regions (marked by red arrows). The white arrows point to tracer uptake in the healing surgical scar. (Adopted from Original submitted manuscript III).

5.3.2 *Ex vivo* gamma counting and autoradiography

The whole heart was excised and measured with gamma counter. The measurement of the whole heart is not representative to confirm the *in vivo* SUV uptake, which were measured exclusively on LV chamber for at least 3 planes of segmented PET image. Hence, there were no significant difference of [^{18}F]AlF-NOTA-D10CM accumulation detected in heart of the MI group and Sham group either on Day 3 and Day 7. However, the gamma counting confirmed that the high [^{18}F]AlF-NOTA-D10CM accumulation were in line with our previous study in healthy rats (I) and mice (II) which were highest in mannose receptor associated tissues including liver, spleen and bone marrow.

Autoradiography for the LV sections supported the *in vivo* PET imaging results. Significantly higher uptake of [^{18}F]AlF-NOTA-D10CM were found to be in MI area compared to remote area (PSL/mm^2 100.04 ± 34.81 *vs.* 45.83 ± 18.79; $P = 0.005$) and myocardium of Sham operated rats (65.56 ± 11.03, $P = 0.043$) at day 3 time point. Similarly at day 7 time point, [^{18}F]AlF-NOTA-D10CM uptake were significantly higher in MI area compared to remote area (PSL/mm^2 139.07 ± 64.46 *vs.* 70.021 ± 29.70; $P = 0.021$) and myocardium of Sham operated rats (71.90 ± 14.16, $P = 0.022$).

5.3.3 Histology and immunohistochemical staining

All the rats that were screened by [^{18}F]FDG were indeed showing histological sign of MI. The H&E staining of the LV showed that the MI area were co-localized with the [^{18}F]AlF-NOTA-D10CM autoradiography hotspot and CD206 overexpression. On the other hand, there were no indication of infarction in LV section of Sham operated rats based on the histological staining. Thus, as expected, no visible uptake of [^{18}F]AlF-NOTA-D10CM found in LV of Sham operated rats as supported by autoradiography and confirmed by CD206 staining. These findings are shown in **Figure 26**.

Quantification of CD206 from CD206 immunohistochemical staining supported the PET study and autoradiography results. The highest CD206 area-% were found in MI area compared to remote area and myocardium of sham-operated rats at 3 days time point (31.14 ± 7.08 *vs*. 4.02 ± 0.38 *vs.* 2.37 ± 0.29, respectively; $P < 0.001$) and at 7 days time point (24.07 ± 5.29 *vs.* 10.77 ± 9.90, $P = 0.007$, *vs.* 1.80 ± 0.31, respectively; $P < 0.001$).

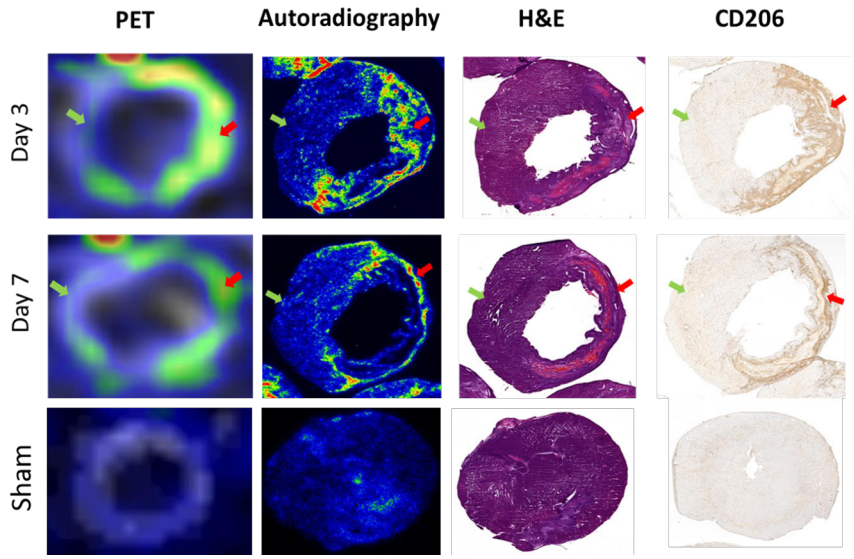

Figure 26. Representative axial plane, autoradiography of [^{18}F]AlF-NOTA-D10CM, H&E staining and CD206 immunostaining of LV at 3 days and 7 days post LAD ligation surgery, and sham control. Hotspot were visible on axial slice of LV in LAD ligated rats, but not in Sham control. The hotspot were co-localized with the focal [^{18}F]AlF-NOTA-D10CM autoradiography uptake. The hotspot were confirmed to be in MI area according to H&E staining and co-localized with CD206 overexpression (positive stained seen as brown color). Red arrow: infarct area, green arrow: remote area. (Modified from Andriana *et al*., 2022)

In addition, we found that PET uptake were positively correlated to CD206 positive area-% (r = 0.451, P = 0.006) and to autoradiography uptake (r = 0.290, P = 0.039) in MI region both on day 3 and day 7 time point. CD206 positive area-% were also found to be positively correlated with autoradiography uptake in infarcted area of MI Day 3 (r = 0.655, P = 0.028) but not in MI Day 7 group (r = 0.440, P = 0.073).

We complemented this study with double immunofluorescence staining of CD206 to mark mannose receptor CD206 and CD68 to mark macrophages. The results showed that mannose receptor expressed on MI area were indeed expressed by macrophages instead of any other type of CD206 expressing leukocytes.

6 Discussion

The studies in this thesis aimed to develop a new PET tracer targeting the mannose receptor CD206 and assess its ability to detect inflammation. Study I focused on establishing a radiolabeling method for the tracer. We successfully radiolabeled the D10CM precursor with fluorine-18 to produce the mannose receptor-targeting PET tracer, [^{18}F]AlF-NOTA-D10CM. This tracer demonstrated the ability to specifically target mannose receptor-rich tissues, such as the liver, spleen, and bone marrow, using PET imaging, making it a promising candidate for further animal model studies (Andriana *et al*. 2023).

In Study II, we evaluated the ability of [^{18}F]AlF-NOTA-D10CM to detect inflammation. [^{18}F]AlF-NOTA-D10CM showed significantly higher uptake in the inflamed areas of the foot pad skin and popliteal lymph nodes of mice with CFA-induced inflammation, both in the acute and chronic phases. In addition, an in vivo comparison study of CD206$^{-/-}$ KO versus WT mice revealed that the tracer's uptake was significantly reduced in mannose receptor-associated tissues in CD206$^{-/-}$ KO mice, but not in WT mice, indicating the specific uptake of [^{18}F]AlF-NOTA-D10CM by the mannose receptor CD206. These findings support further evaluation in animal models of inflammatory-related diseases (Andriana *et al*. 2024).

Building on these results, we studied a rat model of acute myocardial infarction, in which inflammation has been studied extensively (Frangogianis, 2015; Frangogiannis *et al*., 2002). Our study showed that [^{18}F]AlF-NOTA-D10CM had significantly higher uptake in the MI area compared to remote areas and the myocardium of sham-operated rats. Notably, the tracer was able to detect inflammation in the MI area as early as three days after LAD surgery, suggesting its potential as a tool for studying the early inflammatory response after MI (submitted manuscript). All of these constructed studies highlight the promising role of CD206-targeted PET imaging in inflammation detection.

6.1 Production and characterization of [^{18}F]AlF-NOTA-D10CM (Study I)

In Study I, we aimed to develop a new PET tracer targeting the macrophage mannose receptor CD206, [^{18}F]AlF-NOTA-D10CM, an ^{18}F-labeled mannosylated dextran

derivative, for initial PET studies in healthy rats. Study I demonstrated that [^{18}F]AlF-NOTA-D10CM is a suitable tracer for PET imaging and is able to specifically target CD206-associated tissues.

The macrophage mannose receptor CD206 targeting mechanism is used in the US Food and Drug Administration-approved SPECT radiopharmaceutical 99mTc-Tilmanocept, a Technetium 99m-labeled mannosylated dextran, for lymphoscintigraphy and sentinel lymph node mapping (Leong, 2022; Surasi *et al*., 2015). Pirmettis and co-workers then developed a new Technetium 99m-labeled mannosylated dextran derivative DCM20 for sentinel lymph node mapping, introducing S-derivatized cysteine as the chelator instead of DTPA, which is considered less ideal for ^{99m}Tc stabilization (Pirmettis *et al*., 2012; Eckelman, 1995). Further, different sizes of mannosylated dextran (21.3-805.6 kDa) with 19-645 units of mannose and dextran with a molecular weight of 10-500 kDa were compared. The study revealed that ^{99m}Tc-labeled D75CM with 75 kDa dextran and 74 mannose units (111.2 kDa) was superior due to the highest sentinel lymph node accumulation after subcutaneous injection (Papasavva *et al*., 2021). The intravenous administration showed the highest uptake in the liver, which is known to be CD206-rich tissue (Papasavva *et al*., 2021; Linehan *et al*., 1999). All these preceding studies indicate the specificity of the mannosylated dextran derivative in mannose receptor CD206 targeting.

Correspondingly, we explored a smaller mannosylated dextran derivative D10CM (21.3 kDa) with 10 kDa dextran decorated with 7 free cysteines and 17 mannosylated S-derivatized cysteines per molecule of D10CM to achieve a better biodistribution profile for molecular imaging of small targets (Jeong JM, 2015). Fluorine-18 was chosen in this study due to its obvious advantages over other PET radionuclides. To name a few, in addition to its dominance in clinical PET practice along with the radiometal gallium-68, fluorine-18 has a longer physical half-life compared to ^{68}Ga, low positron energy (0.635 MeV), easy transport to a non-cyclotron equipped facility, and is preferable for imaging low-density receptors/targets in tissue due to its ideally high molar activity. Additionally, it offers higher spatial resolution than common PET radiometals (e.g. ^{68}Ga, ^{89}Zr, and ^{124}I) (Ajenjo *et al*., 2021; Eskola *et al*., 2012; Van Dalen *et al*., 2008; McBride *et al*., 2013).

Even though S-derivatized cysteine in the D10CM structure is not intended for ^{18}F-fluorination, we maintained a similar structure to preserve tracer stability and favorable biokinetics achieved in previous studies (Papasavva *et al*., 2021; Pirmettis *et al*., 2012). Instead, to achieve optimum chemical stability for the ^{18}F-labeled compound, the NOTA chelator was incorporated into the D10CM structure. Several bifunctional chelators have been tested to potimize the [^{18}F]AlF labelling method. The study by Archibald and Allot on 2021 investigated the potential chelators as

mentioned earlier in ^{18}F-fluorination chapter. According to their finding, NOTA and NODA are the most popular chelators of choice for [^{18}F]AlF-based PET tracer development owing to some considerations such as their commercial availibility, stability, radiochemical purity and radiochemical yield, radiolabelling efficiency and kinetic barrier for aluminum bond to the chelator. The [^{18}F]AlF radiolabelling method favors the hexadentate ligand such as NOTA and DOTA, where one coordination site is occupied by [^{18}F]F$^-$ and 5 other sites anchor the [^{18}F]AlF^{2+} (Archibald *et al*., 2021). These coordinations provide complex stability which subsequently generate more radiolabelling efficiency at elevated temperature used in [^{18}F]AlF-NOTA-D10CM radiosynthesis protocol (100 ℃). However, among the available chelators, NOTA is likely the most widely used in clinical applications. The [^{18}F]AlF-NOTA complex has demonstrated excellent *in vivo* stability in both animal and human studies (Fersing C *et al*., 2019; Giesel FL *et al*., 2021). To date, no clinical safety concerns have been reported regarding the [^{18}F]AlF-NOTA moiety in radiopharmaceuticals used for imaging. While DOTA has higher kinetic barrier for radiolabelling and thus may require higher temperature compared to NOTA to complete the [^{18}F]AlF^{2+} chelating reaction, which can affect the stability and radiochemical purity of the product. Consequently, we chose [^{18}F]AlF-NOTA chelation chemistry for labeling D10CM.

The sugar nature of the dextran backbone affects the hydrophilicity of the tracer and contributes to the tracer distribution through blood circulation after intravenous injection. This was demonstrated by the coefficient distribution study of [^{18}F]AlF-NOTA-D10CM with a Log*D* of -3.10, indicating a hydrophilic profile. Hydrophilic tracers contribute to better tracer's distribution via blood circulation following intravenous injection, lower nonspecific uptake and faster blood clearance and renal excretion (Liu, 2008).

Among all the options, the chelation-based fluorination method with [^{18}F]AlF is an excellent choice for ^{18}F-labeling of biomolecules. The strong bond formation between aluminum and fluorine-18 will facilitate the indirect ^{18}F-fluorination of D10CM via the chelator attached to its structure (McBride WJ, *et al*., 2009). However, [^{18}F]AlF is a pH-sensitive reaction that requires a consistent pH between 4 and 5 to avoid the formation of impurities other than [^{18}F]AlF-NOTA. This can be achieved by strictly maintaining the reaction in a pH 4-5 buffer solution. In study I, $AlCl_3$ was dissolved in a pH 4 acetate buffer. Another consideration for efficient fluorination with [^{18}F]AlF is the possible competition from metal impurities to bond with [^{18}F]F$^-$. These metal impurities are sometimes unavoidable, even in trace amounts, and can originate from simple contamination in the solvents used, metal utensils, and trace metals from prior [^{18}F]F$^-$ production. All of these side product formations can lower the molar activity of the final product, which is essential for molecular imaging of smaller targets. To minimize this contamination effect, the

strict use of trace metal-free solvents is mandatory. In addition, using a high amount of precursor is useful to avoid the possible covalent bonding of ^{18}F-F^- with other metals. However, increased mass of precursor decreases the apparent molar activity where the non-labled precursor can saturate the target and compete with the radiolabelled precursor for binding sites. Indeed, apparent molar activity remains an important factor in PET tracer development and future labeling strategy should aim to further optimize this parameter without compromising yield or biological activity. However, under given condition, [^{18}F]AlF-NOTA-D10CM still demonstrated a reliable performance in CD206 targeting by PET and in this initial study, lower apparent molar activity was considered a reasonable trade-off.

Indeed, NOTA-D10CM fluorination was accomplished in a relatively short time (90 minutes) using the straightforward and robust [^{18}F]AlF labeling protocol with a starting [^{18}F]F^- activity of 6 GBq per synthesis batch. The use of approximately 65 nmol resulted in approximately 800 MBq of [^{18}F]AlF-NOTA-D10CM at EOS, starting from 6 GBq of [^{18}F]fluoride, which was sufficient to facilitate a 60-minute dynamic PET imaging protocol for 4 or more rats. Furthermore, despite the potential metal contamination in the [^{18}F]AlF labeling technique mentioned earlier, [^{18}F]AlF-NOTA-D10CM was produced with moderate molar activity (9.9 GBq/μmol). In comparison, mannosylated dextran Lymphoseek labeled with another fluorination technique—covalent bond formation with a boron-based fluorine-18 labeling method—produced [^{18}F]BOMB Lymphoseek with lower molar activity (1.85 GBq/μmol) compared to [^{18}F]AlF-NOTA-D10CM (Ting *et al*., 2010). However, higher molar activity could possibly be achieved using nucleophilic fluorination such as TSPO targeting tracer [^{18}F]F-DPA which reported molar activities of 990 ± 150 GBq/μmol (Keller *et al*., 2018). However, a higher molar activity does not always guarantee better targeting properties (Wurzer *et al*., 2018). For instance, for PSMA-targeting PET tracers, lower molar acitivty resulted in substantial better tumor to organ ratio, suggesting that an optimal balance of molar activity is crucial for effective PET uptake. Depending on the application, high A_m is critical in situations such as imaging low-density receptors, studying bioactive or potentially toxic molecules, or when studying kinetic modeling parameter. In contrast, high A_m is less critical in cases where endogenous compounds are abundant—such as in glucose metabolism—or when the biological target is not easily saturated.

The highest [^{18}F]AlF-NOTA-D10CM uptake from *in vivo* PET imaging in Study I was found in mannose receptor CD206-rich tissues, including the liver, spleen, and bone marrow. This result is similar to another study that targeted CD206 with mannosylated compounds, including ^{68}Ga-labeled human serum albumin (^{68}Ga-NOTA-MSA) (Choi *et al*., 2011). The blocking experiment in Study I, which involved a 100-fold mannan injection 15 minutes prior to the [^{18}F]AlF-NOTA-D10CM injection, demonstrated a dramatic reduction in [^{18}F]AlF-NOTA-D10CM

uptake in those mannose receptor CD206-associated tissues, indicating the tracer's specificity towards mannose receptor CD206.

[^{18}F]AlF-NOTA-D10CM was produced with consistently excellent radiochemical purity of >99% for every batch and *in vivo* stability, with approximately 84% of total plasma radioactivity originating from intact [^{18}F]AlF-NOTA-D10CM at 60 minutes after intravenous injection (Study I). This result can be attributed to the use of the NOTA chelator, which is known to be one of the most widely used chelators in clinical practice and has shown *in vitro* and *in vivo* stability in complexation with [^{18}F]AlF (Fersing *et al*., 2019; Giesel *et al*., 2021).

The relatively high uptake observed in the femur might be misleading and interpreted as defluorination, a common concern with [^{18}F]-labeled tracers where free [^{18}F]$^-$ accumulates in osseous tissue. However, according to *in vivo* stability studies in both rats and mice, [^{18}F]AlF-NOTA-D10CM remains metabolically stable. Additionally, CD206 immunohistochemical staining revealed high CD206 expression in the bone marrow, supporting the interpretation that the observed uptake reflects target-specific binding to CD206-positive macrophages rather than nonspecific tracer degradation. This high bone marrow uptake is consistent with other preclinical and clinical studies using CD206 targeting PET tracers mentioned earlier (Choi *et al*., 2019; Gondry *et al*., 2023).

The biodistribution data suggest that [^{18}F]AlF-NOTA-D10CM is primarily cleared via the renal route, as evidenced by the high urinary bladder uptake observed in the blocking condition, where CD206 binding sites were saturated by mannan blocker. In contrast, bladder activity was low in the non-blocked condition, indicating that a larger proportion of the tracer was retained in CD206-expressing tissues. Additionally, minimal uptake in the liver and gastrointestinal tract supports negligible hepatobiliary clearance. Furthermore, the *in vivo* blocking study confirmed a dramatically reduced uptake in CD206-rich tissues such as the liver, spleen, and bone marrow, while renal and bladder signals remained significantly high, strengthening the interpretation of target-specific binding and renal excretion as independent processes. These findings support renal clearance as the dominant elimination route for [^{18}F]AlF-NOTA-D10CM.

Altogether, [^{18}F]AlF-NOTA-D10CM is reproducible with favorable characteristics by the pseudo-metal [^{18}F]AlF fluorination method. Initial [^{18}F]AlF-NOTA-D10CM PET study results justify our next step to evaluate [^{18}F]AlF-NOTA-D10CM PET in an animal model with inflammation.

6.2 Validation study in mice with skin inflammation (Study II)

In Study II, we aimed to validate mannose receptor CD206 targeting for the detection of inflammation using [^{18}F]AlF-NOTA-D10CM PET in an animal model with skin inflammation. To demonstrate the [^{18}F]AlF-NOTA-D10CM's inflammation targeting ability, C57BL/6N mice were induced with CFA to develop inflammation in the foot pad. CFA contains heat-killed Mycobacterium tuberculosis, which is emulsified with an antigen and widely used as an autoimmune disease inducer in animal experimental models by enhancing IL-6 production during the initiation of the immune response. IL-6 is required to induce the trafficking of inflammatory dendritic cells to the draining lymph node following immunization (Fontes *et al*., 2017). This was an excellent model to showcase the inflammation targeting ability and lymph node activation mapping by intravenous and subcutaneous injection of [^{18}F]AlF-NOTA-D10CM, respectively. Furthermore, the CFA-induced mice were divided into two groups: 5 and 14 days after CFA induction, to represent the acute and chronic inflammation groups, respectively.

In vivo PET imaging of [^{18}F]AlF-NOTA-D10CM in Study II showed a significantly higher uptake in inflamed foot pad skin compared to healthy skin in control mice, with no significant difference between CFA Day 5 and CFA Day 14. Autoradiography uptake in inflamed foot pad skin showed a high target-to-background ratio in both groups.When comparing this result to other inflammation detection studies using CD206 targeting, this study results showed a comparable performance.

Several PET tracers target CD206 with mannosylated structures, including ^{68}Ga-labeled mannosylated human serum albumin ([^{68}Ga]Ga-NOTA-MSA) for sentinel lymph nodes detection, fluorine-18 or ^{68}Ga-labeled anti-MMR antibody or antibody fragment ([^{68}Ga]Ga-NOTA-anti-MMR Nb, [^{18}F]FB-anti-MMR-sdAb and [^{68}Ga]Ga-NOTA-anti-MMR-sdAb) used in myocardial infarction and atherosclerosis models and to detect CD206-positive tumor-associated macrophages, and ^{68}Ga-labeled peptide ([^{68}Ga]RP832c) for tumor-associated macrophages (Varasteh *et al*., 2022; Varasteh *et al*., 2019; Choi *et al*., 2019; Blykers *et al*., 2015; Xavier *et al*., 2019; Gondry *et al*., 2023; Parker *et al*., 2023). All these studies showed promising results in inflammation detection which support the CD206 targeting concept for imaging of inflammatory process. Our decision to employ a mannosylated dextran-based tracer for CD206 targeting was guided by the precedent of ^{99m}Tc-labeled mannosylated dextran based platform, ^{99m}Tc-tilmanocept, an FDA approved radiotracer for lymphoscintigraphy and lymph node mapping by SPECT demonstrating the feasibility in CD206 targeting, safety, and clinical acceptance of this molecular architecture.

Furthermore, regarding potential advantages of the new tracer, we have expanded the discussion comparing different CD206-targeted tracers and their application in imaging inflammatory response after MI. Compared to previously reported CD206-targeted tracers, [^{18}F]AlF-NOTA-D10CM offers several notable advantages. This tracer selectively binds to CD206 expressed on M2 macrophages and demonstrates favorable pharmacokinetics, characterized by rapid clearance from the blood circulation and selective tissue accumulation. These distribution patterns are consistent with CD206-mediated binding, and are corroborated by anti-CD206 immunohistochemical staining conducted in this study. Importantly, because CD206 expression reflects a functional macrophage phenotype rather than a specific immune cell lineage - unlike tracers that selectively target T cells or activated neutrophils - [^{18}F]AlF-NOTA-D10CM may offer broader applicability across diverse stages of immune response. In comparison to peptide-based CD206-targeted tracers, mannosylated dextran platform employed here confers several advantages including enhanced *in vivo* stability, reduced susceptibility to enzymatic degradation, and increased binding avidity. The latter arises from multivalent mannose presentation, achieved through the attachment of multiple mannose moieties to a single D10CM molecule. Moreover, while peptide-based tracers frequently exhibit elevated renal uptake due to their small molecular size, dextran-based constructs such as [^{18}F]AlF-NOTA-D10CM display more favorable biodistribution profiles for imaging inflammatory processes. Finally, the dextran scaffold contributes to the overall biocompatibility and safety of the tracer, supporting its suitability for clinical translation. From a radiopharmaceutical production standpoint, [^{18}F]AlF-radiolabeling chemistry offers a straightforward approach that is highly compatible with fully automated manufacturing process (Archibald *et al*., 2021), thereby supporting its clinical application and potential for widespread implementation.

Regarding [^{18}F]AlF-NOTA-D10CM specificity, the involvement of wild-type and CD206-deficient mice is an elegant way to demonstrate the specific uptake of [^{18}F]AlF-NOTA-D10CM *in vivo*. The results were as expected, as shown by the significantly lower uptake in CD206-associated organs, including the liver, spleen, and bone marrow. While moderate blocking of splenic uptake was observed in wild-type rats, the persistently high uptake in CD206-deficient mice indicates that this signal is not primarily driven by CD206 binding. The spleen is a highly perfused organ that functions as a blood reservoir, and in both the CD206 knockout and blocking conditions, elevated blood radioactivity was observed. This suggests that the increased splenic signal may reflect a “blood bank” effect, rather than specific tracer retention. The spleen is known to express high levels of CD206, as confirmed by our IHC staining and consistent with previous reports identifying the spleen as a CD206-rich organ (Martinez-Pomares, 2012; Martinez-Pomares *et al*., 1998; Miller

et al., 2008). Nonetheless, while spleen uptake is consistent with CD206 expression, it should be interpreted cautiously and not be relied upon as the sole evidence of tracer specificity

In Study II, intradermal injections were also performed for lymph node activation mapping following the study's finding that foot-draining popliteal LNs were used to characterize the LN response to acute inflammatory stimuli in the foot (Angeli *et al*., 2006). Since the CFA was subcutaneously injected into the back of the left hind leg of the mice, the first lymphatic drainage would be to the popliteal LN. Normally, the lymphatic drainage in healthy mice continues to the iliac LNs and then to the renal LNs. When the alternative lymphatic drainage is activated from the popliteal to the inguinal and then to the axillary LNs, it becomes an indicator of a more chronic phase, which is usually used for the diagnosis of metastasis in several cancers (Morton *et al*., 2003; Turner *et al*., 1997). The results of this study are consistent with the concept of the FDA-approved ^{99m}Tc-lymphoseek for lymphoscintigraphy and sentinel LN mapping.

Another important finding was that there was a positive correlation between the percentage of the CD206 positive area and the uptake of [^{18}F]AlF-NOTA-D10CM autoradiography in inflammation foci. In addition, the specificity of [^{18}F]AlF-NOTA-D10CM uptake in mannose receptor CD206 was verified by the reduced uptake in tissues associated with the mannose receptor, including the liver, spleen, bone marrow, and other CD206-associated organs in CD206 KO mice, compared to WT mice.

All these results confirmed that [^{18}F]AlF-NOTA-D10CM is capable of detecting inflammation through PET imaging by specifically targeting the overexpression of the mannose receptor CD206 in the inflamed areas and draining lymph nodes. Overall, Study II demonstrated that CD206 targeting with [^{18}F]AlF-NOTA-D10CM is a promising tool for the detection of inflammation.

6.3 PET imaging in experimental acute myocardial infarction (Study III)

In Study III, we translate the inflammation detection ability of [^{18}F]AlF-NOTA-D10CM to detect acute MI in rats. The MIs were induced in male Sprague Dawley rats by permanent LAD ligation.

Studies indicate that M2 macrophages are heavily involved in the inflammation resolution process and contribute to cardiac healing and remodeling post-MI (Frangogiannis, 2014). The mannose receptor CD206 is a signature of M2 macrophages, providing a foundation for investigating M2 macrophage targeting via CD206 for the detection of inflammation in myocardial infarction (Rőszer, 2015).

Hypothetically, targeting M2 macrophages reflects the inflammation resolution phase post-MI.

Compared to previous PET tracers targeting CD206 in animal models with LAD ligation, our PET study results showed similar outcomes with some differences regarding the tracer chemical structures. One study using ^{68}Ga-labeled anti-MMR nanobody, [^{68}Ga]Ga-NOTA-anti-MMR Nb, in rats and mice with LAD ligation was conducted (Varasteh *et al*., 2022). The similarities with Study III results are evident in the PET imaging findings, where the highest uptake of [^{68}Ga]Ga-NOTA-anti-MMR Nb and [^{18}F]AlF-NOTA-D10CM was found in the liver and spleen. Additionally, high [^{18}F]AlF-NOTA-D10CM uptake was also observed in the bone marrow, which aligns with the Phase I [^{68}Ga]Ga-NOTA-anti-CD206-sdAb human study targeting CD206 (Gondry *et al*., 2023).

[^{18}F]AlF-NOTA-D10CM PET uptake in the infarct area was significantly higher compared to the remote area and the myocardium of the sham-operated control group, with the infarct-to-remote area ratio being 1.5 ± 0.3 (Study III). This result is also consistent with [^{68}Ga]Ga-NOTA-anti-MMR Nb, which showed a high infarct-to-remote area ratio of 1.3 ± 0.2 (Varasteh *et al*., 2022). Even though these two results are aligned, it is duly noted that [^{18}F]AlF-NOTA-D10CM and [^{68}Ga]Ga-NOTA-anti-MMR Nb binding mechanisms to CD206 are theoretically different. While mannosylated dextran is a glycan-based molecule recognized by the carbohydrate recognition domain (CRD), this is not true of the anti-MMR nanobody-based structure in [^{68}Ga]Ga-NOTA-anti-MMR which binds to CD206 via a peptide or protein binding domain, such as the collagen-binding fibronectin Type II domain (Martinez-Pomares, 2012). Thus, theoretically, [^{68}Ga]Ga-NOTA-anti-MMR will not be able to block [^{18}F]AlF-NOTA-D10CM uptake in CD206 but they may complement each other. Despite the different binding mechanisms, both [^{18}F]AlF-NOTA-D10CM and [^{68}Ga]Ga-NOTA-anti-MMR Nb are specifically targeted to the macrophage mannose receptor CD206, as confirmed by the colocalization of CD206 and CD68 using double immunofluorescence staining.

Studies suggest that M2 macrophage expression dominates on days 5 to 7 post-MI, while days 1 to 3 are when M1 macrophages are at their highest (Ma *et al*., 2018). Based on this, rats in Study III were divided into two groups: MI Day 3 and MI Day 7 after the LAD ligation. This is also supported by another study indicating that day 3 after LAD ligation is a pro-inflammatory state, while day 7 after LAD ligation is when the anti-inflammatory state peaks (Yan *et al*., 2013). Consistently, the PET study results of Study III and Varasteh and colleagues show that the uptake of [^{18}F]AlF-NOTA-D10CM and [^{68}Ga]Ga-NOTA-anti-MMR Nb was elevated on day 7. The uptake in the infarct area on day 3 after MI was also higher than in the remote area and sham-operated control. These results indicate that macrophages

have been polarized into M2 macrophages, suggesting that the healing process following MI actually begins even earlier than day 7 and possibly day 5 post-MI.

Interestingly, the quantification of CD206 area-% measured from CD206 immunohistochemical staining in Study III provides another insight into the immune response following MI demonstrating that it is not completely clear-cut. CD206 area-% was higher on day 3 post-MI. This was assumed to be associated with M2 macrophage phagocytosis function, which aims to clean up damaged or dead cells. After the clean-up, the recovery process follows and causes the formation of scar tissue and wall thinning, and M2 macrophages are not necessarily needed any longer after the formation of fibrotic tissue as a result of the healing process. Consequently, the population of CD206-positive cells was visibly reduced by immunostaining. These phenomena make sense since on the day of inflammation triggered by physical damage from LAD ligation, the anti-inflammatory cells responded quickly, and both pro- and anti-inflammatory states may overlap (Mouton *et al*., 2018). The M1 macrophage staining on day 3 can help clarify the dynamics of these macrophages after MI, which was not performed in Study III.

However, PET *in vivo* results in Study III were not supported by *ex vivo* gamma counting of the hearts due to the different measurement regions used in *in vivo* PET imaging analysis and in *ex vivo* gamma counting. However, *ex vivo* results still confirmed that the highest uptake was consistently in line with the previous study, which found it to be in the liver, spleen, and bone marrow.

Regarding the specificity study of [^{18}F]AlF-NOTA-D10CM, due to the nature of the heart as a blood-rich tissue, an *in vivo* blocking study will not be feasible to prove the specific uptake of [^{18}F]AlF-NOTA-D10CM by the myocardial infarction in the heart. Alternatively, we performed an in vitro competition study on the infarcted LV section using an excess of unlabeled NOTA-D10CM as the blocker. The competition study showed that the uptake in the MI area was reduced by approximately 85% compared to the total binding sections.

Another limitation that was taken into account was the fact that the highest SUV in the liver would interfere with the SUV measurement in the MI area, especially at the apex. However, *in vivo* analysis using a heart tool, where the ROIs in the MI area were defined on horizontal and vertical long axis and short axis, avoided the areas that were affected by liver spillover. This study found a positive correlation between PET SUV and CD206 positive area-% in the left ventricular myocardium, in addition to autoradiography uptake, indicating that the higher the SUV, the higher the inflammation resolution process. However, it should be noted that the inflammation resolution process does not directly reflect that the myocardium is healed. It is better interpreted that the higher inflammation resolution process reflects the more severe MI. This feature provided by M2 macrophages targeting for imaging of MI can be useful for monitoring therapy efficacy.

Overall, Study III revealed that CD206 targeting with [^{18}F]AlF-NOTA-D10CM could be a useful tool for monitoring the inflammatory response following MI.

6.4 Clinical importance of CD206 targeting PET tracer

The results of this study contribute to the growing body of research supporting Mannose Receptor CD206 as a relevant imaging target for inflammation, particularly in the context of tissue healing and immune cell dynamics. In the clinical setting, a CD206-targeted PET tracer could provide a non-invasive biomarker for assessing post-infarct healing, monitoring therapeutic efficacy, or potentially differentiating inflammatory phenotypes in various cardiovascular and inflammatory diseases. This would offer clinicians a valuable tool for precision medicine — allowing tailored treatment strategies based on real-time imaging of immune activity.

The promising preclinical performance of the [^{18}F]AlF-NOTA-D10CM tracer supports its potential for clinical translation. If any opportunity occurs, future steps should include toxicity and safety evaluation, radiochemical scale-up, and initial human studies to confirm biodistribution and target engagement in patients. If successful, CD206 PET imaging could become an important modality in the evaluation and management of inflammation-related cardiovascular conditions, and possibly extend to other diseases where CD206 expression plays a key role (e.g., atherosclerosis, chronic lung disease, or cancer-associated macrophages).

To justify, following myocardial infarction, the immune system plays a key role in both clearing necrotic tissue and initiating repair mechanisms. However, the balance and timing of this immune response are critical — excessive or prolonged inflammation can lead to adverse remodeling, fibrosis, and heart failure, while inadequate immune activation may impair tissue repair.

Currently, clinicians lack effective tools to non-invasively assess the dynamics of immune cell activity in the myocardium. A PET tracer targeting CD206 — a marker of alternatively activated (M2-like) macrophages involved in tissue repair — could provide valuable insight into the healing process, enabling clinicians to stratify patients at risk of adverse remodeling, monitor the efficacy of anti-inflammatory or regenerative therapies, and guide the timing of therapeutic interventions.

Few examples of therapeutic interventions where immune response imaging could inform the optimal therapeutic window:

1. Anti-inflammatory therapies (e.g., IL-1β inhibitors like canakinumab)

These therapies aim to reduce excessive inflammation after MI, but giving them too early may blunt necessary clearance of dead tissue, while too late may miss the window to prevent adverse remodeling. In this scenario, CD206 imaging helps

identifying the transition from pro-inflammatory to reparative macrophage activity, which could help guide the ideal time to initiate anti-inflammatory treatment without impairing natural healing.

2. Cell-based regenerative therapies (e.g., stem cell or exosome therapy)

These interventions may depend on a supportive immune environment to integrate or exert paracrine effects. High CD206 expression could indicate a pro-reparative immune phase, suggesting a window of opportunity for therapy delivery to enhance repair.

3. Immunomodulatory agents targeting macrophage polarization

Some experimental drugs aim to shift macrophages from M1 (pro-inflammatory) to M2 (reparative) phenotypes. PET imaging of mannose receptor CD206 could track the effect of such therapies in real time, allowing dose optimization and early identification of responders vs. non-responders.

4. Timing of cardiac rehabilitation or mechanical interventions

Decisions around interventions (e.g., ventricular assist devices or cardiac pacing) can benefit from knowing the state of myocardial inflammation and healing. Mannose receptor CD206 PET imaging may visualize the immune landscape and help avoid interventions during vulnerable inflammatory stages, reducing risk of complications.

6.5 Study limitations

We acknowledge that this study has some limitation which we have tried to improve.

In Study II, we observed a notable difference in the SUV of foot pads between C57BL/6N WT control mice in the CFA study (SUV = 0.04) and those used in the CD206-deficient comparison (SUV = 0.21). While both groups consisted of the same strain, this discrepancy is most likely due to biological variation, particularly in foot pad size and overall body growth. The WT control mice in the CFA study were visibly smaller than both the CFA-treated mice and the WT mice in the CD206-deficient study, which may have affected quantitative PET signal due to partial volume effects and differences in tissue geometry. Moreover, the age distribution differed: CFA controls were approximately 9 weeks old, whereas WT mice in the knockout study ranged from 10–15 weeks, which could significantly impact body size and organ development. The small sample size in the CFA WT control group (n = 4) may have also contributed to variability and reduced statistical power. While this variation may partly influence the observed group differences, the uptake pattern in CFA-treated mice remains consistent with expected inflammatory responses and

immune cell activation. This could be a reference for future study to use the same age for each group to avoid the variability which may affect the quantitative analysis.

In study III, the high mortality rate of the LAD ligated rats were a major concern for the continuation of the study. The preclinical evaluation conducted in this study was firmly grounded in the principles of the 3Rs — Replacement, Reduction, and Refinement.

All animal experiments were approved by the national Project Authorization Board in Finland (license numbers ESAVI/43134/2019, ESAVI/8648/2020, and ESAVI/14685/2020) and conducted in compliance with EU Directive 2010/63/EU on the protection of animals used for scientific purposes. Specifically, for Study III, animal studies were conducted in close coordination with the veterinaries at the University of Turku Central Animal Laboratory (UTUCAL), in line with the principles of the 3Rs — Replacement, Reduction, and Refinement — several measures were taken to ensure the ethical and responsible use of animals throughout this study.

With respect to Refinement, multiple adjustments were made to improve animal welfare at all stages of the LAD ligation protocol. Medication regimens were optimized in collaboration with veterinary experts to ensure effective anesthesia, perioperative analgesia, and post-operative recovery. Enhanced monitoring protocols were applied to minimize animal distress and ensure adherence to humane endpoints. Despite these efforts, a relatively high mortality rate was observed in the myocardial infarction (MI) model, typically occurring immediately, within a few hours, or up to 24 hours post-surgery. These outcomes were most likely due to the extent of infarction caused by coronary artery ligation, which remains difficult to control and predict in small animal models. Additional anatomical limitations in rats made it challenging to consistently achieve an optimal ligation site and tension, contributing to variability in infarct size and survival.

In accordance with the Reduction principle, the number of animals used was minimized through strategic planning of group sizes and imaging schedules. Due to the expected mortality and variability in infarct development, group sizes were calculated to yield approximately 3–4 MI-confirmed animals per imaging day — the practical maximum that could be scanned in a single session. This strategy ensured that each imaging slot was used efficiently, while avoiding unnecessary animal use. As the PET scanner is a shared, high-demand, and high-cost resource, optimizing each allocated session was essential to uphold both scientific integrity and ethical responsibility.

Regarding the Replacement principle, *in vitro* or *ex vivo* models were considered during the planning phase. However, *in vivo* PET imaging was essential to evaluate tracer biodistribution, pharmacokinetics, and target specificity under physiologically relevant conditions — parameters that cannot be adequately assessed using non-

living systems. As the tracer is being developed for potential clinical PET imaging, it was necessary to conduct whole-body imaging in live animals to ensure translational relevance. While full replacement of animal models was not possible, several methodological refinements were adopted as ethical replacements of previous protocols. These included improved anesthesia, analgesia, and post-operative care procedures, introduced following the guidance of the ethical board and veterinary staff to maximize animal welfare.

The use of the MI model was also scientifically justified based on the research focus of our group, which investigates inflammation and its role in cardiovascular disease. Post-infarct inflammation represents a well-established and clinically relevant process, making the MI model highly appropriate for evaluating a PET tracer targeting inflammation-associated mechanisms in the heart.

7 Summary/Conclusions

This thesis investigated the macrophage mannose receptor CD206 targeting for imaging inflammation using the PET modality. The investigation began with the development of the mannose receptor CD206 targeting tracer [^{18}F]AlF-NOTA-D10CM, and we evaluated its characteristics and feasibility for initial PET imaging. The next step was validating the uptake of [^{18}F]AlF-NOTA-D10CM in inflammation foci using mice with footpad skin inflammation induced by Complete Freund's adjuvant. In addition, we also evaluated the specificity of [^{18}F]AlF-NOTA-D10CM uptake by the mannose receptor through a comparative study in CD206-deficient mice against WT mice. Study III aimed to translate the inflammation-targeting ability of [^{18}F]AlF-NOTA-D10CM for the detection of acute myocardial infarction in rats developed through permanent coronary artery ligation surgery. We complemented this last study with a binding specificity uptake assay of NOTA-D10CM by M2 macrophages and assessed the binding affinity of [^{18}F]AlF-NOTA-D10CM to CHO-CD206^{+} cells. The main findings from these three studies were:

1. [^{18}F]AlF-NOTA-D10CM was successfully developed in a robust and straightforward manner, resulting in a PET tracer with favorable radiochemical purity, radioactivity yield, *in vitro* and *in vivo* stability, solubility, and a decent molar activity. Initial in vivo PET imaging in healthy rats demonstrated that [^{18}F]AlF-NOTA-D10CM specifically targeted mannose receptor-rich tissues, including the liver, spleen, and bone marrow. This was confirmed by the in vivo blocking study using the mannose ligand mannan, which dramatically reduced the uptake of [^{18}F]AlF-NOTA-D10CM in those mannose receptor-associated tissues.

2. [^{18}F]AlF-NOTA-D10CM uptake by the mannose receptor was specifically validated by the significantly reduced uptake of [^{18}F]AlF-NOTA-D10CM in mannose receptor-rich tissues in CD206-deficient mice compared to wild-type mice. Further investigation in CFA-induced mice successfully showcased the ability of [^{18}F]AlF-NOTA-D10CM to specifically target the inflammation foci from the acute to chronic phase. Statistically, the SUVs in the inflamed

footpad skin and inflamed popliteal lymph nodes were significantly higher than the tissue background.

3. [^{18}F]AlF-NOTA-D10CM PET detects overexpression of CD206 after ischemic myocardial injury, making it a suitable biomarker for detecting M2-type macrophages during resolution of the inflammatory process post-MI.

To summarize, CD206 targeting demonstrated potential for detecting skin inflammation and experimental acute myocardial infarction, providing a foundation for further translational studies for the diagnosis of inflammatory-related diseases by PET, especially for early detection. The specificity studies confirmed that [^{18}F]AlF-NOTA-D10CM was taken up by the mannose receptor CD206 on M2 macrophages, which are also known as anti-inflammatory macrophages involved in the inflammation resolution process. Given its relevance in inflammation resolution and the promising results from our preclinical evaluation, targeting CD206 is a well-justified approach for evaluating its utility as a biomarker to monitor the immune response, particularly during the resolution phase of inflammation, assess therapeutic efficacy, or serve as a diagnostic tool.

Acknowledgements

To the readers, I hope this thesis contributes in some way to your scientific quest.
Disclaimer: I might be writing a really long acknowledgement section, and still I don't feel it will ever be enough to express my gratitude. All my heartfelt thoughts are poured into this.

My PhD training was hosted at the Turku PET Centre, University of Turku, and carried out across several laboratories, including the BioCity Preclinical Imaging Facility (–1 floor), RK2 laboratory, PETlabra (2nd floor), Oxygen Laboratory (Happi Labra), Aurum Radionuclide Laboratory, and MediCity Radionuclide Laboratory. I have gained many skills by working across these different facilities.

During the first to third years of my PhD, I focused on animal work: assisting LAD surgeries, monitoring animal care, performing cannulation of rats, prep the rats for PET imaging, conducting *ex vivo* gamma counting, and analyzing PET images and other types of images, and drafting the publication.

Later, starting gradually from the 3rd year of my PhD until now, my interest shifted toward radiochemistry. I received my first tracer radiosynthesis training with a gallium-68-labeled tracer in Happi Labra. From there, I expanded my skills to radiolabeling with fluorine-18 for some tracers targeting CD206 (my own), folate receptor-β, and FAP. And eventually, I also took part in radiometabolite analysis of these tracers.

All of these experiences made me versatile enough to cover many aspects of PET tracer development and preclinical imaging by *in vivo*, *ex vivo*, and *in vitro* evaluations. In addition, due to the heavy involvement of immunology and cardiovascular diseases in preclinical tracer evaluation, I also deepened my understanding in these fields—something I am truly happy to have learned.

Just like muscle growth, these skills have been built through consistent and heavy effort. I would not have achieved this growth without the many people who gave their time and support to help me complete my studies.

Throughout my PhD training**, I am very grateful for the financial support** that made the journey a little easier from 2019 to its completion in 2025. My sincere thanks go to the Turku University Foundation, Orion Foundation, and Finnish Foundation for Cardiovascular Research, UTUGS Drug Research Doctoral

Programme, InFLAMES Research Flagship, Finnish Society of Nuclear Medicine (Lääketieteellinen Radioisotooppiyhdistys), and to my supervisors for allowing me to use a portion of their Sigrid Jusélius Foundation grant when my own funding was limited.

I'd like to sincerely thank Prof. Juhani Knuuti, Director of the Turku PET Centre, who has done a great job with his team providing one of the best PET Centre facilities in the world for conducting basic to translational PET imaging research.

I also express my sincere gratitude to the two reviewers—both experts in their fields—who provided me with constructive comments, criticism, suggestions, and advice. I truly admire that despite their many responsibilities, they took the time to offer valuable guidance to improve my thesis.

I am especially grateful to Professor Olof Eriksson from Uppsala University, Sweden, who kindly approached me at the 2021 iSRS meeting in Nantes, France, upon learning that I was from the Turku PET Centre. **I am equally thankful to Associate Professor Outi Keinänen from the University of Alabama at Birmingham**, United States, whom I have not yet met in person, but whose name I heard echoed at the 2023 iSRS meeting in Honolulu, Hawaii.

Both are inspiring young leaders with exciting scientific work. I know they are among those who have devoted their time and energy to science—a path I continue to aspire to follow.

My sincere gratitude also goes to Professor Adriana Tavares from the University of Edinburgh. In fact, I had already bookmarked her name a year before my thesis writing, knowing her special role and the possibility that she would become my opponent for the defense.

Thank you so much for kindly accepting the role as my esteemed opponent. Not to mention that we share a beautifully similar name, I truly admire your work and dedication to PET imaging and inflammation. You are an inspiring young leader in the field. I admire young leaders who dedicate their time and energy to the knowledge they believe will help humankind.

I can see that three of you—Olof Erikkson, Outi Keinänen, and Adriana Tavares, are so excited doing your own science! I love to see that and love to be that.

My PhD training would not have been possible without the support of my three awesome supervisors, all experts in their respective fields: Professor Anne Roivainen, Professor Antti Saraste, and Associate Professor Xiang-Guo Li.

I first met Anne during my short visit to Turku after a conference in Bergen, Norway. Working with her has taught me that she is a sharp and detail-oriented leader. I've tried to adopt that nature, though it may take me a while to fully "paste" it. Anne has consistently shown me not to settle for less. Her supervision and expertise in preclinical imaging, inflammation and drug development provided the core guidance I needed to complete this study successfully. Her guidance taught me to be more independent in finding the solutions in my own research. I'm so sure that

she's much occupied and thus, her supervision has been so efficient and effective when we were facing a problem. Thank you for being patience with me. I might not have broken any speed records in learning, but I sure made it memorable!

Antti joined me and Anne at our first meeting, bringing his expertise in cardiovascular disease research to the table. Together we decided to evaluate my M2 macrophage-targeting tracer in a rat model of myocardial infarction. Antti is one of the busiest people I've ever met, yet he always makes time for his students and efficiently revises manuscripts with sharp, constructive feedback. A brilliant cardiologist, his dedication to developing PET tracers for imaging inflammation in cardiovascular diseases has been vital to the progress of our group. I am truly a fan of his sharp mind, and he inspired me to explore cardiovascular research more deeply—a field I am glad to have studied.

Xiang, I've known you since your hands-on days in the lab—guiding me through radiosynthesis, running synthesis for students—and now I see you leading your own research group. You consistently show how to move forward with purpose and clarity. Beyond your radiochemistry expertise, you've been a kind and approachable mentor. Your openness and the friendly atmosphere you've created made it easy for students to invite you for coffee or lunch and discuss not only science but also life—making PhD life more bearable and joyful. Your advice, "Don't be afraid of doing anything," has stayed with me and given me the confidence to work independently.

I'd also like to extend my gratitude to Academician Professor Sirpa Jalkanen, a member of my doctoral committee who monitored the progress of my PhD journey. Sirpa is an incredibly inspiring person, and you can truly see the flames in her eyes when you discuss research with her—the kind of scientist I have always aspired to become. In fact, it was because of her that I was encouraged to deepen my understanding of immunology. I couldn't just show up in her office talking about PET research without knowing the basics of immunology! I regret not making more time for meetings with you due to all the things happening during my PhD training, but I hope I'll have more opportunities to connect with you in the future.

To Jukka Kemppainen, Chief of Clinical Physiology and Nuclear Medicine, where I pursued my major—thank you very much for your efficient support, which allowed me to continue my research smoothly.

To the animal caretakers—Terhi, Joonas, and Tiina—thank you for assisting me in taking care of my patients (rats and mice).

To UTUCAL team: Emrah Yatkin, Nina Kulmala, Varpu Laine and Aino Suni—your efforts and collaboration were crucial in optimizing the LAD ligation protocol in rats. I learned so much through trial and error while developing the experimental acute myocardial infarction animal model. Thank you so much!

To HistoCore facility—Marja-Riitta Kajaala and Erica Nyman—thank you for your patience and hard work in providing excellent cryosections, histological,

and immunohistochemical stainings. Without both of you, I wouldn't have the beautiful figures featured in my publications.

To nurses in PETlabra—Sanna Suominen, Heidi Partanen, Minna Atsinki, and others—thank you for being patient with me in the lab. Sometimes you'd find chaos or something wrong the next morning (that was probably me!). I really appreciated that when I had metabolite analysis experiments that ran as late as 19:00, even 20:00, at least one of you was still there—Jukka Ihalainen, Heidi Partanen, Anne Helminen, Hidehiro-sensei. The next early morning you saw me again, you'd greet me, "Did you go home at all?" or simply "mitä menee?"

It's also a privilege to have become acquainted with such talented PIs, leaders, and researchers as Kirsi Virtanen, Ilkka Heinonen, Kari Kalliokoski, Tuula Tolvanen, Mika Teräs, Heikki Minh, Marko Seppänen, and many more. I feel truly blessed to be in an environment that continually exemplifies what it means to be an excellent scientist.

To the inflammation group (alumni and present): Olli Moisio, Riika Viitanen, Maria Grönman, Petri Elo, Helena Virtanen; senior scientists and postdocs: Senthil Palani, Jenni Virta, Mia Ståhle, Arina, Max Miner, Prince Dadson; PhD fellows: Erika, Imran, Armand, Shifa, Mitra, Ade; and researchers Heidi Liljenbäck and Aake Honkaniemi—thank you very much for your support, guidance, collaboration, and company both inside and outside of work. I owe you all so much!

To group of PET pals, PET beers, PET avanto, and PET knit—Erika Atencio, Tatsiana (my defence and karonkka dress designer), Jonne, Petter, Anting, Pyry, Emel, Negar, Milena (and Erico), Francisco Acosta, Teemu Sari, Mueez, Maria, Prince Dadson, Marjo Nylund, Eveliina Honkonen, Venla Ahola, Imran Waggan, Markus Mättiläinen, and others I can't mention one by one—you filled my PhD life with laughter and ease. I'm deeply thankful for your company inside and outside PET. I feel like I have been adopted by the group of Li, Virtanen and Airas. Erika, nobody can tell how much personal growth we have been trough by supporting each others.

To Rami Mikkola and the IT support team—thank you so much for helping me tackle tech issues (which I'm terrible at!) and for providing the gadget I needed for my research.

To the preclinical team in MediCity—thank you for your support and assistance while I was working on the 4th floor. You have been incredibly helpful. Toove Grönros, Francisco Lopez, Jatta Helin, Richard Aarnio, Marko Vehmanen, Merja Harparanta Solin, and all others who are equally thanked.

A special shoutout to Heidi Liljenbäck and Aake Honkaniemi. Heidi, you were instrumental in my research. Your dedication to animal handling and care helped shape my own skills in animal study. I always carry your words with me: "You're permitted to disagree. That's how you grow into a mature scientist." Thank

you for your guidance, patience, and friendship! Aake, your management skills were invaluable—without them, there wouldn't have been any animal scans or completed studies. Both of you encouraged us researchers to be independent, vocalize our thoughts, and to stand up for ourselves. Cheers to that!

To all of my co-authors—thank you very much for contributing your expertise so we could produce high-quality work! Prof. Marko Salmi and Ruth Fair-Mäkelä, thank you so much for your collaboration in our inflammation study in mice. Prof. Ioannis Pirmettis and Konstantina Makrypidi from NSCR "Demokritos", Athens, Greece, thank you very much for being there from day 1 of my research with your valuable NOTA-D10CM precursors ! Small amount but huge impact on my life. Prof. Luisa Martinez-Pomares from University of Nottingham, as I mentioned to you, I'm a big fan of your work with mannose receptor CD206 as it became such a big inspiration and answers to many questions in my research.

To the DRDP coordinators (past and present)—Eeva Valve and Marja Peura, and **to the DRDP directors (past and present)** Erika Savontaus, Ullamari Pesonen, and the current one, Matti Poutanen—thank you for your dedication in building a supportive environment for DRDP students and organizing annual meetings that no other UTU doctoral program offers. You've been an inspiring group of people to know and learn from.

To the DRDP council members (alumni and current ones) —Alejandra Verhassel, Gabby, Shrikar, Imran Waggan, Olli Moisio, Max Miner, Tatsiana, Paula, Emmi, Miika, Marjo, Edla, and others I can't mention all—thank you for your company and your service to our community.

To beautiful ladies at secretariat sectors, Lenita Saloranta (past) and Minna Kangasperko (present)—thank you for smoothing out all my administrative affairs and for your invaluable help!

I also want to thank all people in cardiovascular projects! My bad I many times didn't attend the meeting. But your support and advices for my cardiac project are so appreciated.

To everyone at RK2—thank you for your support during my PhD. Special thanks to the managers Jörgen Bergman (former) and Sarita Försback (current) for granting me access to radiochemistry work and for providing the resources needed to complete it. Your management contributed immensely to my research. Semi Helin**,** thank you for your guidance in radiochemistry. Johan Rajander, Mikael Bergelin and Joakim Slotte —thank you for providing the valuable fluoride. To other colleague in RK2, and those who I used to share the test lab with: Nina Lauren, Thomas Keller, Esa Kokkomäki, Aleksi Vianto, Edla Kerminen, Noora Kajala, Simo Salo, Anna Kirjavainen, and others I couldn't name one by one—thank you for your assistance and good luck with your work!

To the Aurum team—Anu Airaksinen, thank you for letting me work in the radioisotope lab and for managing such an excellent space for "hot" researchers. My gratitude also goes to Risto for his guidance and being a great company while working in Aurum. Thanks to all the Aurum folks who were patient with me (and my singing): Jesse Ponkamo, Heather, Pyry, Jonne, Petter, Erika, Emel, Negar, David, Sami and to the junior researchers—Dominika, Johanna, Nelson and others. Good luck with your researches and take it easy on the synthesis days!

To my office roommies (past and present): Erika, Petter and Jonne —thank you for your patience, especially with my non-stop singing**. To my long distance friends**: Dora (her parents, her siblings, her grandparents, her whole family) and Marco Bentele, thanks for the warm support and keeping me company virtually.

To PETs and Boys —you will always have a special place in my heart. This band has been therapeutic for me. Being surrounded by inspiring *young* professors/researchers was one of my main motivations for joining (aside from the free singing practice!). I've always loved being around people who know more than I do and listen to their stories. Juhani, thank you for keeping the band alive! A very busy person yet never run out of contagious spirit. I have told my self many times that I want to be a celebrity scientist like you! Spreading science and music to society. I'm also inspired by the other busy members whose great qualities I continue to learn from: Jörgen, an amazing radiochemistry mentor and a really patient guitar teacher (though sometimes I hardly understood what he meant); Lauri, I admire the research you're leading—Emotion study, it's the kind of work I want to do, given that I always wanted to be psychologist when I was younger. Sometimes I also think if you can read minds; Olli Raitakari, a quiet presence but with great keyboard skills and an inspiring research portfolio; Jouni, one of my favorite guitarists (who mostly playing notes instead of chords) and one of the kindest person I know (my friends agree); Leo, a great, young bassist whose stories added so much fun to our band chats; Mikko the drummer and Marco Bucci, our new keyboardist—thank you for completing the band; Jussi the DJ and sound (engineer.. ?), always hilarious in any language, makes the rehearsal even more fun; Max Kiugel, a fantastic singer, a helpful and supportive mentor in singing; Anniina Snellman, short run but we had great time being the singers of the famous PETs and Boys band. Long live PETs and BOYs!

Last but not least, to my brother, thank you for being there keeping our mom company, while I'm barely at home.

Those whose name are not yet mentioned, pleaso do know that I'm running out of pages, and that I'm sincerely grateful for knowing you and for your support.

June 15th, 2025
Putri Andriana

Putri Andriana

Born and raised in Indonesia, where her curiosity for science slowly grew into a passion. After earning her bachelor's degree in Pharmaceutical Science, she ventured to Japan to pursue a master's degree in the Department of Diagnostic Radiology and Isotope Medicine at Gunma University, Japan. There, she began her journey into the world of radiopharmaceuticals, developing pre-labeling methods for on-site preparation of radiometal-labeled antibodies with Copper-64.

In 2019, her path led her to Turku, Finland, where she embarked on her doctoral training at the Turku PET Centre, Department of Clinical Physiology and Nuclear Medicine, University of Turku. Under the supervision of Prof. Anne Roivainen, Prof. Antti Saraste and Assistant Prof. Xiang-Guo Li, she focused on preclinical imaging of inflammation, using fluorine-18 labeled mannose receptor CD206-targeting tracers to visualize M2 macrophages in animal models of inflammation.

Throughout her PhD, her thesis projects were conducted in multidisciplinary nature — blending preclinical imaging, immunology, radiochemistry, and cardiovascular disease — while also contributing to the development of several PET tracers to her team and PET colleagues (e.g. synthesis of fluorine-18 and gallium-68 labeled targeting folate receptor-β, fibroblast activation protein, and CD206 targeting tracers). Collaborating with colleagues and contributing her preclinical evaluations skills have been an important part of her scientific journey.

Outside the lab, she finds her salvation in singing, playing guitar, and running — small but meaningful moments that bring balance and joy to her life in research.

References

Aarnio, R., Alzghool, O. M., Wahlroos, S., O'Brien-Brown, J., Kassiou, M., Solin, O., Rinne, J. O., Forsback, S., & Haaparanta-Solin, M. (2022). Novel plasma protein binding analysis method for a PET tracer and its radiometabolites: A case study with [^{11}C]SMW139 to explain the high uptake of radiometabolites in mouse brain. *Journal of pharmaceutical and biomedical analysis*, *219*, 114860.

Aarnio, R., Kirjavainen, A., Rajander, J., Forsback, S., Kalliokoski, K., Nuutila, P., Milicevic, Z., Coskun, T., Haupt, A., Laitinen, I., & Haaparanta-Solin, M. (2024). New improved radiometabolite analysis method for [^{18}F]FTHA from human plasma: a test-retest study with postprandial and fasting state. *EJNMMI research*, *14*(1), 53.

Abdulkhaleq, L. A., Assi, M. A., Abdullah, R., Zamri-Saad, M., Taufiq-Yap, Y. H., & Hezmee, M. N. M. (2018). The crucial roles of inflammatory mediators in inflammation: A review. *Veterinary world*, *11*(5), 627–635.

Abudukelimu, A., Barberis, M., Redegeld, F. A., Sahin, N., & Westerhoff, H. V. (2018). Predictable Irreversible Switching Between Acute and Chronic Inflammation. *Frontiers in immunology*, *9*, 1596.

Acton, P. D., & Kung, H. F. (2003). Small animal imaging with high resolution single photon emission tomography. *Nuclear medicine and biology*, *30*(8), 889–895.

Ajenjo, J., Destro, G., Cornelissen, B., & Gouverneur, V. (2021). Closing the gap between ^{19}F and ^{18}F chemistry. *EJNMMI radiopharmacy and chemistry*, *6*(1), 33.

Alauddin M. M. (2012). Positron emission tomography (PET) imaging with ^{18}F-based radiotracers. *American journal of nuclear medicine and molecular imaging*, *2*(1), 55–76.

Allott, L., Da Pieve, C., Turton, D. R., & Smith, G. (2017). A general [^{18}F]AlF radiochemistry procedure on two automated synthesis platforms. *Reaction Chemistry & Engineering*, *2*(1), 68-74.

Alqahtani F. F. (2023). SPECT/CT and PET/CT, related radiopharmaceuticals, and areas of application and comparison. *Saudi pharmaceutical journal : SPJ : the official publication of the Saudi Pharmaceutical Society*, *31*(2), 312–328.

Ametamey, S. M., Honer, M., & Schubiger, P. A. (2008). Molecular imaging with PET. *Chemical reviews*, *108*(5), 1501–1516.

Andersen, V. L., Soerensen, M. A., Dam, J. H., Langkjaer, N., Petersen, H., Bender, D. A., Fugloe, D., & Huynh, T. H. V. (2021). GMP production of 6-[^{18}F]Fluoro-L-DOPA for PET/CT imaging by different synthetic routes: a three center experience. *EJNMMI radiopharmacy and chemistry*, *6*(1), 21.

Anderson, J. L., & Morrow, D. A. (2017). Acute Myocardial Infarction. *The New England journal of medicine*, *376*(21), 2053–2064.

Andriana, P., Liljenbäck, H., Iqbal, I., Palani, S., Makrypidi, K., Virta, J., Herre, E.A., Jalkanen, S., Knuuti, J., Pirmettis, I., Li, X. G., Saraste, A., & Roivainen, A. (2022). Exploring macrophage mannose receptor expression after myocardial infarction by [^{18}F]AlF-NOTA-DCM positron emission tomography. *European Heart Journal*, *43*, Issue Supplement_2.

Andriana, P., Fair-Mäkelä, R., Liljenbäck, H., Kärnä, S., Iqbal, I., Makrypidi, K., Rajander, J., Pirmettis, I., Li, X. G., Jalkanen, S., Saraste, A., Salmi, M., & Roivainen, A. (2024). Macrophage mannose

receptor CD206 targeting of fluoride-18 labeled mannosylated dextran: A validation study in mice. *European journal of nuclear medicine and molecular imaging*, *51*(8), 2216–2228.

Andriana, P., Makrypidi, K., Liljenbäck, H., Rajander, J., Saraste, A., Pirmettis, I., Roivainen, A., & Li, X. G. (2023). Aluminum Fluoride-18 Labeled Mannosylated Dextran: Radiosynthesis and Initial Preclinical Positron Emission Tomography Studies. *Molecular imaging and biology*, *25*(6), 1094–1103.

Angeli, V., Ginhoux, F., Llodrà, J., Quemeneur, L., Frenette, P. S., Skobe, M., Jessberger, R., Merad, M., & Randolph, G. J. (2006). B cell-driven lymphangiogenesis in inflamed lymph nodes enhances dendritic cell mobilization. *Immunity*, *24*(2), 203–215.

Apostolopoulos, V., Pietersz, G. A., Gordon, S., Martinez-Pomares, L., & McKenzie, I. F. (2000). Aldehyde-mannan antigen complexes target the MHC class I antigen-presentation pathway. *European journal of immunology*, *30*(6), 1714–1723.

Apostolopoulos, V., Pietersz, G. A., Loveland, B. E., Sandrin, M. S., & McKenzie, I. F. (1995). Oxidative/reductive conjugation of mannan to antigen selects for T1 or T2 immune responses. *Proceedings of the National Academy of Sciences of the United States of America*, *92*(22), 10128–10132.

Archibald, S. J., & Allott, L. (2021). The aluminium-[^{18}F]fluoride revolution: simple radiochemistry with a big impact for radiolabelled biomolecules. *EJNMMI radiopharmacy and chemistry*, *6*(1), 30.

Arora, S., Dev, K., Agarwal, B., Das, P., & Syed, M. A. (2018). Macrophages: Their role, activation and polarization in pulmonary diseases. *Immunobiology*, *223*(4-5), 383–396.

Asija, R., Prajapat, R., Vyas, P., & Kumar, V. (2014). A brief cause of acute inflammation: an overview. *Journal of Drug Discovery and Therapeutics*, *2*(22), 31-35.

Askari, A. T., Unzek, S., Popovic, Z. B., Goldman, C. K., Forudi, F., Kiedrowski, M., ... & Penn, M. S. (2003). Effect of stromal-cell-derived factor 1 on stem-cell homing and tissue regeneration in ischaemic cardiomyopathy. *The Lancet*, *362*(9385), 697-703.

Astarie-Dequeker, C., N'Diaye, E. N., Le Cabec, V., Rittig, M. G., Prandi, J., & Maridonneau-Parini, I. (1999). The mannose receptor mediates uptake of pathogenic and nonpathogenic mycobacteria and bypasses bactericidal responses in human macrophages. *Infection and immunity*, *67*(2), 469–477.

Atri, C., Guerfali, F. Z., & Laouini, D. (2018). Role of human macrophage polarization in inflammation during infectious diseases. *International journal of molecular sciences*, *19*(6), 1801.

Autio, A., Jalkanen, S., & Roivainen, A. (2013). Nuclear imaging of inflammation: homing-associated molecules as targets. *EJNMMI research*, *3*(1), 1.

Azad, A. K., Rajaram, M. V., & Schlesinger, L. S. (2014). Exploitation of the Macrophage Mannose Receptor (CD206) in Infectious Disease Diagnostics and Therapeutics. *Journal of cytology & molecular biology*, *1*(1), 1000003.

Bajénoff, M., Granjeaud, S., & Guerder, S. (2003). The strategy of T cell antigen-presenting cell encounter in antigen-draining lymph nodes revealed by imaging of initial T cell activation. *The Journal of experimental medicine*, *198*(5), 715–724.

Barton G. M. (2008). A calculated response: control of inflammation by the innate immune system. *The Journal of clinical investigation*, *118*(2), 413–420.

Bauer, D., Cornejo, M. A., Hoang, T. T., Lewis, J. S., & Zeglis, B. M. (2023). Click Chemistry and Radiochemistry: An Update. *Bioconjugate chemistry*, *34*(11), 1925–1950.

Bedoui, S., Gebhardt, T., Gasteiger, G., & Kastenmüller, W. (2016). Parallels and differences between innate and adaptive lymphocytes. *Nature immunology*, *17*(5), 490–494.

Behrendt, N., Jensen, O. N., Engelholm, L. H., Mørtz, E., Mann, M., & Danø, K. (2000). A urokinase receptor-associated protein with specific collagen binding properties. *The Journal of biological chemistry*, *275*(3), 1993–2002.

Bennett, J. M., Reeves, G., Billman, G. E., & Sturmberg, J. P. (2018). Inflammation-Nature's Way to Efficiently Respond to All Types of Challenges: Implications for Understanding and Managing "the Epidemic" of Chronic Diseases. *Frontiers in medicine*, *5*, 316.

Bentsen, S., Jensen, J. K., Christensen, E., Petersen, L. R., Grandjean, C. E., Follin, B., Madsen, J. S., Christensen, C., Clemmensen, A., Binderup, T., Hasbak, P., Ripa, R. S., & Kjaer, A. (2023). [^{68}Ga]Ga-NODAGA-E[(cRGDyK)]$_2$ angiogenesis PET following myocardial infarction in an experimental rat model predicts cardiac functional parameters and development of heart failure. *Journal of nuclear cardiology : official publication of the American Society of Nuclear Cardiology*, *30*(5), 2073–2084.

Berger A. (2003). How does it work? Positron emission tomography. *BMJ (Clinical research ed.)*, 326(7404), 1449.

Bergman, J. (2001). *Aspects on the specific radioactivity in the synthesis of ^{18}F-labelled radiopharmaceuticals*. Åbo Akademi.

Bergman, J., & Solin, O. (1997). Fluorine-18-labeled fluorine gas for synthesis of tracer molecules. *Nuclear medicine and biology*, *24*(7), 677–683.

Bergman, J., Bergman, J., Solin, O., & Solin, O. (1997). Fluorine-18-labeled fluorine gas for synthesis of tracer molecules. *Nuclear medicine and biology, 24 7*, 677-83 .

Beutler B. A. (2009). TLRs and innate immunity. *Blood*, *113*(7), 1399–1407.

Blanchardon, E., Challeton-de Vathaire, C., Boisson, P., Célier, D., Martin, J. C., Cassot, S., Herbelet, G., Franck, D., Jourdain, J. R., & Biau, A. (2005). Long term retention and excretion of 201Tl in a patient after myocardial perfusion imaging. *Radiation protection dosimetry*, *113*(1), 47–53.

Blykers, A., Schoonooghe, S., Xavier, C., D'hoe, K., Laoui, D., D'Huyvetter, M., Vaneycken, I., Cleeren, F., Bormans, G., Heemskerk, J., Raes, G., De Baetselier, P., Lahoutte, T., Devoogdt, N., Van Ginderachter, J. A., & Caveliers, V. (2015). PET Imaging of Macrophage Mannose Receptor-Expressing Macrophages in Tumor Stroma Using ^{18}F-Radiolabeled Camelid Single-Domain Antibody Fragments. *Journal of nuclear medicine : official publication, Society of Nuclear Medicine*, *56*(8), 1265–1271.

Boerman, O. C., Rennen, H., Oyen, W. J., & Corstens, F. H. (2001). Radiopharmaceuticals to image infection and inflammation. *Seminars in nuclear medicine*, *31*(4), 286–295.

Bonilla, F. A., & Oettgen, H. C. (2010). Adaptive immunity. *The Journal of allergy and clinical immunology*, *125*(2 Suppl 2), S33–S40.

Boskovic, J., Arnold, J. N., Stilion, R., Gordon, S., Sim, R. B., Rivera-Calzada, A., Wienke, D., Isacke, C. M., Martinez-Pomares, L., & Llorca, O. (2006). Structural model for the mannose receptor family uncovered by electron microscopy of Endo180 and the mannose receptor. *The Journal of biological chemistry*, *281*(13), 8780–8787.

Boutilier, A. J., & Elsawa, S. F. (2021). Macrophage Polarization States in the Tumor Microenvironment. *International journal of molecular sciences*, *22*(13), 6995.

Bratteby, K., Shalgunov, V., & Herth, M. M. (2021). Aliphatic ^{18}F-Radiofluorination: Recent Advances in the Labeling of Base-Sensitive Substrates*. *ChemMedChem*, *16*(17), 2612–2622.

Brechbiel M. W. (2008). Bifunctional chelates for metal nuclides. *The quarterly journal of nuclear medicine and molecular imaging : official publication of the Italian Association of Nuclear Medicine (AIMN) [and] the International Association of Radiopharmacology (IAR), [and] Section of the Society of...*, *52*(2), 166–173.

Brömmel, K., Konken, C. P., Börgel, F., Obeng-Darko, H., Schelhaas, S., Bulk, E., Budde, T., Schwab, A., Schäfers, M., & Wünsch, B. (2021). Synthesis and biological evaluation of PET tracers designed for imaging of calcium activated potassium channel 3.1 (K_{Ca}3.1) channels *in vivo*. *RSC advances*, *11*(48), 30295–30304.

Brooks D. J. (2005). Positron emission tomography and single-photon emission computed tomography in central nervous system drug development. *NeuroRx : the journal of the American Society for Experimental NeuroTherapeutics*, *2*(2), 226–236.

Brown, R. S., & Wahl, R. L. (1993). Overexpression of Glut-1 glucose transporter in human breast cancer. An immunohistochemical study. *Cancer*, *72*(10), 2979–2985.

Buck, A. K., & Reske, S. N. (2004). Cellular origin and molecular mechanisms of ^{18}F-FDG uptake: is there a contribution of the endothelium?. *Journal of nuclear medicine : official publication, Society of Nuclear Medicine*, *45*(3), 461–463.

Burgdorf, S., Schölz, C., Kautz, A., Tampé, R., & Kurts, C. (2008). Spatial and mechanistic separation of cross-presentation and endogenous antigen presentation. *Nature immunology*, *9*(5), 558–566.

Butler, M., Morel, A. S., Jordan, W. J., Eren, E., Hue, S., Shrimpton, R. E., & Ritter, M. A. (2007). Altered expression and endocytic function of CD205 in human dendritic cells, and detection of a CD205-DCL-1 fusion protein upon dendritic cell maturation. *Immunology*, *120*(3), 362–371.

Butterfield, T. A., Best, T. M., & Merrick, M. A. (2006). The dual roles of neutrophils and macrophages in inflammation: a critical balance between tissue damage and repair. *Journal of athletic training*, *41*(4), 457–465.

Byrne, R. A., Rossello, X., Coughlan, J. J., Barbato, E., Berry, C., Chieffo, A., Claeys, M. J., Dan, G. A., Dweck, M. R., Galbraith, M., Gilard, M., Hinterbuchner, L., Jankowska, E. A., Jüni, P., Kimura, T., Kunadian, V., Leosdottir, M., Lorusso, R., Pedretti, R. F. E., Rigopoulos, A. G., … ESC Scientific Document Group (2023). 2023 ESC Guidelines for the management of acute coronary syndromes. *European heart journal*, *44*(38), 3720–3826.Cai, L., Lu, S., & Pike, V. W. (2008). Chemistry with [^{18}F]fluoride ion. *European Journal of Organic Chemistry*, *2008*(17), 2853-2873.

Cai, L., Lu, S., & Pike, V.W. (2008). Chemistry with [^{18}F]Fluoride ion. *European journal of organic chemistry*, 2853 —2873.

Cardinale, J., Martin, R., Remde, Y., Schäfer, M., Hienzsch, A., Hübner, S., Zerges, A. M., Marx, H., Hesse, R., Weber, K., Smits, R., Hoepping, A., Müller, M., Neels, O. C., & Kopka, K. (2017). Procedures for the GMP-Compliant Production and Quality Control of [^{18}F]PSMA-1007: A Next Generation Radiofluorinated Tracer for the Detection of Prostate Cancer. *Pharmaceuticals (Basel, Switzerland)*, *10*(4), 77.

Casella, V., Ido, T., Wolf, A. P., Fowler, J. S., MacGregor, R. R., & Ruth, T. J. (1980). Anhydrous ^{18}F-labeled eslemental flurine for radiopharmaceutical preparation. Journal of nuclear medicine : official publication, Society of Nuclear Medicine, 21(8), 750–757.

Cavaillon J. M. (2021). Once upon a time, inflammation. *The journal of venomous animals and toxins including tropical diseases*, *27*, e20200147.

Chai, J. Y., Cha, H., Lee, S. S., Oh, Y. H., Lee, S., & Chi, D. Y. (2021). Mechanistic study of nucleophilic fluorination for the synthesis of fluorine-18 labeled fluoroform with high molar activity from *N*-difluoromethyltriazolium triflate. *RSC advances*, *11*(11), 6099–6106.

Chakravarty, R., Shetty, P., Nair, K. V. V., Rajeswari, A., Jagadeesan, K. C., Sarma, H. D., Rangarajan, V., Krishnatry, R., & Chakraborty, S. (2020). Reactor produced [^{64}Cu]$CuCl_2$ as a PET radiopharmaceutical for cancer imaging: from radiochemistry laboratory to nuclear medicine clinic. *Annals of nuclear medicine*, *34*(12), 899–910.

Chang, Y. S., Jeong, J. M., Lee, Y. S., Kim, H. W., Ganesha, R. B., Kim, Y. J., Lee, D. S., Chung, J. K., & Lee, M. C. (2006). Synthesis and evaluation of benzothiophene derivatives as ligands for imaging beta-amyloid plaques in Alzheimer's disease. *Nuclear medicine and biology*, *33*(6), 811–820.

Chao, P. H., Lazari, M., Hanet, S., Narayanam, M. K., Murphy, J. M., & van Dam, R. M. (2018). Automated concentration of [^{18}F]fluoride into microliter volumes. *Applied radiation and isotopes : including data, instrumentation and methods for use in agriculture, industry and medicine*, *141*, 138–148.

Chaplin D. D. (2003). 1. Overview of the immune response. *The Journal of allergy and clinical immunology*, *111*(2 Suppl), S442–S459.

Chen L., Deng H., Cui H., Fang J., Zuo Z., Deng J., Li Y., Wang X., Zhao L. (2018). Inflammatory responses and inflammation-associated diseases in organs. Oncotarget. *9*: 7204-7218.

Chen, S., Saeed, A. F. U. H., Liu, Q., Jiang, Q., Xu, H., Xiao, G. G., Rao, L., & Duo, Y. (2023). Macrophages in immunoregulation and therapeutics. *Signal transduction and targeted therapy*, *8*(1), 207.

Chen, X., Liu, Y., Gao, Y., Shou, S., & Chai, Y. (2021). The roles of macrophage polarization in the host immune response to sepsis. *International immunopharmacology*, *96*, 107791.

Chen, Y., Liu, S., & Leng, S. X. (2019). Chronic Low-grade Inflammatory Phenotype (CLIP) and Senescent Immune Dysregulation. *Clinical therapeutics*, *41*(3), 400–409.

Cherry, S. R., Sorenson, J. A., & Phelps, M. E. (2012). *Physics in nuclear medicine* (4th ed.). Elsevier.

Chi, H., Pepper, M., & Thomas, P. G. (2024). Principles and therapeutic applications of adaptive immunity. *Cell*, *187*(9), 2052–2078.

Choi, J. Y., Jeong, J. M., Yoo, B. C., Kim, K., Kim, Y., Yang, B. Y., Lee, Y. S., Lee, D. S., Chung, J. K., & Lee, M. C. (2011). Development of ^{68}Ga-labeled mannosylated human serum albumin (MSA) as a lymph node imaging agent for positron emission tomography. *Nuclear medicine and biology*, *38*(3), 371–379.

Cicchese, J. M., Evans, S., Hult, C., Joslyn, L. R., Wessler, T., Millar, J. A., Marino, S., Cilfone, N. A., Mattila, J. T., Linderman, J. J., & Kirschner, D. E. (2018). Dynamic balance of pro- and anti-inflammatory signals controls disease and limits pathology. *Immunological reviews*, *285*(1), 147–167.

Cifarelli, V., Kuda, O., Yang, K., Liu, X., Gross, R. W., Pietka, T. A., Heo, G. S., Sultan, D., Luehmann, H., Lesser, J., Ross, M., Goldberg, I. J., Gropler, R. J., Liu, Y., & Abumrad, N. A. (2022). Cardiac immune cell infiltration associates with abnormal lipid metabolism. *Frontiers in cardiovascular medicine*, *9*, 948332.

Cleeren, F., Lecina, J., Ahamed, M., Raes, G., Devoogdt, N., Caveliers, V., McQuade, P., Rubins, D. J., Li, W., Verbruggen, A., Xavier, C., & Bormans, G. (2017). Al^{18}F-Labeling Of Heat-Sensitive Biomolecules for Positron Emission Tomography Imaging. *Theranostics*, *7*(11), 2924–2939.

Cleeren, F., Lecina, J., Billaud, E. M., Ahamed, M., Verbruggen, A., & Bormans, G. M. (2016). New Chelators for Low Temperature Al[^{8}F]-Labeling of Biomolecules. *Bioconjugate chemistry*, *27*(3), 790–798.

Coenen H. H. (2007). Fluorine-18 labeling methods: Features and possibilities of basic reactions. *Ernst Schering Research Foundation workshop*, (62), 15–50.

Cole, E. L., Stewart, M. N., Littich, R., Hoareau, R., & Scott, P. J. (2014). Radiosyntheses using fluorine-18: the art and science of late stage fluorination. *Current topics in medicinal chemistry*, *14*(7), 875–900.

Conway J. (2012). Lung imaging - two dimensional gamma scintigraphy, SPECT, CT and PET. *Advanced drug delivery reviews*, *64*(4), 357–368.

Contessotto, P., Ellis, B. W., Jin, C., Karlsson, N. G., Zorlutuna, P., Kilcoyne, M., & Pandit, A. (2020). Distinct glycosylation in membrane proteins within neonatal versus adult myocardial tissue. *Matrix biology : journal of the International Society for Matrix Biology*, *85-86*, 173–188.

Corthay A. (2009). How do regulatory T cells work?. *Scandinavian journal of immunology*, *70*(4), 326–336.

Costa, F. G., & Horswill, A. R. (2022). Overcoming pH defenses on the skin to establish infections. *PLoS pathogens*, *18*(5), e1010512.

Crișan, G., Moldovean-Cioroianu, N. S., Timaru, D. G., Andrieș, G., Căinap, C., & Chiș, V. (2022). Radiopharmaceuticals for PET and SPECT Imaging: A Literature Review over the Last Decade. *International journal of molecular sciences*, *23*(9), 5023.

Cronkite, D. A., & Strutt, T. M. (2018). The Regulation of Inflammation by Innate and Adaptive Lymphocytes. *Journal of immunology research, 2018*, 1467538.

Curino, A. C., Engelholm, L. H., Yamada, S. S., Holmbeck, K., Lund, L. R., Molinolo, A. A., Behrendt, N., Nielsen, B. S., & Bugge, T. H. (2005). Intracellular collagen degradation mediated by uPARAP/Endo180 is a major pathway of extracellular matrix turnover during malignancy. *The Journal of cell biology*, *169*(6), 977–985.

Cutolo, M., Campitiello, R., Gotelli, E., & Soldano, S. (2022). The Role of M1/M2 Macrophage Polarization in Rheumatoid Arthritis Synovitis. *Frontiers in immunology*, *13*, 867260.

Cutolo, M., Soldano, S., & Smith, V. (2019). Pathophysiology of systemic sclerosis: current understanding and new insights. *Expert review of clinical immunology*, *15*(7), 753–764.

Da Pieve, C., Allott, L., Martins, C. D., Vardon, A., Ciobota, D. M., Kramer-Marek, G., & Smith, G. (2016). Efficient [^{18}F]AlF Radiolabeling of ZHER3:8698 Affibody Molecule for Imaging of HER3 Positive Tumors. *Bioconjugate chemistry*, *27*(8), 1839–1849.

Da Pieve, C., Makarem, A., Turnock, S., Maczynska, J., Smith, G., & Kramer-Marek, G. (2020). Thiol-Reactive PODS-Bearing Bifunctional Chelators for the Development of EGFR-Targeting [^{18}F]AlF-Affibody Conjugates. *Molecules (Basel, Switzerland)*, *25*(7), 1562.

Dalm, V. A., van Hagen, P. M., van Koetsveld, P. M., Achilefu, S., Houtsmuller, A. B., Pols, D. H., van der Lely, A. J., Lamberts, S. W., & Hofland, L. J. (2003). Expression of somatostatin, cortistatin, and somatostatin receptors in human monocytes, macrophages, and dendritic cells. *American journal of physiology. Endocrinology and metabolism*, *285*(2), E344–E353.

Davis, K. M., Ryan, J. L., Aaron, V. D., & Sims, J. B. (2020). PET and SPECT Imaging of the Brain: History, Technical Considerations, Applications, and Radiotracers. *Seminars in ultrasound, CT, and MR*, *41*(6), 521–529.

Davis, T.S., Binder, M.S., & Amin, A.M.H. (2025). *A Common Diagnostic Dilemma: Inflammation or Infarction*. *Journal of the American College of Cardiology: Case Reports*, *30*(2), 102722.

Dhalla, N. S., Elmoselhi, A. B., Hata, T., & Makino, N. (2000). Status of myocardial antioxidants in ischemia-reperfusion injury. *Cardiovascular research*, *47*(3), 446–456.

Diekmann, J., Koenig, T., Zwadlo, C., Derlin, T., Neuser, J., Thackeray, J. T., Schäfer, A., Ross, T. L., Bauersachs, J., & Bengel, F. M. (2021). Molecular Imaging Identifies Fibroblast Activation Beyond the Infarct Region After Acute Myocardial Infarction. *Journal of the American College of Cardiology*, *77*(14), 1835–1837.

Dornan, M. H., Simard, J. M., Leblond, A., Juneau, D., Delouya, G., Saad, F., Ménard, C., & DaSilva, J. N. (2018). Simplified and robust one-step radiosynthesis of [^{18}F]DCFPyL via direct radiofluorination and cartridge-based purification. *Journal of labelled compounds & radiopharmaceuticals*, 10.1002/jlcr.3632. Advance online publication.

Dong, Y., Wang, Z., Hu, X., Sun, Y., Qin, J., Qin, Q., Liu, S., Yuan, S., Yu, J., & Wei, Y. (2024). [^{18}F]AlF-NOTA-FAPI-04 PET/CT for Predicting Pathologic Response of Resectable Esophageal Squamous Cell Carcinoma to Neoadjuvant Camrelizumab and Chemotherapy: A Phase II Clinical Trial. *Journal of nuclear medicine : official publication, Society of Nuclear Medicine*, *65*(11), 1702–1709.

Duatti A. (2021). Review on ^{99m}Tc radiopharmaceuticals with emphasis on new advancements. *Nuclear medicine and biology*, *92*, 202–216.

East, L., & Isacke, C. M. (2002). The mannose receptor family. *Biochimica et biophysica acta*, *1572*(2-3), 364–386.

Eckelman W. C. (1995). Radiolabeling with technetium-99m to study high-capacity and low-capacity biochemical systems. *European journal of nuclear medicine*, *22*(3), 249–263.

Ekinci, M., Santos-oliveira, R., & İlem-özdemir, D. (2022). QUALITY ASSURANCE AND QUALITY CONTROL OF RADIOPHARMACEUTICALS: AN OVERVIEW. Journal of Faculty of Pharmacy of Ankara University, 46(3), 1044-1063.

Endo, Y., Iwamura, C., Kuwahara, M., Suzuki, A., Sugaya, K., Tumes, D. J., Tokoyoda, K., Hosokawa, H., Yamashita, M., & Nakayama, T. (2011). Eomesodermin controls interleukin-5 production in memory T helper 2 cells through inhibition of activity of the transcription factor GATA3. *Immunity*, *35*(5), 733–745.

Eo, J. S., Paeng, J. C., Lee, S., Lee, Y. S., Jeong, J. M., Kang, K. W., Chung, J. K., & Lee, D. S. (2013). Angiogenesis imaging in myocardial infarction using ^{68}Ga-NOTA-RGD PET: characterization and application to therapeutic efficacy monitoring in rats. *Coronary artery disease*, *24*(4), 303–311.

Eskola, O., Grönroos, T. J., Naum, A., Marjamäki, P., Forsback, S., Bergman, J., Länkimäki, S., Kiss, J., Savunen, T., Knuuti, J., Haaparanta, M., & Solin, O. (2012). Novel electrophilic synthesis of 6-[^{18}F]fluorodopamine and comprehensive biological evaluation. *European journal of nuclear medicine and molecular imaging*, *39*(5), 800–810.

Espinosa Gonzalez, M., Volk-Draper, L., Bhattarai, N., Wilber, A., & Ran, S. (2022). Th2 Cytokines IL-4, IL-13, and IL-10 Promote Differentiation of Pro-Lymphatic Progenitors Derived from Bone Marrow Myeloid Precursors. *Stem cells and development*, *31*(11-12), 322–333.

European Pharmacopoeia Commission. (2007). *European Pharmacopoeia. 6th ed.* Strasbourg, France: Council of Europe, 1167–1173.

Fang, P., Li, X., Dai, J., Cole, L., Camacho, J. A., Zhang, Y., Ji, Y., Wang, J., Yang, X. F., & Wang, H. (2018). Immune cell subset differentiation and tissue inflammation. *Journal of hematology & oncology*, *11*(1), 97.

Farber, D. L., Netea, M. G., Radbruch, A., Rajewsky, K., & Zinkernagel, R. M. (2016). Immunological memory: lessons from the past and a look to the future. *Nature reviews. Immunology*, *16*(2), 124–128.

Felgueiras H. P. (2023). Biomolecule-Based Biomaterials and Their Application in Drug Delivery Systems. *International journal of molecular sciences*, *24*(7), 6425.

Fernandes, B., Antunes, I. F., Prasad, K., Vazquez-Matias, D. A., De Mattos, E. P., Szymanski, W., Jeckel, C. M. M., de Vries, E. F. J., & Elsinga, P. H. (2024). Synthesis and preclinical evaluation of [^{18}F]AlF-NODA-MP-C6-CTHRSSVVC as a PET tracer for CD163-positive tumor-infiltrating macrophages. *Nuclear medicine and biology*, *138-139*, 108946.

Fersing, C., Bouhlel, A., Cantelli, C., Garrigue, P., Lisowski, V., & Guillet, B. (2019). A Comprehensive Review of Non-Covalent Radiofluorination Approaches Using Aluminum [^{18}F]fluoride: Will [^{18}F]AlF Replace ^{68}Ga for Metal Chelate Labeling?. *Molecules (Basel, Switzerland)*, *24*(16), 2866.

Fioranelli, M., Roccia, M. G., Flavin, D., & Cota, L. (2021). Regulation of Inflammatory Reaction in Health and Disease. *International journal of molecular sciences*, *22*(10), 5277.

Fletcher, J. W., Djulbegovic, B., Soares, H. P., Siegel, B. A., Lowe, V. J., Lyman, G. H., Coleman, R. E., Wahl, R., Paschold, J. C., Avril, N., Einhorn, L. H., Suh, W. W., Samson, D., Delbeke, D., Gorman, M., & Shields, A. F. (2008). Recommendations on the use of [^{18}F]FDG PET in oncology. *Journal of nuclear medicine : official publication, Society of Nuclear Medicine, 49*(3), 480–508.

Florentin, J., Zhao, J., Tai, Y. Y., Vasamsetti, S. B., O'Neil, S. P., Kumar, R., Arunkumar, A., Watson, A., Sembrat, J., Bullock, G. C., Sanders, L., Kassa, B., Rojas, M., Graham, B. B., Chan, S. Y., & Dutta, P. (2021). Interleukin-6 mediates neutrophil mobilization from bone marrow in pulmonary hypertension. *Cellular & molecular immunology*, *18*(2), 374–384.

Fontes, J. A., Barin, J. G., Talor, M. V., Stickel, N., Schaub, J., Rose, N. R., & Čiháková, D. (2017). Complete Freund's adjuvant induces experimental autoimmune myocarditis by enhancing IL-6 production during initiation of the immune response. *Immunity, inflammation and disease*, *5*(2), 163–176.

Forsback, S. & Solin, O. (2015). Post-target produced [^{18}F]F_2 in the production of PET radiopharmaceuticals. *Radiochimica Acta*, *103*(3), 219-226.

Frangogiannis N. G. (2014). The inflammatory response in myocardial injury, repair, and remodelling. *Nature reviews. Cardiology*, *11*(5), 255–265.

Frangogiannis N. G. (2015). Pathophysiology of Myocardial Infarction. *Comprehensive Physiology*, *5*(4), 1841–1875.

Frangogiannis, N. G., Smith, C. W., & Entman, M. L. (2002). The inflammatory response in myocardial infarction. *Cardiovascular research*, *53*(1), 31–47.

Frank, A., Bonney, M., Bonney, S., Weitzel, L., Koeppen, M., & Eckle, T. (2012). Myocardial ischemia reperfusion injury: from basic science to clinical bedside. *Seminars in cardiothoracic and vascular anesthesia*, *16*(3), 123–132.

Fukushima, K., Bravo, P. E., Higuchi, T., Schuleri, K. H., Lin, X., Abraham, M. R., Xia, J., Mathews, W. B., Dannals, R. F., Lardo, A. C., Szabo, Z., & Bengel, F. M. (2012). Molecular hybrid positron emission tomography/computed tomography imaging of cardiac angiotensin II type 1 receptors. *Journal of the American College of Cardiology*, *60*(24), 2527–2534.

Furman, D., Campisi, J., Verdin, E., Carrera-Bastos, P., Targ, S., Franceschi, C., Ferrucci, L., Gilroy, D. W., Fasano, A., Miller, G. W., Miller, A. H., Mantovani, A., Weyand, C. M., Barzilai, N., Goronzy, J. J., Rando, T. A., Effros, R. B., Lucia, A., Kleinstreuer, N., & Slavich, G. M. (2019). Chronic inflammation in the etiology of disease across the life span. *Nature medicine*, *25*(12), 1822–1832.

Furtado, M. B., Nim, H. T., Boyd, S. E., & Rosenthal, N. A. (2016). View from the heart: cardiac fibroblasts in development, scarring and regeneration. *Development (Cambridge, England)*, *143*(3), 387–397.

Furusho, Y., Miyata, M., Matsuyama, T., Nagai, T., Li, H., Akasaki, Y., Hamada, N., Miyauchi, T., Ikeda, Y., Shirasawa, T., Ide, K., & Tei, C. (2012). Novel Therapy for Atherosclerosis Using Recombinant Immunotoxin Against Folate Receptor β-Expressing Macrophages. *Journal of the American Heart Association*, *1*(4), e003079.

Gao, H., Lang, L., Guo, N., Cao, F., Quan, Q., Hu, S., Kiesewetter, D. O., Niu, G., & Chen, X. (2012). PET imaging of angiogenesis after myocardial infarction/reperfusion using a one-step labeled integrin-targeted tracer ^{18}F-AlF-NOTA-PRGD2. *European journal of nuclear medicine and molecular imaging*, *39*(4), 683–692.

García, R. A., Lupisella, J. A., Ito, B. R., Hsu, M. Y., Fernando, G., Carson, N. L., Allocco, J. J., Ryan, C. S., Zhang, R., Wang, Z., Heroux, M., Carrier, M., St-Onge, S., Bouvier, M., Dudhgaonkar, S., Nagar, J., Bustamante-Pozo, M. M., Garate-Carrillo, A., Chen, J., Ma, X., … Villarreal, F. (2021). Selective FPR2 Agonism Promotes a Proresolution Macrophage Phenotype and Improves Cardiac Structure-Function Post Myocardial Infarction. *JACC. Basic to translational science*, *6*(8), 676–689.

Gaudino, S. J., & Kumar, P. (2019). Cross-Talk Between Antigen Presenting Cells and T Cells Impacts Intestinal Homeostasis, Bacterial Infections, and Tumorigenesis. *Frontiers in immunology*, *10*, 360.

Gazi, U., & Martinez-Pomares, L. (2009). Influence of the mannose receptor in host immune responses. *Immunobiology*, *214*(7), 554–561.

Germolec, D. R., Shipkowski, K. A., Frawley, R. P., & Evans, E. (2018). Markers of Inflammation. *Methods in molecular biology (Clifton, N.J.)*, *1803*, 57–79.

Giesel, F. L., Adeberg, S., Syed, M., Lindner, T., Jiménez-Franco, L. D., Mavriopoulou, E., Staudinger, F., Tonndorf-Martini, E., Regnery, S., Rieken, S., El Shafie, R., Röhrich, M., Flechsig, P., Kluge, A., Altmann, A., Debus, J., Haberkorn, U., & Kratochwil, C. (2021). FAPI-74 PET/CT Using Either ^{18}F-AlF or Cold-Kit ^{68}Ga Labeling: Biodistribution, Radiation Dosimetry, and Tumor Delineation in Lung Cancer Patients. *Journal of nuclear medicine : official publication, Society of Nuclear Medicine*, *62*(2), 201–207.

Giglio, J., Fernández, S., Jentschel, C., Pietzsch, H. J., Papadopoulos, M., Pelecanou, M., Pirmettis, I., Paolino, A., & Rey, A. (2013). Design and development of (99m)tc-'4+1'-labeled dextran-mannose derivatives as potential radiopharmaceuticals for sentinel lymph node detection. *Cancer biotherapy & radiopharmaceuticals*, *28*(7), 541–551.

Giglio, J., Zeni, M., Savio, E., & Engler, H. (2018). Synthesis of an Al^{18}F radiofluorinated GLU-UREA-LYS(AHX)-HBED-CC PSMA ligand in an automated synthesis platform. *EJNMMI radiopharmacy and chemistry*, *3*(1), 4.

Gitto, S. B., Beardsley, J. M., Nakkina, S. P., Oyer, J. L., Cline, K. A., Litherland, S. A., Copik, A. J., Khaled, A. S., Fanaian, N., Arnoletti, J. P., & Altomare, D. A. (2020). Identification of a novel IL-5 signaling pathway in chronic pancreatitis and crosstalk with pancreatic tumor cells. *Cell communication and signaling : CCS*, *18*(1), 95.

Gomes, C. M., Abrunhosa, A. J., Ramos, P., & Pauwels, E. K. (2011). Molecular imaging with SPECT as a tool for drug development. *Advanced drug delivery reviews*, *63*(7), 547–554.

Gondry, O., Xavier, C., Raes, L., Heemskerk, J., Devoogdt, N., Everaert, H., Breckpot, K., Lecocq, Q., Decoster, L., Fontaine, C., Schallier, D., Aspeslagh, S., Vaneycken, I., Raes, G., Van Ginderachter, J. A., Lahoutte, T., Caveliers, V., & Keyaerts, M. (2023). Phase I Study of [^{68}Ga]Ga-Anti-CD206-sdAb for PET/CT Assessment of Protumorigenic Macrophage Presence in Solid Tumors (MMR Phase I). *Journal of nuclear medicine : official publication, Society of Nuclear Medicine*, *64*(9), 1378–1384.

Goodsell, D. S. (2002). The molecular perspective: VEGF and angiogenesis. *The oncologist*, *7*(6), 569-570.

Gordon S. (2003). Alternative activation of macrophages. *Nature reviews. Immunology*, *3*(1), 23–35.

Gordon S. (2016). Phagocytosis: An Immunobiologic Process. *Immunity*, *44*(3), 463–475.

Gormsen, L. C., Haraldsen, A., Kramer, S., Dias, A. H., Kim, W. Y., & Borghammer, P. (2016). A dual tracer [^{68}Ga]Ga-DOTANOC PET/CT and [^{18}F]-FDG PET/CT pilot study for detection of cardiac sarcoidosis. *EJNMMI research*, *6*(1), 52.

Gotthardt, M., Bleeker-Rovers, C. P., Boerman, O. C., & Oyen, W. J. (2010). Imaging of inflammation by PET, conventional scintigraphy, and other imaging techniques. *Journal of nuclear medicine : official publication, Society of Nuclear Medicine*, *51*(12), 1937–1949.

Graf, S., Gyöngyösi, M., Khorsand, A., Nekolla, S. G., Pirich, C., Kletter, K., Dudczak, R., Glogar, D., Porenta, G., & Sochor, H. (2004). Electromechanical properties of perfusion/metabolism mismatch: comparison of nonfluoroscopic electroanatomic mapping with ^{18}F-FDG PET. *Journal of nuclear medicine : official publication, Society of Nuclear Medicine*, *45*(10), 1611–1618.

Graham, M. M., Peterson, L. M., Muzi, M., Graham, B. B., Spence, A. M., Link, J. M., & Krohn, K. A. (1998). 1-[Carbon-11]-glucose radiation dosimetry and distribution in human imaging studies. *Journal of nuclear medicine : official publication, Society of Nuclear Medicine*, *39*(10), 1805–1810.

Grassi, I., Nanni, C., Allegri, V., Morigi, J. J., Montini, G. C., Castellucci, P., & Fanti, S. (2012). The clinical use of PET with ^{11}C-acetate. *American journal of nuclear medicine and molecular imaging*, *2*(1), 33–47.

Green C. H. (2012). Technetium-99m production issues in the United Kingdom. *Journal of medical physics*, *37*(2), 66–71.

Grines, C. L., & Marshall, J. J. (2020). Invasive imaging of myocardial infarction patients: Is less or more better?. *Catheterization and cardiovascular interventions : official journal of the Society for Cardiac Angiography & Interventions*, *95*(4), 704–705.

Gröner, B., Willmann, M., Donnerstag, L., Urusova, E. A., Neumaier, F., Humpert, S., Endepols, H., Neumaier, B., & Zlatopolskiy, B. D. (2023). 7-[^{18}F]Fluoro-8-azaisatoic Anhydrides: Versatile Prosthetic Groups for the Preparation of PET Tracers. *Journal of medicinal chemistry*, *66*(17), 12629–12644.

Grönman, M., Tarkia, M., Kiviniemi, T., Halonen, P., Kuivanen, A., Savunen, T., Tolvanen, T., Teuho, J., Käkelä, M., Metsälä, O., Pietilä, M., Saukko, P., Ylä-Herttuala, S., Knuuti, J., Roivainen, A., & Saraste, A. (2017). Imaging of $\alpha_v\beta_3$ integrin expression in experimental myocardial ischemia with [^{68}Ga]NODAGA-RGD positron emission tomography. *Journal of translational medicine*, *15*(1), 144.

Guan, T., Zhou, X., Zhou, W., & Lin, H. (2023). Regulatory T cell and macrophage crosstalk in acute lung injury: future perspectives. *Cell death discovery*, *9*(1), 9.

Gupta, S. K., Pillarisetti, K., & Lysko, P. G. (1999). Modulation of CXCR4 expression and SDF-1α functional activity during differentiation of human monocytes and macrophages. *Journal of leukocyte biology*, *66*(1), 135-143.

He, P., Haswell, S. J., Pamme, N., & Archibald, S. J. (2014). Advances in processes for PET radiotracer synthesis: separation of [^{18}F]fluoride from enriched [^{18}O]water. *Applied radiation and isotopes :*

including data, instrumentation and methods for use in agriculture, industry and medicine, *91*, 64–70.

Hellberg, S., Silvola, J. M. U., Kiugel, M., Liljenbäck, H., Savisto, N., Li, X. G., Thiele, A., Lehmann, L., Heinrich, T., Vollmer, S., Hakovirta, H., Laine, V. J. O., Ylä-Herttuala, S., Knuuti, J., Roivainen, A., & Saraste, A. (2017). 18-kDa translocator protein ligand ^{18}F-FEMPA: Biodistribution and uptake into atherosclerotic plaques in mice. *Journal of nuclear cardiology : official publication of the American Society of Nuclear Cardiology*, *24*(3), 862–871.

Heo, G. S., Kopecky, B., Sultan, D., Ou, M., Feng, G., Bajpai, G., Zhang, X., Luehmann, H., Detering, L., Su, Y., Leuschner, F., Combadière, C., Kreisel, D., Gropler, R. J., Brody, S. L., Liu, Y., & Lavine, K. J. (2019). Molecular Imaging Visualizes Recruitment of Inflammatory Monocytes and Macrophages to the Injured Heart. *Circulation research*, *124*(6), 881–890.

Herrero, P., Laforest, R., Shoghi, K., Zhou, D., Ewald, G., Pfeifer, J., Duncavage, E., Krupp, K., Mach, R., & Gropler, R. (2012). Feasibility and dosimetry studies for ^{18}F-NOS as a potential PET radiopharmaceutical for inducible nitric oxide synthase in humans. *Journal of nuclear medicine : official publication, Society of Nuclear Medicine*, *53*(6), 994–1001.

Higuchi, T., Bengel, F. M., Seidl, S., Watzlowik, P., Kessler, H., Hegenloh, R., Reder, S., Nekolla, S. G., Wester, H. J., & Schwaiger, M. (2008). Assessment of alphavbeta3 integrin expression after myocardial infarction by positron emission tomography. *Cardiovascular research*, *78*(2), 395–403.

Higuchi, T., Fukushima, K., Xia, J., Mathews, W. B., Lautamäki, R., Bravo, P. E., Javadi, M. S., Dannals, R. F., Szabo, Z., & Bengel, F. M. (2010). Radionuclide imaging of angiotensin II type 1 receptor upregulation after myocardial ischemia-reperfusion injury. *Journal of nuclear medicine : official publication, Society of Nuclear Medicine*, *51*(12), 1956–1961.

Hofmann, U., & Frantz, S. (2016). Role of T-cells in myocardial infarction. *European heart journal*, *37*(11), 873–879.

Hong, H., Zhang, Y., Orbay, H., Valdovinos, H. F., Nayak, T. R., Bean, J., Theuer, C. P., Barnhart, T. E., & Cai, W. (2013). Positron emission tomography imaging of tumor angiogenesis with a (61/64)Cu-labeled F(ab')(2) antibody fragment. *Molecular pharmaceutics*, *10*(2), 709–716.

Hoxha, E., Kneißler, U., Stege, G., Zahner, G., Thiele, I., Panzer, U., Harendza, S., Helmchen, U. M., & Stahl, R. A. (2012). Enhanced expression of the M-type phospholipase A2 receptor in glomeruli correlates with serum receptor antibodies in primary membranous nephropathy. *Kidney international*, *82*(7), 797–804.

Hunter, M. C., Teijeira, A., & Halin, C. (2016). T Cell Trafficking through Lymphatic Vessels. *Frontiers in immunology*, *7*, 613.

Hutton B. F. (2014). The origins of SPECT and SPECT/CT. *European journal of nuclear medicine and molecular imaging*, *41 Suppl 1*, S3–S16.

Israel, O., Pellet, O., Biassoni, L., De Palma, D., Estrada-Lobato, E., Gnanasegaran, G., Kuwert, T., la Fougère, C., Mariani, G., Massalha, S., Paez, D., & Giammarile, F. (2019). Two decades of SPECT/CT - the coming of age of a technology: An updated review of literature evidence. *European journal of nuclear medicine and molecular imaging*, *46*(10), 1990–2012.

Iwaszko, M., Biały, S., & Bogunia-Kubik, K. (2021). Significance of Interleukin (IL)-4 and IL-13 in Inflammatory Arthritis. *Cells*, *10*(11), 3000.

Jacobs, A. H., Tavitian, B., & INMiND Consortium. (2012). Noninvasive molecular imaging of neuroinflammation. *Journal of Cerebral Blood Flow & Metabolism*, *32*(7), 1393-1415.

Jacobson, O., & Chen, X. (2010). PET designated flouride-18 production and chemistry. *Current topics in medicinal chemistry*, *10*(11), 1048–1059.

Jacobson, O., Kiesewetter, D. O., & Chen, X. (2015). Fluorine-18 radiochemistry, labeling strategies and synthetic routes. *Bioconjugate chemistry*, *26*(1), 1–18.

Jaime-Sanchez, P., Uranga-Murillo, I., Aguilo, N., Khouili, S. C., Arias, M. A., Sancho, D., & Pardo, J. (2020). Cell death induced by cytotoxic $CD8^+$ T cells is immunogenic and primes caspase-3-

dependent spread immunity against endogenous tumor antigens. *Journal for immunotherapy of cancer*, *8*(1), e000528.

Jamar, F., van der Laken, C. J., Panagiotidis, E., Steinz, M. M., van der Geest, K. S. M., Graham, R. N. J., & Gheysens, O. (2023). Update on Imaging of Inflammatory Arthritis and Related Disorders. *Seminars in nuclear medicine*, *53*(2), 287–300.

Jayasingam, S. D., Citartan, M., Thang, T. H., Mat Zin, A. A., Ang, K. C., & Ch'ng, E. S. (2020). Evaluating the Polarization of Tumor-Associated Macrophages Into M1 and M2 Phenotypes in Human Cancer Tissue: Technicalities and Challenges in Routine Clinical Practice. *Frontiers in oncology*, *9*, 1512.

Jenkins, W. S., Vesey, A. T., Stirrat, C., Connell, M., Lucatelli, C., Neale, A., Moles, C., Vickers, A., Fletcher, A., Pawade, T., Wilson, I., Rudd, J. H., van Beek, E. J., Mirsadraee, S., Dweck, M. R., & Newby, D. E. (2017). Cardiac $\alpha v\beta_3$ integrin expression following acute myocardial infarction in humans. *Heart (British Cardiac Society)*, *103*(8), 607–615.

Jeong J. M. (2016). Application of a Small Molecule Radiopharmaceutical Concept to Improve Kinetics. *Nuclear medicine and molecular imaging*, *50*(2), 99–101.

Jiang, W., Swiggard, W. J., Heufler, C., Peng, M., Mirza, A., Steinman, R. M., & Nussenzweig, M. C. (1995). The receptor DEC-205 expressed by dendritic cells and thymic epithelial cells is involved in antigen processing. *Nature*, *375*(6527), 151–155.

Jiang, X., Wang, X., Shen, T., Yao, Y., Chen, M., Li, Z., Li, X., Shen, J., Kou, Y., Chen, S., Zhou, X., Luo, Z., & Cheng, Z. (2021). FAPI-04 PET/CT Using [^{18}F]AlF Labeling Strategy: Automatic Synthesis, Quality Control, and *In Vivo* Assessment in Patient. *Frontiers in oncology*, *11*, 649148.

Jiang, Y., Cai, R., Huang, Y., Zhu, L., Xiao, L., Wang, C., & Wang, L. (2024). Macrophages in organ fibrosis: from pathogenesis to therapeutic targets. *Cell death discovery*, *10*(1), 487.

Junttila I. S. (2018). Tuning the Cytokine Responses: An Update on Interleukin (IL)-4 and IL-13 Receptor Complexes. *Frontiers in immunology*, *9*, 888.

Kalló, G., Kumar, A., Tőzsér, J., & Csősz, É. (2022). Chemical Barrier Proteins in Human Body Fluids. *Biomedicines*, *10*(7), 1472.

Kaneko, K. I., Irie, S., Mawatari, A., Igesaka, A., Hu, D., Nakaoka, T., Hayashinaka, E., Wada, Y., Doi, H., Watanabe, Y., & Cui, Y. (2022). [^{18}F]DPA-714 PET imaging for the quantitative evaluation of early spatiotemporal changes of neuroinflammation in rat brain following status epilepticus. *European journal of nuclear medicine and molecular imaging*, *49*(7), 2265–2275.

Kang, P. B., Azad, A. K., Torrelles, J. B., Kaufman, T. M., Beharka, A., Tibesar, E., DesJardin, L. E., & Schlesinger, L. S. (2005). The human macrophage mannose receptor directs Mycobacterium tuberculosis lipoarabinomannan-mediated phagosome biogenesis. *The Journal of experimental medicine*, *202*(7), 987–999.

Kang, S., Zurutuza, I.R., & Zaman, R.T. (2023). Molecular Imaging in Medicine: Past, Present, and Future. *JSM Cardiothorac Surg, 5*(1), 1019.

Kany, S., Vollrath, J. T., & Relja, B. (2019). Cytokines in Inflammatory Disease. *International journal of molecular sciences*, *20*(23), 6008.

Kaur, B., & Singh, P. (2022). Inflammation: Biochemistry, cellular targets, anti-inflammatory agents and challenges with special emphasis on cyclooxygenase-2. Bioorganic chemistry, 121, 105663.

Kazakauskaite, E., Vajauskas, D., Bardauskiene, L., Ordiene, R., Zabiela, V., Zaliaduonyte, D., Gustiene, O., Lapinskas, T., & Jurkevicius, R. (2023). The incremental value of myocardial viability, evaluated by [^{18}F]fluorodeoxyglucose positron emission tomography, and cardiovascular magnetic resonance for mortality prediction in patients with previous myocardial infarction and symptomatic heart failure. *Perfusion*, *38*(6), 1288–1297.

Keller, T., López-Picón, F. R., Krzyczmonik, A., Forsback, S., Kirjavainen, A. K., Takkinen, J. S., Alzghool, O., Rajander, J., Teperi, S., Cacheux, F., Damont, A., Dollé, F., Rinne, J. O., Solin, O., & Haaparanta-Solin, M. (2018). [^{18}F]F-DPA for the detection of activated microglia in a mouse model of Alzheimer's disease. *Nuclear medicine and biology*, *67*, 1–9.

Keller, T., López-Picón, F. R., Krzyczmonik, A., Forsback, S., Takkinen, J. S., Rajander, J., Teperi, S., Dollé, F., Rinne, J. O., Haaparanta-Solin, M., & Solin, O. (2020). Comparison of high and low molar activity TSPO tracer [^{18}F]F-DPA in a mouse model of Alzheimer's disease. *Journal of cerebral blood flow and metabolism : official journal of the International Society of Cerebral Blood Flow and Metabolism*, *40*(5), 1012–1020.

Kersemans, K., De Man, K., Courtyn, J., Van Royen, T., Piron, S., Moerman, L., Brans, B., & De Vos, F. (2018). Automated radiosynthesis of Al[^{18}F]PSMA-11 for large scale routine use. *Applied radiation and isotopes : including data, instrumentation and methods for use in agriculture, industry and medicine*, *135*, 19–27.

Kessler, L., Kupusovic, J., Ferdinandus, J., Hirmas, N., Umutlu, L., Zarrad, F., Nader, M., Fendler, W. P., Totzeck, M., Wakili, R., Schlosser, T., Rassaf, T., Rischpler, C., & Siebermair, J. (2021). Visualization of Fibroblast Activation After Myocardial Infarction Using ^{68}Ga-FAPI PET. *Clinical nuclear medicine*, *46*(10), 807–813.

Khalil, M. M., Tremoleda, J. L., Bayomy, T. B., & Gsell, W. (2011). Molecular SPECT Imaging: An Overview. *International journal of molecular imaging*, *2011*, 796025.

Khan, A. A., & T M de Rosales, R. (2021). Radiolabelling of Extracellular Vesicles for PET and SPECT imaging. *Nanotheranostics*, *5*(3), 256–274.

Kiesewetter, D. O., Jacobson, O., Lang, L., & Chen, X. (2011). Automated radiochemical synthesis of [^{18}F]FBEM: a thiol reactive synthon for radiofluorination of peptides and proteins. *Applied radiation and isotopes : including data, instrumentation and methods for use in agriculture, industry and medicine*, *69*(2), 410–414.

Kim, D. W., Jeong, H. J., Lim, S. T., Sohn, M. H., Katzenellenbogen, J. A., & Chi, D. Y. (2008). Facile nucleophilic fluorination reactions using tert-alcohols as a reaction medium: significantly enhanced reactivity of alkali metal fluorides and improved selectivity. *The Journal of organic chemistry*, *73*(3), 957–962.

Kim, E. J., Kim, S., Seo, H. S., Lee, Y. J., Eo, J. S., Jeong, J. M., Lee, B., Kim, J. Y., Park, Y. M., & Jeong, M. (2016). Novel PET Imaging of Atherosclerosis with ^{68}Ga-Labeled NOTA-Neomannosylated Human Serum Albumin. *Journal of nuclear medicine : official publication, Society of Nuclear Medicine*, *57*(11), 1792–1797.

Kim, G. R., Paeng, J. C., Jung, J. H., Moon, B. S., Lopalco, A., Denora, N., Lee, B. C., & Kim, S. E. (2018). Assessment of TSPO in a Rat Experimental Autoimmune Myocarditis Model: A Comparison Study between [^{18}F]Fluoromethyl-PBR28 and [^{18}F]CB251. *International journal of molecular sciences*, *19*(1), 276.

Kiugel, M., Dijkgraaf, I., Kytö, V., Helin, S., Liljenbäck, H., Saanijoki, T., Yim, C. B., Oikonen, V., Saukko, P., Knuuti, J., Roivainen, A., & Saraste, A. (2014). Dimeric [^{68}Ga]DOTA-RGD peptide targeting αvβ 3 integrin reveals extracellular matrix alterations after myocardial infarction. *Molecular imaging and biology*, *16*(6), 793–801.

Kjøller, L., Engelholm, L. H., Høyer-Hansen, M., Danø, K., Bugge, T. H., & Behrendt, N. (2004). uPARAP/endo180 directs lysosomal delivery and degradation of collagen IV. *Experimental cell research*, *293*(1), 106–116.

Klein, R., Celiker-Guler, E., Rotstein, B. H., & deKemp, R. A. (2020). PET and SPECT Tracers for Myocardial Perfusion Imaging. *Seminars in nuclear medicine*, *50*(3), 208–218.

Kniess, T., Laube, M., Brust, P., & Steinbach, J. (2015). 2-[^{18}F] Fluoroethyl tosylate–a versatile tool for building ^{18}F-based radiotracers for positron emission tomography. *MedChemComm*, *6*(10), 1714-1754.

Knight, J. C., & Cornelissen, B. (2014). Bioorthogonal chemistry: implications for pretargeted nuclear (PET/SPECT) imaging and therapy. *American journal of nuclear medicine and molecular imaging*, *4*(2), 96–113.

Koniar, H., McNeil, S., Wharton, L., Ingham, A., Van de Voorde, M., Ooms, M., Sekar, S., Rodríguez-Rodríguez, C., Kunz, P., Radchenko, V., Rahmim, A., Uribe, C., Yang, H., & Schaffer, P. (2024).

Quantitative SPECT imaging of ^{155}Tb and ^{161}Tb for preclinical theranostic radiopharmaceutical development. *EJNMMI physics*, *11*(1), 77.

Kosinska, M., Misiewicz, P., Kalita, K., Fijuth, J., Foks, M., Kuncman, L., & Gottwald, L. (2023). The value of [^{18}F]FDG PET/CT examination in the detection and differentiation of recurrent ovarian cancer. *Nuclear medicine review. Central & Eastern Europe*, *26*(0), 98–105.

Kumagai, Y., & Akira, S. (2010). Identification and functions of pattern-recognition receptors. *The Journal of allergy and clinical immunology*, *125*(5), 985–992.

Kumar, R., Basu, S., Torigian, D., Anand, V., Zhuang, H., & Alavi, A. (2008). Role of modern imaging techniques for diagnosis of infection in the era of [^{18}F]fluorodeoxyglucose positron emission tomography. *Clinical microbiology reviews*, *21*(1), 209–224.

Kumar, V., Abbas, A. K., & Aster, J. C. (Eds.). (2012). *Robbins basic pathology e-book*. Elsevier Health Sciences.

Lahdenpohja, S. O., Rajala, N. A., Rajander, J., & Kirjavainen, A. K. (2019). Fast and efficient copper-mediated ^{18}F-fluorination of arylstannanes, aryl boronic acids, and aryl boronic esters without azeotropic drying. *EJNMMI radiopharmacy and chemistry*, *4*(1), 28.

Laitinen, I., Notni, J., Pohle, K., Rudelius, M., Farrell, E., Nekolla, S. G., Henriksen, G., Neubauer, S., Kessler, H., Wester, H. J., & Schwaiger, M. (2013). Comparison of cyclic RGD peptides for αvβ3 integrin detection in a rat model of myocardial infarction. *EJNMMI research*, *3*(1), 38.

Lambeau, G., Schmid-Alliana, A., Lazdunski, M., & Barhanin, J. (1990). Identification and purification of a very high affinity binding protein for toxic phospholipases A2 in skeletal muscle. *The Journal of biological chemistry*, *265*(16), 9526–9532.

Lambert, J. M., Lopez, E. F., & Lindsey, M. L. (2008). Macrophage roles following myocardial infarction. *International journal of cardiology*, *130*(2), 147–158.

Lang, C. I., Döring, P., Gäbel, R., Vasudevan, P., Lemcke, H., Müller, P., Stenzel, J., Lindner, T., Joksch, M., Kurth, J., Bergner, C., Wester, H. J., Ince, H., Steinhoff, G., Vollmar, B., David, R., & Krause, B. J. (2020). [^{68}Ga]-NODAGA-RGD Positron Emission Tomography (PET) for Assessment of Post Myocardial Infarction Angiogenesis as a Predictor for Left Ventricular Remodeling in Mice after Cardiac Stem Cell Therapy. *Cells*, *9*(6), 1358.

Lange, T., Gertz, R. J., Schulz, A., Backhaus, S. J., Evertz, R., Kowallick, J. T., Hasenfuß, G., Desch, S., Thiele, H., Stiermaier, T., Eitel, I., & Schuster, A. (2023). Impact of myocardial deformation on risk prediction in patients following acute myocardial infarction. *Frontiers in cardiovascular medicine*, *10*, 1199936.

Langer, L. B. N., Hess, A., Korkmaz, Z., Tillmanns, J., Reffert, L. M., Bankstahl, J. P., Bengel, F. M., Thackeray, J. T., & Ross, T. L. (2021). Molecular imaging of fibroblast activation protein after myocardial infarction using the novel radiotracer [^{68}Ga]MHLL1. *Theranostics*, *11*(16), 7755–7766.

Lanier, L. L., & Sun, J. C. (2009). Do the terms innate and adaptive immunity create conceptual barriers?. *Nature reviews. Immunology*, *9*(5), 302–303.

Lapa, C., Reiter, T., Li, X., Werner, R. A., Samnick, S., Jahns, R., Buck, A. K., Ertl, G., & Bauer, W. R. (2015). Imaging of myocardial inflammation with somatostatin receptor based PET/CT - A comparison to cardiac MRI. *International journal of cardiology*, *194*, 44–49.

Lapa, C., Reiter, T., Werner, R. A., Ertl, G., Wester, H. J., Buck, A. K., Bauer, W. R., & Herrmann, K. (2015). [^{68}Ga]Pentixafor-PET/CT for Imaging of Chemokine Receptor 4 Expression After Myocardial Infarction. *JACC. Cardiovascular imaging*, *8*(12), 1466–1468.

Lau, J., Rousseau, E., Kwon, D., Lin, K. S., Bénard, F., & Chen, X. (2020). Insight into the Development of PET Radiopharmaceuticals for Oncology. *Cancers*, *12*(5), 1312.

Lauwers, Y., De Groof, T. W. M., Vincke, C., Van Craenenbroeck, J., Jumapili, N. A., Barthelmess, R. M., Courtoy, G., Waelput, W., De Pauw, T., Raes, G., Devoogdt, N., & Van Ginderachter, J. A. (2024). Imaging of tumor-associated macrophage dynamics during immunotherapy using a CD163-specific nanobody-based immunotracer. *Proceedings of the National Academy of Sciences of the United States of America*, *121*(52), e2409668121.

Lavine, K. J., Epelman, S., Uchida, K., Weber, K. J., Nichols, C. G., Schilling, J. D., Ornitz, D. M., Randolph, G. J., & Mann, D. L. (2014). Distinct macrophage lineages contribute to disparate patterns of cardiac recovery and remodeling in the neonatal and adult heart. *Proceedings of the National Academy of Sciences of the United States of America*, *111*(45), 16029–16034.

Le Cabec, V., Emorine, L. J., Toesca, I., Cougoule, C., & Maridonneau-Parini, I. (2005). The human macrophage mannose receptor is not a professional phagocytic receptor. *Journal of leukocyte biology*, *77*(6), 934–943.

Lee, B., Kim, Y. K., Lee, J. Y., Kim, Y. J., Lee, Y. S., Lee, D. S., Chung, J. K., & Jeong, J. M. (2017). Preclinical anaylses of [^{18}F]cEFQ as a PET tracer for imaging metabotropic glutamate receptor type 1 (mGluR1). *Journal of cerebral blood flow and metabolism : official journal of the International Society of Cerebral Blood Flow and Metabolism*, *37*(6), 2283–2293.

Lee, C. Z. W., & Ginhoux, F. (2022). Biology of resident tissue macrophages. Development (Cambridge, England), 149(8), dev200270.

Lee, E., Hooker, J. M., & Ritter, T. (2012). Nickel-mediated oxidative fluorination for PET with aqueous [^{18}F] fluoride. *Journal of the American Chemical Society*, *134*(42), 17456–17458.

Lee, E., Kamlet, A. S., Powers, D. C., Neumann, C. N., Boursalian, G. B., Furuya, T., Choi, D. C., Hooker, J. M., & Ritter, T. (2011). A fluoride-derived electrophilic late-stage fluorination reagent for PET imaging. *Science (New York, N.Y.)*, *334*(6056), 639–642.

Lee, S. P., Im, H. J., Kang, S., Chung, S. J., Cho, Y. S., Kang, H., Park, H. S., Hwang, D. W., Park, J. B., Paeng, J. C., Cheon, G. J., Lee, Y. S., Jeong, J. M., & Kim, Y. J. (2017). Noninvasive Imaging of Myocardial Inflammation in Myocarditis using ^{68}Ga-tagged Mannosylated Human Serum Albumin Positron Emission Tomography. *Theranostics*, *7*(2), 413–424.

Lee, W. W., & K-SPECT Group (2019). Clinical Applications of Technetium-99m Quantitative Single-Photon Emission Computed Tomography/Computed Tomography. *Nuclear medicine and molecular imaging*, *53*(3), 172–181.

Lefer, D. J., & Granger, D. N. (2000). Oxidative stress and cardiac disease. *The American journal of medicine*, *109*(4), 315–323.

Leong S. P. (2022). Detection of melanoma, breast cancer and head and neck squamous cell cancer sentinel lymph nodes by Tc-99m Tilmanocept (Lymphoseek®). *Clinical & experimental metastasis*, *39*(1), 39–50.

Leupe, H., Pauwels, E., Vandamme, T., Van den Broeck, B., Lybaert, W., Dekervel, J., Van Herpe, F., Jaekers, J., Cleeren, F., Hofland, J., Brouwers, A., Koole, M., Bormans, G., Van Cutsem, E., Geboes, K., Laenen, A., Verslype, C., Stroobants, S., & Deroose, C. M. (2024). Clinical impact of using [^{18}F]AlF-NOTA-octreotide PET/CT instead of [^{68}Ga]Ga-DOTA-SSA PET/CT: Secondary endpoint analysis of a multicenter, prospective trial. *Journal of neuroendocrinology*, *36*(8), e13420.

Lever, S. Z., Fan, K. H., & Lever, J. R. (2017). Tactics for preclinical validation of receptor-binding radiotracers. *Nuclear medicine and biology*, *44*, 4–30.

Li, D., & Wu, M. (2021). Pattern recognition receptors in health and diseases. *Signal transduction and targeted therapy*, *6*(1), 291.

Li, T., Yan, Z., Fan, Y., Fan, X., Li, A., Qi, Z., & Zhang, J. (2023). Cardiac repair after myocardial infarction: A two-sided role of inflammation-mediated. *Frontiers in cardiovascular medicine*, *9*, 1077290.

Libby, P., Nahrendorf, M., & Swirski, F. K. (2016). Leukocytes Link Local and Systemic Inflammation in Ischemic Cardiovascular Disease: An Expanded "Cardiovascular Continuum". *Journal of the American College of Cardiology*, *67*(9), 1091–1103.

Linehan, S. A., Martínez-Pomares, L., Stahl, P. D., & Gordon, S. (1999). Mannose receptor and its putative ligands in normal murine lymphoid and nonlymphoid organs: In situ expression of mannose receptor by selected macrophages, endothelial cells, perivascular microglia, and mesangial cells, but not dendritic cells. *The Journal of experimental medicine*, *189*(12), 1961–1972.

Liu, C., Tang, J., Xu, Y., Cao, S., Fang, Y., Zhao, C., & Chen, Z. (2021). Molar activity of [^{18}F]FP-(+)-DTBZ radiopharmaceutical: Determination and its effect on quantitative analysis of VMAT2 autoradiography. *Journal of pharmaceutical and biomedical analysis*, *203*, 114212.

Liu, S. (2008). Bifunctional coupling agents for radiolabeling of biomolecules and target-specific delivery of metallic radionuclides. *Advanced drug delivery reviews*, *60*(12), 1347–1370.

Liu, X., Li, F., Wen, X., Zheng, J., Pan, W., & Li, Z. (2024). ^{18}F-Labeled dihydropyridines via Hantzsch reaction for positron emission tomography of P-glycoprotein dysfunction. *Bioorganic & medicinal chemistry letters*, *109*, 129818.

Liu, Y. C., Zou, X. B., Chai, Y. F., & Yao, Y. M. (2014). Macrophage polarization in inflammatory diseases. *International journal of biological sciences*, *10*(5), 520–529.

Liu, Y., Pressly, E. D., Abendschein, D. R., Hawker, C. J., & Woodard, G. E. (2012). Chelation of aluminum [^{18}F]fluoride by macrocyclic chelators for potential radiopharmaceutical applications. *Journal of Nuclear Medicine, 53*(Supplement 1), 1452.

Liu, Z., & Chen, X. (2016). Simple bioconjugate chemistry serves great clinical advances: albumin as a versatile platform for diagnosis and precision therapy. *Chemical Society reviews*, *45*(5), 1432–1456.

Llorca O. (2008). Extended and bent conformations of the mannose receptor family. *Cellular and molecular life sciences : CMLS*, *65*(9), 1302–1310.

Locke, L. W., Mayo, M. W., Yoo, A. D., Williams, M. B., & Berr, S. S. (2012). PET imaging of tumor associated macrophages using mannose coated 64Cu liposomes. *Biomaterials*, *33*(31), 7785–7793.

Loke, I., Kolarich, D., Packer, N. H., & Thaysen-Andersen, M. (2016). Emerging roles of protein mannosylation in inflammation and infection. *Molecular aspects of medicine*, *51*, 31–55.

Long, N. M., & Smith, C. S. (2011). Causes and imaging features of false positives and false negatives on F-PET/CT in oncologic imaging. *Insights into imaging*, *2*(6), 679–698.

Löser, R., Fischer, S., Hiller, A., Köckerling, M., Funke, U., Maisonial, A., Brust, P., & Steinbach, J. (2013). Use of 3-[^{18}F]fluoropropanesulfonyl chloride as a prosthetic agent for the radiolabelling of amines: Investigation of precursor molecules, labelling conditions and enzymatic stability of the corresponding sulfonamides. *Beilstein journal of organic chemistry*, *9*, 1002–1011.

Loveless V. (2009). *Quality control of compounded radiopharmaceuticals, continuing education for nuclear pharmacist and nuclear medicine professionals*. University of New Mexico Health Sciences Center College of Pharmacy, Albuquerque.

Lucinian, Y. A., Martineau, P., Abikhzer, G., Harel, F., & Pelletier-Galarneau, M. (2024). Novel tracers to assess myocardial inflammation with radionuclide imaging. *Journal of nuclear cardiology : official publication of the American Society of Nuclear Cardiology*, *42*, 102012.

Luckheeram, R. V., Zhou, R., Verma, A. D., & Xia, B. (2012). CD4$^+$T cells: differentiation and functions. *Clinical & developmental immunology*, *2012*, 925135.

Ludwig, F.-A., Laurini, E., Schmidt, J., Pricl, S., Deuther-Conrad, W., & Wünsch, B. (2024). [^{18}F]Fluspidine—A PET Tracer for Imaging of σ_1 Receptors in the Central Nervous System. *Pharmaceuticals*, *17*(2), 166.

Lukovic, D., Gyöngyösi, M., Pavo, I. J., Mester-Tonczar, J., Einzinger, P., Zlabinger, K., Kastner, N., Spannbauer, A., Traxler, D., Pavo, N., Goliasch, G., Pils, D., Jakab, A., Szankai, Z., Michel-Behnke, I., Zhang, L., Devaux, Y., Graf, S., Beitzke, D., & Winkler, J. (2024). Increased [^{18}F]FDG uptake in the infarcted myocardial area displayed by combined PET/CMR correlates with snRNA-seq-detected inflammatory cell invasion. *Basic research in cardiology*, *119*(5), 807–829.

Lütje, S., Franssen, G. M., Herrmann, K., Boerman, O. C., Rijpkema, M., Gotthardt, M., & Heskamp, S. (2019). In Vitro and In Vivo Characterization of an [^{18}F]AlF-Labeled PSMA Ligand for Imaging of PSMA-Expressing Xenografts. *Journal of nuclear medicine : official publication, Society of Nuclear Medicine*, *60*(7), 1017–1022.

Luurtsema, G., Pichler, V., Bongarzone, S., Seimbille, Y., Elsinga, P., Gee, A., & Vercouillie, J. (2021). EANM guideline for harmonisation on molar activity or specific activity of radiopharmaceuticals: impact on safety and imaging quality. *EJNMMI radiopharmacy and chemistry*, *6*(1), 34.

Ma, Y., Mouton, A. J., & Lindsey, M. L. (2018). Cardiac macrophage biology in the steady-state heart, the aging heart, and following myocardial infarction. *Translational research : the journal of laboratory and clinical medicine*, *191*, 15–28.

Maaniitty, T., Knuuti, J., & Saraste, A. (2020). 15O-Water PET MPI: Current Status and Future Perspectives. *Seminars in nuclear medicine*, *50*(3), 238–247.

MacRitchie, N., Frleta-Gilchrist, M., Sugiyama, A., Lawton, T., McInnes, I. B., & Maffia, P. (2020). Molecular imaging of inflammation - Current and emerging technologies for diagnosis and treatment. *Pharmacology & therapeutics*, *211*, 107550.

Mahieu, R., Krijger, G. C., Ververs, F. F. T., de Roos, R., de Bree, R., & de Keizer, B. (2021). [^{68}Ga]Ga-tilmanocept PET/CT lymphoscintigraphy for sentinel lymph node detection in early-stage oral cavity carcinoma. *European journal of nuclear medicine and molecular imaging*, *48*(4), 1246–1247.

Maioli, C., Luciniani, G., Strinchini, A., Tagliabue, L., & Del Sole, A. (2017). Quality control on radiochemical purity in Technetium-99m radiopharmaceuticals labelling: three years of experience on 2280 procedures. *Acta bio-medica : Atenei Parmensis*, *88*(1), 49–56.

Makowski, M. R., Rischpler, C., Ebersberger, U., Keithahn, A., Kasel, M., Hoffmann, E., Rassaf, T., Kessler, H., Wester, H. J., Nekolla, S. G., Schwaiger, M., & Beer, A. J. (2021). Multiparametric PET and MRI of myocardial damage after myocardial infarction: correlation of integrin αvβ3 expression and myocardial blood flow. *European journal of nuclear medicine and molecular imaging*, *48*(4), 1070–1080.

Malpetti, M., Passamonti, L., Jones, P. S., Street, D., Rittman, T., Fryer, T. D., Hong, Y. T., Vàsquez Rodriguez, P., Bevan-Jones, W. R., Aigbirhio, F. I., O'Brien, J. T., & Rowe, J. B. (2021). Neuroinflammation predicts disease progression in progressive supranuclear palsy. *Journal of neurology, neurosurgery, and psychiatry*, *92*(7), 769–775.

Mandic, L., Traxler, D., Gugerell, A., Zlabinger, K., Lukovic, D., Pavo, N., Goliasch, G., Spannbauer, A., Winkler, J., & Gyöngyösi, M. (2016). Molecular Imaging of Angiogenesis in Cardiac Regeneration. *Current cardiovascular imaging reports*, *9*(10), 27.

Mantovani, A., Sica, A., Sozzani, S., Allavena, P., Vecchi, A., & Locati, M. (2004). The chemokine system in diverse forms of macrophage activation and polarization. *Trends in immunology*, *25*(12), 677–686.

Margraf, A., & Perretti, M. (2022). Immune Cell Plasticity in Inflammation: Insights into Description and Regulation of Immune Cell Phenotypes. *Cells*, *11*(11), 1824.

Maródi, L., Korchak, H. M., & Johnston, R. B., Jr (1991). Mechanisms of host defense against Candida species. I. Phagocytosis by monocytes and monocyte-derived macrophages. *Journal of immunology (Baltimore, Md. : 1950)*, *146*(8), 2783–2789.

Marshall, J. S., Warrington, R., Watson, W., & Kim, H. L. (2018). An introduction to immunology and immunopathology. *Allergy, asthma, and clinical immunology : official journal of the Canadian Society of Allergy and Clinical Immunology*, *14*(Suppl 2), 49.

Martin R. B. (1988). Ternary hydroxide complexes in neutral solutions of Al3+ and F-. *Biochemical and biophysical research communications*, *155*(3), 1194–1200.

Martinez-Pomares L. (2012). The mannose receptor. *Journal of leukocyte biology*, *92*(6), 1177–1186.

Martinez-Pomares, L., Wienke, D., Stillion, R., McKenzie, E. J., Arnold, J. N., Harris, J., McGreal, E., Sim, R. B., Isacke, C. M., & Gordon, S. (2006). Carbohydrate-independent recognition of collagens by the macrophage mannose receptor. *European journal of immunology*, *36*(5), 1074–1082.

Martynova, E., Rizvanov, A., Urbanowicz, R. A., & Khaiboullina, S. (2022). Inflammasome Contribution to the Activation of Th1, Th2, and Th17 Immune Responses. *Frontiers in microbiology*, *13*, 851835.

Masuda, A., Nemoto, A., Yamaki, T., Oriuchi, N., Takenoshita, S., & Takeishi, Y. (2018). Assessment of myocardial viability of a patient with old myocardial infarction by [^{18}F]fluorodeoxyglucose PET/MRI. *Journal of nuclear cardiology : official publication of the American Society of Nuclear Cardiology*, *25*(4), 1423–1426.

Matter, M. A., Paneni, F., Libby, P., Frantz, S., Stähli, B. E., Templin, C., Mengozzi, A., Wang, Y. J., Kündig, T. M., Räber, L., Ruschitzka, F., & Matter, C. M. (2024). Inflammation in acute myocardial infarction: the good, the bad and the ugly. *European heart journal*, *45*(2), 89–103.

McAleer, J. P., & Vella, A. T. (2008). Understanding how lipopolysaccharide impacts CD4 T-cell immunity. *Critical reviews in immunology*, *28*(4), 281–299.

McBride, W. J., Sharkey, R. M., & Goldenberg, D. M. (2013). Radiofluorination using aluminum-fluoride (Al[^{18}F]). *EJNMMI research*, *3*(1), 36.

McBride, W. J., Sharkey, R. M., Karacay, H., D'Souza, C. A., Rossi, E. A., Laverman, P., Chang, C. H., Boerman, O. C., & Goldenberg, D. M. (2009). A novel method of ^{18}F-radiolabeling for PET. *Journal of nuclear medicine : official publication, Society of Nuclear Medicine*, *50*(6), 991–998.

McCOLL, B. K., Stacker, S. A., & Achen, M. G. (2004). Molecular regulation of the VEGF family–inducers of angiogenesis and lymphangiogenesis. *Apmis*, *112*(7-8), 463-480.

Medina K. L. (2016). Overview of the immune system. Handbook of clinical neurology, 133, 61–76.

Medzhitov R. (2008). Origin and physiological roles of inflammation. *Nature*, *454*(7203), 428–435.

Medzhitov R. (2010). Inflammation 2010: new adventures of an old flame. *Cell*, *140*(6), 771–776.

Mercado, R., Lagos, S., & Velásquez, E. (2023). Radiochemical Purity and Identity in Radiopharmaceuticals: Design and Improvement of Quality Control Methods by HPLC. IntechOpen.

Mikolajczak, R., Huclier-Markai, S., Alliot, C., Haddad, F., Szikra, D., Forgacs, V., & Garnuszek, P. (2021). Production of scandium radionuclides for theranostic applications: towards standardization of quality requirements. *EJNMMI radiopharmacy and chemistry*, *6*(1), 19.

Milenkovic, V. M., Stanton, E. H., Nothdurfter, C., Rupprecht, R., & Wetzel, C. H. (2019). The Role of Chemokines in the Pathophysiology of Major Depressive Disorder. *International journal of molecular sciences*, *20*(9), 2283.

Miller, J. L., de Wet, B. J., Martinez-Pomares, L., Radcliffe, C. M., Dwek, R. A., Rudd, P. M., & Gordon, S. (2008). The mannose receptor mediates dengue virus infection of macrophages. *PLoS pathogens*, *4*(2), e17.

Miller, C. D., Mahler, S. A., Snavely, A. C., Raman, S. V., Caterino, J. M., Clark, C. L., Jones, A. E., Hall, M. E., Koehler, L. E., Lovato, J. F., Hiestand, B. C., Stopyra, J. P., Park, C. J., Vasu, S., Kutcher, M. A., & Hundley, W. G. (2023). Cardiac Magnetic Resonance Imaging Versus Invasive-Based Strategies in Patients With Chest Pain and Detectable to Mildly Elevated Serum Troponin: A Randomized Clinical Trial. *Circulation. Cardiovascular imaging*, *16*(6), e015063.

Mitsdoerffer, M., Lee, Y., Jäger, A., Kim, H. J., Korn, T., Kolls, J. K., Cantor, H., Bettelli, E., & Kuchroo, V. K. (2010). Proinflammatory T helper type 17 cells are effective B-cell helpers. *Proceedings of the National Academy of Sciences of the United States of America*, *107*(32), 14292–14297.

Mogensen T. H. (2009). Pathogen recognition and inflammatory signaling in innate immune defenses. *Clinical microbiology reviews*, *22*(2), 240–273.

Morais, M., Subramanian, S., Pandey, U., Samuel, G., Venkatesh, M., Martins, M., Pereira, S., Correia, J. D., & Santos, I. (2011). Mannosylated dextran derivatives labeled with fac-[M(CO)$_3$]+ (M = (99m)Tc, Re) for specific targeting of sentinel lymph node. *Molecular pharmaceutics*, *8*(2), 609–620.

Morooka, M., Kubota, K., Kadowaki, H., Ito, K., Okazaki, O., Kashida, M., Mitsumoto, T., Iwata, R., Ohtomo, K., & Hiroe, M. (2009). ^{11}C-methionine PET of acute myocardial infarction. *Journal of nuclear medicine : official publication, Society of Nuclear Medicine*, *50*(8), 1283–1287.

Morton, D. L., Hoon, D. S., Cochran, A. J., Turner, R. R., Essner, R., Takeuchi, H., Wanek, L. A., Glass, E., Foshag, L. J., Hsueh, E. C., Bilchik, A. J., Elashoff, D., & Elashoff, R. (2003). Lymphatic mapping and sentinel lymphadenectomy for early-stage melanoma: therapeutic utility and implications of nodal microanatomy and molecular staging for improving the accuracy of detection of nodal micrometastases. *Annals of surgery*, *238*(4), 538–550.

Moses, J. E., & Moorhouse, A. D. (2007). The growing applications of click chemistry. *Chemical Society reviews*, *36*(8), 1249–1262.

Mosser, D. M., & Edwards, J. P. (2008). Exploring the full spectrum of macrophage activation. Nature reviews. *Immunology*, *8*(12), 958–969.

Mosser, D. M., Hamidzadeh, K., & Goncalves, R. (2021). Macrophages and the maintenance of homeostasis. *Cellular & molecular immunology*, *18*(3), 579–587.

Mouton, A. J., DeLeon-Pennell, K. Y., Rivera Gonzalez, O. J., Flynn, E. R., Freeman, T. C., Saucerman, J. J., Garrett, M. R., Ma, Y., Harmancey, R., & Lindsey, M. L. (2018). Mapping macrophage polarization over the myocardial infarction time continuum. *Basic research in cardiology*, *113*(4), 26.

Müller, C., Domnanich, K. A., Umbricht, C. A., & van der Meulen, N. P. (2018). Scandium and terbium radionuclides for radiotheranostics: current state of development towards clinical application. *The British journal of radiology*, *91*(1091), 20180074.

Müller, C., Fischer, E., Behe, M., Köster, U., Dorrer, H., Reber, J., Haller, S., Cohrs, S., Blanc, A., Grünberg, J., Bunka, M., Zhernosekov, K., van der Meulen, N., Johnston, K., Türler, A., & Schibli, R. (2014). Future prospects for SPECT imaging using the radiolanthanide terbium-155 - production and preclinical evaluation in tumor-bearing mice. *Nuclear medicine and biology*, *41 Suppl*, e58–e65.

Nahrendorf, M., Pittet, M. J., & Swirski, F. K. (2010). Monocytes: protagonists of infarct inflammation and repair after myocardial infarction. *Circulation*, *121*(22), 2437–2445.

Nahrendorf, M., Swirski, F. K., Aikawa, E., Stangenberg, L., Wurdinger, T., Figueiredo, J. L., Libby, P., Weissleder, R., & Pittet, M. J. (2007). The healing myocardium sequentially mobilizes two monocyte subsets with divergent and complementary functions. *The Journal of experimental medicine*, *204*(12), 3037–3047.

Nakayama, T., Hirahara, K., Onodera, A., Endo, Y., Hosokawa, H., Shinoda, K., Tumes, D. J., & Okamoto, Y. (2017). Th2 Cells in Health and Disease. *Annual review of immunology*, *35*, 53–84.

Napper, C. E., Drickamer, K., & Taylor, M. E. (2006). Collagen binding by the mannose receptor mediated through the fibronectin type II domain. *The Biochemical journal*, *395*(3), 579–586.

Nathan C. (2006). Neutrophils and immunity: challenges and opportunities. *Nature reviews. Immunology*, *6*(3), 173–182.

Needham, E. J., Helmy, A., Zanier, E. R., Jones, J. L., Coles, A. J., & Menon, D. K. (2019). The immunological response to traumatic brain injury. *Journal of neuroimmunology*, *332*, 112–125.

Nelson, B. J. B., Wilson, J., Richter, S., Duke, M. J. M., Wuest, M., & Wuest, F. (2020). Taking cyclotron ^{68}Ga production to the next level: Expeditious solid target production of ^{68}Ga for preparation of radiotracers. *Nuclear medicine and biology*, *80-81*, 24–31.

Netea, M. G., Schlitzer, A., Placek, K., Joosten, L. A. B., & Schultze, J. L. (2019). Innate and Adaptive Immune Memory: an Evolutionary Continuum in the Host's Response to Pathogens. *Cell host & microbe*, *25*(1), 13–26.

Netea, M. G., Balkwill, F., Chonchol, M., Cominelli, F., Donath, M. Y., Giamarellos-Bourboulis, E. J., Golenbock, D., Gresnigt, M. S., Heneka, M. T., Hoffman, H. M., Hotchkiss, R., Joosten, L. A. B., Kastner, D. L., Korte, M., Latz, E., Libby, P., Mandrup-Poulsen, T., Mantovani, A., Mills, K. H. G., Nowak, K. L., … Dinarello, C. A. (2017). A guiding map for inflammation. *Nature immunology*, *18*(8), 826–831.

Nikovics, K., Favier, A. L., Rocher, M., Mayinga, C., Gomez, J., Dufour-Gaume, F., & Riccobono, D. (2023). In Situ Identification of Both IL-4 and IL-10 Cytokine-Receptor Interactions during Tissue Regeneration. *Cells*, *12*(11), 1522.

Nock, B. A., Maina, T., Krenning, E. P., & de Jong, M. (2014). "To serve and protect": enzyme inhibitors as radiopeptide escorts promote tumor targeting. *Journal of nuclear medicine : official publication, Society of Nuclear Medicine*, *55*(1), 121–127.

Noriega-Álvarez, E., & Martín-Comín, J. (2023). Molecular Imaging in Inflammatory Bowel Disease. *Seminars in nuclear medicine*, *53*(2), 273–286.

Norikane, T., Yamamoto, Y., Takami, Y., Mitamura, K., Kobata, T., Maeda, Y., Noma, T., & Nishiyama, Y. (2024). Physiological myocardial [^{18}F]FDG uptake pattern in oncologic PET/CT: comparison with findings in cardiac sarcoidosis. *Asia Oceania journal of nuclear medicine & biology*, *12*(1), 1–10.

Notohamiprodjo, S., Nekolla, S. G., Robu, S., Villagran Asiares, A., Kupatt, C., Ibrahim, T., Laugwitz, K. L., Makowski, M. R., Schwaiger, M., Weber, W. A., & Varasteh, Z. (2022). Imaging of cardiac fibroblast activation in a patient after acute myocardial infarction using ^{68}Ga-FAPI-04. *Journal of nuclear cardiology : official publication of the American Society of Nuclear Cardiology*, *29*(5), 2254–2261.

Nyolczas, N., Gyöngyösi, M., Beran, G., Dettke, M., Graf, S., Sochor, H., Christ, G., Edes, I., Balogh, L., Krause, K. T., Jaquet, K., Kuck, K. H., Benedek, I., Hintea, T., Kiss, R., Préda, I., Kotevski, V., Pejkov, H., Dudek, D., Heba, G., … Glogar, D. (2007). Design and rationale for the Myocardial Stem Cell Administration After Acute Myocardial Infarction (MYSTAR) Study: a multicenter, prospective, randomized, single-blind trial comparing early and late intracoronary or combined (percutaneous intramyocardial and intracoronary) administration of nonselected autologous bone marrow cells to patients after acute myocardial infarction. *American heart journal*, *153*(2), 212.e1–212.e2127.

Okin, D., & Medzhitov, R. (2012). Evolution of inflammatory diseases. *Current biology : CB*, *22*(17), R733–R740.

Omami, G., Tamimi, D., & Branstetter, B. F. (2014). Basic principles and applications of [^{18}F]FDG PET/CT in oral and maxillofacial imaging: A pictorial essay. *Imaging science in dentistry*, *44*(4), 325–332.

Ong, S. B., Hernández-Reséndiz, S., Crespo-Avilan, G. E., Mukhametshina, R. T., Kwek, X. Y., Cabrera-Fuentes, H. A., & Hausenloy, D. J. (2018). Inflammation following acute myocardial infarction: Multiple players, dynamic roles, and novel therapeutic opportunities. *Pharmacology & therapeutics*, *186*, 73–87.

Orbay, H., Zhang, Y., Valdovinos, H. F., Song, G., Hernandez, R., Theuer, C. P., Hacker, T. A., Nickles, R. J., & Cai, W. (2013). Positron emission tomography imaging of CD105 expression in a rat myocardial infarction model with (64)Cu-NOTA-TRC105. *American journal of nuclear medicine and molecular imaging*, *4*(1), 1–9.

Oronsky, B., Caroen, S., & Reid, T. (2022). What Exactly Is Inflammation (and What Is It Not?). *International journal of molecular sciences*, *23*(23), 14905.

Osborn, E. A., & Jaffer, F. A. (2013). The advancing clinical impact of molecular imaging in CVD. *JACC. Cardiovascular imaging*, *6*(12), 1327–1341.

Pahwa, R., Goyal, A., & Jialal, I. (2023). Chronic Inflammation. In *StatPearls*. StatPearls Publishing.

Palm, N. W., Rosenstein, R. K., & Medzhitov, R. (2012). Allergic host defences. *Nature*, *484*(7395), 465–472.

Pandey, M. K., Byrne, J. F., Jiang, H., Packard, A. B., & DeGrado, T. R. (2014). Cyclotron production of ^{68}Ga via the ^{68}Zn(p,n)^{68}Ga reaction in aqueous solution. *American journal of nuclear medicine and molecular imaging*, *4*(4), 303–310.

Papagiannopoulou D. (2017). Technetium-99m radiochemistry for pharmaceutical applications. *Journal of labelled compounds & radiopharmaceuticals*, *60*(11), 502–520.

Papasavva, A., Shegani, A., Kiritsis, C., Roupa, I., Ischyropoulou, M., Makrypidi, K., Pilatis, I., Loudos, G., Pelecanou, M., Papadopoulos, M., & Pirmettis, I. (2021). Comparative Study of a Series of ^{99m}Tc(CO)$_3$ Mannosylated Dextran Derivatives for Sentinel Lymph Node Detection. *Molecules*, *26*(16), 4797.

Park, J. B., Suh, M., Park, J. Y., Park, J. K., Kim, Y. I., Kim, H., Cho, Y. S., Kang, H., Kim, K., Choi, J. H., Nam, J. W., Kim, H. K., Lee, Y. S., Jeong, J. M., Kim, Y. J., Paeng, J. C., & Lee, S. P. (2020). Assessment of Inflammation in Pulmonary Artery Hypertension by ^{68}Ga-Mannosylated Human Serum Albumin. *American journal of respiratory and critical care medicine*, *201*(1), 95–106.

Parker, C. C., Bin Salam, A., Song, P. N., Gallegos, C., Hunt, A., Yates, C., Jaynes, J., Lopez, H., Massicano, A. V. F., Sorace, A. G., Fernandez, S., Houson, H. A., & Lapi, S. E. (2023). Evaluation of a CD206-Targeted Peptide for PET Imaging of Macrophages in Syngeneic Mouse Models of Cancer. *Molecular pharmaceutics*, *20*(5), 2415–2425.

Pasotti, M., Prati, F., & Arbustini, E. (2006). The pathology of myocardial infarction in the pre- and post-interventional era. *Heart (British Cardiac Society)*, *92*(11), 1552–1556.

Passchier J. (2009). Fast high performance liquid chromatography in PET quality control and metabolite analysis. *The quarterly journal of nuclear medicine and molecular imaging : official publication of the Italian Association of Nuclear Medicine (AIMN) [and] the International Association of Radiopharmacology (IAR), [and] Section of the Society of...*, *53*(4), 411–416.

Paul W. E. (2015). History of interleukin-4. *Cytokine*, *75*(1), 3–7.

Paveley, R. A., Aynsley, S. A., Turner, J. D., Bourke, C. D., Jenkins, S. J., Cook, P. C., Martinez-Pomares, L., & Mountford, A. P. (2011). The Mannose Receptor (CD206) is an important pattern recognition receptor (PRR) in the detection of the infective stage of the helminth Schistosoma mansoni and modulates IFNγ production. *International journal for parasitology*, *41*(13-14), 1335–1345.

Pedretti, R. F. E., Genovese, L., Alberti, L., Cecilia, A., Cellamare, M., Crippa, M., Dacquino, G. M. Danza, A., Torre, M. D., Bravo, F. F., Galati, G., Torlone, F., Braga, S. S. (2024). Role of nuclear medicine assessing patients with suspected coronary artery disease: Nuclear medicine and coronary artery disease. *European Atherosclerosis Journal*, *3*, 4-6).

Pees, A., Windhorst, A.D., Vosjan, M. J. W. D., Tadino, V., & Vugts, D. J. (2020). Synthesis of [^{18}F]Fluoroform with high molar activity. *European journal of organic chemistry*, 1177 —1185.

Perez, J., Viollet, C., Doublier, S., Videau, C., Epelbaum, J., & Baud, L. (2003). Somatostatin binds to murine macrophages through two distinct subsets of receptors. *Journal of neuroimmunology*, *138*(1-2), 38–44.

Perrio, C., Schmitt, S., Pla, D., Gabbaï, F. P., Chansaenpak, K., Mestre-Voegtle, B., & Gras, E. (2016). [^{18}F]-Fluoride capture and release: azeotropic drying free nucleophilic aromatic radiofluorination assisted by a phosphonium borane. *Chemical communications (Cambridge, England)*, *53*(2), 340–343.

Pichler, V., Berroterán-Infante, N., Philippe, C., Vraka, C., Klebermass, E. M., Balber, T., Pfaff, S., Nics, L., Mitterhauser, M., & Wadsak, W. (2018). An Overview of PET Radiochemistry, Part 1: The Covalent Labels ^{18}F, ^{11}C, and ^{13}N. *Journal of nuclear medicine : official publication, Society of Nuclear Medicine*, *59*(9), 1350–1354.

Pijl, J. P., Nienhuis, P. H., Kwee, T. C., Glaudemans, A. W. J. M., Slart, R. H. J. A., & Gormsen, L. C. (2021). Limitations and Pitfalls of FDG-PET/CT in Infection and Inflammation. *Seminars in nuclear medicine*, *51*(6), 633–645.

Pirmettis, I., Arano, Y., Tsotakos, T., Okada, K., Yamaguchi, A., Uehara, T., Morais, M., Correia, J. D., Santos, I., Martins, M., Pereira, S., Triantis, C., Kyprianidou, P., Pelecanou, M., & Papadopoulos, M. (2012). New (99m)Tc(CO)(3) mannosylated dextran bearing S-derivatized cysteine chelator for sentinel lymph node detection. *Molecular pharmaceutics*, *9*(6), 1681–1692.

Pittman, K., & Kubes, P. (2013). Damage-associated molecular patterns control neutrophil recruitment. *Journal of innate immunity*, *5*(4), 315–323.

Prabhu, S. D., & Frangogiannis, N. G. (2016). The Biological Basis for Cardiac Repair After Myocardial Infarction: From Inflammation to Fibrosis. *Circulation research*, *119*(1), 91–112.

Punchard, N. A., Whelan, C. J., & Adcock, I. (2004). *The Journal of Inflammation. Journal of inflammation (London, England)*, *1*(1), 1.

Pysz, M. A., Gambhir, S. S., & Willmann, J. K. (2010). Molecular imaging: current status and emerging strategies. *Clinical radiology*, *65*(7), 500–516.

Qiao, P., Wang, Y., Zhu, K., Zheng, D., Song, Y., Jiang, D., Qin, C., & Lan, X. (2022). Noninvasive Monitoring of Reparative Fibrosis after Myocardial Infarction in Rats Using ^{68}Ga-FAPI-04 PET/CT. *Molecular pharmaceutics*, *19*(11), 4171–4178.

Ragland, S. A., & Criss, A. K. (2017). From bacterial killing to immune modulation: Recent insights into the functions of lysozyme. *PLoS pathogens*, *13*(9), e1006512.

Raj, V., Karunasaagarar, K., Rudd, J. H., Screaton, N., & Gopalan, D. (2010). Complications of myocardial infarction on multidetector-row computed tomography of chest. *Clinical radiology*, *65*(11), 930–936.

Raposo, F., Ramos, M., & Lúcia Cruz, A. (2021). Effects of exercise on knee osteoarthritis: A systematic review. *Musculoskeletal care*, *19*(4), 399–435.

Reed, G. W., Rossi, J. E., & Cannon, C. P. (2017). Acute myocardial infarction. *Lancet (London, England)*, *389*(10065), 197–210.

Reily, C., Stewart, T. J., Renfrow, M. B., & Novak, J. (2019). Glycosylation in health and disease. Nature reviews. *Nephrology*, *15*(6), 346–366.

Reiner, T., & Zeglis, B. M. (2014). The inverse electron demand Diels-Alder click reaction in radiochemistry. *Journal of labelled compounds & radiopharmaceuticals*, *57*(4), 285–290.

Rempel, A., Mathupala, S. P., Griffin, C. A., Hawkins, A. L., & Pedersen, P. L. (1996). Glucose catabolism in cancer cells: amplification of the gene encoding type II hexokinase. *Cancer research*, *56*(11), 2468-2471.

Reske, S. N., Grillenberger, K. G., Glatting, G., Port, M., Hildebrandt, M., Gansauge, F., & Beger, H. G. (1997). Overexpression of glucose transporter 1 and increased FDG uptake in pancreatic carcinoma. *Journal of Nuclear Medicine*, *38*(9), 1344-1348.

Rich D. A. (1997). A brief history of positron emission tomography. *Journal of nuclear medicine technology*, *25*(1), 4–11.

Rischpler, C., Dirschinger, R. J., Nekolla, S. G., Kossmann, H., Nicolosi, S., Hanus, F., van Marwick, S., Kunze, K. P., Meinicke, A., Götze, K., Kastrati, A., Langwieser, N., Ibrahim, T., Nahrendorf, M., Schwaiger, M., & Laugwitz, K. L. (2016). Prospective Evaluation of [^{18}F]Fluorodeoxyglucose Uptake in Postischemic Myocardium by Simultaneous Positron Emission Tomography/Magnetic Resonance Imaging as a Prognostic Marker of Functional Outcome. *Circulation. Cardiovascular imaging*, *9*(4), e004316.

Rodriguez-Porcel, M., Cai, W., Gheysens, O., Willmann, J. K., Chen, K., Wang, H., Chen, I. Y., He, L., Wu, J. C., Li, Z. B., Mohamedali, K. A., Kim, S., Rosenblum, M. G., Chen, X., & Gambhir, S. S. (2008). Imaging of VEGF receptor in a rat myocardial infarction model using PET. *Journal of nuclear medicine : official publication, Society of Nuclear Medicine*, *49*(4), 667–673.

Romagnani S. (1991). Type 1 T helper and type 2 T helper cells: functions, regulation and role in protection and disease. *International journal of clinical & laboratory research*, *21*(2), 152–158.

Rong, J., Haider, A., Jeppesen, T. E., Josephson, L., & Liang, S. H. (2023). Radiochemistry for positron emission tomography. *Nature communications*, *14*(1), 3257.

Rőszer T. (2015). Understanding the Mysterious M2 Macrophage through Activation Markers and Effector Mechanisms. *Mediators of inflammation*, *2015*, 816460.

Rowland, D. J., & Cherry, S. R. (2008). Small-animal preclinical nuclear medicine instrumentation and methodology. *Seminars in nuclear medicine*, *38*(3), 209–222.

Ruan, S., Xu, L., Sheng, Y., Wang, J., Zhou, X., Zhang, C., Guo, L., Li, W., & Han, C. (2023). Th1 promotes M1 polarization of intestinal macrophages to regulate colitis-related mucosal barrier damage. *Aging*, *15*(14), 6721–6735.

Russelli, L., Martinelli, J., De Rose, F., Reder, S., Herz, M., Schwaiger, M., Weber, W., Tei, L., & D'Alessandria, C. (2020). Room Temperature Al[^{18}F]-labeling of 2-Aminomethylpiperidine-Based Chelators for PET Imaging. *ChemMedChem*, *15*(3), 284–292.

Ruytinx, P., Proost, P., Van Damme, J., & Struyf, S. (2018). Chemokine-Induced Macrophage Polarization in Inflammatory Conditions. *Frontiers in immunology*, *9*, 1930.

Sandhu, G. S., Solorio, L., Broome, A. M., Salem, N., Kolthammer, J., Shah, T., Flask, C., & Duerk, J. L. (2010). Whole animal imaging. *Wiley interdisciplinary reviews. Systems biology and medicine*, *2*(4), 398–421.

Sansonetti, M., Al Soodi, B., Thum, T., & Jung, M. (2024). Macrophage-based therapeutic approaches for cardiovascular diseases. *Basic research in cardiology*, *119*(1), 1–33.

Saraiva, M., & O'Garra, A. (2010). The regulation of IL-10 production by immune cells. *Nature reviews. Immunology*, *10*(3), 170–181.

Savisto, N., Bergman, J., Aromaa, J., Forsback, S., Eskola, O., Viljanen, T., Rajander, J., Johansson, S., Grigg, J., Luthra, S., & Solin, O. (2018). Influence of transport line material on the molar activity of cyclotron produced [^{18}F]fluoride. *Nuclear medicine and biology*, *64-65*, 8–15.

Schieber, A. M., & Ayres, J. S. (2016). Thermoregulation as a disease tolerance defense strategy. *Pathogens and disease*, *74*(9), ftw106.

Schnaar R. L. (2016). Glycobiology simplified: diverse roles of glycan recognition in inflammation. *Journal of leukocyte biology*, *99*(6), 825–838.

Schulert, G. S., & Allen, L. A. (2006). Differential infection of mononuclear phagocytes by Francisella tularensis: role of the macrophage mannose receptor. *Journal of leukocyte biology*, *80*(3), 563–571.

Schultze, J. L., & Schmidt, S. V. (2015). Molecular features of macrophage activation. *Seminars in immunology*, *27*(6), 416–423.

Scott, A., Khan, K. M., Cook, J. L., & Duronio, V. (2004). What is "inflammation"? Are we ready to move beyond Celsus?. *British journal of sports medicine*, *38*(3), 248–249.

Sergeev, M. E., Lazari, M., Morgia, F., Collins, J., Javed, M. R., Sergeeva, O., Jones, J., Phelps, M. E., Lee, J. T., Keng, P. Y., & van Dam, R. M. (2018). Performing radiosynthesis in microvolumes to maximize molar activity of tracers for positron emission tomography. *Communications chemistry*, *1*(1), 10.

Serhan, C. N., & Savill, J. (2005). Resolution of inflammation: the beginning programs the end. *Nature immunology*, *6*(12), 1191–1197.

Severin, G. W., Engle, J. W., Valdovinos, H. F., Barnhart, T. E., & Nickles, R. J. (2012). Cyclotron produced ^{44}gSc from natural calcium. *Applied radiation and isotopes : including data, instrumentation and methods for use in agriculture, industry and medicine*, *70*(8), 1526–1530.

Shah, K., Al-Haidari, A., Sun, J., & Kazi, J. U. (2021). T cell receptor (TCR) signaling in health and disease. *Signal transduction and targeted therapy*, *6*(1), 412.

Shen, S., Wang, L., Liu, Q., Wang, X., Yuan, Q., Zhao, Y., Hu, H., & Ma, L. (2025). Macrophage-to-myofibroblast transition and its role in cardiac fibrosis. *International immunopharmacology*, *146*, 113873.

Sherif, H. M., Saraste, A., Nekolla, S. G., Weidl, E., Reder, S., Tapfer, A., Rudelius, M., Higuchi, T., Botnar, R. M., Wester, H. J., & Schwaiger, M. (2012). Molecular imaging of early αvβ3 integrin expression predicts long-term left-ventricle remodeling after myocardial infarction in rats. *Journal of nuclear medicine : official publication, Society of Nuclear Medicine*, *53*(2), 318–323.

Sheu, K. M., & Hoffmann, A. (2022). Functional Hallmarks of Healthy Macrophage Responses: Their Regulatory Basis and Disease Relevance. *Annual review of immunology*, *40*, 295–321.

Shiraishi, M., Shintani, Y., Shintani, Y., Ishida, H., Saba, R., Yamaguchi, A., Adachi, H., Yashiro, K., & Suzuki, K. (2016). Alternatively activated macrophages determine repair of the infarcted adult murine heart. *The Journal of clinical investigation*, *126*(6), 2151–2166.

Shreve, P. D., Anzai, Y., & Wahl, R. L. (1999). Pitfalls in oncologic diagnosis with FDG PET imaging: physiologic and benign variants. *Radiographics : a review publication of the Radiological Society of North America, Inc*, *19*(1), 61–151.

Sica, A., & Mantovani, A. (2012). Macrophage plasticity and polarization: in vivo veritas. *The Journal of clinical investigation*, *122*(3), 787–795.

Silvola, J. M. U., Li, X. G., Virta, J., Marjamäki, P., Liljenbäck, H., Hytönen, J. P., Tarkia, M., Saunavaara, V., Hurme, S., Palani, S., Hakovirta, H., Ylä-Herttuala, S., Saukko, P., Chen, Q., Low, P. S., Knuuti, J., Saraste, A., & Roivainen, A. (2018). Aluminum fluoride-18 labeled folate enables in vivo detection of atherosclerotic plaque inflammation by positron emission tomography. *Scientific reports*, *8*(1), 9720.

Slomka, P. J., Dey, D., Sitek, A., Motwani, M., Berman, D. S., & Germano, G. (2017). Cardiac imaging: working towards fully-automated machine analysis & interpretation. *Expert review of medical devices*, *14*(3), 197–212.

Soares, C. L. R., Wilairatana, P., Silva, L. R., Moreira, P. S., Vilar Barbosa, N. M. M., da Silva, P. R., Coutinho, H. D. M., de Menezes, I. R. A., & Felipe, C. F. B. (2023). Biochemical aspects of the inflammatory process: A narrative review. *Biomedicine & pharmacotherapy = Biomedecine & pharmacotherapie*, *168*, 115764.

Soderlund, A. T., Chaal, J., Tjio, G., Totman, J. J., Conti, M., & Townsend, D. W. (2015). Beyond [^{18}F]FDG: Characterization of PET/CT and PET/MR Scanners for a Comprehensive Set of Positron Emitters of Growing Application--^{18}F, ^{11}C, ^{89}Zr, ^{124}I, ^{68}Ga, and ^{90}Y. *Journal of nuclear medicine : official publication, Society of Nuclear Medicine*, *56*(8), 1285–1291.

Sogbein, O. O., Pelletier-Galarneau, M., Schindler, T. H., Wei, L., Wells, R. G., & Ruddy, T. D. (2014). New SPECT and PET radiopharmaceuticals for imaging cardiovascular disease. *BioMed research international*, *2014*, 942960.

Solin, O., Bergman, J., Haaparanta, M., & Reissell, A. (1988). Production of ^{18}F from water targets. Specific radioactivity and anionic contaminants. *International Journal of Radiation Applications and Instrumentation. Part A. Applied Radiation and Isotopes*, *39*(10), 1065-1071.

Son, H., Jang, K., Lee, H., Kim, S. E., Kang, K. W., & Lee, H. (2019). Use of Molecular Imaging in Clinical Drug Development: a Systematic Review. *Nuclear medicine and molecular imaging*, *53*(3), 208–215.

Song, J., Frieler, R. A., Whitesall, S. E., Chung, Y., Vigil, T. M., Muir, L. A., Ma, J., Brombacher, F., Goonewardena, S. N., Lumeng, C. N., Goldstein, D. R., & Mortensen, R. M. (2021). Myeloid interleukin-4 receptor α is essential in postmyocardial infarction healing by regulating inflammation and fibrotic remodeling. American journal of physiology. *Heart and circulatory physiology*, *320*(1), H323–H337.

Speakman J. R. (2007). A nonadaptive scenario explaining the genetic predisposition to obesity: the "predation release" hypothesis. *Cell metabolism*, *6*(1), 5–12.

Spinks, T.J. (1999). *PET, Theory*. Academic Press. 1782-1791.

Spoelstra, G. B., Blok, S. N., Reali Nazario, L., Noord, L., Fu, Y., Simeth, N. A., IJpma, F. F. A., van Oosten, M., van Dijl, J. M., Feringa, B. L., Szymanski, W., & Elsinga, P. H. (2024). Synthesis and preclinical evaluation of novel ^{18}F-vancomycin-based tracers for the detection of bacterial infections using positron emission tomography. *European journal of nuclear medicine and molecular imaging*, *51*(9), 2583–2596.

Stein, M., Keshav, S., Harris, N., & Gordon, S. (1992). Interleukin 4 potently enhances murine macrophage mannose receptor activity: a marker of alternative immunologic macrophage activation. *The Journal of experimental medicine*, *176*(1), 287–292.

Stephens, N. R., Restrepo, C. S., Saboo, S. S., & Baxi, A. J. (2019). Overview of complications of acute and chronic myocardial infarctions: revisiting pathogenesis and cross-sectional imaging. *Postgraduate medical journal*, *95*(1126), 439–450.

Stone, K. D., Prussin, C., & Metcalfe, D. D. (2010). IgE, mast cells, basophils, and eosinophils. *The Journal of allergy and clinical immunology*, *125*(2 Suppl 2), S73–S80.

Strauss L. G. (1996). Fluorine-18 deoxyglucose and false-positive results: a major problem in the diagnostics of oncological patients. *European journal of nuclear medicine*, *23*(10), 1409–1415.

Strunk, M., Heo, G. S., Hess, A., Luehmann, H., Ross, T. L., Gropler, R. J., Bengel, F. M., Liu, Y., & Thackeray, J. T. (2024). Toward Quantitative Multisite Preclinical Imaging Studies in Acute

Myocardial Infarction: Evaluation of the Immune-Fibrosis Axis. *Journal of nuclear medicine : official publication, Society of Nuclear Medicine*, *65*(2), 287–293.

Subramaniam, R. M., & Lowe, V. J. (2007). Squamous Cell Carcinoma: Restaging and Response to Therapy. *PET clinics*, *2*(4), 481–487.

Sun, Y., Zeng, Y., Zhu, Y., Feng, F., Xu, W., Wu, C., Xing, B., Zhang, W., Wu, P., Cui, L., Wang, R., Li, F., Chen, X., & Zhu, Z. (2014). Application of (68)Ga-PRGD2 PET/CT for αvβ3-integrin imaging of myocardial infarction and stroke. *Theranostics*, *4*(8), 778–786.

Surasi, D. S., O'Malley, J., & Bhambhvani, P. (2015). 99mTc-Tilmanocept: A Novel Molecular Agent for Lymphatic Mapping and Sentinel Lymph Node Localization. *Journal of nuclear medicine technology*, *43*(2), 87–91.

Sureshkumar, A., Hansen, B., & Ersahin, D. (2020). Role of Nuclear Medicine in Imaging. *Seminars in ultrasound, CT, and MR*, *41*(1), 10–19.

Swirski, F. K., & Nahrendorf, M. (2013). Leukocyte behavior in atherosclerosis, myocardial infarction, and heart failure. *Science (New York, N.Y.)*, *339*(6116), 161–166.

Taddio, M. F., Castro Jaramillo, C. A., Runge, P., Blanc, A., Keller, C., Talip, Z., Béhé, M., van der Meulen, N. P., Halin, C., Schibli, R., & Krämer, S. D. (2021). In Vivo Imaging of Local Inflammation: Monitoring LPS-Induced CD80/CD86 Upregulation by PET. *Molecular imaging and biology*, *23*(2), 196–207.

Tauber A. I. (2003). Metchnikoff and the phagocytosis theory. *Nature reviews. Molecular cell biology*, *4*(11), 897–901.

Tachado, S. D., Zhang, J., Zhu, J., Patel, N., Cushion, M., & Koziel, H. (2007). Pneumocystis-mediated IL-8 release by macrophages requires coexpression of mannose receptors and TLR2. *Journal of leukocyte biology*, *81*(1), 205–211.

Tahara, N., Mukherjee, J., de Haas, H. J., Petrov, A. D., Tawakol, A., Haider, N., Tahara, A., Constantinescu, C. C., Zhou, J., Boersma, H. H., Imaizumi, T., Nakano, M., Finn, A., Fayad, Z., Virmani, R., Fuster, V., Bosca, L., & Narula, J. (2014). 2-deoxy-2-[^{18}F]fluoro-D-mannose positron emission tomography imaging in atherosclerosis. *Nature medicine*, *20*(2), 215–219.

Taïeb, D., Jha, A., Treglia, G., & Pacak, K. (2019). Molecular imaging and radionuclide therapy of pheochromocytoma and paraganglioma in the era of genomic characterization of disease subgroups. *Endocrine-related cancer*, *26*(11), R627–R652.

Takeuchi, O., & Akira, S. (2010). Pattern recognition receptors and inflammation. *Cell*, *140*(6), 805–820.

Tan, Y., Zanoni, I., Cullen, T. W., Goodman, A. L., & Kagan, J. C. (2015). Mechanisms of Toll-like Receptor 4 Endocytosis Reveal a Common Immune-Evasion Strategy Used by Pathogenic and Commensal Bacteria. *Immunity*, *43*(5), 909–922.

Tang, D., Kang, R., Coyne, C. B., Zeh, H. J., & Lotze, M. T. (2012). PAMPs and DAMPs: signal 0s that spur autophagy and immunity. *Immunological reviews*, *249*(1), 158–175.

Tarkin, J. M., Joshi, F. R., Evans, N. R., Chowdhury, M. M., Figg, N. L., Shah, A. V., Starks, L. T., Martin-Garrido, A., Manavaki, R., Yu, E., Kuc, R. E., Grassi, L., Kreuzhuber, R., Kostadima, M. A., Frontini, M., Kirkpatrick, P. J., Coughlin, P. A., Gopalan, D., Fryer, T. D., Buscombe, J. R., … Rudd, J. H. (2017). Detection of Atherosclerotic Inflammation by ^{68}Ga-DOTATATE PET Compared to [^{18}F]FDG PET Imaging. *Journal of the American College of Cardiology*, *69*(14), 1774–1791.

Taylor, M. E., Bezouska, K., & Drickamer, K. (1992). Contribution to ligand binding by multiple carbohydrate-recognition domains in the macrophage mannose receptor. *The Journal of biological chemistry*, *267*(3), 1719–1726.

Taylor, P. R., Gordon, S., & Martinez-Pomares, L. (2005). The mannose receptor: linking homeostasis and immunity through sugar recognition. *Trends in immunology*, *26*(2), 104–110.

Taylor, P. R., Martinez-Pomares, L., Stacey, M., Lin, H. H., Brown, G. D., & Gordon, S. (2005). Macrophage receptors and immune recognition. *Annual review of immunology*, *23*, 901–944.

Thackeray, J. T., Bankstahl, J. P., Wang, Y., Korf-Klingebiel, M., Walte, A., Wittneben, A., Wollert, K. C., & Bengel, F. M. (2015). Targeting post-infarct inflammation by PET imaging: comparison of [^{68}Ga]citrate and [^{68}Ga]DOTATATE with [^{18}F]FDG in a mouse model. *European journal of nuclear medicine and molecular imaging*, *42*(2), 317–327.

Thackeray, J. T., Bankstahl, J. P., Wang, Y., Wollert, K. C., & Bengel, F. M. (2016). Targeting Amino Acid Metabolism for Molecular Imaging of Inflammation Early After Myocardial Infarction. *Theranostics*, *6*(11), 1768–1779.

Thackeray, J. T., Derlin, T., Haghikia, A., Napp, L. C., Wang, Y., Ross, T. L., Schäfer, A., Tillmanns, J., Wester, H. J., Wollert, K. C., Bauersachs, J., & Bengel, F. M. (2015). Molecular Imaging of the Chemokine Receptor CXCR4 After Acute Myocardial Infarction. *JACC. Cardiovascular imaging*, *8*(12), 1417–1426.

Thackeray, J. T., Hupe, H. C., Wang, Y., Bankstahl, J. P., Berding, G., Ross, T. L., Bauersachs, J., Wollert, K. C., & Bengel, F. M. (2018). Myocardial Inflammation Predicts Remodeling and Neuroinflammation After Myocardial Infarction. *Journal of the American College of Cardiology*, *71*(3), 263–275.

Thomas, E. K., Nakamura, M., Wienke, D., Isacke, C. M., Pozzi, A., & Liang, P. (2005). Endo180 binds to the C-terminal region of type I collagen. *The Journal of biological chemistry*, *280*(24), 22596–22605.

Thompson, M. R., Kaminski, J. J., Kurt-Jones, E. A., & Fitzgerald, K. A. (2011). Pattern recognition receptors and the innate immune response to viral infection. *Viruses*, *3*(6), 920–940.

Thorp E. B. (2023). Cardiac macrophages and emerging roles for their metabolism after myocardial infarction. *The Journal of clinical investigation*, *133*(18), e171953.

Thygesen, K., Alpert, J. S., Jaffe, A. S., Chaitman, B. R., Bax, J. J., Morrow, D. A., White, H. D., & Executive Group on behalf of the Joint European Society of Cardiology (ESC)/American College of Cardiology (ACC)/American Heart Association (AHA)/World Heart Federation (WHF) Task Force for the Universal Definition of Myocardial Infarction (2018). Fourth Universal Definition of Myocardial Infarction (2018). *Journal of the American College of Cardiology*, *72*(18), 2231–2264.Thygesen, K., Alpert, J. S., Jaffe, A. S., Simoons, M. L., Chaitman, B. R., White, H. D., Joint ESC/ACCF/AHA/WHF Task Force for Universal Definition of Myocardial Infarction, Authors/Task Force Members Chairpersons, Thygesen, K., Alpert, J. S., White, H. D., Biomarker Subcommittee, Jaffe, A. S., Katus, H. A., Apple, F. S., Lindahl, B., Morrow, D. A., ECG Subcommittee, Chaitman, B. R., Clemmensen, P. M., … Wagner, D. R. (2012). Third universal definition of myocardial infarction. *Journal of the American College of Cardiology*, *60*(16), 1581–1598.

Tillmanns, J., Hoffmann, D., Habbaba, Y., Schmitto, J. D., Sedding, D., Fraccarollo, D., Galuppo, P., & Bauersachs, J. (2015). Fibroblast activation protein alpha expression identifies activated fibroblasts after myocardial infarction. *Journal of molecular and cellular cardiology*, *87*, 194–203.

Toomey, J. S., Bhatia, S., Moon, L. W. T., Orchard, E. A., Tainter, K. H., Lokitz, S. J., ... & Penman, A. D. (2012). PET imaging a MPTP-induced mouse model of Parkinson's disease using the fluoropropyl-dihydrotetrabenazine analog [^{18}F]DTBZ (AV-133). *PLoS One*, *7*(6), e39041.

Tracey K. J. (2002). The inflammatory reflex. *Nature*, *420*(6917), 853–859.

Tsai, D. Y., Hung, K. H., Chang, C. W., & Lin, K. I. (2019). Regulatory mechanisms of B cell responses and the implication in B cell-related diseases. *Journal of biomedical science*, *26*(1), 64.

Tshibangu, T., Cawthorne, C., Serdons, K., Pauwels, E., Gsell, W., Bormans, G., Deroose, C. M., & Cleeren, F. (2020). Automated GMP compliant production of [^{18}F]AlF-NOTA-octreotide. *EJNMMI radiopharmacy and chemistry*, *5*(1), 4.

Tsoukalas, C., Lazopoulos, A., Boschetti, F., Triantis, C., Bouziotis, P., Pelecanou, M., Papadopoulos, M., & Pirmettis, I. (2014). Labeling of a NOTA mannosylated dextran with ^{68}Ga. *Nuclear medicine and biology*, *41*(10), 801.

Turner, M. D., Nedjai, B., Hurst, T., & Pennington, D. J. (2014). Cytokines and chemokines: At the crossroads of cell signalling and inflammatory disease. *Biochimica et biophysica acta*, *1843*(11), 2563–2582.

Turner, R. R., Ollila, D. W., Krasne, D. L., & Giuliano, A. E. (1997). Histopathologic validation of the sentinel lymph node hypothesis for breast carcinoma. *Annals of surgery*, *226*(3), 271–278.

Turvey, S. E., & Broide, D. H. (2010). Innate immunity. *The Journal of allergy and clinical immunology*, *125*(2 Suppl 2), S24–S32.

Vaidyanathan, G., & Zalutsky, M. R. (2006). Synthesis of N-succinimidyl 4-[^{18}F]fluorobenzoate, an agent for labeling proteins and peptides with ^{18}F. *Nature protocols*, *1*(4), 1655–1661.

Vaknin, I., & Baniyash, M. (2011). *Inflammatory Response and Immunity. In: Schwab, M. (eds) Encyclopedia of Cancer*. Springer, Berlin, Heidelberg.

Valero-Martínez, C., Castillo-Morales, V., Gómez-León, N., Hernández-Pérez, I., Vicente-Rabaneda, E. F., Uriarte, M., & Castañeda, S. (2024). Application of Nuclear Medicine Techniques in Musculoskeletal Infection: Current Trends and Future Prospects. *Journal of clinical medicine*, *13*(4), 1058.

Van Audenhaege, K., Van Holen, R., Vandenberghe, S., Vanhove, C., Metzler, S. D., & Moore, S. C. (2015). Review of SPECT collimator selection, optimization, and fabrication for clinical and preclinical imaging. *Medical physics*, *42*(8), 4796–4813.

Van Dalen, J., Visser, E., Laverman, P., Vogel, W., Oyen, W., Corstens, F., & Boerman, O. (2008). Effect of the positron range on the spatial resolution of a new generation pre-clinical PET-scanner using ^{18}F, ^{68}Ga, ^{89}Zr and ^{124}I (abstract). *Journal of nuclear medicine*, *49*, s404P.

Vaquero, J. J., & Kinahan, P. (2015). Positron Emission Tomography: Current Challenges and Opportunities for Technological Advances in Clinical and Preclinical Imaging Systems. *Annual review of biomedical engineering*, *17*, 385–414.

Varasteh, Z., Mohanta, S., Li, Y., López Armbruster, N., Braeuer, M., Nekolla, S. G., Habenicht, A., Sager, H. B., Raes, G., Weber, W., Hernot, S., & Schwaiger, M. (2019). Targeting mannose receptor expression on macrophages in atherosclerotic plaques of apolipoprotein E-knockout mice using ^{68}Ga-NOTA-anti-MMR nanobody: non-invasive imaging of atherosclerotic plaques. *EJNMMI research*, *9*(1), 5.

Varasteh, Z., Mohanta, S., Robu, S., Braeuer, M., Li, Y., Omidvari, N., Topping, G., Sun, T., Nekolla, S. G., Richter, A., Weber, C., Habenicht, A., Haberkorn, U. A., & Weber, W. A. (2019). Molecular Imaging of Fibroblast Activity After Myocardial Infarction Using a ^{68}Ga-Labeled Fibroblast Activation Protein Inhibitor, FAPI-04. *Journal of nuclear medicine : official publication, Society of Nuclear Medicine*, *60*(12), 1743–1749.

Varasteh, Z., Braeuer, M., Mohanta, S., Steinsiek, A. L., Habenicht, A., Omidvari, N., Topping, G. J., Rischpler, C., Weber, W. A., Sager, H. B., Raes, G., Hernot, S., & Schwaiger, M. (2022). *In vivo* Visualization of M2 Macrophages in the Myocardium After Myocardial Infarction (MI) Using ^{68}Ga-NOTA-Anti-MMR Nb: Targeting Mannose Receptor (MR, CD206) on M2 Macrophages. *Frontiers in cardiovascular medicine*, *9*, 889963. Varasteh, Z., Weber, W. A., & Rischpler, C. (2022). Nuclear Molecular Imaging of Cardiac Remodeling after Myocardial Infarction. *Pharmaceuticals (Basel, Switzerland)*, *15*(2), 183.

Varela, M. L., Mogildea, M., Moreno, I., & Lopes, A. (2018). Acute Inflammation and Metabolism. *Inflammation*, *41*(4), 1115–1127.

Varki, A., Cummings, R. D., Esko, J. D., Freeze, H. H., Stanley, P., Bertozzi, C. R., Hart, G. W., & Etzler, M. E. (Eds.). (2009). *Essentials of Glycobiology*. (2nd ed.). Cold Spring Harbor Laboratory Press.

Varki, A. (2017). Biological roles of glycans. *Glycobiology*, *27*(1), 3-49.

Vera, D. R., Wallace, A. M., Hoh, C. K., & Mattrey, R. F. (2001). A synthetic macromolecule for sentinel node detection: (99m)Tc-DTPA-mannosyl-dextran. *Journal of nuclear medicine : official publication, Society of Nuclear Medicine*, *42*(6), 951–959.

Vercammen, E., Staal, J., & Beyaert, R. (2008). Sensing of viral infection and activation of innate immunity by toll-like receptor 3. *Clinical microbiology reviews*, *21*(1), 13–25.

Verjans, J. W., Lovhaug, D., Narula, N., Petrov, A. D., Indrevoll, B., Bjurgert, E., Krasieva, T. B., Petersen, L. B., Kindberg, G. M., Solbakken, M., Cuthbertson, A., Vannan, M. A., Reutelingsperger, C. P., Tromberg, B. J., Hofstra, L., & Narula, J. (2008). Noninvasive imaging of angiotensin receptors after myocardial infarction. *JACC. Cardiovascular imaging*, *1*(3), 354–362.

Verweij, N. J. F., Yaqub, M., Bruijnen, S. T. G., Pieplenbosch, S., Ter Wee, M. M., Jansen, G., Chen, Q., Low, P. S., Windhorst, A. D., Lammertsma, A. A., Hoekstra, O. S., Voskuyl, A. E., & van der Laken, C. J. (2020). First in man study of [^{18}F]fluoro-PEG-folate PET: a novel macrophage imaging technique to visualize rheumatoid arthritis. *Scientific reports*, *10*(1), 1047.

Viola, A., Munari, F., Sánchez-Rodríguez, R., Scolaro, T., & Castegna, A. (2019). The Metabolic Signature of Macrophage Responses. *Frontiers in immunology*, *10*, 1462.

Wahl, R. L., Dilsizian, V., & Palestro, C. J. (2021). At Last, [^{18}F]FDG for Inflammation and Infection!. *Journal of nuclear medicine : official publication, Society of Nuclear Medicine*, *62*(8), 1048–1049.

Waite, J. C., & Skokos, D. (2012). Th17 response and inflammatory autoimmune diseases. *International journal of inflammation*, *2012*, 819467.

Walker, J. A., & McKenzie, A. N. J. (2018). TH2 cell development and function. *Nature reviews. Immunology*, *18*(2), 121–133.

Wallace, A. M., Han, L. K., Povoski, S. P., Deck, K., Schneebaum, S., Hall, N. C., Hoh, C. K., Limmer, K. K., Krontiras, H., Frazier, T. G., Cox, C., Avisar, E., Faries, M., King, D. W., Christman, L., & Vera, D. R. (2013). Comparative evaluation of [(99m)tc]tilmanocept for sentinel lymph node mapping in breast cancer patients: results of two phase 3 trials. *Annals of surgical oncology*, *20*(8), 2590–2599.

Wallace, A. M., Hoh, C. K., Vera, D. R., Darrah, D. D., & Schulteis, G. (2003). Lymphoseek: a molecular radiopharmaceutical for sentinel node detection. *Annals of surgical oncology*, *10*(5), 531–538.

Wanat K. (2020). Biological barriers, and the influence of protein binding on the passage of drugs across them. *Molecular biology reports*, *47*(4), 3221–3231.

Wang, C., Zhang, S., Zou, Y., Ma, H., Jiang, D., Sheng, L., Sang, S., Jin, L., Guan, Y., Gui, Y., Xu, Z., & Zhong, C. (2020). A novel PET tracer ^{18}F-deoxy-thiamine: synthesis, metabolic kinetics, and evaluation on cerebral thiamine metabolism status. *EJNMMI research*, *10*(1), 126.

Wang, L., Zhang, Y., Zhang, N., Xia, J., Zhan, Q., & Wang, C. (2019). Potential role of M2 macrophage polarization in ventilator-induced lung fibrosis. *International immunopharmacology*, *75*, 105795.

Wang, Q., Biosca, M., Himo, F., & Szabó, K. J. (2021). Electrophilic Fluorination of Alkenes via Bora-Wagner-Meerwein Rearrangement. Access to β-Difluoroalkyl Boronates. *Angewandte Chemie (International ed. in English)*, *60*(50), 26327–26331.

Wang, R., Lan, C., Benlagha, K., Camara, N. O. S., Miller, H., Kubo, M., Heegaard, S., Lee, P., Yang, L., Forsman, H., Li, X., Zhai, Z., & Liu, C. (2024). The interaction of innate immune and adaptive immune system. *MedComm*, *5*(10), e714.

Wang, Y., Zhao, M., Liu, S., Guo, J., Lu, Y., Cheng, J., & Liu, J. (2020). Macrophage-derived extracellular vesicles: diverse mediators of pathology and therapeutics in multiple diseases. *Cell death & disease*, *11*(10), 924.

Weber K. T. (1997). Extracellular matrix remodeling in heart failure: a role for de novo angiotensin II generation. *Circulation*, *96*(11), 4065–4082.

Wei, W., Rosenkrans, Z. T., Liu, J., Huang, G., Luo, Q. Y., & Cai, W. (2020). ImmunoPET: Concept, Design, and Applications. *Chemical reviews*, *120*(8), 3787–3851.

Weissleder, R., & Mahmood, U. (2001). Molecular imaging. *Radiology*, *219*(2), 316–333.

Welsh J. S. (2007). Beta decay in science and medicine. *American journal of clinical oncology*, *30*(4), 437–439.

Werling, D., & Coffey, T. J. (2007). Pattern recognition receptors in companion and farm animals - the key to unlocking the door to animal disease?. *Veterinary journal (London, England : 1997)*, *174*(2), 240–251.

Westman, J., Grinstein, S., & Marques, P. E. (2020). Phagocytosis of Necrotic Debris at Sites of Injury and Inflammation. *Frontiers in immunology*, *10*, 3030.

Wetherill, R. R., Doot, R. K., Young, A. J., Lee, H., Schubert, E. K., Wiers, C. E., Leone, F. T., Mach, R. H., Kranzler, H. R., & Dubroff, J. G. (2023). Molecular Imaging of Pulmonary Inflammation in Users of Electronic and Combustible Cigarettes: A Pilot Study. *Journal of nuclear medicine : official publication, Society of Nuclear Medicine*, *64*(5), 797–802.

Wienke, D., MacFadyen, J. R., & Isacke, C. M. (2003). Identification and characterization of the endocytic transmembrane glycoprotein Endo180 as a novel collagen receptor. *Molecular biology of the cell*, *14*(9), 3592–3604.

Wurzer, A., Pollmann, J., Schmidt, A., Reich, D., Wester, H. J., & Notni, J. (2018). Molar Activity of ^{68}Ga Labeled PSMA Inhibitor Conjugates Determines PET Imaging Results. *Molecular pharmaceutics*, *15*(9), 4296–4302.

Wynn, T. A., & Vannella, K. M. (2016). Macrophages in Tissue Repair, Regeneration, and Fibrosis. *Immunity*, *44*(3), 450–462.

Wynn, T. A., Chawla, A., & Pollard, J. W. (2013). Macrophage biology in development, homeostasis and disease. *Nature*, *496*(7446), 445–455.

Xavier, C., Blykers, A., Laoui, D., Bolli, E., Vaneyken, I., Bridoux, J., Baudhuin, H., Raes, G., Everaert, H., Movahedi, K., Van Ginderachter, J. A., Devoogdt, N., Caveliers, V., Lahoutte, T., & Keyaerts, M. (2019). Clinical Translation of [^{68}Ga]Ga-NOTA-anti-MMR-sdAb for PET/CT Imaging of Protumorigenic Macrophages. *Molecular imaging and biology*, *21*(5), 898–906.

Xia, T., Fu, S., Yang, R., Yang, K., Lei, W., Yang, Y., Zhang, Q., Zhao, Y., Yu, J., Yu, L., & Zhang, T. (2023). Advances in the study of macrophage polarization in inflammatory immune skin diseases. *Journal of inflammation (London, England)*, *20*(1), 33.

Xie, B., Wang, J., Xi, X. Y., Guo, X., Chen, B. X., Li, L., Hua, C., Zhao, S., Su, P., Chen, M., & Yang, M. F. (2022). Fibroblast activation protein imaging in reperfused ST-elevation myocardial infarction: comparison with cardiac magnetic resonance imaging. *European journal of nuclear medicine and molecular imaging*, *49*(8), 2786–2797.

Xu, C., Mu, L., Roes, I., Miranda-Nieves, D., Nahrendorf, M., Ankrum, J. A., Zhao, W., & Karp, J. M. (2011). Nanoparticle-based monitoring of cell therapy. *Nanotechnology*, *22*(49), 494001.

Yadav, S., Dwivedi, A., & Tripathi, A. (2022). Biology of macrophage fate decision: Implication in inflammatory disorders. *Cell biology international*, *46*(10), 1539–1556.

Yamaguchi, A., Hanaoka, H., Pirmettis, I., Uehara, T., Tsushima, Y., Papadopoulos, M., & Arano, Y. (2015). Injection site radioactivity of (99m)Tc-labeled mannosylated dextran for sentinel lymph node mapping. *Molecular pharmaceutics*, *12*(2), 514–519.

Yan, X., Anzai, A., Katsumata, Y., Matsuhashi, T., Ito, K., Endo, J., Yamamoto, T., Takeshima, A., Shinmura, K., Shen, W., Fukuda, K., & Sano, M. (2013). Temporal dynamics of cardiac immune cell accumulation following acute myocardial infarction. *Journal of molecular and cellular cardiology*, *62*, 24–35.

Yandrapalli, S., & Puckett, Y. (2022). SPECT Imaging. In *StatPearls*. StatPearls Publishing.

Yousuf, A., Ibrahim, W., Greening, N. J., & Brightling, C. E. (2019). T2 Biologics for Chronic Obstructive Pulmonary Disease. *The journal of allergy and clinical immunology. In practice*, *7*(5), 1405–1416.

Yu S. (2006). Review of F-FDG Synthesis and Quality Control. *Biomedical imaging and intervention journal*, *2*(4), e57.

Yue, X., Yan, X., Wu, C., Niu, G., Ma, Y., Jacobson, O., Shen, B., Kiesewetter, D. O., & Chen, X. (2014). One-pot two-step radiosynthesis of a new ^{18}F-labeled thiol reactive prosthetic group and its conjugate for insulinoma imaging. *Molecular pharmaceutics*, *11*(11), 3875–3884.

Zaia J. (2023). The 2022 Nobel Prize in Chemistry for the development of click chemistry and bioorthogonal chemistry. *Analytical and bioanalytical chemistry*, *415*(4), 527–532.

Zambrano-Zaragoza, J. F., Romo-Martínez, E. J., Durán-Avelar, M.deJ., García-Magallanes, N., & Vibanco-Pérez, N. (2014). Th17 cells in autoimmune and infectious diseases. *International journal of inflammation*, *2014*, 651503.

Zammit, M., Tao, Y., Olsen, M. E., Metzger, J., Vermilyea, S. C., Bjornson, K., Slesarev, M., Block, W. F., Fuchs, K., Phillips, S., Bondarenko, V., Zhang, S. C., Emborg, M. E., & Christian, B. T. (2020). [^{18}F]FEPPA PET imaging for monitoring CD68-positive microglia/macrophage neuroinflammation in nonhuman primates. *EJNMMI research*, *10*(1), 93.

Zhang, X., Heo, G. S., Li, A., Lahad, D., Detering, L., Tao, J., Gao, X., Zhang, X., Luehmann, H., Sultan, D., Lou, L., Venkatesan, R., Li, R., Zheng, J., Amrute, J., Lin, C. Y., Kopecky, B. J., Gropler, R. J., Bredemeyer, A., Lavine, K., … Liu, Y. (2024). Development of a CD163-Targeted PET Radiotracer That Images Resident Macrophages in Atherosclerosis. *Journal of nuclear medicine : official publication, Society of Nuclear Medicine*, *65*(5), 775–780.

Zhang, Y., Hong, H., Orbay, H., Valdovinos, H. F., Nayak, T. R., Theuer, C. P., Barnhart, T. E., & Cai, W. (2013). PET imaging of CD105/endoglin expression with a $^{61/64}$Cu-labeled Fab antibody fragment. *European journal of nuclear medicine and molecular imaging*, *40*(5), 759–767.

Zhao, K., Huang, Z., Lu, H., Zhou, J., & Wei, T. (2010). Induction of inducible nitric oxide synthase increases the production of reactive oxygen species in RAW264.7 macrophages. *Bioscience reports*, *30*(4), 233–241.

Zhao, Q., Wang, Q., Wang, T., Xu, J., Li, T., Liu, Q., Yao, Q., & Wang, P. (2021). Pattern Recognition Receptors (PRRs) in Macrophages Possess Prognosis and Immunotherapy Potential for Melanoma. *Frontiers in immunology*, *12*, 765615.

Zhu J. (2015). T helper 2 (Th2) cell differentiation, type 2 innate lymphoid cell (ILC2) development and regulation of interleukin-4 (IL-4) and IL-13 production. *Cytokine*, *75*(1), 14–24.

List of Figures, Tables and Appendices

Figures

Tables

Appendices

Appendices

Appendix 1. DM automation with the intregated valves purposed for safe remote controlling radiolabelling operation. The device include heating apparatus, preparative column for purification, collection tubes inside the hotcell.

Appendix 2. This painting, titled **Mother Earth Heart**, was inspired by my scientific research on inflammation and tissue healing in infarcted hearts — where ongoing damage from inflammation coexists with the body's continuous effort to repair itself. Mother Earth Heart was exhibited in European Society of Cardiology Conference in Barcelona, Spain on 2022.

The swirling organic forms reflect the biological processes I study: the fire-like zones symbolize ongoing inflammatory injury, while the green represents the healing forces spreading to restore balance — much like how nature fights to heal after disruption.

The use of pink in this piece serves as a **symbol** — not of gender itself, but of nurturing, caregiving, softness, and emotional strength. These qualities belong to both mothers and fathers, to anyone who holds the responsibility of care and healing. Just as nature protects and regenerates life, caregiving and resilience are shared human experiences that transcend gender.

This work blends my scientific work as a woman researcher with my personal reflections on healing, caregiving, and resilience — both within the body and within emotional life.

Appendix 3 Coupling process of NIR dye AlexaFluor-488 tetrafluorophenyl to NOTA-D10CM precursor. Purification of ALEXA-488 coupled to NOTA-D10CM using spin filter by 5 time of washing with 20% EtOH in water and centrifuged for 1 hour each time (**A**) and the identification of the compound using iTLC with mobile phase water : acetronitrile (20:80) (**B**).

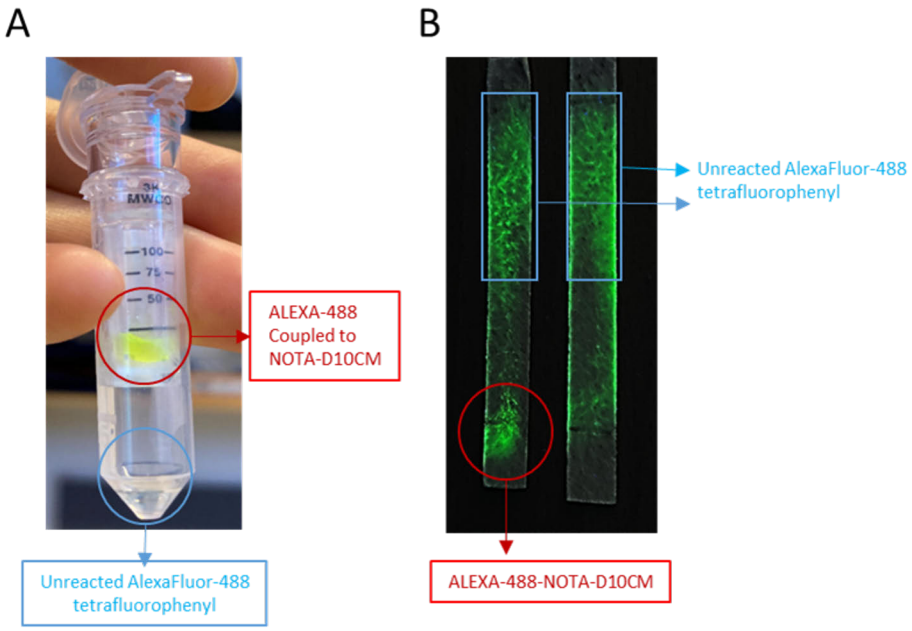

Appendix 4 Working flow on animal imaging day. ^{18}F-labeled tracer is used as the representative tracer to illustrate the workflow, starting from ^{18}F-F^{-} production, radiolabeling, *in vivo* PET animal imaging, *ex vivo* study, metabolite analysis, autoradiography and stainings.

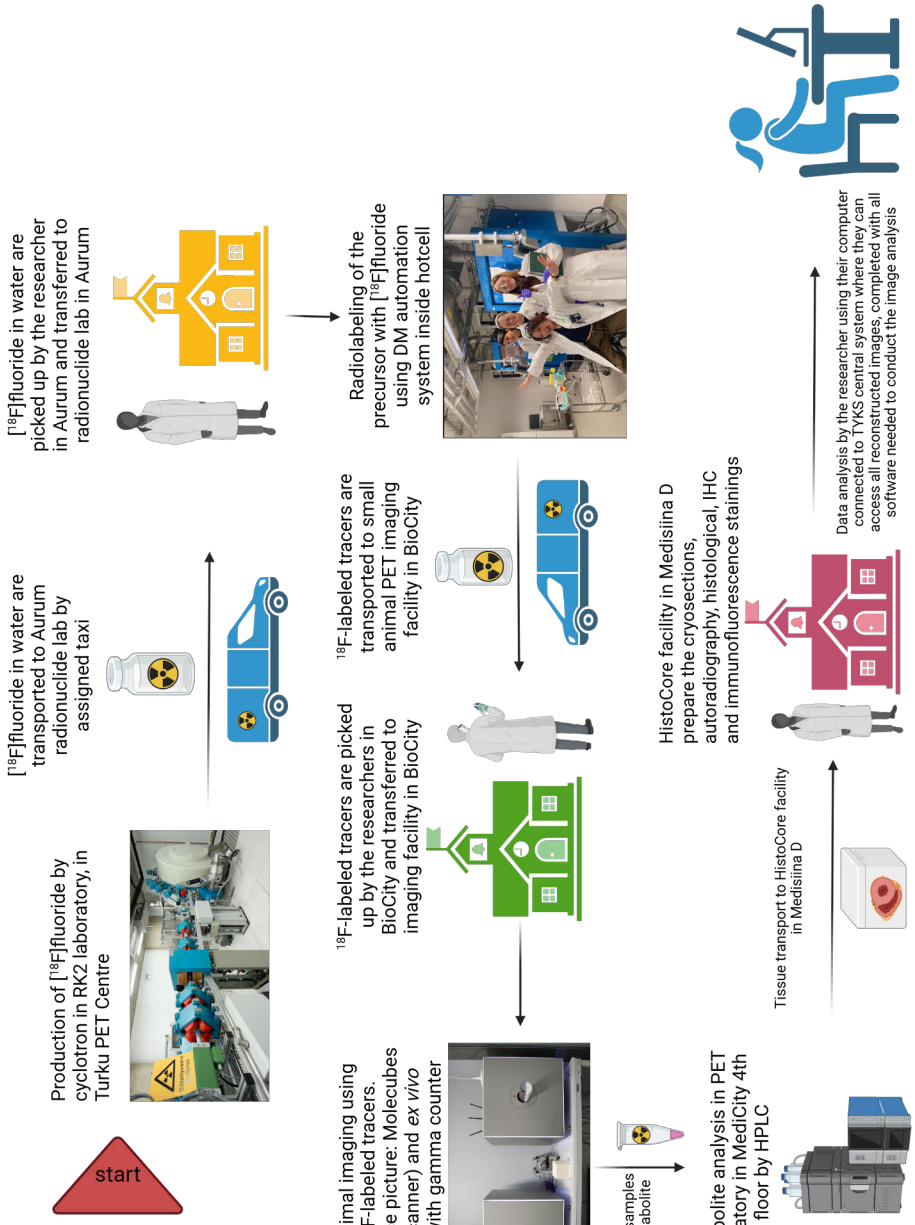

This dissertation presents the development and preclinical evaluation of [^{18}F]AlF-NOTA-D10CM, a novel PET tracer targeting the macrophage mannose receptor CD206, predominantly expressed on M2 macrophages involved in inflammation resolution and tissue repair. The tracer's ability to detect inflammation was evaluated in animal models of skin inflammation and acute myocardial infarction, compared to healthy groups and Sham control. This study covers a full pipeline of PET tracer development, including radiosynthesis, *in vivo* imaging, *ex vivo* biodistribution, autoradiography, *in vitro* assays, and metabolite analysis, confirmed by histological, immunohistochemical, and immunofluorescence staining. Complementary evaluation in CD206-deficient mice confirmed the tracer's uptake specificity. Altogether, this dissertation showcases a comprehensive framework for developing and validating a targeted PET tracer for imaging inflammation and immune response.

TURUN YLIOPISTO
UNIVERSITY OF TURKU

Painosalama, Turku, Finland 2025

ISBN 978-952-02-0253-8 (PRINT)
ISBN 978-952-02-0254-5 (PDF)
ISSN 0355-9483 (Print)
ISSN 2343-3213 (Online)